

## Uitnodiging

voor het bijwonen van de  
openbare verdediging van het  
proefschrift

**Anisotropic Nanocolloids:  
Self-Assembly, Interfacial Adsorption,  
and Electrostatic Screening**

op maandag 25 juni 2012 om  
10.30 uur in de Senaatzaal van het  
Academiegebouw

Domplein 29  
3512 JE Utrecht

en de aansluitende receptie

Joost de Graaf  
[j.degraaf1@uu.nl](mailto:j.degraaf1@uu.nl)

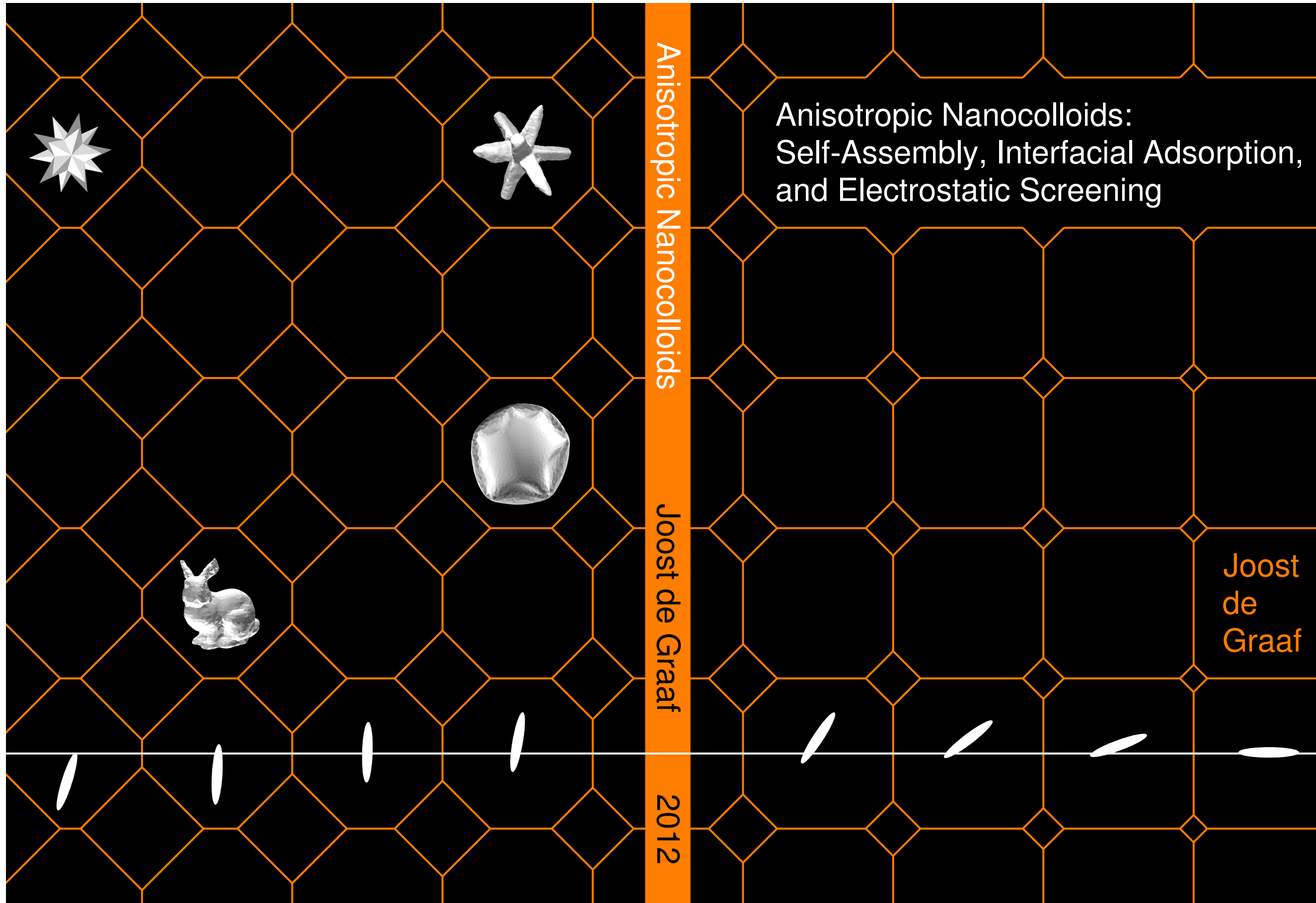
Joost  
de  
Graaf

# Anisotropic Nanocolloids: Self-Assembly, Interfacial Adsorption, and Electrostatic Screening

Anisotropic Nanocolloids

Joost de Graaf

2012



**Anisotropic Nanocolloids:  
Self-Assembly, Interfacial Adsorption, and  
Electrostatic Screening**

---

**Cover:** A series of snapshots showing the adsorption of an ellipsoidal colloid (white contour) to a flat liquid-liquid interface (white line). The colloid moves from its initial configuration (back, left-most) to its equilibrium configuration (front, right-most) by minimizing the free energy of adsorption in the most efficient way possible. (back) Four representations of anisotropic shapes studied in this thesis: an octapod, a great stellated dodecahedron, a colloidal cap, and a Stanford bunny.

PhD thesis, Utrecht University, the Netherlands, June 2012.

ISBN: 978-90-393-5797-2

A digital version of this thesis is available at <http://web.science.uu.nl/SCM/>

**Anisotropic Nanocolloids:  
Self-Assembly, Interfacial Adsorption, and  
Electrostatic Screening**

---

Anisotrope Nanocolloïden:  
Zelforganisatie, Grensvlakadsorptie en  
Elektrostatische Afscherming

(met een samenvatting in het Nederlands)

Proefschrift

ter verkrijging van de graad van doctor aan de Universiteit Utrecht op gezag van de rector magnificus, prof. dr. G. J. van der Zwaan, ingevolge het besluit van het college voor promoties in het openbaar te verdedigen op maandag 25 juni 2012 des ochtends te 10.30 uur

door

Joost de Graaf

geboren op 2 juni 1985 te Middelburg.

**Promotor:** Prof. dr. ir. M. Dijkstra  
**Co-promotor:** Dr. R.H.H.G. van Roij

# Contents

<b>1</b>	<b>Introduction</b>	<b>1</b>
1.1	Colloids and Nanoparticles	2
1.2	Structure and Interactions	3
1.3	Anisotropic Particles	4
1.4	Interfaces and Adsorption	5
1.5	Crystal-Structure Prediction	7
1.6	Charged Particles in Electrolytes	9
1.7	Thesis Outline	12
<b>2</b>	<b>Triangular Tessellation and the Free Energy of Adsorption</b>	<b>13</b>
2.1	Introduction	14
2.2	Theory and Methods	15
2.2.1	The Free Energy of Adsorption	15
2.2.2	The Triangular-Tessellation Technique	17
2.3	Interfacial Adsorption of Anisotropic Colloids	21
2.3.1	Ellipsoids	22
2.3.2	Cylinders and Spherocylinders	25
2.4	Triangular Tessellation and Confocal Microscopy	27
2.5	Conclusion and Outlook	29
2.6	Acknowledgements	30
<b>3</b>	<b>Adsorption Trajectories for a Colloidal Particle at an Interface</b>	<b>31</b>
3.1	Introduction	32
3.2	Theoretical Considerations	32
3.2.1	Adsorption Trajectories and Separatrices	32
3.2.2	The Time Dependence of Colloid Motion	33
3.3	Anisotropy and Interfacial Adsorption	34
3.3.1	Adsorption of Ellipsoidal Particles	34
3.3.2	Trajectories for Cylindrical Colloids	36
3.3.3	Special Configurations for Short Cylinders	39
3.4	Discussion	41
3.4.1	Flow Lines and the Langevin Equation	41
3.4.2	Suggestions for Improvement	43
3.5	Conclusion and Outlook	44

<b>4</b>	<b>Triangular Tessellation and Nonconvex Patterned Particles</b>	<b>45</b>
4.1	Introduction	46
4.2	Theoretical Model	46
4.3	Improved Numerical Technique	48
4.4	Interfacial Adsorption of a Truncated Cube	51
4.4.1	The Truncated Cube Model	52
4.4.2	The Free Energy of Adsorption	53
4.4.3	Equilibrium Adsorption Configurations	56
4.4.4	Comparison to the Adsorption of a Cube	59
4.5	Nonconvex Shapes and Confocal Microscopy	59
4.6	Towards Interfacial Deformation	63
4.7	Conclusion and Outlook	69
<b>5</b>	<b>The Floppy-Box Monte Carlo Algorithm</b>	<b>71</b>
5.1	Introduction	72
5.2	Characterisation of the Method	73
5.3	The Ensemble and Monte Carlo Moves	74
5.4	Construction of the Image-Lists	76
5.5	Hard-Particle Overlap Algorithms	79
5.5.1	The Method of Separating Axes	80
5.5.2	Triangular-Tessellation-Based Overlap Algorithms	81
5.6	Unphysical Distortions and Lattice Reduction	82
5.7	Soft Interactions and External Fields	84
5.8	Compression and Crystal Structure Prediction	84
5.9	Discussion and Outlook	85
5.10	Acknowledgements	86
<b>6</b>	<b>Dense Regular Packings of Irregular Nonconvex Particles</b>	<b>87</b>
6.1	Introduction	88
6.2	Method: Accuracy, Efficiency, and Applications	89
6.3	General Properties of Convex Polyhedra	92
6.4	Analytic Construction of Two Densest Packings	94
6.4.1	Rhombicuboctahedra	94
6.4.2	Rhombic Enneacontrahedra	96
6.5	Denser-Packing Crystal Structure for Enneagons	97
6.6	A Family of Truncated Cubes	99
6.7	The Phase Behaviour of Hard Octahedra	106
6.8	Conclusion and Outlook	111
6.9	Acknowledgements	112
<b>7</b>	<b>Hierarchical Self-Assembly of Octapod-Shaped Nanoparticles</b>	<b>113</b>
7.1	Introduction	114
7.2	Experimental Results	114
7.3	Monte Carlo Simulations of Octapods	116
7.3.1	Hard Octapods	116

7.3.2	Attractive Interactions	119
7.3.3	Self-Assembly into Interlocking Chains	120
7.3.4	Opportunities for Improvement	121
7.4	Van-der-Waals Interactions between Octapods	121
7.4.1	Numerical Integration of the Dispersion Forces	122
7.4.2	Hamaker Constants and Steric Repulsion	123
7.4.3	Van-der-Waals Interactions in Toluene	124
7.4.4	Relation to the Simulation Model	126
7.5	Mechanism for the Hierarchical Self-Assembly	126
7.6	Conclusion and Outlook	127
7.7	Acknowledgements	129
<b>8</b>	<b>Electrostatic Interactions between Janus particles</b>	<b>131</b>
8.1	Introduction	132
8.2	Simulations and Theory	133
8.2.1	Ewald Sums and Monte Carlo Simulations	134
8.2.2	The Poisson-Boltzmann Approach	135
8.3	Ionic Screening of Janus Particles	137
8.3.1	Method of Comparison	138
8.3.2	Homogeneously Charged Spherical Particles	141
8.3.3	Janus-Dipole Charge Distributions	143
8.3.4	Hemispherical Charge Distributions	145
8.4	Conclusion and Outlook	148
8.5	Acknowledgements	150
<b>A</b>	<b>Analytic Expressions for the Free Energy of Adsorption</b>	<b>151</b>
A.1	Semianalytic Free-Energy Expressions	152
A.2	Ellipsoids	152
A.3	Cylinders	154
A.4	Spherocylinders	155
A.4.1	Prolate Spherocylinders	156
A.4.2	Oblate Spherocylinders	158
A.5	Plane-Particle Intersection	160
A.5.1	Ellipsoids	161
A.5.2	Cylinders	162
A.5.3	Spherocylinders	163
<b>B</b>	<b>Properties of Dense Regular Packings</b>	<b>167</b>
B.1	Tables of Packing Properties	168
B.2	Dimer Structure for Truncated Tetrahedra	185
B.3	Vertices of a Rhombic Enneacontrahedron	186
B.4	Additional Visual Representations	189
	<b>References</b>	<b>193</b>
	<b>Summary</b>	<b>211</b>

<b>Samenvatting</b>	<b>215</b>
<b>Acknowledgements</b>	<b>219</b>
<b>List of Peer-Reviewed Publications</b>	<b>221</b>
<b>Oral and Poster Presentations</b>	<b>223</b>
<b>Curriculum Vitae</b>	<b>225</b>

---

## Introduction

---

In this chapter we give a brief introduction to the systems that we analysed in this thesis. We start with a description of colloids and nanoparticles and the interactions that drive them to form ordered structures. This is followed by an overview of recent developments in the synthesis of particles with anisotropic interactions. Our exposition continues with a more in-depth discussion of the three specific systems studied in this thesis: particles at an interface, crystal structures that form by self-assembly, and charged colloids in an electrolyte.

## 1.1 Colloids and Nanoparticles

In this thesis we studied systems consisting of colloids. A particle is referred to as a colloid when one of its dimensions is between 1 nm and 1  $\mu\text{m}$  [1]. The word colloid was introduced circa 1860 by Thomas Graham, who analysed the process of dialysis. He found that for certain aqueous suspensions a sticky substance consisting of - what he concluded to be - small particles formed on one side of a semipermeable parchment membrane [2]. Graham coined the term *colloid* after the Greek word for glue  $\kappa\acute{o}\lambda\lambda\alpha$  to describe his finding. Colloids are an integral part of our daily lives: paints, toothpaste, butter, lipstick, etc. all contain these particles. A few other examples of colloids are fat droplets and protein clusters suspended in a water-like medium (milk), soot particles suspended in air (smoke), air bubbles suspended in soapy water (foam), and small silica spheres stacked in a regular arrangement (opals). Besides the length scale of the constituent particles, there is another property that these systems have in common: the colloids are larger than the solvent molecules, but small enough for Brownian motion to determine their dynamics. In the case of a colloidal solid, such as an opal, the dynamics refers to the lattice vibrations.

*Brownian motion* is the random motion of a suspended particle that is caused by collisions with solvent molecules. The change of the particle's (angular) momentum induced by these collisions averages out for sufficiently large objects on the time scale that is relevant to their motion, resulting in movement according to the laws of classical mechanics only. Colloids are so small that the impact of solvent molecules strongly influences their trajectory, which, as a consequence of the molecular bombardment, contains a random component. The discovery of this random motion is credited to the botanist Robert Brown, who in 1827 reported on his study of the "particles contained in the pollen of plants" [3]. He also extended his observation to inorganic substances, even going as far as pulverizing a piece of the Sphinx and suspending the powder in water [4]. However, there are records that predate Brown's publication, such as the work of the Dutch physician Jan Ingenhousz, which was published in 1785, see Refs. [5, 6] for details. Arguably, the first time 'Brownian' motion was mentioned is in *De Rerum Natura* (Book II, verse 112 - 141) by the Roman philosopher Lucretius, who described the behaviour of dust particles in air and used their erratic motion to justify the existence of atoms [7]. With this historical hindsight it seems fitting that the theoretical description of Brownian motion by Albert Einstein and William Sutherland in terms of the interaction between molecules and larger objects [8, 9] and the subsequent experimental verification by Jean Baptiste Perrin [10, 11] led to the widespread acceptance of the atomistic view of matter in the early 20th century.

Returning to colloids after this brief excursion into Brownian motion, we modify the definition of Ref. [1] to be more representative of the particles we are interested in. In this thesis a colloid is considered a small particle, which is roughly 1 nm to 5  $\mu\text{m}$  in size and which experiences Brownian motion when suspended in an appropriate medium. The definition of a *nanoparticle* overlaps with that of a colloid: it is a microscopic object that has at least one dimension smaller than 100 nm [12]. As such, many colloids are nanoparticles, although for colloids smaller than 100 nm the term nanoparticle is preferred. The distinction is made because nanoparticles often have properties that differ substantially from the corresponding bulk material due to their small size. For instance, gold particles

dispersed in water appear red to purple, depending on their diameter [13]. The terms nanocrystal, nanocolloid, and colloidal nanoparticle are also used in literature. Note that the length-scale requirement in the definitions of Refs. [1, 12] allows colloids and nanoparticles to be macroscopic in two directions, for example, graphene sheets [14]. We are, however, not interested in such objects and we therefore consider a nanoparticle to be a colloid according to our definition with dimensions smaller than roughly 100 nm. Colloids and nanoparticles form a subset of what is referred to as *mesoscopic matter* [15], i.e., matter that has a length scale between that of atoms and macroscopic particles, which behave according to the laws of classical mechanics. For completeness, we mention the term *soft matter* that often comes up in reference to colloidal systems. Soft matter describes the property of certain materials to easily deform under external influences, such as thermal fluctuations, stress, shear, electric fields, or gravity [16]. Many colloidal systems have this ‘soft’ quality, e.g., foams and gels.

## 1.2 Structure and Interactions

The spatial organization of colloids and nanoparticles and their orientation in a phase determines the bulk properties of a material. An important advantage of this mesoscopic matter over atomic and simple molecular systems is the far greater level of structural complexity that can be achieved. In addition to the gas, liquid, glass, and solid phase found for atomic systems, colloids can form isotropic, nematic, smectic and biaxial phases [17–24], to name but a few. To exploit the unusual properties of these phases in new materials is of primary importance to materials science. Consequently, there have been many studies which focussed on controlling the formation of colloidal structures by using a wide range of colloidal building blocks [25–33]. However, only in the last decade has the synthesis and functionalization of (inorganic) nanoparticles reached the point where large samples of sufficient quality could be produced to perform structure-formation experiments [32, 34–53]. The recent success in achieving hierarchical organization of inorganic nanocrystals [54] has paved the way to design structures with even greater complexity. Here the connection with the richness of biological materials can be made, since in nature hierarchical structures are ubiquitous [55–63].

Typically, the organization of particles into a specific structure is accomplished by suspending the colloids/nanoparticles in a liquid. By imposing the volume fraction the particles can be guided into a desired state. Under these conditions there are two factors that contribute to the formation of a phase: the interaction of the particles with the medium, which induces Brownian motion, and the interactions between the particles themselves. Brownian motion allows the particles to explore phase space efficiently and the particle interactions determine the structure that this exploration results in. The process of particles achieving a desired phase/structure is called *self-assembly* when the particles (reversibly) organize in a specific way as a consequence of the particle-particle interactions [64]. The exploration of phase space and the particle-particle interactions that effect self-assembly give rise to a strong relation between the organization of colloids and nanoparticles into structures and the way in which molecular systems form phases. Not only can colloids be used to go beyond molecular matter in the structural complexity

that may be achieved, but these particles also allow us to understand processes that play a role in molecular systems [65, 66]. The use of ‘colloidal molecules’ has the advantage that the time and length scales on which self-assembly occurs are experimentally accessible by conventional optical techniques, such as ordinary light microscopy or confocal [67, 68] microscopy. This offers a tremendous opportunity to learn by analogy about dynamical processes, such as melting, nucleation, and defect formation, in molecular and atomic systems, where it is often not possible to perform a real-time analysis.

There is a large variety of particle-particle interactions that drive colloid and nanoparticle self-assembly [69]: hard-core repulsions, van-der-Waals (vdW) attractions, electric and magnetic interactions, steric repulsion, solvophobic interactions, etc. Typically, these interactions are combined to yield inter-particle forces that are weak compared to those between atoms, which explains why colloidal materials are often soft. Many of the traditionally studied systems have roughly isotropic interactions, i.e., uniform in all directions. For example, particles that are (almost) hard spheres have been synthesized [70–73]. These and other hard-sphere-like particles can self-assemble into a myriad of structures depending on the size ratio or level of polydispersity and the volume fraction that is used in experiments [40, 49, 74, 75]. By considering systems with soft (short- and long-range) interactions many more structures can be formed [76, 77]. However, the level of complexity that may be achieved for isotropic interactions pales in comparison to the possibilities that anisotropic interactions have to offer. In this thesis we examined the influence of such anisotropy on colloid and nanoparticle structures as well as the behaviour of individual particles. We mainly focussed on the shape-anisotropic and charge-patterned particles that have recently become experimentally available.

### 1.3 Anisotropic Particles

Simple shape-anisotropic particles such as plate- [79] and rod-like [24, 80, 81] particles have been available for a long time. However, recent advances in particle synthesis have yielded a huge variety of new colloid and nanoparticle building blocks [82, 83]. In particular, the number of convex shape-anisotropic particles has grown tremendously over the past years, there are for example, cubes [84–86], superballs [87, 88], octahedra [89, 90], tetrahedra [91, 92], and many more [33, 93–96]. Perhaps the most remarkable advancement is the synthesis of nonconvex (irregular) particles, e.g., dumbbells [97], colloidal clusters [29, 98], branched colloids and nanocrystals such as octapods [54, 78, 99–101] and tetrapods [102, 103], nanostars [104–106], and colloidal caps [107–109]. Figure 1.1 shows an octapod-shaped nanocrystal.

Examples of the boom in the synthesis of particles with short- and long-range anisotropic interactions can be found in Refs. [110–116], which describe the preparation of so-called Janus particles. A Janus particle [117–119] consists of two opposing parts (usually hemispheres) with different properties for the charge, contact angle, chemical functionality, etc. Even more complex forms of electric and/or solvophobic patterning have recently become available [32]. DNA-functionalization has also been employed to modify the strength and directionality of the inter-particle forces [38, 39, 46], as well as, bifunctional linkers and key-lock principles [48, 83].

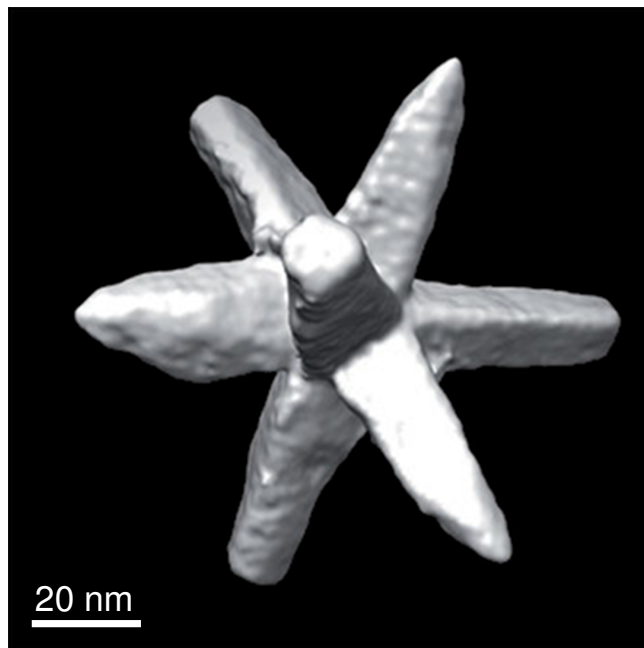


**Figure 1.1:** A high-resolution tomographical reconstruction of an eight-fold branched nanocrystal with octahedral symmetry [54]. This particle, which is referred to as an octapod, consists of a CdSe octahedral core on which eight CdS pods are grown. The synthesis of these octapods is described in detail in Refs. [54, 78].

In this thesis we restricted ourselves to study three topics, for which shape and/or interaction anisotropy plays an important role and for which the development of the aforementioned particles has had a strong impact on the research that is carried out into these topics. (i) The adsorption of single particles at a liquid-liquid interface. (ii) Crystal-structure prediction for colloidal systems and the related phase behaviour. (iii) The ion distribution around particles suspended in a dielectric medium. In the following sections we give an introduction to these topics.

## 1.4 Interfaces and Adsorption

The behaviour of small particles adsorbed to a liquid-liquid interface is not only of fundamental importance to our understanding of phase transitions and critical phenomena in 2D fluids [120–122], but also has great potential for use in industry, e.g., the encapsulation of drugs in small emulsion droplets for biomedical applications [123] and the stabilization of foams and Pickering emulsions [124–127], which are relevant to the food industry [128]. The properties of the 2D structures that form when particles are in contact with an interface have therefore received tremendous interest from the materials science community [26, 129–136]. Although many of these properties have been elucidated, little is known about the mechanisms which underlie the dynamics of adsorption. This is perhaps most clearly illustrated by a very recent experimental study [137] in which it was

shown that the dynamics of adsorption is logarithmic in nature, rather than exponential as was widely believed to be the case [138, 139].

In this thesis we aimed to address some of the longstanding questions concerning the dynamics of interfacial adsorption using a theoretical approximation to describe the complex physics that occur at an interface. We followed the approach outlined by Pawel Pieranski, who analysed the unusual strength of adsorption - binding to the interface with several thousand times the thermal energy is not uncommon - that was observed for colloids at an interface [129]. Pieranski described the adsorption of spherical colloids in terms of a free energy that is based on the surface-tension properties and contact areas of the three materials in the system: the colloid and the two liquids that form the interface. For a spherical particle of radius  $a$  this free energy  $F_P$  is a simple analytic function of the height  $h$  at which it is adsorbed to a flat interface ( $h = 0$ ):

$$F_P(h) = \pi\gamma(h - a\cos\theta)^2, \quad (1.1)$$

with  $\gamma$  the surface tension of the interface and  $\theta$  the contact angle, which is determined by the surface tensions of the three materials according to Young's equation [140]. At the equilibrium height  $h = a\cos\theta$  the free energy assumes its minimum, set to  $F_P = 0$  here. Since this free-energy approach was first formulated by Pieranski in 1980, the method has been successfully applied to gauge the adsorption behaviour for a variety of systems [141–148] and has also been extended to give a more accurate description of interfacial phenomenology [149–157].

The introduction of shape-anisotropy and contact-angle patterning introduces an orientational dependence into the free energy. Unfortunately, it proves difficult, if not impossible, to derive analytical expressions for the contact areas that contribute to the free energy as a function of the adsorption height and particle orientation, even for simple anisotropic shapes [147]. This is one of the reasons why only a few studies have been carried out that take such an orientational dependence into account [143, 144, 147, 148] compared to the far greater number that only consider one or two suitably chosen orientations of the anisotropic particle [141, 142, 145, 149, 150, 156, 158–161].

We developed a numerical method by which we can easily approximate the relevant areas for shape-anisotropic convex particles with homogeneous surface properties, regardless of the particle's orientation, to overcome the problems posed by anisotropy-induced orientational dependence. This method is based on approximating the particle's surface by triangles and we therefore refer to it as a *triangular-tessellation*-based technique [147]. Using our technique we analysed the free energy of adsorption for three colloidal shapes: ellipsoids, spherocylinders, and cylinders.

We were interested in these particles since experimental studies [26, 27, 134, 155, 162, 163] found that under certain conditions (typically high particle concentrations) rod-like particles did not lie along the interface as is expected, but were instead oriented perpendicular to it. As an initial step towards understanding these results we considered the possibility of obtaining such unusual orientations for single particles. The insights gained for these 'ultra low concentrations' may prove useful in interpreting the experimental observations at higher concentrations. We found that single ellipsoids and spherocylinders were always oriented along the interface in their equilibrium configuration within the confines of our model. However, there could also be a (meta)stable minimum in the free

energy of a cylindrical particle associated with perpendicular adsorption. On the basis of our results we concluded that the perpendicular orientations observed in the current experimental studies were probably induced by many-body effects, but that for cylinders it may be possible to prepare systems with the perpendicular orientation for greater dilutions.

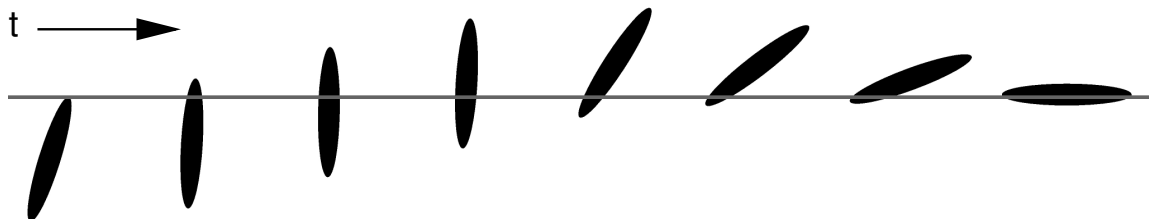


**Figure 1.2:** Snapshots of an ellipsoidal colloid (black silhouette) adsorbing to a flat interface (grey line) for various times during the adsorption process. The first snapshot shows the colloid’s orientation at its initial contact with the interface and the final snapshot shows its equilibrium position, see Chapter 3 for more information.

To further gauge the effect that shape-anisotropy has on the adsorption of particles, we introduced a simple approximation for the dynamics of this process in the overdamped regime of fluid friction. Using this model we were able to obtain the trajectory through phase space from the time of the particle’s initial contact with the interface to the time it reached the equilibrium position or became trapped in a metastable minimum. Figure 1.2 shows an example of such a trajectory. We found that the metastable minimum for cylindrical colloids is attractive to a surprisingly large range of initial-contact orientations. Although colloid adsorption was typically very strong, we also found that there may be situations where adsorption does not occur at all and a particle passes through the interface unhindered. This exotic behaviour was observed for short cylinders and large values of the contact angle.

Finally, we extend our numerical scheme to handle nonconvex contact-angle-patterned particles. We studied a system of truncated cubes, of which the facets have different surface properties, to show that our method can be applied to such patterned particles. This is also experimentally relevant, because the adsorption of these particles has recently been investigated [164]. We showed that within the confines of our model the equilibrium orientations of these truncated cubes fall into three distinct categories, depending on the details of the contact-angle pattern. We also showed that the extended method can be applied to nonconvex particles by considering an octapod-shaped particle. As a small aside we commented on the application of the triangular-tessellation-based algorithm to gain a better understanding of confocal image data and to gauge the quality of particle-tracking algorithms.

## 1.5 Crystal-Structure Prediction

The development of new materials through the organization of colloids and nanoparticles is one of the key problems facing the materials science community. Although there has been

a tremendous increase in the ability to control the ways in which colloids and nanoparticles self-assemble, there are still many unanswered questions with regards to determining the specific particle properties that result in a desired structure. In particular, predicting crystal structures based solely on knowledge of the interactions between particles has proven very challenging. This problem has therefore received a lot of attention over the past few decades [165], but truly general and effective algorithms have yet to be developed.

The synthesis of convex faceted particles (such as cubes, octahedra, and tetrahedra) has sparked a strong interest in the type of crystals these particles can form [166–174]. However, the structures that arise from the self-assembly of irregular nonconvex solids have hardly been investigated in experiments and simulations. For the latter, this can be explained by the fact that the overlap algorithm for such particles is often difficult to implement. Only recently the first attempts were made to study nonconvex colloid systems using simulations, namely for superdisks [175] and bowls [176]. Commonly used techniques to predict crystal structures rely on stimulated annealing [177, 178], make use of genetic algorithms [179, 180], or employ Monte Carlo (MC) basin-hopping methods [181]. When the free energy has a large entropic contribution, e.g., for hard particles, crystal-structure prediction becomes more complicated. However, it is still possible to obtain candidate structures using an ergodicity search algorithm [182] or the metadynamics method of Ref. [183]. A recently introduced alternative to these techniques, the floppy-box Monte Carlo (FBMC) method of Laura Filion *et al.* [75], also allows for the prediction of crystal structures for hard particles.

Our interest in the prediction of crystal structures for highly anisotropic particles stemmed not only from a materials science perspective, but also from a more mathematical perspective. In discrete geometry, number theory, and computer science there are many fundamental questions to be answered, which require the analysis of dense (regular/crystalline) packings. A particularly famous problem is Kepler’s conjecture [184], which states that for equally sized spheres the face-centred-cubic and hexagonal-close-packing structures have the greatest average density of all space-filling arrangements. This conjecture was only recently ‘proven’ [184–186] and the proof has had wide-spread implications, among which is the possibility to construct an upper bound to the packing fraction of the densest packing for nonspherical particles [167]. There are also many conjectures concerning the packing of shape-anisotropic objects that have yet to be proven, such as Ulam’s conjecture [187], which states that all (nonspherical) convex particles can achieve a monodisperse space-filling packing which is denser than that of spheres. These mathematical considerations are not just of a fundamental nature, they also have a bearing on materials science, since the densest-packed structures are thermodynamically stable at infinite pressure. These structures can therefore be used as a starting point for computer simulations of the phase behaviour at finite pressures by melting [170–172].

In this thesis we combined the FBMC method with an overlap routine based on triangular tessellation to determine the densest-packed regular structures for highly irregular (nonconvex) objects. Using this combined technique, we analysed a huge set of 142 convex polyhedra and 17 irregular nonconvex shapes to quantify the properties of their densest regular packings, see Fig. 1.3 for an example. Our investigation allowed us to extend the verification of Ulam’s conjecture to the entire set of convex particles we considered and to improve upon the densest-known packing fraction for several particle species. We also

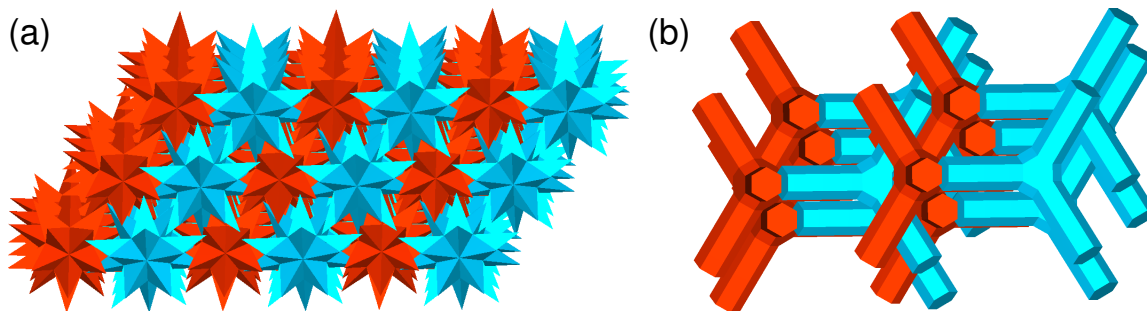


**Figure 1.3:** The densest-known regular structures for two nonconvex particles predicted by our algorithm, which combines the floppy-box Monte Carlo (FBMC) technique with a triangular-tessellation-based overlap routine, see Chapter 6 for more information. (a) Piece of the predicted crystal for great stellated dodecahedra, which has a dimer lattice structure as indicated by the use of red and blue. (b) The densest-known crystal structure for tetrapods, again a dimer lattice.

proved that we have discovered the densest-packed configurations for rhombicuboctahedra and rhombic enneacontrahedra.

To address the application of the FBMC technique to the wide variety of nanoparticle and colloid shapes that have become available, we investigated a family of truncated cubes, which interpolates between a cube and an octahedron. We obtained a stunning richness in the crystal phases that form: relatively large structural differences occurred for relatively small variations of the level of truncation. The phase behaviour of octahedra was analysed by melting the densest-packed crystal to obtain the equation of state and by performing free-energy calculations [171]. We found three phases: a liquid, a body-centred-cubic rotator phase, and a crystal phase. Our calculations showed that there is a first-order phase transition between the liquid and crystal phase. The rotator phase was shown to be metastable with respect to this transition.

Finally, we used our triangular-tessellation-based overlap routine to investigate the experimentally observed hierarchical self-assembly of octapods into interlocking chains and superstructures [54]. We also performed a Hamaker-de-Boer-type [69] theoretical calculation of the van-der-Waals (vdW) interaction between octapods. By combining our simulation results with the results of the theoretical calculation we were able to propose a self-assembly mechanism that can explain the experimental observations, see Fig. 1.4. This mechanism is based on anisotropic hard-particle and vdW forces only. The directionality of the vdW forces could be solely attributed to the peculiar shape of the octapods and the strength of the vdW interaction could be influenced by changing the polarity of the suspending medium, which proved important to guiding the hierarchical self-assembly of the octapods.

## 1.6 Charged Particles in Electrolytes

In many colloidal suspensions electrostatic interactions play an important role [21, 66, 76, 77, 131, 132, 188–191] and it is therefore important to characterise the nature of such electrostatic interactions using theory and simulations. However, even for systems

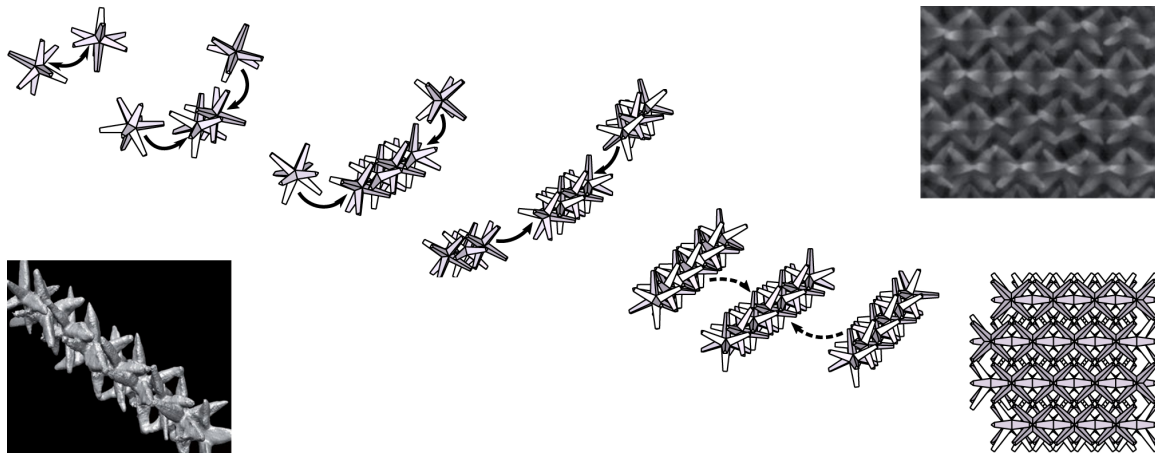


**Figure 1.4:** A sketch of the proposed mechanism for the hierarchical self-assembly of octapod-shaped nanocrystals, also see Chapter 7. Initially, linear chains with an interlocking nature are formed (solid arrows). The bottom-left inset shows a tomographical reconstruction of one of the interlocking chains found in experiments [54]. When the chains are of sufficient length they aggregate sideways (dashed arrows) to form a three-dimensional (3D) superstructure. The top-right inset shows a Scanning Electron Microscopy (SEM) image of these chain clusters [54].

containing only homogeneously charged colloids studying the physical properties by theory or by simulations is difficult due to the long range of the Coulomb interactions. These long-range interactions coupled with the presence of mobile ions that screen the colloid's bare charge present a complex many-body problem, which cannot be easily unravelled to yield effective colloid-colloid interactions. For anisotropic charge distributions the complexity of the problem increases significantly.

Several theoretical models were formulated over the years to describe the electric double layer around a charged particle and the phenomenon of screening. One of the first is a linear screening theory developed by Boris Derjaguin, Lev Landau, Evert Verwey, and Theo Overbeek, the so-called DLVO theory [192, 193]. This approximation is applicable in a limited parameter range, mostly for monovalent ions, high-polarity solvents, low surface charge, and high ionic strength. To extend the parameter regime for which theory gives an accurate description of experimental systems the nonlinear Poisson-Boltzmann (PB) theory [194, 195] was developed, which is based on a mean-field approximation that ignores ion-ion correlations. PB theory can be applied at high temperatures, high dielectric constants, low ion valence, and low salt concentrations. Strong-Coupling (SC) theory [196–198] was introduced to study charged particles in the regime where ion-ion correlations become important.

The simulation studies of charged particles in an electrolyte can roughly be divided into two categories: ones that take the ions into account explicitly (e.g., Refs. [199–204]) and ones that coarse grain the system to consider only effective colloid-colloid interactions (e.g., using a DLVO approximation [77, 205–208]). The former have the advantage that very accurate results can be obtained when ion-ion correlations or the ion's size is important. However, the use of explicit ions is computationally expensive and the system sizes that can be studied are therefore limited. The latter have the advantage

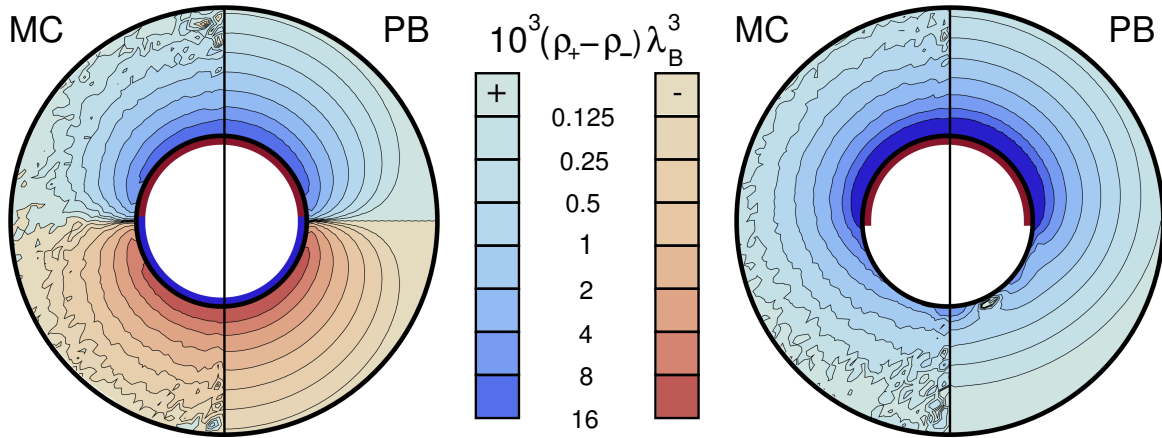


**Figure 1.5:** A contour plot of the azimuthally averaged ion excess ( $\rho_+ - \rho_-$ ) in terms of the Bjerrum length  $\lambda_B$  for the ionic screening of a dipole (left) and of a hemispherical charge distribution (right), respectively. See Chapter 8 for more information. Each contour plot is bisected by a vertical black line. The Monte Carlo (MC) simulation results are given to the left of this line and the Poisson-Boltzmann (PB) theory results to the right. The radius of the colloid is indicated by the inner black circle. The charge distribution inside the colloid is represented by a red (and blue) semicircle. For this choice of parameters there is good correspondence between the MC and PB results.

that large systems containing many colloids can be studied to determine the phase behaviour of the colloids. However, the usefulness of these simulations is limited by the quality of the coarse-graining approximation. Establishing effective interaction potentials for charged particles in an electrolyte is a good example of the synergy that can be achieved between simulations and theory. Theory is used to derive simple pair potentials for effective-interaction simulations and the validity of this theoretical approximation can be determined using explicit-ion simulations.

In this thesis we used explicit-ion Monte Carlo (MC) simulations to probe the range for which the nonlinear PB theory of Refs. [209–212] accurately describes the double layer around a charged colloid with a Janus-type charge pattern, see Fig. 1.5 for an example. This PB theory used Fourier-Legendre mode expansion to decompose the complex three-dimensional (3D) PB equation into relatively simple, coupled PB equations for the monopole, dipole, and higher-order contributions to the charge density. The ion profile that was established using MC averaging was decomposed in a similar way and this allowed us to compare the two results on a mode-by-mode basis. We introduced a set of parameters, which map out parameter space for charged Janus particles, to make the connection between our results and the field-theoretical studies that probed the applicability of DH, PB, and SC theory for homogeneously charged flat surfaces [213, 214]. Our results for spherical geometries and charge-patterned particles predict a range of validity for PB theory that is remarkably similar to the one given in Refs. [213, 214]. We are therefore confident that in this range we can construct effective pair potentials according to the methods of Ref. [212], which can be used in future simulation studies of the phase behaviour of charged Janus colloids.

## 1.7 Thesis Outline

The three topics analysed in this thesis are divided over 7 chapters and 2 appendices. The first three chapters describe our investigation of the adsorption of anisotropic colloids at a liquid-liquid interface. Chapter 2 introduces the numerical triangular-tessellation-based approach to determine the free energy of adsorption and demonstrates its effectiveness. In Chapter 3 we consider the dynamics of adsorption by applying a simple model for particle motion to our free-energy result. Finally, in Chapter 4 we extend the triangular-tessellation-based technique to handle nonconvex and contact-angle-patterned particles. We also show preliminary results for the adsorption of patterned truncated cubes. In Chapters 5 - 7 we present results obtained by our crystal-structure-prediction algorithm for irregular (nonconvex) faceted particles and we study the phase behaviour of octahedra and octapods. The method of floppy-box Monte Carlo (FBMC) is described in detail in Chapter 5. We apply this technique to determine the densest-known regular structure for a large set of polyhedra and a family of truncated cubes in Chapter 6. Here we also consider the phase behaviour of hard octahedra. In Chapter 7 we conclude this topic with an analysis of the hierarchical self-assembly of octapods into 3D superstructures using a combination of theory and simulations. We discuss our findings for particles with a Janus-type charge patterning in Chapter 8. Here we compare the results obtained by MC simulations and by nonlinear mode-expanded PB theory to determine the latter's range of validity.



---

## Triangular Tessellation and the Free Energy of Adsorption

---

In this chapter we introduce the numerical technique of triangular tessellation to determine the surface areas and contact-line length that are associated with a plane-particle intersection. Even for simple particles establishing analytic expressions for these values is a daunting challenge due to the complex geometry that is involved. Our method allows us to establish the values quickly and with a high level of precision for in principle arbitrary shapes. To demonstrate the uses of our method we consider the adsorption of a single anisotropic colloidal particle at a flat liquid-liquid interface. We formulate a simple free-energy model for this system and determine the positional and orientational dependence of the free energy for three species of particle: ellipsoids, cylinders, and spherocylinders. We establish that for ellipsoids and spherocylinders there is one minimum in the free energy, corresponding to the equilibrium configuration within the confines of our model, and that for cylinders there can be a metastable minimum as well. Finally, we consider our triangular-tessellation technique's ability to determine plane-particle cross sections. This may be of use to help understand image data obtained by confocal microscopy and to verify the quality of tracking algorithms.

## 2.1 Introduction

Small particles at liquid-liquid interfaces are of scientific interest, but can also be exploited for industrial applications. The two-dimensional (2D) particle structures [26, 129–135] that form at an interface may for example be utilized for the encapsulation of drugs in emulsion droplets for biomedical applications [123], in the stabilization of foams and emulsions [124–127], which are relevant to the food industry [128], and in many more applications [215]. The range of sizes, shapes, and material properties with which colloids can be endowed [82, 83], makes them the ideal constituents for such self-assembled macroscopic 2D structures at an interface. A more fundamental impetus to study colloid adsorption, is based on gaining a better understanding of phase transitions and critical phenomena of 2D systems, by modelling these using nanoparticles at an interface [120–122]. Finally, the study of anisotropic colloids adsorbed to an air-water interface can also be relevant to biology [216].

Many theoretical investigations of colloids at an interface are based on studies into the behaviour of a single particle. The stability of an adsorbed particle and the manner in which it attaches to the interface gives insight into the way particles behave at higher (2D) concentrations. The adsorption of colloids at an interface and the high level of stability this process exhibits were already considered in 1988 by Pawel Pieranski [129], who studied the free energy of adsorption for spheres based on surface-tension arguments. This ground breaking work was built upon to encompass effects, such as line tension [150, 155], capillary rise [149, 153, 154, 156, 157], interfacial deformation due to gravity on the particle [153], surface heterogeneities [145, 146], and electrostatic effects [151–153]. The influence of particle shape on colloid adsorption has also been considered for, for instance, ellipsoids [143, 144, 150, 156], other rod-like [143, 155] and platelet-like [150, 156] particles, as well as more complex shapes [163, 217]. Despite this tremendous effort, there are still many unanswered questions concerning the adsorption of a single particle at an interface.

To the best of our knowledge only two theoretical studies were undertaken into the effects of anisotropic particles adsorbed to the interface as a function of the particle's orientation [143, 144] prior to our investigation. Other studies were limited to several highly symmetric particle orientations, namely parallel or perpendicular to the interfacial normal [145, 149, 150, 156, 158–161], which were also found in experimental systems [26, 27, 134, 155, 162, 163]. However, the insights gained by the theoretical investigation of these two orientations cannot be used to analyse the mechanisms by which colloids end up in the parallel or perpendicular orientation, or why these particular orientations are preferred over others. One of the reasons why only a few studies considered the orientational dependence for anisotropic colloids adsorbed at an interface is the complex geometry that is involved. Recently, we overcame this problem by using the triangular-tessellation technique to numerically determine the free energy of adsorption as a function of the particle's position and orientation [147].

In this chapter we examine the adsorption of homogeneous uniaxial convex colloids at liquid-liquid interfaces. In Section 2.2.1 we formulate a set of equations that specify the free energy of adsorption, in the approximation outlined by Pieranski. Determining this free energy proves to be technically difficult for all but the most basic shapes. Therefore, we introduce a numerical method in Section 2.2.2, which we refer to as the

*triangular-tessellation technique*, to compute the free energy of adsorption. The accuracy of this technique is verified by comparing the numerical results with results obtained by a semianalytic approach for ellipsoids, cylinders, and spherocylinders in Section 2.3. These semianalytic results are derived by methods similar to those used in Refs. [143, 144] and are presented in Appendix A. We also investigate the properties of our model and recover the expected equilibrium orientations for ellipsoids and cylinders in Section 2.3. Finally, we consider the application of the triangular-tessellation technique to a seemingly unrelated field, namely that of 2D confocal microscopy in Section 2.4.

## 2.2 Theory and Methods

In this section we describe the theoretical model we used to study the adsorption of a single anisotropic colloid at a liquid-liquid interface. We also introduce the numerical technique of triangular-tessellation by which the orientational dependence of colloid adsorption may be investigated.

### 2.2.1 The Free Energy of Adsorption

We consider a planar liquid-liquid interface separating two homogeneous halfspaces,  $M_1$  and  $M_2$ , and a solid uniaxial convex colloid adsorbed at this interface, with  $a$  the length of its rotational symmetry semiaxis,  $b$  the length of the perpendicular semiaxis, and  $m \equiv a/b$  its *aspect ratio*. The normal of the interface is parallel to the  $z$ -axis of a Cartesian coordinate frame. The *depth*  $z$  gives the position of the interface with respect to the particle's centre, at which the origin of the system is located, and is measured along the  $z$ -axis, see Fig. 2.1. The *polar angle*  $\phi \in [0, \pi/2]$  measures the angle between the colloid's rotational symmetry axis and interfacial normal. For convenience we assume that this axis is located in the  $xz$ -plane.

In the spirit of Pieranski's approximation [129] we consider only surface-area and contact-line contributions to the free energy of adsorption. There are four surface areas that contribute to this free energy: (i) the surface area of the colloid above the interface  $S_1$ , (ii) the surface area of the colloid below the interface  $S_2$ , (iii) the surface area excluded from the interface by the presence of the colloid  $S_{12}$ , and (iv) the total surface area of the interface (without adsorption)  $A$ . The contact line has length  $L$  and the total surface area of the colloid is  $S = S_1 + S_2$ . For a specific configuration, characterised by  $z$  and  $\phi$ , the free energy of adsorption can be written as

$$V(z, \phi) = \gamma_{12}(A - S_{12}) + \gamma_{1c}S_1 + \gamma_{2c}S_2 + \tau L, \quad (2.1)$$

where  $\gamma_{12}$  is the  $M_1$ - $M_2$  interfacial surface tension,  $\gamma_{1c}$  is the  $M_1$ -colloid surface tension,  $\gamma_{2c}$  is the  $M_2$ -colloid surface tension, and  $\tau$  is the line tension [150, 161]. We have dropped the  $z$  and  $\phi$  dependence of  $S_1(z, \phi)$ ,  $S_2(z, \phi)$ ,  $S_{12}(z, \phi)$ , and  $L(z, \phi)$  to simplify the notation.

It is convenient to define the free energy of adsorption with respect to a reference state, in this case the particle being completely immersed in  $M_1$ . This free energy

$$F(z, \phi) = (\gamma_{1c} - \gamma_{2c})(S_1 - S) - \gamma_{12}S_{12} + \tau L, \quad (2.2)$$

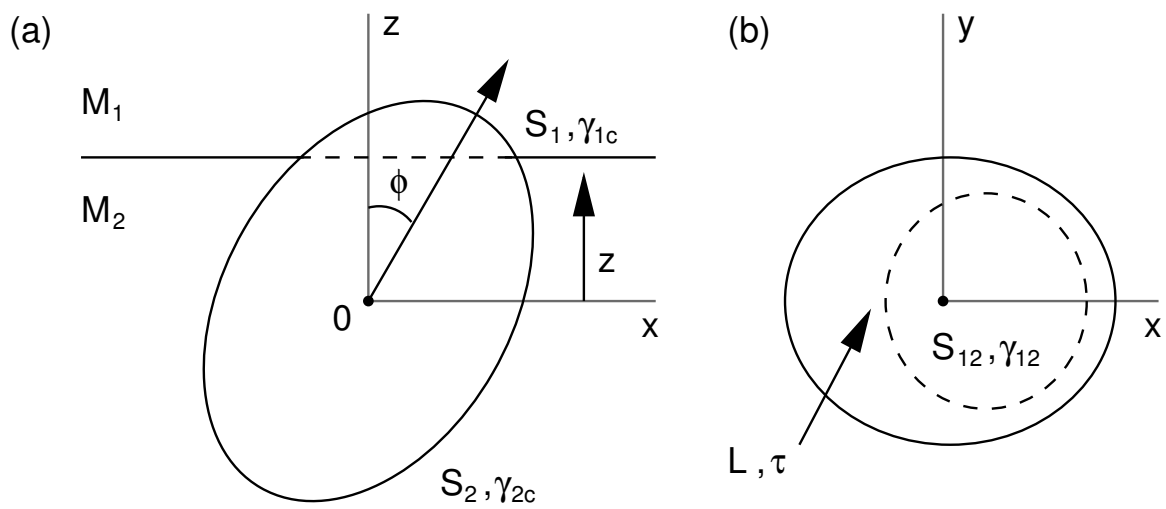


**Figure 2.1:** A side and top view of an ellipsoidal colloid at a liquid-liquid interface, which indicate the parameters used in our model. (a) The  $xz$ -plane cross section of the colloid and interface. The interface (solid line) located at depth  $z$ , measured from the centre of the colloid (marked by a dot), dividing medium 1 ( $M_1$ ) and medium 2 ( $M_2$ ). The polar angle  $\phi$  measures the angle between the interfacial normal and the colloid's rotational symmetry axis. The interface has total area  $A$  with corresponding interfacial tension  $\gamma_{12}$ . The surface area of the colloid above the interface is denoted by  $S_1$ , with  $\gamma_{1c}$  the  $M_1$ -colloid surface tension, and the surface area of the colloid below the interface is denoted by  $S_2$ , with  $\gamma_{2c}$  the  $M_2$ -colloid surface tension. The presence of the adsorbed colloid causes an area  $S_{12}$  to be excluded from the interface, as indicated by the dashed curve. (b) The excluded surface area - the region enclosed by the dashed curve, which itself represents the contact line. The contact line has length  $L$  and corresponding line tension  $\tau$ . The projected outline of the colloid (solid ellipse) is also shown.

is obtained by subtracting  $\gamma_{12}A + \gamma_{1c}S$  from  $V(z, \phi)$ , such that  $F(z, \phi)$  is zero when the colloid is completely immersed in  $M_1$ . Only systems with  $\gamma_{12} \neq 0$  are considered and we write  $\gamma_{12} \cos \theta = \gamma_{1c} - \gamma_{2c}$ , where the *contact angle*  $\theta$  is introduced via Young's equation [140]. Using this definition Eq. (2.2) reads

$$F(z, \phi) = \gamma_{12}[(S_1 - S) \cos \theta - S_{12}] + \tau L. \quad (2.3)$$

The contact angle  $\theta$  is a quantity, which depends only on the physical properties of the three components present at the interface, whereas the polar angle  $\phi$  is a degree of freedom of the particle.

Dividing the free energy of adsorption by  $\gamma_{12}S$  and introducing  $z = z^* \sqrt{a^2 + 2b^2}$ , the following reduced free energy of adsorption is derived

$$f(z^*, \phi) = \frac{F(z, \phi)}{\gamma_{12}S} = \cos \theta (r_1 - 1) - r_{12} + \tau^* l, \quad (2.4)$$

where  $r_1 \equiv S_1/S$  and  $r_{12} \equiv S_{12}/S$  are surface area ratios,

$$\tau^* \equiv \frac{\tau}{\gamma_{12}\sqrt{S}}, \quad (2.5)$$

is the reduced line tension, and  $l \equiv L/\sqrt{S}$  is a reduced contact-line length. The value  $\sqrt{a^2 + 2b^2}$  is the length of the semidiagonal of a rectangular beam with sides  $2a \times 2b \times 2b$ , this normalization ensures that  $-1 \leq z^* \leq 1$  for all uniaxial rotationally symmetric convex shapes at any angle  $\phi$  with respect to the interface. Two inequalities -  $0 \leq r_1(z^*, \phi) \leq 1$  and  $0 \leq r_{12}(z^*, \phi) < 1$  - hold for any value of  $z^*$  and  $\phi$ . The reduced free energy of adsorption  $f(z^*, \phi)$  is independent of the size of the colloid, but implicitly depends on the shape of the particle.

Before we present our numerical technique, we first introduce quantities that prove useful to describe our results. The location of a minimum in the free energy of adsorption in Eq. (2.4) is denoted by  $(z_{\text{ad}}^*, \phi_{\text{ad}})$  and is referred to as an *adsorption configuration*. The corresponding free energy is  $f_{\text{ad}} \equiv f(z_{\text{ad}}^*, \phi_{\text{ad}})$ . There may be multiple minima, in which case there can be metastable adsorption configurations. For a given  $\phi$ ,  $z_{\text{det}}^*(\phi)$  is defined as the positive value of  $z^*$  for which the interface just touches the particle. The colloid is detached from the interface when  $z^* < -z_{\text{det}}^*(\phi)$  or  $z^* > z_{\text{det}}^*(\phi)$ . The quantity  $z_{\text{min}}^*(\phi)$  is defined as the value of  $z^*$  for which  $f(z^*, \phi)$  assumes its minimum for a given  $\phi$ . The corresponding free energy of adsorption is denoted by  $f_{\text{min}}(\phi) \equiv f(z_{\text{min}}^*(\phi), \phi)$ . It is a priori not excluded that for a given  $\phi$  the equi- $\phi$ -curve has two or more (metastable) minima. Often we will write  $z_{\text{det}}^*$  and  $z_{\text{min}}^*$  for  $z_{\text{det}}^*(\phi)$  and  $z_{\text{min}}^*(\phi)$  respectively, taking the polar-angle dependence to be implicit.

## 2.2.2 The Triangular-Tessellation Technique

Determining the dependence of  $S_1$ ,  $S_{12}$ , and  $L$  on  $z$  and  $\phi$ , or equivalently  $r_1$ ,  $r_{12}$ , and  $l$  on  $z^*$  and  $\phi$ , is highly nontrivial in general, and deriving analytic expressions is impractical, if not impossible, for all but the simplest of particle shapes and orientations, see Appendix A. To analyse colloids adsorbed at an interface the following numerical technique is employed.

The surface of the colloid under consideration is bijectively parametrized by two angles, namely  $\alpha_1 \in [0, 2\pi]$  (azimuthal) and  $\alpha_2 \in [0, \pi]$  (polar). A parametrization can, for instance, take the form

$$P(\alpha_1, \alpha_2) = \begin{pmatrix} r(\alpha_1, \alpha_2) \cos \alpha_1 \sin \alpha_2 \\ r(\alpha_1, \alpha_2) \sin \alpha_1 \sin \alpha_2 \\ r(\alpha_1, \alpha_2) \cos \alpha_2 \end{pmatrix}, \quad (2.6)$$

where  $r(\alpha_1, \alpha_2)$  is some suitable radial function, but many other forms are imaginable. The strip  $[0, 2\pi] \times [0, \pi]$  is divided into triangles, the vertices of which are mapped onto the surface of the particle by means of the parametrization  $P(\alpha_1, \alpha_2)$ , see Fig. 2.2. A *mapped triangle* is formed between these vertices. The object, on which the strip's triangle mesh is mapped, is referred to as being *tessellated* with triangles. The above method of modelling a 2D or 3D object by triangles (more generally polygons) is well known in computer science [218–220] and has been successfully applied to various surface-tension related problems in physics [221–223]. The surface area of the colloid is now approximated by summing the surface areas of the mapped triangles. Suppose that the vertices of a mapped triangle are given by  $\mathbf{x}$ ,  $\mathbf{y}$ , and  $\mathbf{z}$ , then its surface area is given by a simple cross-product  $|(\mathbf{z} - \mathbf{x}) \times (\mathbf{y} - \mathbf{x})|/2$ . This procedure can yield in principle arbitrary precision by sufficiently refining the triangular mesh. It should be noted that depending on the parametrization some triangles have a vanishingly small or zero contribution to the surface area. For example, in the case of a sphere several vertices coincide at the poles resulting in degenerate triangles, see Fig. 2.2. This mapping is not bijective, but only on a set of which the image has measure zero. Such zero-measure sets may be ignored, but some care should be taken that they do not introduce an unacceptable amount of noise in the numerical approximation.

The method described above can be amended in the following manner to enable calculation of  $S_1$ ,  $S_2$ ,  $S_{12}$ , and  $L$ . Suppose that the tessellated object is intersected by a plane, then some of the triangles which comprise the object lie above it and others below it. Let  $\Delta_\uparrow$  denote the set of triangles which lie strictly above the interface,  $\Delta_\downarrow$  the set of triangles which lie strictly below the interface, and  $\Delta_p$  the set of triangles which intersect the interface or touch it. The surface of the colloid is approximated by  $\tilde{S} = \sum_i \Delta_{\uparrow,i}^s + \sum_j \Delta_{\downarrow,j}^s + \sum_k \Delta_{p,k}^s$ , where the tilde indicates that this is an approximation,  $i$ ,  $j$ , and  $k$  are indices, and  $\Delta_{*,i}^s$  is the surface area of the  $i$ -th triangle  $\Delta_{*,i} \in \Delta_*$ . Each intersected triangle  $\Delta_{p,i}$  is divided into three subtriangles  $\Delta_{r,i}$ ,  $\Delta_{s,i}$ , and  $\Delta_{t,i}$  in the manner indicated in Fig. 2.3. Two of these lie on one side of the plane, and one on the other. Applying this technique to all triangles in  $\Delta_p$  a set of partitioned triangles  $\tilde{\Delta}_p$  is obtained, of which the members only have some vertices in common with the plane and do not intersect it. Let  $\tilde{\Delta}_{p,\uparrow}$  and  $\tilde{\Delta}_{p,\downarrow}$  be the sets of triangles in  $\tilde{\Delta}_p$  which lie above and below the interface respectively, and let  $\tilde{\Delta}_\uparrow = \Delta_\uparrow \cup \tilde{\Delta}_{p,\uparrow}$  and  $\tilde{\Delta}_\downarrow = \Delta_\downarrow \cup \tilde{\Delta}_{p,\downarrow}$ . Using these sets the surface areas  $S_1$  and  $S_2$  are approximated in the following way

$$\tilde{S}_1 = \sum_i \tilde{\Delta}_{\uparrow,i}^s, \quad (2.7)$$

$$\tilde{S}_2 = \sum_i \tilde{\Delta}_{\downarrow,i}^s. \quad (2.8)$$

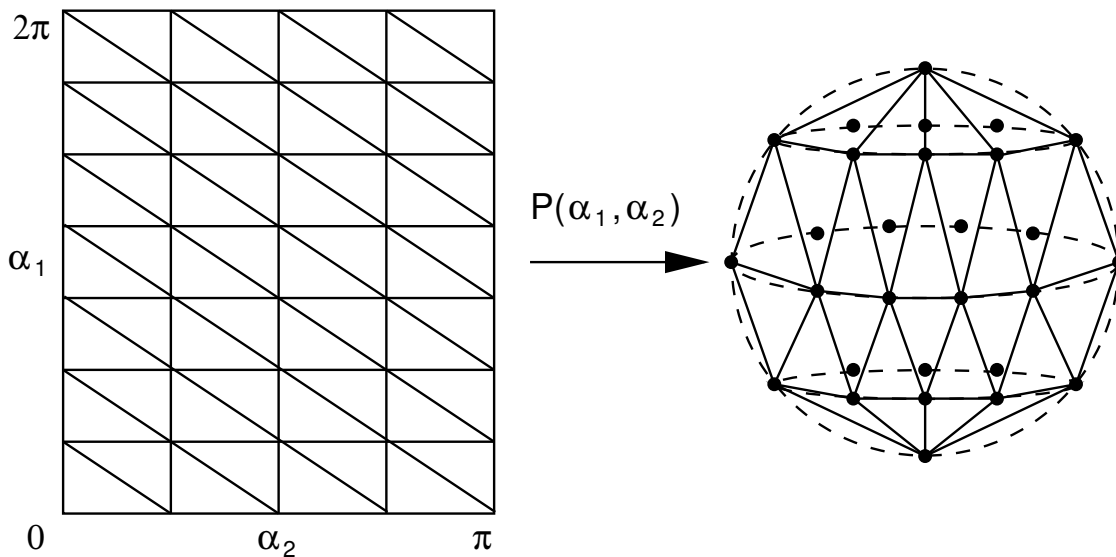


**Figure 2.2:** Example of a parametrization  $P(\alpha_1, \alpha_2)$  used to tessellate an object with triangles. The parametrization maps the vertices of triangles in the strip  $(\alpha_1, \alpha_2) \in [0, 2\pi] \times [0, \pi]$  to points on a sphere. In between these points ‘mapped triangles’ are formed corresponding to the original triangles in the strip. The points at the poles are degenerate, all vertices with  $\alpha_2 = 0$  and  $\alpha_2 = \pi$  coincide at the north and south pole, respectively. Only the front half of the sphere is tessellated for clarity.

Note that by virtue of this *triangular-tessellation technique* the equality  $\tilde{S} = \tilde{S}_1 + \tilde{S}_2$  still holds, which can be used as a consistency check.

From the set of triangles  $\tilde{\Delta}_p$  the points where the plane intersects the original tessellation are extracted. These points form a 2D data set that approximates colloid-interface cross section, i.e., the shape of the surface excluded from the interface, see Fig. 2.4. From this collection of points  $S_{12}$  and  $L$  can be computed. Typically the boundary consists of several hundred grid points, depending on the size of the triangular mesh. The approximate surface area  $\tilde{S}_{12}$  is obtained by means of trapezoidal integration, which is applied to the points above and below the  $x$ -axis after sorting these by increasing  $x$ -coordinate. Because we assume that the colloid is convex, this procedure may be applied, i.e., the plane-particle intersection is a connected convex set. However, for nonconvex colloids the surface excluded from the interface can consist of two or more disjoint nonconvex pieces. Such complex sets require a more general algorithm to calculate the surface area, see Chapter 4. A straightforward implementation of the sorting algorithm can introduce significant numerical noise into the value of  $\tilde{S}_{12}$ , as illustrated in Fig. 2.4a. This problem can easily be overcome by constructing the convex hull of the data set, Fig. 2.4b. Considering the convex hull does come at the price of reducing the number of data points, however, for several hundred grid points the loss of precision is negligible. The convex hull of the boundary points is also used to determine  $\tilde{L}$ , the approximate length of the contact line.

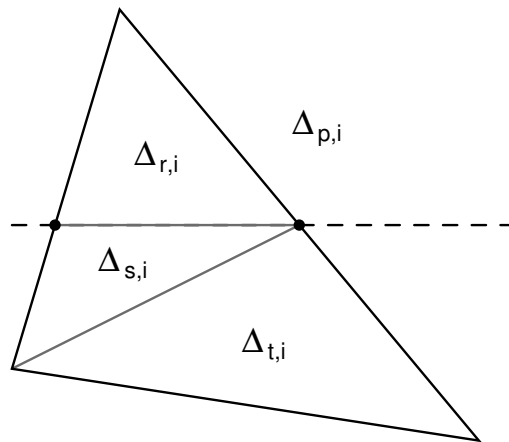


**Figure 2.3:** An example of the subdivision applied to a triangle that intersects the interface (dashed line). The triangle  $\Delta_{p,i}$  can be cut into three pieces,  $\Delta_{r,i}$ ,  $\Delta_{s,i}$ , and  $\Delta_{t,i}$  as indicated above. In this case, the first piece lies above the interface and the second and third piece below it. The two new vertices (thick dots) are formed by the subdivision. These are located at the interface.

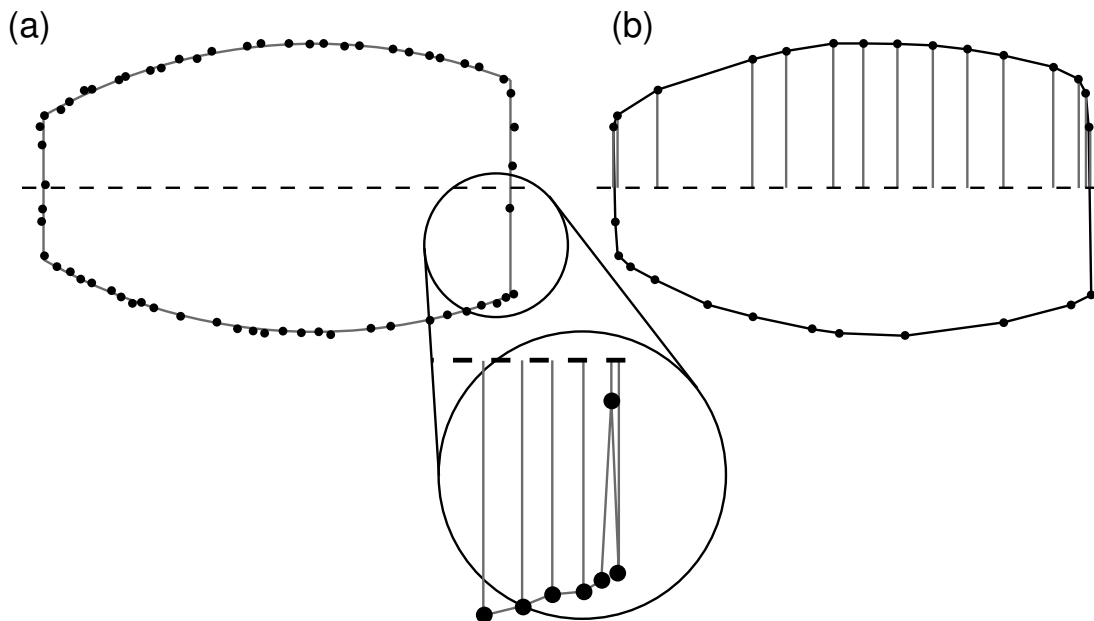


**Figure 2.4:** A sketch of the procedure used to determine the area  $S_{12}$  of the surface excluded from the interface by the presence of the particle. (a) The boundary points of the intersection of a colloidal cylinder with a planar interface - obtained using the triangular-tessellation technique, together with its actual outline (full curve). The inset shows the error introduced by not constructing a convex hull. (b) Only those points which are in the convex hull of the original set. The surface area  $S_{12}$  is computed using trapezoidal integration as shown for the area above the  $x$ -axis. From the convex hull the length of the contact line  $L$  can also be determined.

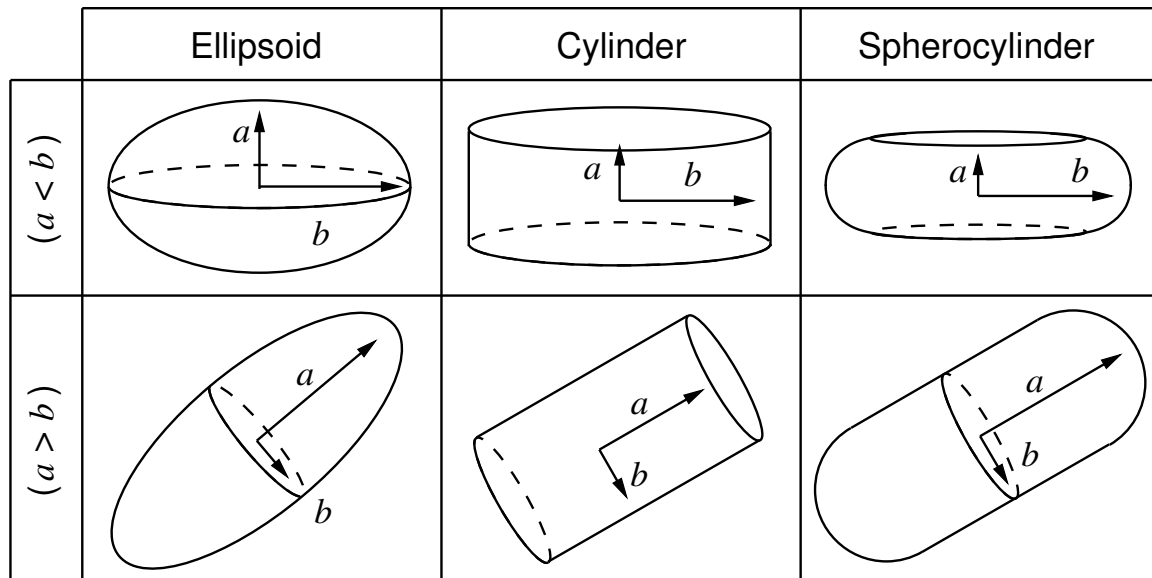


**Figure 2.5:** Impression of the various colloidal shapes considered in this chapter. The top row represents oblate particles ( $a < b, m < 1$ ), the bottom row prolate particles ( $a > b, m > 1$ ). Note the difference in shape between oblate and prolate spherocylinders.

## 2.3 Interfacial Adsorption of Anisotropic Colloids

In this section we discuss the free energy of adsorption for several particle shapes, namely ellipsoids, cylinders, and spherocylinders, as shown in Fig. 2.5. We focus on these three types of particle, as they are frequently used to model experimentally available colloidal platelet- and rod-like colloids in theoretical work and computer simulations [224–227]. In addition, these particle shapes can smoothly transition from *prolate* ( $m > 1$ ) to *oblate* ( $m \leq 1$ ) aspect ratios, and they have relatively simple parametrizations. For a prolate spherocylinder the length of the long semiaxis  $a$  includes the hemispherical caps. The semiaxis  $b$  includes the rounded side of an oblate spherocylinder. We refer to Section 4.6 for a more in-depth analysis of spherical colloids.

Our investigation limited itself to two aspect ratios  $m = 1/4$  and  $m = 4$ . We considered  $\cos \theta = -1/2$  and several values of  $\tau^*$ , where we chose  $\cos \theta < 0$  such that the particle prefers  $M_1$ . The line tension can be both positive and negative [228] and it is currently believed that  $|\tau| \approx 10^{-11}$  N/m gives the most reasonable values [228, 229]. However, we often used values outside this range to better illustrate the effects of line tension and make visual comparison to the results of Ref. [143] possible. The value of the contact angle is experimentally reasonable [230].

For the triangular tessellation we employed equidistant meshes with  $200 \times 200$  to  $400 \times 400$  vertices, which were mapped onto the shapes of interest using various parametrizations resulting in a heterogeneous tessellation. For future reference we denote a  $N \times N$ -vertex grid as a  $N^2$ -vertex grid, with  $N$  the number of vertices. Our choice for the numerical approximation yielded fractional uncertainties in the range  $10^{-3}$  to  $10^{-5}$  for the surface areas and contact-line length when compared to the semianalytic results given in Appendix A. The term semianalytic implies that one dimensional integrals need to be numerically eval-

uated to obtain a value. More than 5,000 nonequidistant grid points were used to ensure convergence of the numerical integration to within a fractional deviation of  $10^{-6}$  (the magnitude was determined using grid reduction). Higher accuracy triangular-tessellation results were obtained using meshes of  $1,000^2$  vertices, although in most cases these results were indistinguishable from the  $400^2$ -vertex or the semianalytic results. We are therefore confident that the numerical scheme is sufficiently stable to be applied to shapes for which we have not performed semianalytic verification.

### 2.3.1 Ellipsoids

We calculated the free energy of adsorption  $f(z^*, \phi)$  for an ellipsoid with aspect ratio  $m = 4$ . Figure 2.6a shows  $f(z^*, \phi)$  in a 3D representation as a function of the depth  $z^*$  and the polar angle  $\phi$  for  $\tau^* = 0$ . In Figs. 2.6(b-f) we give  $\phi$ -sections of the free-energy landscape for several values of  $\tau^*$ . The triangular-tessellation and semianalytic results agree within the line width of the curves, i.e., the relative uncertainty is lower than  $10^{-3}$  for all grid points.

For this ellipsoid we found that for  $\tau^* < 0$  there is a single minimum in all  $\phi$ -sections of the free-energy landscape. This single minimum, located in the range  $z^* \in [-z_{\text{det}}^*, z_{\text{det}}^*]$ , became more shallow with increasing  $\tau^*$  and eventually shifted to a desorbed state with  $z^* < -z_{\text{det}}^*$  and  $f_{\text{min}}(\phi) = 0$ . That is, the particle preferred to be detached from the interface and moved freely in  $M_1$ . For certain  $\tau^* > 0$  a  $\phi$ -section had two minima, for example, when  $\tau^* = 0.05$  and  $\phi = \pi/2$ , see Fig. 2.6f. The absolute minimum was given by the detached state with  $z^* < -z_{\text{det}}^*$ , and a metastable minimum may be observed for  $z^* \in [-z_{\text{det}}^*, z_{\text{det}}^*]$ . For sufficiently positive  $\tau^*$  the presence of this local minimum appeared to be dependent on the value of  $\phi$ . For  $\tau^* = 0.025$ , for instance, we found a local minimum with  $z^* \in [-z_{\text{det}}^*, z_{\text{det}}^*]$  when  $\phi \gtrsim 0.3\pi$ , but this minimum was not present for the  $\phi \lesssim 0.3\pi$  sections, see Figs. 2.6(b-f).

The presence of a local metastable minimum with  $z^* \in [-z_{\text{det}}^*, z_{\text{det}}^*]$  seemed to be related to the appearance of *adsorption barriers* in the free energy for sufficiently positive  $\tau^*$ . The colloid has to cross such a barrier to adsorb at the interface from a completely immersed state. This behaviour is most clearly visible in Fig. 2.6f for  $\phi = \pi/2$  and  $\tau^* = 0.025$ . The height of the barriers varied with the value of the polar angle and they became more pronounced with increasing  $\tau^*$ . These barriers are quite intriguing, since they can prevent a particle from reaching its lowest free-energy state, when it is initially introduced in its least favoured medium. The above results agree with the findings in Ref. [144] and are similar to observations of Ref. [143], where the formation of barriers was also observed. There are, however, several differences between our results and those of Ref. [143], i.e., the expressions in Appendix A and in Ref. [143] do not agree completely. Apart from minor typographical errors, there is a problem with the definition of subdomains on which the equations are defined, as well as the way in which quantities are reduced. Because of notational differences these problems are not immediately obvious, but when comparing the numerical results it is clear that the adsorption barriers induced by the line tension are far less pronounced in our case. We believe that the way in which  $\tau$  is made dimensionfree in Ref. [143] violates scale invariance, but from the description given this is impossible to determine. Despite the discrepancies with previously established results, we are confident

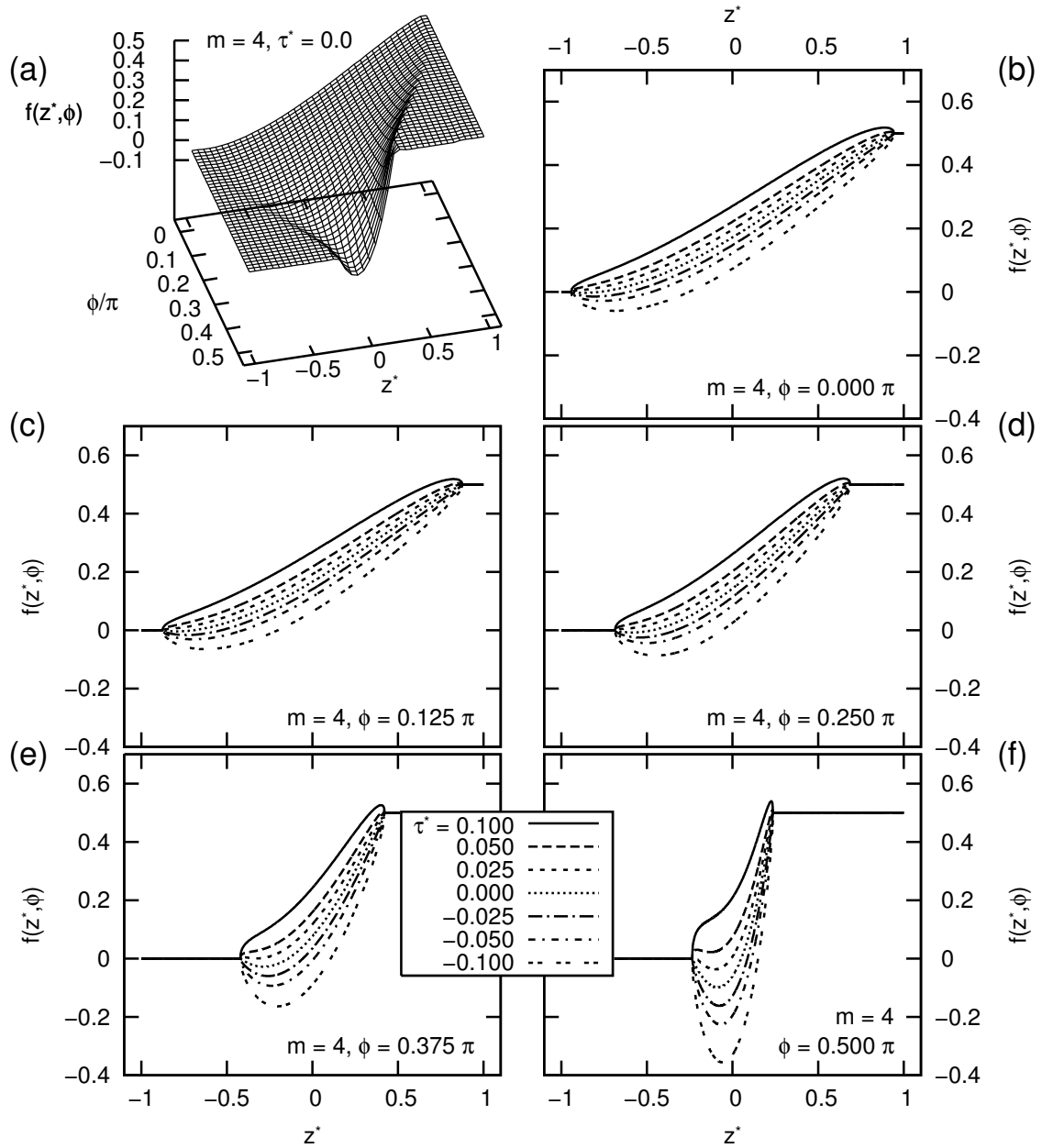


**Figure 2.6:** The free energy of adsorption  $f(z^*, \phi)$  for an ellipsoid with aspect ratio  $m = 4$  and for  $\cos \theta = -1/2$ . (a) 3D representation of the free-energy landscape, i.e.,  $f(z^*, \phi)$  as a function of the depth  $z^*$  and the polar angle  $\phi$  for  $\tau^* = 0$ . (b - f) Several  $\phi$ -sections of this free energy for  $\phi = 0, \pi/8, \pi/4, 3\pi/8$ , and  $\pi/2$  respectively, which show  $\tau^* = -0.1, -0.05, -0.025, 0, 0.025, 0.05$ , and  $0.1$ . The central dotted line in each graph corresponds to a section of the landscape in (a):  $\tau^* = 0$ . Note the appearance of free-energy barriers for  $\tau^* > 0$ , which must be crossed for the particle to adsorb at the interface. When  $\tau^* > 0.05$  the free energy does not have a minimum in the adsorbed state.

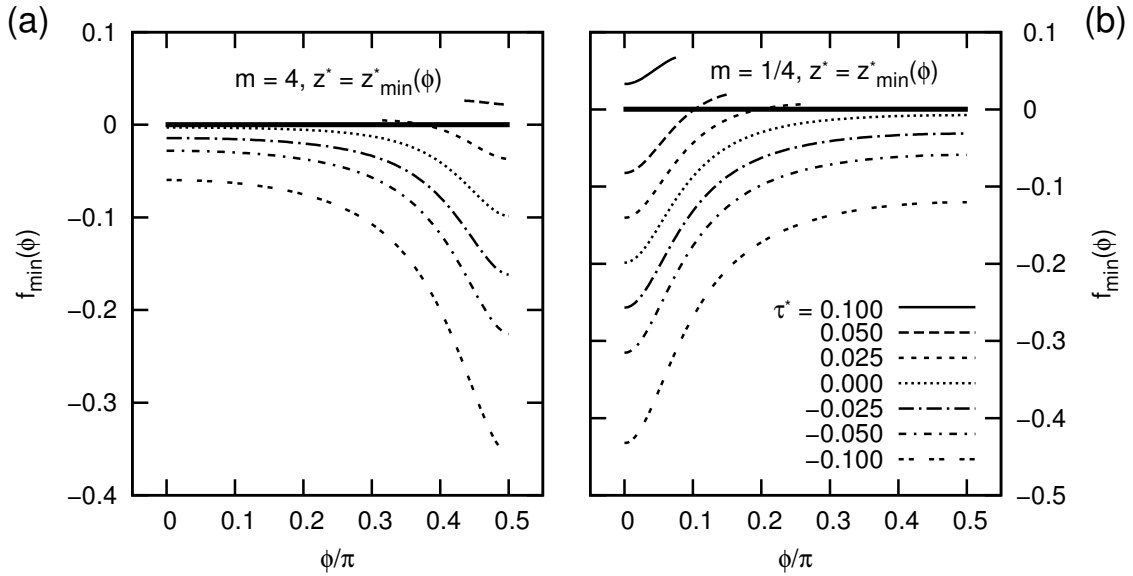


**Figure 2.7:** The minimum free energy of adsorption  $f_{\min}(\phi)$  for ellipsoids with aspect ratio  $m = 4$  (a),  $m = 1/4$  (b),  $\cos \theta = -1/2$ , and several values of the line tension  $\tau^*$ . The thick line indicates  $f_{\min}(\phi) \equiv 0$ , which is the value of the minimum for  $\tau^* \gg 0$ . We also show the metastable part, i.e., secondary minima with  $f_{\min}(\phi) > 0$  for completeness. For  $m = 4$  and  $\tau^* = 0.1$  (a) there is no local minimum in the free energy for  $z^* \in [-z^*_{\text{det}}, z^*_{\text{det}}]$ , in correspondence with the results of Fig. 2.6.

that our results are correct, since we used two independent methods to obtain the same results within numerical uncertainty.

Another way of visualizing the important features of the free-energy landscape is by using  $f_{\min}(\phi)$  curves. We determined for which  $z^* \equiv z^*_{\min}$  the free energy of adsorption  $f(z^*, \phi)$  is minimal as a function of  $\phi$ . Figure 2.7 shows the associated free energy  $f_{\min}(\phi) \equiv f(z^*_{\min}, \phi)$  for ellipsoids with  $m = 4$ ,  $m = 1/4$ ,  $\cos \theta = -1/2$ , and several  $\tau^*$  corresponding to the choices in Fig. 2.6. For certain  $\tau^* > 0$  parts of the  $f_{\min}(\phi)$  curve became metastable with respect to the desorbed state. This local minimum did not appear for all values of  $\phi$ , which is in agreement with the observations in Fig. 2.6(d-f). For  $\tau^* \gg 0$  the configuration where the colloid is immersed in medium  $M_2$ , was also found to be metastable, since the particle was prevented from moving into the preferred medium by the formation of a barrier at  $z^* \approx z^*_{\text{det}}$ , also see Fig. 2.6.

The absolute minimum in the free energy of adsorption is located somewhere on the (stable)  $f_{\min}(\phi)$  curve, per definition. When  $m = 4$  the equilibrium configuration was achieved for  $\phi_{\text{ad}} = \pi/2$  and when  $m = 1/4$  for  $\phi_{\text{ad}} = 0$  ( $\tau^* \leq 0$ ). This observation proved to hold in general for ellipsoids:  $\phi_{\text{ad}}$  is determined solely by the aspect ratio and assumes values  $\phi_{\text{ad}} = 0$  for  $m < 1$  and  $\phi_{\text{ad}} = \pi/2$  for  $m > 1$ . When  $m = 1$  the particle is a sphere and the problem is ill defined. We verified this property for ellipsoids with  $m \in [0.05, 20]$ . We found that  $f_{\min}(\phi)$  is strictly monotonic for  $\tau^* \leq 0$ , thereby also showing that there is only a single minimum in the free energy.

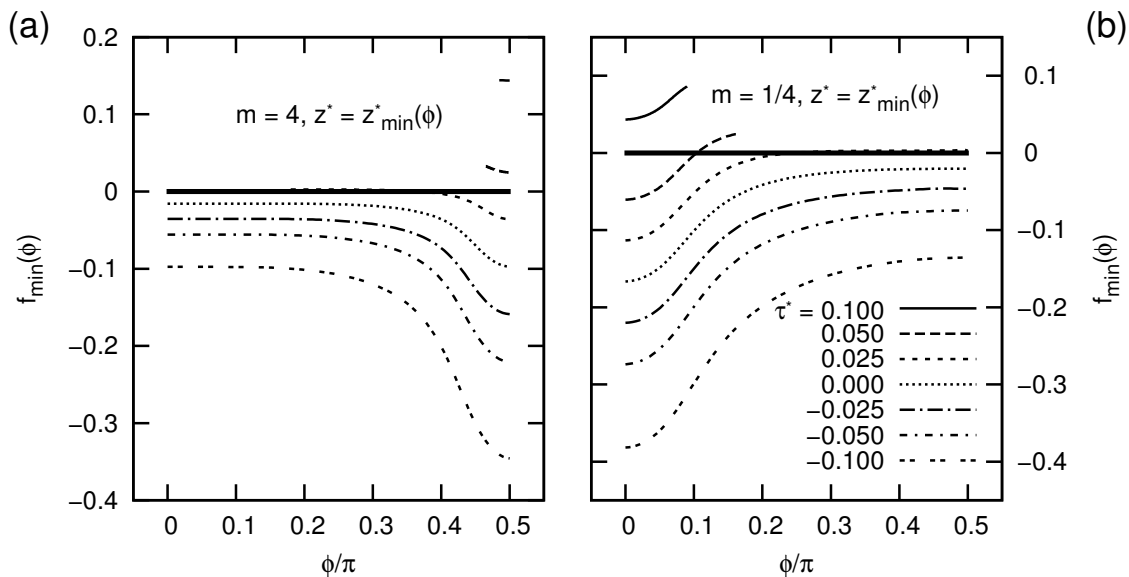


**Figure 2.8:** The  $f_{\min}(\phi)$  curves for a spherocylinder with aspect ratio  $m = 4$  (a),  $m = 1/4$  (b),  $\cos \theta = -1/2$ , and several values of the line tension  $\tau^*$ . The thick line indicates  $f_{\min}(\phi) \equiv 0$ , which is the stable minimum for  $\tau^* \gg 0$ . Note that in both graphs there is only one  $\phi_{\text{ad}}$  per minimum curve.

### 2.3.2 Cylinders and Spherocylinders

We show  $f_{\min}(\phi)$  for spherocylinders in Fig. 2.8 for  $m = 4$  (a),  $m = 1/4$  (b),  $\cos \theta = -1/2$ , and several values of  $\tau^*$ . There is only one minimum per  $f_{\min}(\phi)$  and the curves behave monotonically. Further investigation revealed that for spherocylinders  $\phi_{\text{ad}}$  is also completely determined by the aspect ratio  $m$ , i.e.,  $\phi_{\text{ad}} = 0$  for  $m < 1$  and  $\phi_{\text{ad}} = \pi/2$  for  $m > 1$ , when  $\tau^* \leq 0$ . For  $\tau^* > 0$  adsorption barriers were observed.

Figure 2.9 shows  $f_{\min}(\phi)$  for cylinders with  $m = 4$  (a) and  $m = 1/4$  (b),  $\cos \theta = -1/2$ , and several values of  $\tau^*$ . The results for cylindrical particles were qualitatively different to those of the ellipsoid and spherocylinder. (i) We found two minima in a single  $f_{\min}(\phi)$  curve. For  $m = 4$  the absolute minimum had a polar angle  $\phi_{\text{ad}} = \pi/2$ , which corresponds to the particle lying flat on the interface. The metastable minimum was achieved for  $\phi_{\text{ad}} = 0$  and corresponded to the particle being oriented perpendicular to the interface with one of its disk-shaped caps flush with the interface, but otherwise completely immersed in  $M_1$ . The free-energy reduction obtained by excluding a disk from the interface proved to be sufficient to generate a local metastable minimum. This result is similar to that derived in Ref. [155], where the possible stability of such a configuration was shown. However, our result confirms that it is a truly metastable configuration, since a barrier has to be crossed to reach the equilibrium configuration, also see Chapter 3. (ii) We observed a kink in some of the  $f_{\min}(\phi)$  curves, see Fig. 2.9b. This feature appeared to be related to the sharp transition between the shaft and caps of the cylinder, which gives rise to ridges in the free-energy landscape, also see Chapter 3.

Similar to the results for ellipsoids and spherocylinders we found that for these cylindrical particles adsorption barriers were formed when  $\tau^* > 0$  and that for  $\tau^* > 0.1$  there

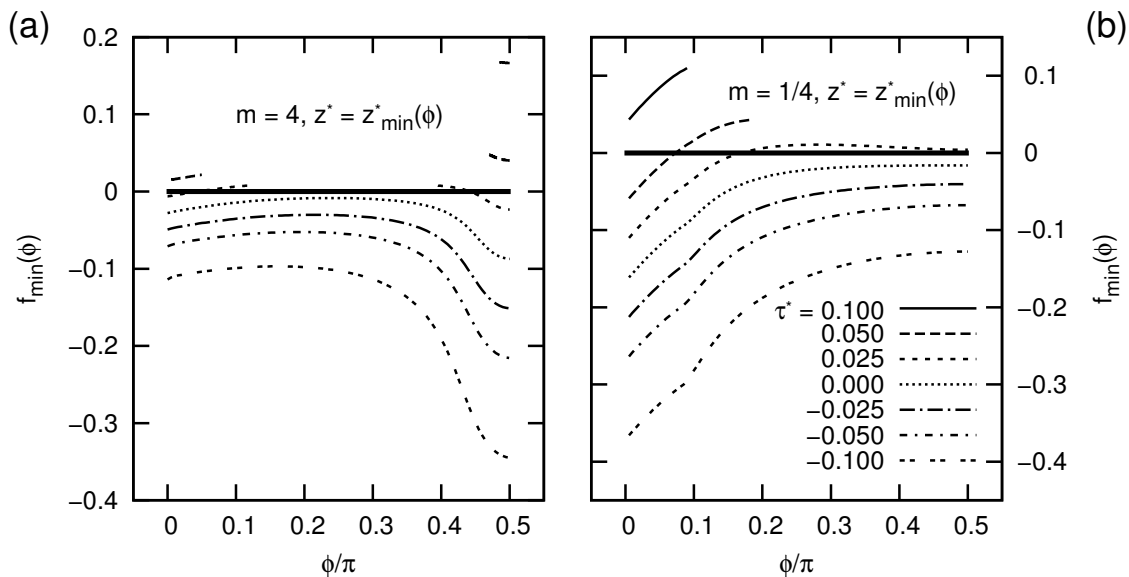


**Figure 2.9:** The minimum curves  $f_{\min}(\phi)$  for  $\cos\theta = -1/2$  and several values of  $\tau^*$  for a cylinder with  $m = 4$  (a), and  $m = 1/4$  (b). The thick line indicates  $f_{\min}(\phi) \equiv 0$ , which is the stable minimum for  $\tau^* \gg 0$ . Note the appearance of a secondary minimum at  $\phi = 0$  (a) in  $f_{\min}(\phi)$ . The kink in the minimum free-energy curves (b) is caused by the sharp transition between the shaft and caps of the cylinder.

was only one minimum in the free energy with  $z_{\min}^* < -z_{\det}^*$ . It was shown that this holds for other aspect ratios as well. Cylinders with aspect ratio  $m = 4$  were also studied in Ref. [143], however, there is no correspondence with our results. The equations presented in Ref. [143] do not appear to sample all possible orientations of the cylinder with respect to the interface. Again our results were verified using the semianalytic results in Appendix A.

Summarizing, we showed that our triangular-tessellation technique can be applied to determine the free-energy of adsorption for anisotropic colloidal particles at a flat liquid-liquid interface using Pieranski's model [129]. We verified that in this approximation there is only one minimum in the free energy for ellipsoids and spherocylinders and negative line-tension values. The orientation of the particles in equilibrium is solely determined by their aspect ratio. For positive values of the line tension we found that adsorption to the interface can be prevented by the formation of adsorption barriers in the free energy. We also showed that there can be two minima in the free energy of a prolate cylindrical particle, one corresponding to the expected flat adsorption of the particle to the interface and one corresponding to a metastable perpendicular adsorption. To what extent these results may be recovered for more complex models of colloid adsorption and in experiments is left for future research.

## 2.4 Triangular Tessellation and Confocal Microscopy

Before we come to the conclusion, we briefly go into another application of the triangular-tessellation technique, which is not related to the prediction of adsorption phenomenology. As explained in Section 2.2.2 the area excluded from the interface, i.e., the part where the colloid penetrates the interface, can be easily determined using triangular tessellation. In this section we discuss how this property may be of use to understand confocal microscopy data and test the quality of particle tracking algorithms.

The confocal microscope was developed to improve the image quality that could be obtained by using traditional wide-field microscopy [231]. Wide-field illumination of a sample results in a relatively high level of light emerging from objects above and below the focal plane, either through scattering or fluorescence, depending on the technique used. Such stray light lowers the signal-to-noise ratio of the light coming from the focal plane, thereby obscuring important details in the sample. The confocal microscope reduces the amount of unwanted light by illuminating only a small (diffraction limited) point in the sample and rejecting out-of-focus light coming from that point using a pinhole [68]. Only a single point is therefore imaged, but a two-dimensional (2D) picture may be formed by scanning a plane. The improvement in resolution achieved by a confocal setup over a traditional wide-field microscope is roughly a factor of three: for a typical sample the resolution can be 200 nm in the direction of the focal plane and 600 nm in the direction perpendicular to it [67, 68].

The 2D image that results from scanning gives an impression of the shape of the object in the focal plane, when an object is sufficiently large compared to the resolution of the microscope. That is to say, the 2D image gives the cross section of the focal plane with the object, convolved with the adjacent planes according to the microscope's point-spread function. Most of light intensity in the confocal image will come from a small region around the focal plane and for a large object the image thus roughly reveals the shape of the plane-particle cross section. By taking several 2D image slices of an object, its shape can be reconstructed [68]. However, this assumes that the object is stationary during the time it takes to obtain several 2D planes. When the time-dependent interaction of several particles is studied this type of 3D reconstruction may not be possible on the time scale of the particles' motion. Any information on the orientation and position of the particles must therefore be inferred from a 2D image. For many of the complex shape-anisotropic particles that have recently become available [24, 82, 83], it is difficult to a priori understand what a sample might look like based only on a 2D confocal image.

Our triangular-tessellation technique's ability to determine the shape of the cross section of a plane and a particle of known shape, see Fig. 2.10 for an example, can be of use in this regard. Calculating what a confocal slice through a particle would look like given the shape and composition of the particle and its position and orientation with respect to the focal plane is quite complicated, since it requires knowledge of the point-spread function and the environment around the particle, which is generally not available. However, our technique offers a simple and efficient way of determining plane-particle cross sections and these give a rough idea of what positions and orientations may correspond to the objects that appear in a 2D image. This may prove useful to interpret 2D confocal data of complex objects.

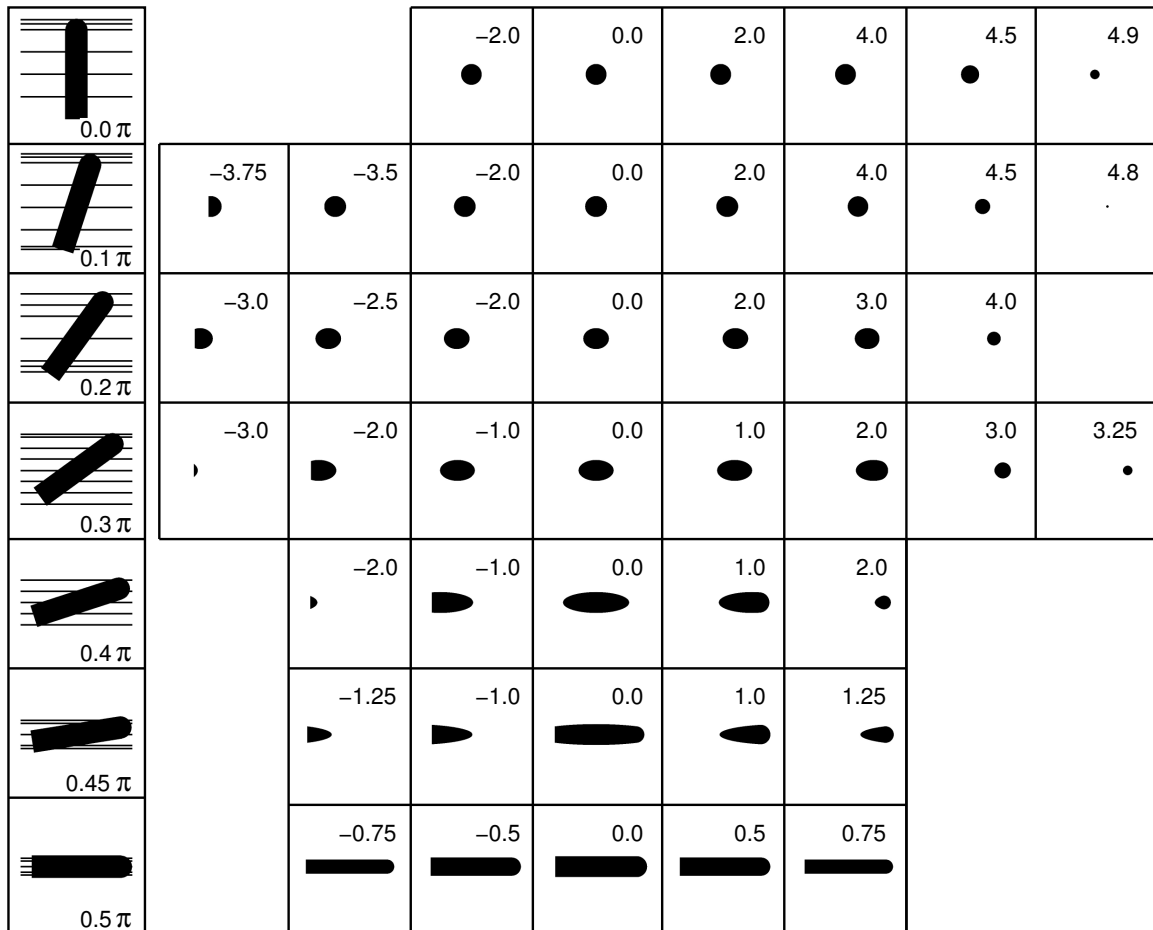


**Figure 2.10:** Several plane-bullet cross sections for various plane heights and bullet orientations. The bullet consists of a cylinder of height 4 and width 1, capped on one end with a hemisphere of radius 1; its total length is therefore 5. The centre of rotation is located at the centre of the cylindrical shaft. (left) A representation of the orientation of the bullet (black silhouette), which is intersected by several planes - represented by thin horizontal lines. The angle  $\phi$  is given in the bottom-right corner. (right) The cross sections (black silhouette) corresponding to the plane height and orientation choices shown to the left. In the top-right corner the height of the plane with respect to the bullet's centre of rotation is given. The projection of the centre of rotation of the bullet is always in the middle of the white squares.

For studies of suspended colloids it is often necessary to use 2D confocal image data to quantify properties of the system, e.g., to determine the velocity profile of charged colloids driven by an electric field in an electrophoresis measurement. This quantification typically requires knowledge of the position (and orientation) of the particles in the system. Tracking algorithms [232, 233] can be applied to extract the relevant coordinates from 2D confocal data. However, for highly anisotropic particles the particle location predicted by a tracking algorithm may deviate substantially from the actual position of the particle's centre of mass.

The triangular-tessellation technique may be used in the following way to probe the quality of the results obtained by employing a particular tracking algorithm. First, we generate a configuration of particles that is representative of the system of interest. For this configuration we can determine the cross sections of a (focal) plane with the particles. By adding Gaussian noise to these cross sections we obtain pseudo confocal-image data. Subsequently, the tracking algorithm is applied to this pseudo data to determine the positions of the particles. Finally, we compare the predicted positions to the actual positions of the particles. This allows us to estimate the level of uncertainty that is to be expected based on using the tracked coordinates.

## 2.5 Conclusion and Outlook

In this chapter we introduced the numerical technique of triangular tessellation to determine the surface areas and contact-line length that are associated with a plane-particle intersection. Our technique allows us to establish these values quickly and with a high level of precision for in principle arbitrary shapes. It therefore has a tremendous advantage over traditionally used semianalytic methods, for which the complex geometry of the problem makes it difficult, if not impossible, to derive manageable expressions for even the simplest of particle shapes.

To demonstrate our method we considered the adsorption of a single anisotropic colloidal particle at a flat liquid-liquid interface. We describe the behaviour of the particle at the interface by a simple free-energy model that is based on surface- and line-tension contributions, in the spirit of the work of Pieranski [129]. Using our triangular-tessellation technique we determined the positional and orientational dependence of the free energy for three species of particle: ellipsoids, cylinders, and spherocylinders. For ellipsoids and spherocylinders we established that there is only one minimum in the free energy for negative line-tension values, in agreement with the result of Ref. [144]. We also improved upon the results of Ref. [143] and we showed that there can be two minima in the free energy of a prolate cylindrical particle: one corresponding to the expected flat adsorption of the particle to the interface and one corresponding to a metastable perpendicular adsorption. Moreover, we re-examined the formation of adsorption barriers for these particles and their dependence on the orientation of the particle. To what extent these results may be recovered for more complex models of colloid adsorption and in experiments is left for future research.

We also commented on another possible application of the triangular-tessellation technique. Its ability to quickly determine the cross section between a plane and a particle,

may prove useful to gain insight into the cross-sectional objects that appear in 2D confocal-microscopy images. In addition the technique, by the procedure outlined in this chapter, offers the possibility to verify the quality of particle tracking algorithms.

In conclusion, the applications of the triangular-tessellation technique presented here are myriad and will undoubtedly be further extended in the foreseeable future.

## 2.6 Acknowledgements

It is a pleasure to thank Thijs Besseling for proofreading the section on confocal microscopy. His explanations have greatly improved my understanding of the available techniques and his suggestions have significantly benefited quality of the text.



---

## **Adsorption Trajectories for a Colloidal Particle at an Interface**

---

We apply the triangular-tessellation technique presented in Chapter 2 to calculate the free energy associated with the adsorption of a single anisotropic colloidal particle at a flat liquid-liquid interface. Using this free energy and simple dynamics we analyse the process of a particle attaching to the interface and relaxing to its equilibrium position and orientation. When there are metastable adsorption configurations, we show that the orientation of a colloid at its initial contact with the interface has a strong influence on its final orientation. Our result is a first step towards understanding the time-dependent behaviour of anisotropic colloids and nanoparticles in contact with an interface.

## 3.1 Introduction

As discussed in Chapters 1 and 2 the adsorption of colloidal (nano)particles at liquid-liquid interfaces is not only of scientific interest, but also relevant for industry. The tunability and variety of colloidal particles currently available [82, 83], coupled with our still limited knowledge on the process of colloid adsorption [137], leaves the study of interfacial phenomenology an open field. To better understand the complex behaviour that is observed when colloidal particles are brought into contact with an interface [26, 27, 134, 155, 162, 163], we developed the triangular-tessellation technique to numerically determine the surface areas and contact-line length required to obtain the free energy of adsorption for a single particle, also see Chapter 2 and Ref. [147]. Our free-energy model is based on surface-tension and line-tension arguments and is similar to the one used by Pawel Pieranski in his ground breaking study of colloid adsorption [129].

In this chapter we use this free energy to perform an initial investigation of the time dependence of the adsorption process. That is, the way in which a colloid moves through the interface from the time it makes initial contact with the interface to the time it reaches its equilibrium configuration. In Section 3.2 we consider a simple model for this process based on flow-line dynamics. In Section 3.3 we study three systems which allow us to showcase the complexity that anisotropy can introduce into adsorption process. We discuss the adsorption of an ellipsoidal particle in Section 3.3.1 with the intent to use this system as a basis for comparison. In Section 3.3.2 we examine the behaviour of a cylindrical particle. For these particles there is a metastable minimum in the free energy, which results in a dependence of the adsorption orientation on the orientation of the colloid at its initial contact with the interface. In Section 3.3.3 we study a cylindrical colloid with aspect ratio 1, for which we observe unusual adsorption behaviour. Finally, we discuss the properties of our model and its shortcomings in Section 3.4.

## 3.2 Theoretical Considerations

Many of the terms and notations used in this chapter are introduced in Chapter 2. We refer the reader to that chapter for a detailed overview of these notations and the triangular-tessellation technique by which the reduced free energy of adsorption  $f(z^*, \phi)$  can be determined as a function of the adsorption depth  $z^*$  and the polar angle  $\phi$  the colloid makes with the interfacial normal. In the following section we assume the reader is familiar with our model and we build upon it to study the adsorption process.

### 3.2.1 Adsorption Trajectories and Separatrices

The free energy of adsorption acts as a potential energy for the colloid, which can be differentiated with respect to its macroscopic coordinates, to obtain a force. The microscopic coordinates of the fluid and the internal ones of the colloidal particle have been integrated out to yield the tension terms. We can therefore define a reduced *vector field*



of adsorption force by determining negative gradient of the free energy

$$\mathcal{F}(z^*, \phi^*) = -\nabla f^*(z^*, \phi^*) \equiv -\left(\hat{\mathbf{z}}^* \frac{\partial}{\partial z^*} + \hat{\boldsymbol{\phi}}^* \frac{\partial}{\partial \phi^*}\right) f^*(z^*, \phi^*), \quad (3.1)$$

with  $\hat{\mathbf{z}}^*$  and  $\hat{\boldsymbol{\phi}}^*$  unit vectors,  $\pi\phi^* \equiv \phi$ , and  $f^*(z^*, \phi^*) \equiv f(z^*, \phi)$ . We use the vector field  $\mathcal{F}$  and the free energy  $f$  to study four features that give insight into the adsorption of colloids at a liquid-liquid interface: (i) flow lines, (ii) minima and maxima, (iii) saddle points, and (iv) separatrices. A *flow line*,  $\eta(t) = (z^*(t), \phi^*(t))$ , is defined as a solution to the differential equation

$$\dot{\eta}(t) \equiv \frac{\partial \eta(t)}{\partial t} = \mathcal{F}(\eta(t)), \quad (3.2)$$

where the dot denotes a time derivative and  $t$  the ‘time’, and the solution is fixed by imposing the initial configuration  $\eta(t=0)$ . We refer to these flow lines as *adsorption trajectories* to stress their relation with the physical path followed by a particle adsorbing to the interface. Each minimum in the free energy is surrounded by a region in parameter space to which that particular minimum is attractive. All flow lines which originate from points in this region reach the local minimum for  $t \rightarrow \infty$ . The dividing line between two attractive regions is referred to as the *separatrix*. This separatrix can contain (local) maxima and saddle points.

### 3.2.2 The Time Dependence of Colloid Motion

It is desirable to review the concept of ‘time’ as introduced by solving the differential equation  $\dot{\eta}(t) = \mathcal{F}(\eta(t))$ . The variable  $t$  in this equation is mathematically only a dummy variable to the parametrization. This variable is however related to physical time. In the Langevin equation for a sphere in a homogeneous medium [234, 235], the time to travel over a short distance  $\Delta l$  is equal to  $M\xi\Delta l/|\mathbf{A}|$ , where  $M$  is the mass,  $\xi^{-1}$  the Brownian time, and  $\mathbf{A}$  is the force. We have an analogous situation for our parametrization, the value  $1/|\mathcal{F}|$  can be considered a measure for the time that it takes to move along a flow line through a specific point. Note that  $1/|\mathcal{F}|$  diverges for extrema in the free energy, which is in accordance with the particle being stationary there.

We determine the flow lines for the free energy using a linear differential solver. The time dependence is introduced as follows. The time step  $\Delta t_i$ , required to traverse a distance  $\Delta l_i$  is defined as  $\Delta t_i = \Delta l_i/|\mathcal{F}_i|$ , with  $|\mathcal{F}_i|$  the size of the force at the point from which the step is taken. By taking  $i = 1, \dots, n$  steps along the flow line we obtain a series of  $\Delta t_i$ . The time  $t(n)$  required to arrive at point  $n$  along the flow line is given by

$$t(n) = \sum_{i=1}^{n-1} \Delta t_i. \quad (3.3)$$

In the limit of an infinitesimally small step size, the solution to the vector field with the initial condition  $\eta(0)$  and the proper time dependence are obtained. We analyse the relation between the reduced time  $t$  and the actual time  $t_r$  in more detail in Section 3.4.

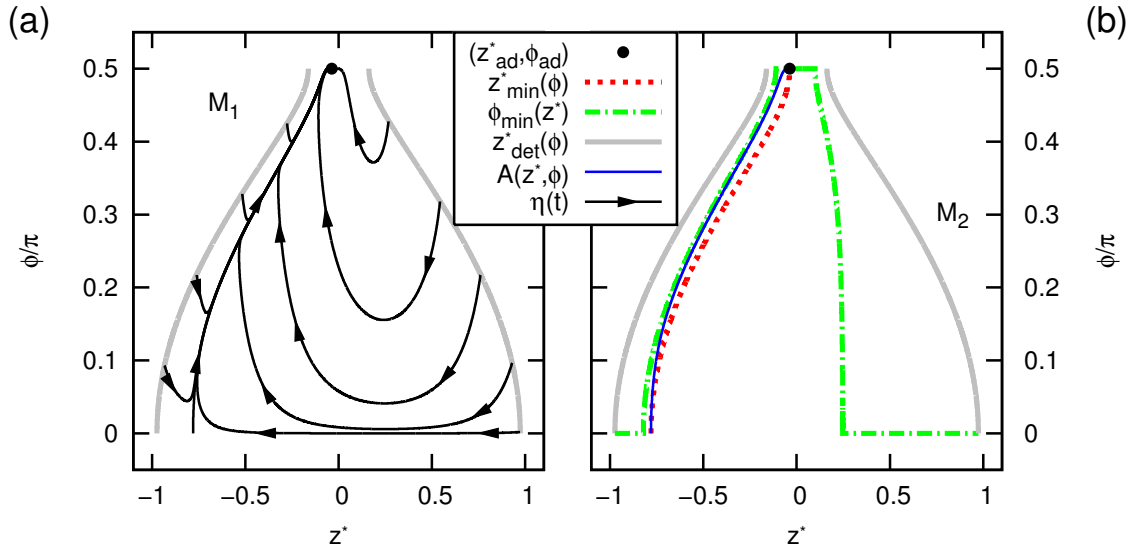


**Figure 3.1:** (a) The adsorption trajectories  $\eta(t)$  for an ellipsoidal particle with aspect ratio  $m = 6$  for  $\cos\theta = -0.5$  and  $\tau^* = -0.1$ . The arrow heads indicate the direction of colloid motion through  $(z^*, \phi)$ -space, the dot marks the location of the minimum, i.e., the adsorption configuration, and the thick grey lines the  $\pm z_{\text{det}}^*(\phi)$  curves. (b) The  $\pm z_{\text{det}}^*(\phi)$  curves are indicated in grey (thick, solid), the  $z_{\text{min}}^*(\phi)$  curve in red (thick, dots), the  $\phi_{\text{min}}(z^*)$  curve in green (thick, dash-dot), and the attractor  $A(z^*, \phi)$  in blue (thin, solid). The location of the minimum is again marked by a dot. The symbols  $M_1$  and  $M_2$  indicate the respective media.

### 3.3 Anisotropy and Interfacial Adsorption

In this section we consider the adsorption of three anisotropic particles, an ellipsoid and two cylinders with different aspect ratios. All data were produced using the triangular-tessellation technique for  $500^2$ -vertex grids, see Chapter 2 and Ref. [147]. The value of  $f^*(z^*, \phi^*)$  was calculated for 250 nonequidistant grid points in  $z^* \in [-z_{\text{det}}^*, z_{\text{det}}^*]$  and  $\phi^* \in [0, 0.5]$ , respectively. We verified that there is a relative uncertainty in our results of less than  $10^{-4}$  per data point. The free energy on this grid was interpolated with a 3rd order polynomial to allow the flow lines to be determined using a linear differential solver. To ensure convergence we reduced the step size until the difference in length between two successive flow lines divided by the average total length is less than  $10^{-4}$ .

#### 3.3.1 Adsorption of Ellipsoidal Particles

Figure 3.1a shows adsorption trajectories  $\eta(t)$  for an ellipsoidal particle with aspect ratio  $m = 6$ , a contact angle  $\cos\theta = -0.5$ , and a reduced line tension  $\tau^* = -0.1$ . We chose these values for  $\cos\theta$  and  $\tau^*$  respectively, because the features in the free energy are more pronounced and the flow lines can therefore be more easily observed. Qualitatively similar results are expected for all  $\tau^* < 0$ ; for  $\tau^* > 0$  there may be adsorption barriers, which would strongly influence the shape of the adsorption trajectories. In Fig. 3.1b the  $\pm z_{\text{det}}^*(\phi)$ ,  $z_{\text{min}}^*(\phi)$ ,  $\phi_{\text{min}}(z^*)$ , and attractor  $A(z^*, \phi)$  curves for this free energy are given. The location of the minimum is indicated with a dot. The term *attractor* is introduced

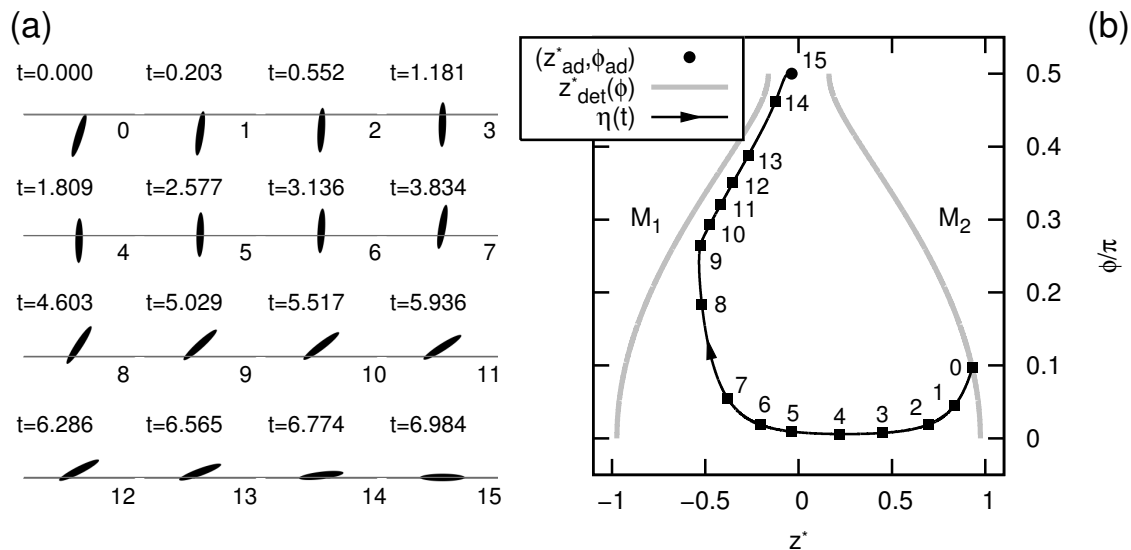


**Figure 3.2:** The process of adsorption to a liquid-liquid interface for an ellipsoidal colloid with  $m = 6$ ,  $\cos \theta = -0.5$ , and  $\tau^* = -0.1$ . (a) Several snapshots of the motion of the colloid through the interface along a flow line (b). An  $xz$ -view of the colloid is represented by a black silhouette and the interface is indicated by a thin grey line. The time is given in the top-left corner of each snapshot. The numbers at the bottom right of the interfacial line, correspond to the numbers in (b). The top medium corresponds to  $M_1$  and the bottom to  $M_2$ , respectively. (b) The flow line for which the snapshots are taken is indicated by an arrowed black curve. We also show  $\pm z_{\text{det}}^*(\phi)$  (thick grey curves), the free-energy minimum (black dot), and the  $(z^*, \phi)$  values for which the snapshots are taken (numbered black squares). The location of the two media is indicated by the symbols  $M_1$  and  $M_2$ .

here to describe a feature in the vector field of adsorption force to which the flow lines are attracted, as can be seen in Fig. 3.1a. Mathematical analysis showed that for points on the attractor one of the eigenvectors of the Hessian matrix  $[(\nabla \nabla^T) f]$  is in the direction of the gradient, with a positive eigenvalue, and the other is perpendicular to it, with a negative eigenvalue. By analysing the free energy using our adsorption trajectories we concluded that the single minimum with  $(z_{\text{ad}}^*, \phi_{\text{ad}}) \approx (-0.0368, 0.5\pi)$  is attractive to the entire region between the  $\pm z_{\text{det}}^*(\phi)$  curves. This was to be expected on the basis of our observations in Chapter 2 and Ref. [147].

The flow lines in Fig. 3.1a give a rather abstract picture of the colloid motion through the interface. To more intuitively illustrate the behaviour of the particle, we have included Fig. 3.2, which shows several snapshots of the motion of the colloid according to the adsorption trajectory with  $\eta(0) \approx (0.930, 0.0965\pi)$ . From Fig. 3.2a it becomes clear that the initial vertical movement of the colloid through the interface is quite fast compared to the rotational movement of colloid towards its equilibrium orientation that follows. This speed difference can be explained by the difference in the gradient of the free energy between points (0–7) and (8–15) in Fig. 3.2b. In part this difference is also caused by our implicit choice for the ratio the translational and rotational friction coefficients. The final part of the movement, achieving the equilibrium position, is exponentially asymptotic.

However, the colloid movement is only asymptotic when it is very close to its adsorption configuration, we have therefore taken the last snapshot at the onset of this regime. Additional representations of the movement along the adsorption trajectories shown in Fig. 3.1a are given in Ref. [148], which links to an electronic repository that contains movies of the adsorption process.

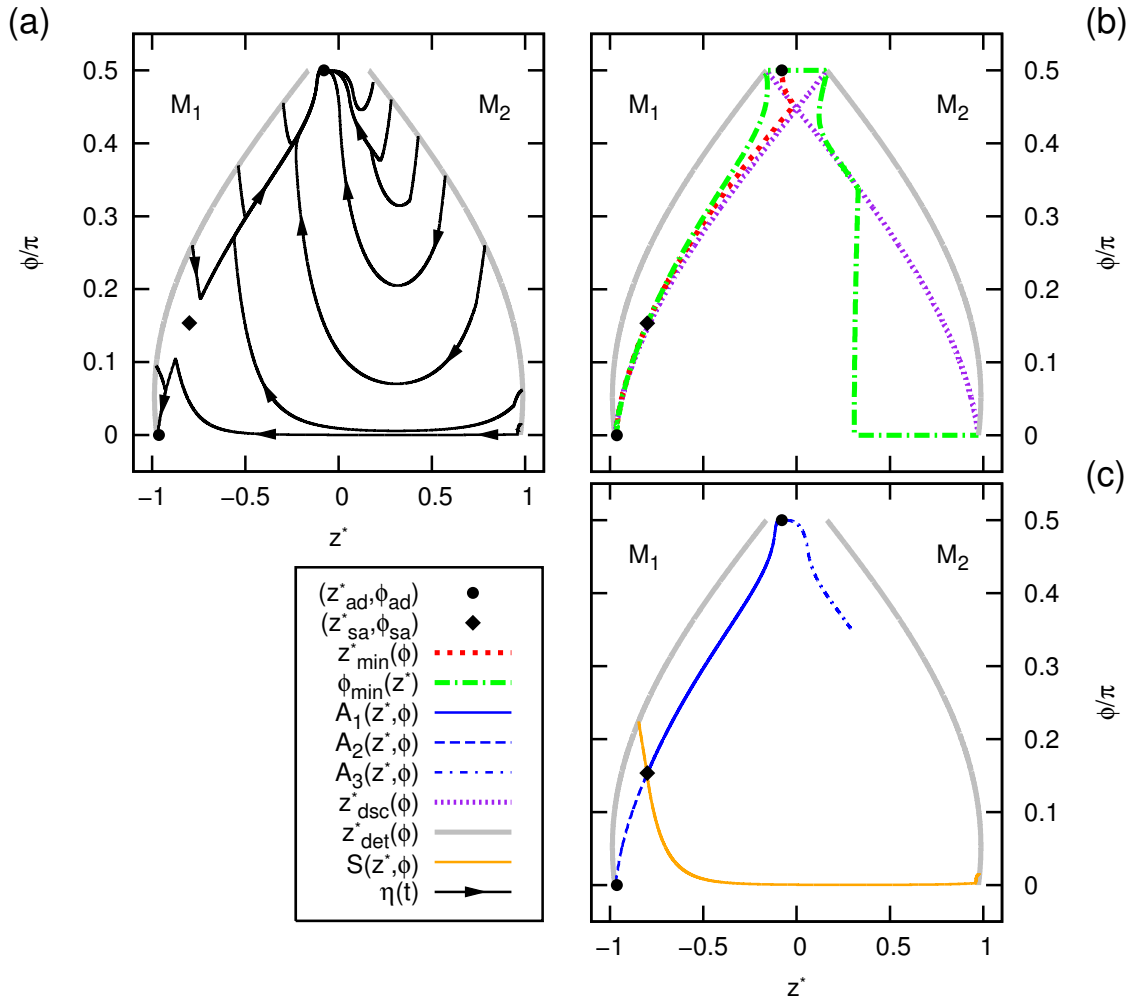
### 3.3.2 Trajectories for Cylindrical Colloids

Figure 3.3 shows the adsorption trajectories for a cylindrical colloid with  $m = 6$ ,  $\cos\theta = -0.5$ , and  $\tau^* = -0.1$ . The free-energy landscape of a cylinder is very different to that of the ellipsoid. For cylinders there are two minima in the free energy at  $(z_{\text{ad}}^*, \phi_{\text{ad}}) \approx (-0.079, 0.5\pi)$  with  $f_{\text{ad}} \approx -0.397$  and at  $(z_{\text{ad}}^*, \phi_{\text{ad}}) \approx (-0.962, 0.0)$  with  $f_{\text{ad}} \approx -0.090$ , respectively. The minimum with  $\phi_{\text{ad}} = 0.5\pi$  is the absolute minimum, the one with  $\phi_{\text{ad}} = 0.0$  is metastable. The latter corresponds to a configuration where one of the caps of the cylinder is flush with the interface and the rest of the colloid is immersed in the favoured medium ( $M_1$  in this case). The kinks in the adsorption trajectories of Fig. 3.3a are directly related to ridges in the free-energy landscape which are caused by the sharp transition between the shaft and caps of the cylinder. These ridges are indicated by the  $\pm z_{\text{dsc}}^*(\phi)$  curves in Fig. 3.3b, where ‘dsc’ stands for discontinuity (in  $\mathcal{F}$ ).

In Fig. 3.3c we show the separatrix  $S(z^*, \phi)$  between the two minima and the three attractors  $A_i(z^*, \phi)$ ,  $i = 1, 2, 3$ , which we find for this free energy of adsorption. There is a saddle point on the separatrix, where  $S(z^*, \phi)$  meets with two of the attractors,  $A_1$  and  $A_2$ . The separatrix forms the divide between the regions to which the respective minima are attractive. Remarkably, the metastable minimum is attractive to a large  $(z^*, \phi)$ -domain even for an aspect ratio as large as  $m = 6$ . A particle attaching to the interface from  $M_1$  with  $\phi \lesssim 0.224\pi$  will move into the metastable minimum. For attachment from  $M_2$  we found that the metastable minimum is attractive to contact orientations with  $\phi \lesssim 0.014\pi$ . Assuming a homogeneous orientational distribution at contact, the probability of reaching to the metastable configuration from the energetically unfavourable medium is quite low ( $\sim 0.001$ ), however, from the preferred medium  $M_1$  it is quite high ( $\sim 0.240$ ).

The appearance of a third attractor  $A_3$ , see Fig. 3.3c, is somewhat surprising. The first and second attractor are merely the split form of a similar feature to the one found for the ellipsoid in Section 3.3.1. This ‘main attractor’ is split, because there are two minima, which causes the separatrix to intersect it. The third attractor, leading to the absolute minimum of the free-energy landscape, is caused by a subtle interplay between the right-most ridge,  $z_{\text{dsc}}^*(\phi)$ , and the  $\phi_{\text{min}}(z^*)$  curve and terminates exactly where  $\phi_{\text{min}}(z^*)$  has a kink. The third attractor strongly influences the behaviour of the adsorption trajectories around it, see Fig. 3.3a and Ref. [148].

For the cylindrical colloid we again expect qualitatively similar results for  $\tau^* < 0$ ; for  $\tau^* > 0$  there may be adsorption barriers, which would strongly influence the shape of the adsorption trajectories. However, the presence of a secondary minimum introduces a strong dependence of the colloid’s behaviour on the value of the contact angle. That is, the position of the separatrix varies significantly with  $\cos\theta$ . We come back to this in Section 3.3.3, when we discuss cylindrical particles with aspect ratio  $m = 1$ .



**Figure 3.3:** Properties of the free-energy landscape for a cylinder with  $m = 6$ ,  $\cos \theta = -0.5$ , and  $\tau^* = -0.1$ . (a) Several adsorption trajectories  $\eta(t)$  (arrowed black curves) are shown, as well as the location of the free-energy minima (dots), the saddle point (diamond), and the media  $M_1$  and  $M_2$ , respectively. Thick grey curves indicate  $\pm z_{\text{det}}^*(\phi)$ . (b) The vector-field discontinuities  $z_{\text{dsc}}^*(\phi)$  are shown in purple (dots). The  $z_{\text{min}}^*(\phi)$  curve is represented in red (dashed) and  $\phi_{\text{min}}(z^*)$  in green (dash-dot). (c) The attractors  $A_i(z^*, \phi)$  and the separatrix  $S(z^*, \phi)$ .

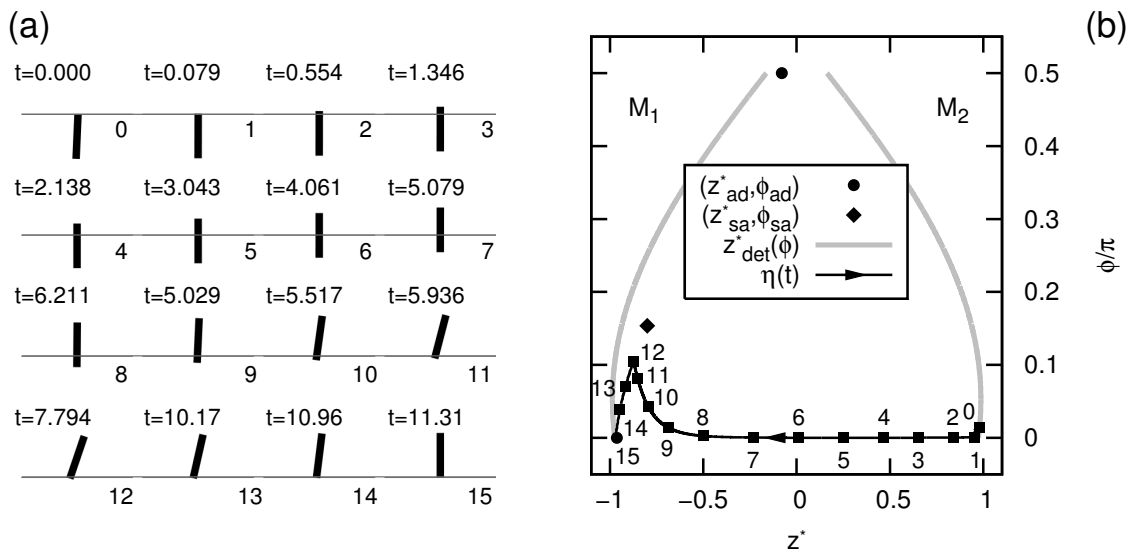


**Figure 3.4:** The process of adsorption for a cylindrical colloid with  $m = 6$ ,  $\cos\theta = -0.5$ , and  $\tau^* = -0.1$ , for which the adsorption becomes arrested in the metastable configuration. (a) Several snapshots of the colloid adsorbing to the interface. An  $xz$ -view of the colloid is represented by a black silhouette and the interface is indicated by a thin grey line. The reduced time is given in the top-left corner (first two rows) and the bottom-left corner (last two rows). The numbers at the bottom right of the interfacial line, correspond to the numbers in (b). The top medium corresponds to  $M_1$  and the bottom to  $M_2$ , respectively. (b) The flow line for which the snapshots are taken is indicated by an arrowed black curve. We also show  $\pm z_{\text{det}}^*(\phi)$  (thick grey curves), the free-energy minima (black dots), the saddle point (black diamond), and the  $(z^*, \phi)$  values for which the snapshots are taken (numbered black squares).

In Fig. 3.4 we consider colloid movement along a flow line with  $\eta(0) \approx (0.979, 0.014\pi)$  that is attracted to the metastable minimum. The cylinder first moves almost vertically through the interface (frame 1 – 8), before it tilts slightly (frame 9 – 11). However, when it touches the interface with the edge of one of its caps (frame 12), it experiences the discontinuity in  $\mathcal{F}$  and changes its direction of motion: it is energetically favourable to move into the metastable minimum by tilting back to the vertical orientation (frame 13 – 15). Finally, the colloid relaxes to its perpendicular adsorption orientation with one of its caps flush with the interface. The trajectory between points 12 and 15 could only be determined with a precision of  $\sim 10^{-2}$ . This is due to the close proximity of the  $\phi_{\min}(z^*)$ ,  $z_{\min}^*(\phi)$ , and  $-z_{\text{dsc}}^*(\phi)$  curves, see Fig. 3.3b. Consequently, the time dependence of this part of the motion has significant uncertainty, which we estimate to be at most 15%.

Additional representations of the movement along the adsorption trajectories shown in Fig. 3.3a are given in Ref. [148].

### 3.3.3 Special Configurations for Short Cylinders

In this section we study the behaviour of a short cylindrical colloid with aspect ratio  $m = 1$  adsorbed at an interface and the dependence of this behaviour on the contact angle. Figure 3.5 shows the minima, saddle points, and separatrices for 11 values of  $\cos\theta$  to illustrate this dependence.

The free energy we found for this short cylinder has the following properties. For  $\cos\theta = 0$  there is a single minimum at  $(z_{\text{ad}}^*, \phi_{\text{ad}}) \approx (0.000, 0.271\pi)$  and for  $\cos\theta = -1$  there is no minimum. When  $-1 < \cos\theta < 0$  there are two minima. One of these is located at  $(z_{\text{ad}}^*, \phi_{\text{ad}}) \approx (-0.571, 0.0)$ , which corresponds to one of the cylinder's caps being flush with the interface and the rest of the particle immersed in medium  $M_1$ . The location of the other minimum changes with the value of  $\cos\theta$ . The minimum with  $(z_{\text{ad}}^*, \phi_{\text{ad}}) \approx (-0.571, 0.0)$  is stable when  $\cos\theta \lesssim -0.23$  and metastable for  $\cos\theta \gtrsim -0.23$ . The separatrices move from the lower-left corner towards the centre of the *adsorption region* - the region enclosed by the  $\pm z_{\text{det}}^*(\phi)$  curves - upon decreasing  $\cos\theta$ . This implies that the perpendicular adsorption orientation becomes more stable and simultaneously becomes less accessible.

For sufficiently low values of  $\cos\theta$  the separatrix splits into two pieces, see Fig. 3.5b. The transition between a one- and two-separatrix regime occurs for  $\cos\theta \approx -0.705$ . The process is as follows. For decreasing  $\cos\theta$  the position of the saddle point moves closer to the boundary of the adsorption region. Around  $\cos\theta = -0.705$  the saddle point makes contact with the boundary and is degenerate. A normal saddle point has two attractive and two repulsive directions, whereas the degenerate saddle point has two repulsive directions, but only one attractive direction. With even lower values of  $\cos\theta$  the saddle point transforms into two degenerate saddle points at the boundary. Both of these have only one attractive and one repulsive direction. In the region between separatrices the particle most efficiently lowers its free energy by moving from the unfavoured medium  $M_2$  directly into  $M_1$ . When the colloid is in  $M_1$ , it does not adsorb if it touches the interface with an orientation that falls between the two  $\phi$  values corresponding to the saddle points, because this would increase its free energy. This is a remarkable and counter-intuitive result, since it implies that adsorption does not necessarily occur, despite the presence of

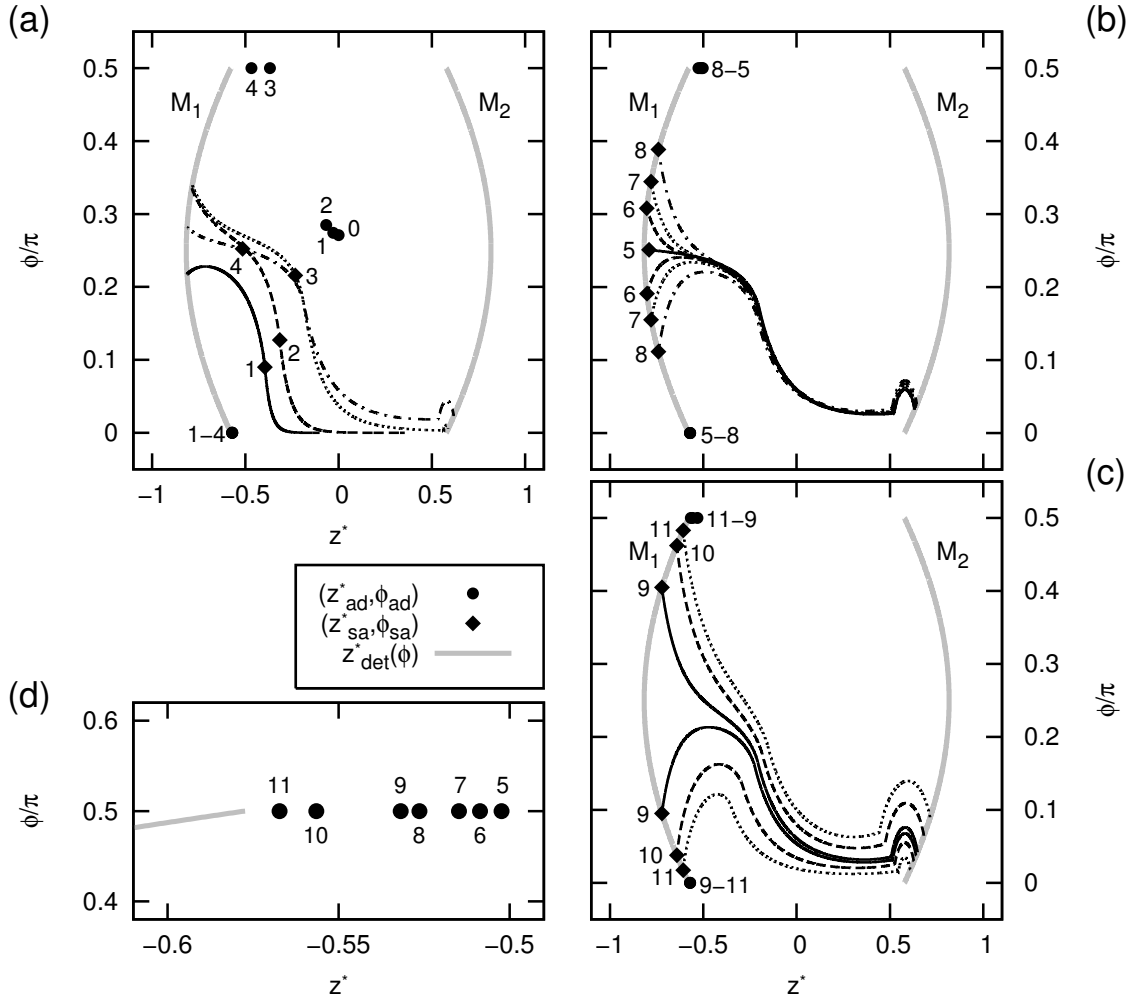


**Figure 3.5:** Properties of the free-energy landscape of a cylinder with aspect ratio  $m = 1$  for  $\tau^* = 0$  and several contact angles. The labelling is as follows: (a)  $\cos\theta = 0.0$  (0),  $-0.1$  (1),  $-0.2$  (2),  $-0.4$  (3), and  $-0.6$  (4); (b)  $\cos\theta = -0.7$  (5),  $-0.72$  (6),  $-0.74$  (7), and  $-0.78$  (8); and (c)  $\cos\theta = -0.8$  (9),  $-0.9$  (10), and  $-0.95$  (11). Minima are given by thick dots, saddle points by diamonds, separatrices by black (patterned) curves, and the  $\pm z_{\text{det}}^*(\phi)$  curves by thick grey curves. The minima and saddle points are numbered according to value of  $\cos\theta$ . In (a) the patterning of the separatrices is (1) solid, (2) dashed, (3) dots, (4) dash-dot; for (0) there is no separatrix. The curves (6-8) in (b) are disjoint, there is one curve for (5). (d) The location of the minima from (c,d) in the top-left corner of the adsorption region.

free-energy minima, which are typically quite deep. Binding to the interface with several hundred or even thousand times the thermal energy is not uncommon for colloids [129].

To illustrate the different adsorption possibilities for this particle, we included Fig. 3.6, which shows snapshots of the movement of the colloid through the interface for three different orientations at contact ( $\cos \theta = -0.95$ ). The first trajectory, Fig. 3.6a, shows the colloid adsorbing to the metastable minimum at  $(z_{\text{ad}}^*, \phi_{\text{ad}}) \approx (-0.567, 0.5\pi)$ . In its final configuration (frame 7), the colloid only barely penetrates the interface and its rotationally symmetry axis is perpendicular to the interfacial normal. Figure 3.6b shows the adsorption to the primary minimum at  $(z_{\text{ad}}^*, \phi_{\text{ad}}) = (-0.571, 0.0)$ , for which the rotational symmetry axis is parallel to the interfacial normal. In Fig. 3.6c snapshots of the movement through the inter-separatrix domain are shown. The colloid moves through the interface and slows down when it approaches the boundary of the adsorption region, since the gradient tends to zero here. The final configuration shows the cylinder touching the interface in a single point, it is essentially detached. Additional representations are given in Ref. [148].

Summarizing, we showed that we can analyse the time dependence of the process of adsorption for an anisotropic colloid attaching to a liquid-liquid interface and relaxing to its equilibrium position. Our simple description used the free energy as a potential of force and dynamics based the associated vector field of adsorption force. The adsorption of cylindrical colloids revealed a strong dependence of the adsorption orientation on the particle's orientation at contact. Moreover, we found that for certain systems the colloid can even pass through the interface without becoming trapped in a free-energy minimum.

## 3.4 Discussion

In Section 3.3 we showed that the time-dependent behaviour of an anisotropic colloid in contact with a liquid-liquid interface can be very rich depending on the specifics of the system. In this section we analyse the relation between the behaviour described by our flow-line model and the behaviour that may be encountered in experiments.

### 3.4.1 Flow Lines and the Langevin Equation

For a particle dispersed in a liquid medium undergoing a force the dynamics is governed by a solution to the Langevin equation [234, 235]. We consider a particle undergoing a force according to the derivative of the unreduced free energy of adsorption  $F$  with respect to the particle's macroscopic coordinates. When we neglect inertia, the random force term, and limit ourselves to studying the time dependence of the position  $z$  and orientation  $\phi$ , the Langevin equation may be rewritten to the following equations of motion (EOMs):

$$\lambda \frac{\partial z(t_r)}{\partial t_r} = -\frac{\partial}{\partial z} F(z(t_r), \phi(t_r)); \quad (3.4)$$

$$\mu \frac{\partial \phi(t_r)}{\partial t_r} = -\frac{\partial}{\partial \phi} F(z(t_r), \phi(t_r)), \quad (3.5)$$

with  $t_r$  is the 'real' unreduced time. The prefactors  $\lambda$  and  $\mu$  represent the translational and rotational friction coefficients, respectively. These coefficients account for the size

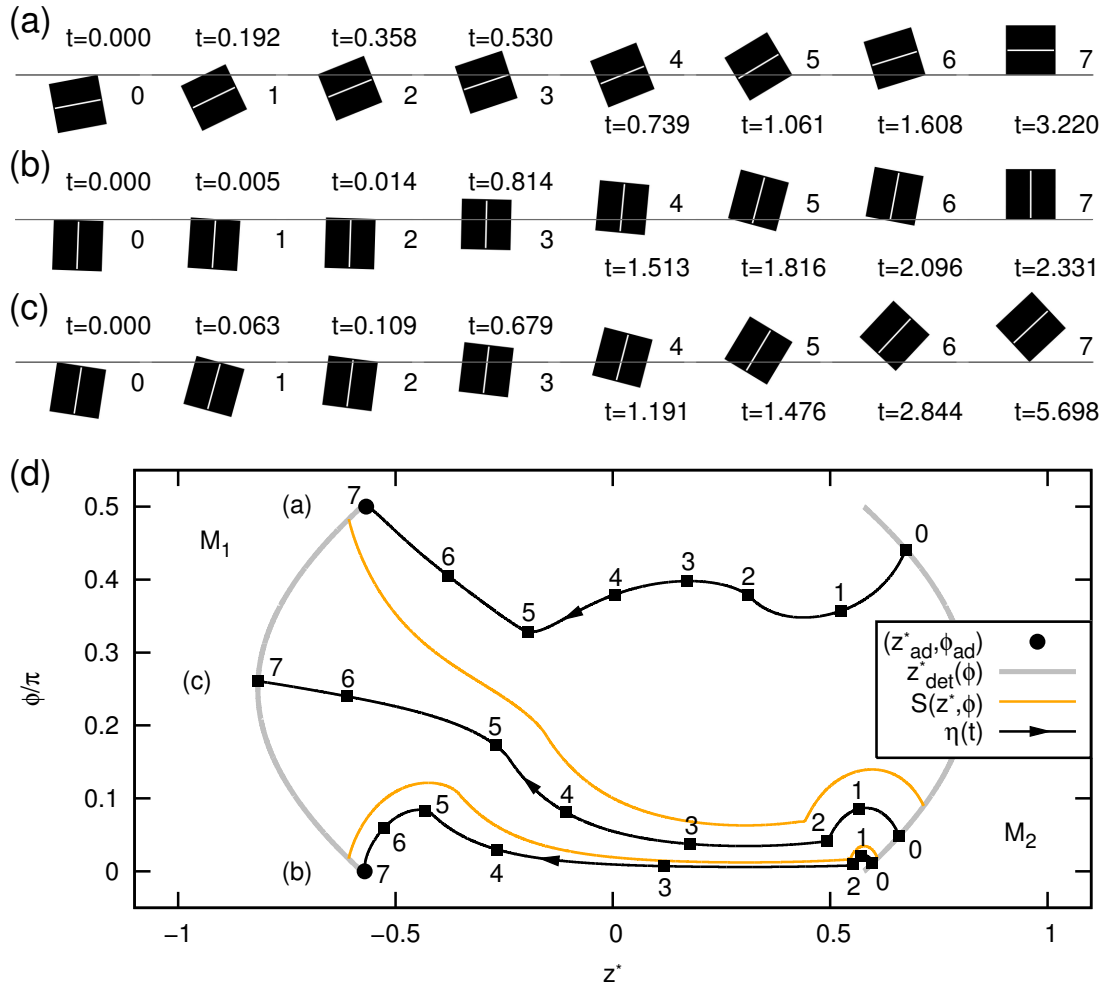


**Figure 3.6:** The adsorption process predicted by our model for three initial configurations of a cylindrical colloid with  $m = 1$  for  $\cos \theta = -0.95$ , and  $\tau^* = 0.0$ . (a-c) Snapshots of the motion of through the interface along three adsorption trajectories in (d). An  $xz$ -view of the colloid is represented by a black silhouette and the interface is indicated by a grey line. The white line on the silhouette is used to indicate the cylinder's rotational symmetry axis. The reduced time is given in the top-left corner (first four) and the bottom-left corner (last four). The numbers at the bottom/top right of the interfacial line, correspond to the numbers in (d). The top medium corresponds to  $M_1$  and the bottom to  $M_2$ , respectively. (d) The three flow lines  $\eta(t)$  (arrowed black lines) corresponding to the snapshots in (a-c), as indicated near the number 7 square/dots. The separatrices  $S(z^*, \phi)$  are given by thin yellow curves, the  $\pm z_{\text{det}}^*(\phi)$  by thick grey curves, the location of the minima by thick dots, and the media by  $M_1$  and  $M_2$ , respectively.

and shape of the particle, as well as for the positional  $z$  and orientational  $\phi$  dependencies of the system, such as the presence of the interface and the difference in viscosity between the two media.

We can recover Eq. (3.2) from Eqs. (3.4) and (3.5) as follows. We assume that  $\lambda$  and  $\mu$  are independent of the shape. We also assume that  $\lambda$  and  $\mu$  are independent of  $z$  and  $\phi$  and coupled according to

$$\mu = \frac{a^2 + 2b^2}{\pi^2} \lambda. \quad (3.6)$$

By writing  $t_r = \kappa t$ , with

$$\kappa = \frac{a^2 + 2b^2}{\gamma_{12} S} \lambda, \quad (3.7)$$

we can recover the relation

$$\dot{\eta}(t) \equiv \frac{\partial \eta(t)}{\partial t} = \mathcal{F}(\eta(t)). \quad (3.8)$$

It is apparent that our description of the system's time dependence on the basis of simple flow lines constitutes a drastic reduction of the physics that underlie the movement of particles in a liquid. However, as a first step towards understanding the behaviour of particles attaching to an interface, the approach we used in this chapter is not entirely unreasonable. By gaining insight into the behaviour of the system in our approximation, we can more easily probe the effect of adding new components to the model to better account for the physics of experimental systems. In the next section we discuss some of the shortcomings of our model give suggestions for improvement in future studies.

### 3.4.2 Suggestions for Improvement

A more accurate model for particles at an interface should include interfacial deformation. Our model assumes a flat undeformed interface for which the angle between the colloid and the interface is not necessarily same as the contact angle. Allowing the three-phase contact line to undulate and achieve the correct (contact) angle along the entire contact line changes the free energy of adsorption significantly even for very simple systems [149, 153, 157, 159], also see Chapter 4. The effect is expected to be far more pronounced when the colloids are anisotropic, especially when there are sharp features on their surface. This has been studied in literature for a limited number of particles and configurations [135, 156, 158, 236–239]. However, the currently available semianalytic techniques cannot give the full positional and orientational dependence of the free energy. Numerical tools such as Surface Evolver [221–223] may be applied, but at the time this research was carried out [147, 148], we found that determining the free-energy landscape was not possible within a reasonable time frame.

The model for the motion of the colloid through the interface should be also be re-considered. Neglecting the anisotropy of the particle and the difference in the viscosity of the media for the friction, as is done for the flow-line-based time dependence, constitutes an oversimplification of the experimental reality. An improved model should at the very least take these effects into account. With future studies in mind, we feel compelled to draw attention to the recent experimental study of Ref. [137]. In Ref. [137] an unexpectedly slow relaxation towards the adsorption equilibrium was observed for microspheres

at a water/oil interface. The relaxation appeared logarithmic in time and seemed to be described well by a model that accounts for hopping of the contact line over nanoscale surface heterogeneities. This result could have strong implications for the appropriateness of traditionally used models for the process of adsorption, e.g., Refs. [138, 139].

There also exists an alternative approach to obtaining the behaviour of particles at an interface. In Ref. [240] the adsorption of ellipsoidal particles was studied using molecular dynamics simulations according to the lattice-Boltzmann method. Note that the adsorption trajectories reported in Ref. [240] are similar to the ones found in this thesis. The simulation-based approach of [240] shows great promise for the analysis of systems, for which traditional theoretical techniques encounter great difficulties in giving an accurate description. However, a drawback of these models is that it is difficult to specify measurable properties such the contact angle.

### 3.5 Conclusion and Outlook

In this chapter we employed the triangular-tessellation technique introduced in Chapter 2 and Ref. [147] to determine the free energy of adsorption for anisotropic colloids at a flat liquid-liquid interface. We used this free energy to construct a vector field of adsorption force and its associated flow lines. These flow lines gave insight into the stability of the minima in the free energy and the time dependence of the adsorption process according to our simple model.

The adsorption of cylindrical colloids revealed a strong dependence of the adsorption orientation on the particle's orientation at contact. For long cylinders we showed that the metastable minimum in the free energy, for which the cylinder is oriented perpendicular to the interface, could be attractive to an unexpectedly large range of initial-contact orientations. Even more remarkably, we found that for short cylinders and for an appropriate choice of the contact angle the colloid could pass through the interface without adsorbing to it. This constituted the first time that this phenomenon was observed theoretically. It was hitherto believed that the enormous strength with which colloids bind to the interface is a guarantee that adsorption occurs in the absence of any barriers, caused by, e.g., positive line tension or electrostatic repulsion. Our results showed that this assumption may not always be valid.

The observations in this chapter were made using a simple model that neglects many elements required to give an accurate description of the physics of experimental systems. However, there are indications [240] that our results may to some extent be recovered by more elaborate models. Our analysis and our approaches can be built upon in future studies to achieve a better understanding of the behaviour of anisotropic colloids at a liquid-liquid interface.



---

## Triangular Tessellation and Nonconvex Patterned Particles

---

In this chapter we extend the numerical technique of triangular tessellation introduced in Chapter 2. This extended technique allows us to numerically determine the free energy of adsorption for a nonconvex colloidal particle with surface patterning at a flat liquid-liquid interface. Two cases are considered: truncated cubes with facets that have different surface properties and octapod-shaped particles. For the former we investigate the adsorption behaviour, for the latter we are interested in the cross-sectional shapes that result from a plane-particle intersection. Such cross sections can be relevant to the analysis of confocal microscopy data. We also investigate the effects of interfacial deformation on the adsorption of a spherical particle and use these results to comment on the validity of the assumptions made in Chapters 2 and 3.

## 4.1 Introduction

Recent advances in the synthesis of colloids and nanoparticles have resulted in a wide range of surface-patterned and/or nonconvex particles [82, 83]. For example, there are (Janus) particles with two different halves [110–119], particles for which the poles and equator are different [32], and many nanoparticles [84–86, 89–93, 95, 96], which have an inherent surface patterning due to their faceted nature [241]. Examples of nonconvex particles include dumbbells [97], colloidal clusters [29, 98], branched colloids and nanocrystals such as octapods [54, 78, 99–101] and tetrapods [102, 103], nanostars [104–106], and colloidal caps [107–109]. The development of these new colloids and nanoparticles, which have complex shapes and (contact-angle) surface heterogeneities, presents many opportunities for the study of particles adsorbed at liquid-liquid and liquid-gas interfaces. The in- and out-of-equilibrium adsorption behaviour of these particles [163, 164, 242] may deviate substantially from that of spheres.

Theoretical analysis of colloids adsorbed at an interface is difficult even for simple homogeneous particles, due to the complex geometry that arises by the particle penetrating the interface [147]. For nonconvex and surface-patterned particles this problem is exacerbated. To the best of our knowledge, only for amphiphilic - having both a hydrophilic and a hydrophobic part - spherical Janus particles [141, 142, 146] and for similarly patterned cylindrical particles [160] was the adsorption considered using a force or free-energy analysis. A technique that may be applied to study the adsorption of complex (surface-patterned) particles at an interface is therefore required.

As an initial step towards such a technique we introduce a generalized version of the theory from Chapter 2 in Section 4.2. In Section 4.3 we extend the triangular-tessellation technique, which is used to numerically approximate this free energy of adsorption, to reflect the changes in our model. In Section 4.4 we investigate the behaviour of truncated nanocubes with surface patterning at an interface and we show that the equilibrium adsorption configurations can be subdivided into three classes. To which class the equilibrium configuration of a system belongs only depends on the properties of the patterning and the level of truncation. We discuss possible plane-octapod cross sections in Section 4.5 to demonstrate the applicability of our method to nonconvex particles. We conclude this chapter by considering the effects of interfacial deformation on the adsorption of a single sphere in Section 4.6.

## 4.2 Theoretical Model

In this section we extend our theory of interfacial adsorption for uniaxial convex colloids from Chapter 2 to a theory for nonconvex colloids with surface patterning. We consider a particle of which the surface has several areas with different liquid-solid surface tension properties (contact-angle patterning), see Fig. 4.1. An axis is fixed through the centre of mass of the particle, at which we locate the origin of the system. The interface is positioned at a height  $z$  with respect to the origin. The polar angle  $\phi$  specifies the angle between the axis and the interfacial normal, and the orientation angle  $\omega$  specifies rotations around the axis.



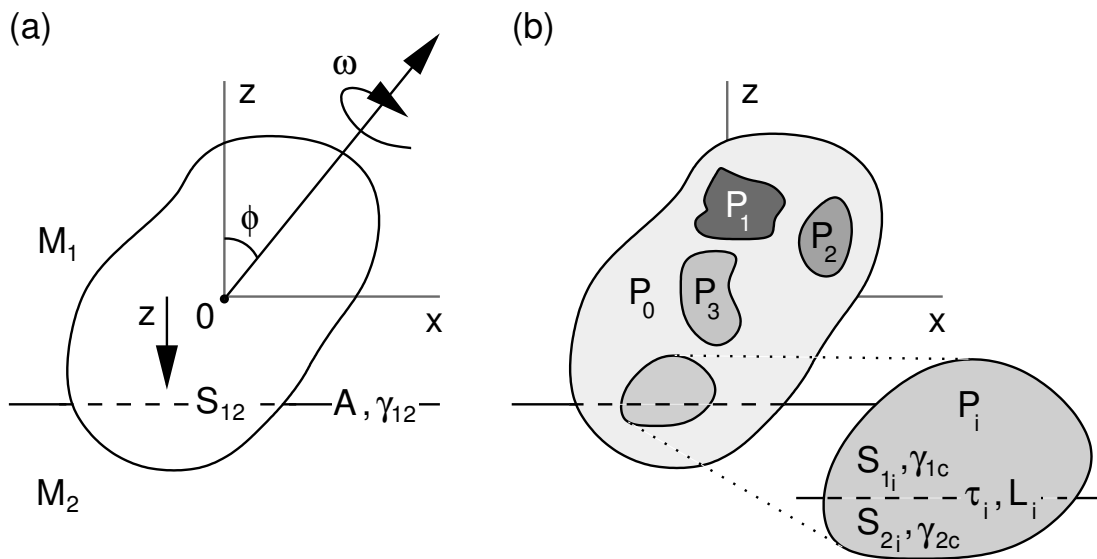


**Figure 4.1:** A schematic view of a nonconvex surface-patterned colloid adsorbed at a liquid-liquid interface (a) and a sketch of the same colloid's surface patterning (b). (a) The particle's position and orientation are described by three quantities. (i) The depth  $z$ . (ii) The polar angle  $\phi$  that some fixed axis through the colloid's centre of mass, where the origin is located, makes with the interfacial normal. (iii) The angle  $\omega$  which specifies rotations around this axis. The parameter  $A$  denotes the total (macroscopic) surface area of the interface,  $S_{12}$  the area excluded from the interface by the presence of the particle, and  $\gamma_{12}$  the medium 1 ( $M_1$ ) - medium 2 ( $M_2$ ) surface tension. The surface patches are labelled  $P_i$ . (b) Each patch has a  $P_i - M_1$  surface tension  $\gamma_{1c_i}$ , a  $P_i - M_2$  surface tension  $\gamma_{2c_i}$ , and a three-phase line tension  $\tau_i$ . The surface area of  $P_i$  in  $M_1$  is given by  $S_{1_i}$ , the surface area in  $M_2$  by  $S_{2_i}$ , and the contact-line length by  $L_i$ .

The free energy of adsorption is specified by the particle's surface properties. Let the surface be partitioned into *patches*  $P_i$ , with  $i = 0, 1, \dots, n$  an index, see Fig. 4.1. Each patch has a specific patch-medium surface tension  $\gamma_{1c_i}$  ( $P_i - M_1$ ) and  $\gamma_{2c_i}$  ( $P_i - M_2$ ), and a line tension  $\tau_i$ . Let  $S_{1_i}$  be the surface area of patch  $P_i$  in  $M_1$ ,  $S_{2_i}$  the surface area in  $M_2$ , and  $L_i$  the length of the associated contact line. The free energy of adsorption for the colloid in our approximation is given by

$$V(z, \phi, \omega) = \gamma_{12}(A - S_{12}) + \sum_{i=0}^n (\gamma_{1c_i} S_{1_i} + \gamma_{2c_i} S_{2_i} + \tau_i L_i). \quad (4.1)$$

We define  $S_i \equiv S_{1_i} + S_{2_i}$ , such that the total surface area is  $S = \sum_{i=0}^n S_i$ . The free energy of adsorption is set to zero in  $M_1$  by subtracting

$$\gamma_{12}A + \sum_{i=0}^n \gamma_{1c_i} S_i, \quad (4.2)$$

to obtain the shifted free energy of adsorption

$$F(z, \phi, \omega) = \sum_{i=0}^n ((\gamma_{1c_i} - \gamma_{2c_i})(S_{1_i} - S_i) + \tau_i L_i) - \gamma_{12} S_{12}. \quad (4.3)$$

The quantities  $f \equiv F/\gamma_{12}S$ ,  $\gamma_{12} \cos \theta_i \equiv \gamma_{1c_i} - \gamma_{2c_i}$  [140],  $r_i \equiv S_i/S$ ,  $r_{1_i} \equiv S_{1_i}/S$ ,  $r_{12} \equiv S_{12}/S$ ,  $l_i \equiv L_i/\sqrt{S}$ , and  $\tau_i^* \equiv \tau_i/\gamma_{12}\sqrt{S}$  are introduced to rewrite Eq. (4.3) to the following elegant form

$$f(z^*, \phi, \omega) = \sum_{i=0}^n (\cos \theta_i (r_{1_i} - r_i) + \tau_i^* l_i) - r_{12}. \quad (4.4)$$

Here  $z^* = z/\mathcal{R}$ , with  $\mathcal{R}$  the radius of the smallest sphere that encloses the particle.

In our model we glanced over one detail, namely that it is possible to have a four-phase contact line on the boundary of two patches, when the interface (partially) coincides with this boundary. We define the contribution to the free energy of adsorption to be the length of this four-phase contact line times the averaged line tension. To the best of our knowledge, only one study considered four-phase contact lines [243], but nothing is known about the associated line tension. However, we believe that the averaging we propose is not unreasonable.

### 4.3 Improved Numerical Technique

To numerically approximate the free energy in Eq. (4.4), the object under consideration is tessellated with triangles using a suitably chosen parametrization, also see Chapter 2. This tessellation obeys the following rules. (i) Patch boundaries are approximated by triangle edges; consequently, a single triangle has a single set of surface properties. (ii) Each triangle is labelled according to the patch it is in, with the label  $P_i$ . (iii) The direction of the surface normal of each triangle is known and is required to point outward from the particle. (iv) A sufficiently large number of small triangles is used where the surface of the particle changes abruptly, either through patterning, a large gradient, or

a cusp-like feature. Determining the approximate total surface area  $\tilde{S}$  is analogous to the procedure outlined in Chapter 2. Similarly, the surface area of the  $i$ -th patch,  $S_i$ , is approximated by summing the surface area of triangles with label  $P_i$ , yielding  $\tilde{S}_i$ . The surface area of a patch above the interface  $S_{1_i}$  is obtained by subdivision the triangle mesh, see Fig. 2.3, and the approximate surface area is denoted by  $\tilde{S}_{1_i}$ . The area  $\tilde{S}_{2_i}$  is established in the same way.

Determining  $\tilde{S}_{12}$  and  $\tilde{L}_i$  is, however, a little more involved. In partitioning the triangle mesh, two points are obtained for each triangle intersected by the interface. These two points span a *line segment*, which is oriented via the normal of the triangle. After partitioning a set of line segments, say  $\Lambda$ , is obtained, see Fig. 4.2a. The members of  $\Lambda$ , say  $\mathbf{\Lambda}_i$ , with  $i$  an index, are encoded with information on the location of the particle as follows. The triangle's normal is projected onto the interface and normalized. This unit vector, referred to as a directional (unit) vector, gives orientation of the line segment. A triangle which is flush with the interface needs to be special cased: all three directional unit vectors point outward. Each  $\mathbf{\Lambda}_i$  has 7 elements, two for the  $xy$ -location of the starting point of the line segment, two for the end point of the segment, another two specify the directional unit vector, and one gives the number of the patch it corresponds to. To determine  $\tilde{S}_{12}$  the set of line segments  $\Lambda$  undergoes several refinement steps which we refer to as *loop reduction*.

Consider all instances of a  $\mathbf{\Lambda}_i$ , for which there is a  $\mathbf{\Lambda}_j$ , that has the same line segment coordinates, but not necessarily the same directional vector, see Fig. 4.2a. There are two situations in which there are 'overlapping' segments. (i) When two triangles are completely on opposite sides of the interface and they share two vertices, we obtain segments with the same directional vector. (ii) When two triangles are both completely on the same side of the interface and they share two vertices located on the interface, or when they are both flush with the interface, we obtain two  $\mathbf{\Lambda}_i$  with antiparallel directional vectors. To eliminate unnecessary segments  $\mathbf{\Lambda}_j$  is removed from  $\Lambda$ , if  $\mathbf{\Lambda}_i$  and  $\mathbf{\Lambda}_j$  have the same directional vector. If, however, the directional vectors are antiparallel both instances are removed, since then these are interior segments or they come from the particle just touching the interface. By subjecting each element in  $\Lambda$  to this procedure a new set  $\tilde{\Lambda}$  is formed. This set contains only segments which are a part of the boundary of  $S_{12}$ , see Fig. 4.2b.

The set  $\tilde{\Lambda}$  is subdivided into closed *loops*. A loop is determined by choosing a segment in  $\tilde{\Lambda}$  and adding its neighbours recursively, until no more new neighbours can be added. This procedure is illustrated as follows. Let  $\mathbf{\Lambda}_i$  be the starting segment. Then after one iteration we obtain the sequence  $\mathbf{\Lambda}_{i-1} - \mathbf{\Lambda}_i - \mathbf{\Lambda}_{i+1}$ , and after  $m$  iterations  $\mathbf{\Lambda}_{i-m} - \dots - \mathbf{\Lambda}_{i-1} - \mathbf{\Lambda}_i - \mathbf{\Lambda}_{i+1} - \dots - \mathbf{\Lambda}_{i+m}$ . The last neighbours to be added are either equal, i.e.,  $\mathbf{\Lambda}_{i-m} = \mathbf{\Lambda}_{i+m}$ , in which case only one is added, or have a common vertex, in which case the loop is also closed. We thus obtain a loop which is ordered by construction. This procedure is repeated until  $\tilde{\Lambda}$  is subdivided into loops. It is a priori not excluded that a loop crosses itself, e.g., a lemniscate-like structure. Crossover points are however easily located, because such a vertex shares an even number of line segments greater than two. We cut all loops into closed pieces which do not cross themselves, see Fig. 4.2c. Let these new loops be denoted by  $\mathcal{C}_i$  with  $i$  an index, then  $\tilde{\Lambda} = \cup \mathcal{C}_i$  and  $\cap \mathcal{C}_i = \emptyset$ .

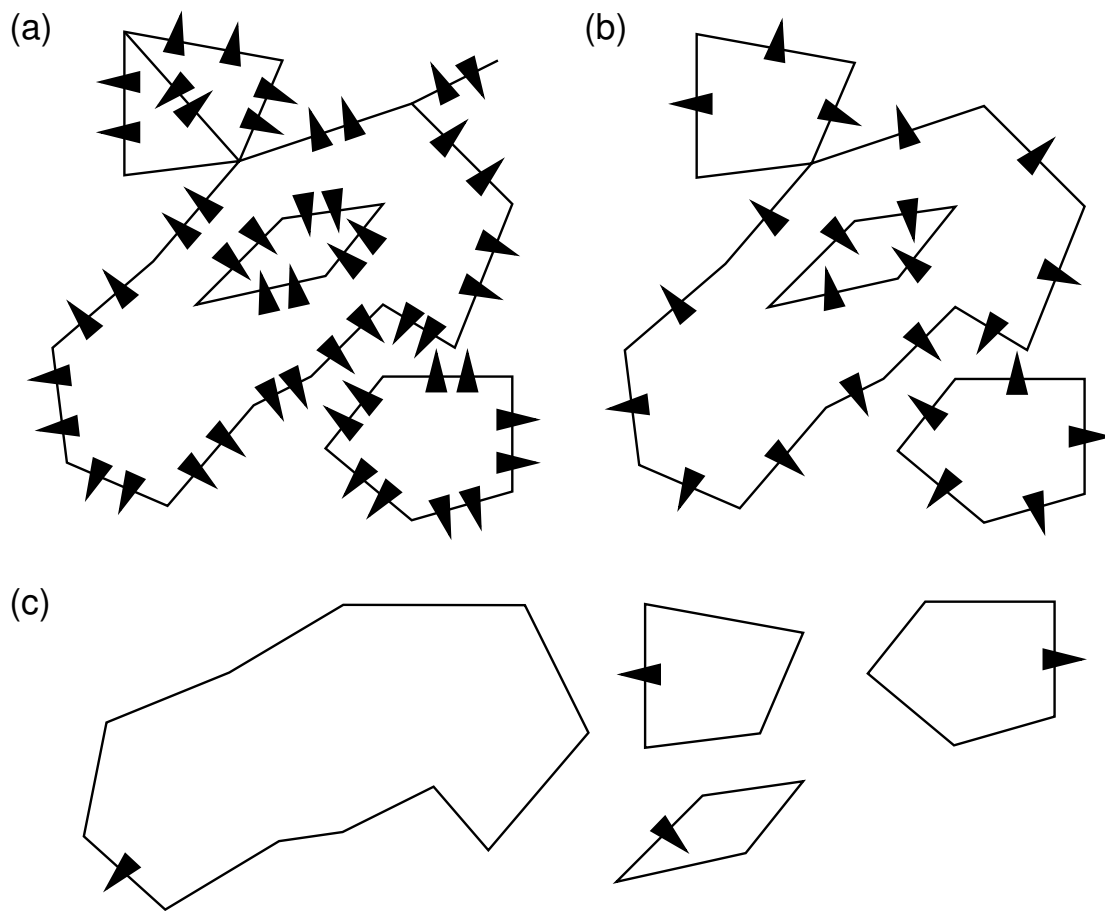


**Figure 4.2:** Illustration of the loop-reduction procedure for the approximate area excluded from the interface  $\tilde{S}_{12}$  by the presence of some nonconvex colloid. (a) The line segments obtained after partitioning triangles form the set  $\Lambda$ . The arrow heads represent the directional unit vectors. (b) The set of segments  $\tilde{\Lambda}$  which is obtained by removing all redundant line segments. (c) The subdivision of  $\tilde{\Lambda}$  into four closed oriented loops.

For each  $\mathcal{C}_i$  we have to determine whether it is outwardly or inwardly oriented. By construction loops cannot contain both outward and inward segments. For a loop where all directional vectors point outward, there is at least one line segment for which one of the halflines drawn through its end points does not intersect another line segment in that loop. Numerically checking this criterion efficiently is not trivial. In practice, it is seldom required to invoke this property to determine the orientation of the loop. Any knowledge on the possible shapes excluded from the interface can be used to make the algorithm more efficient. A dumbbell [97], for instance, only has outwardly oriented loops, which can be easily derived from its symmetry properties. We define the sign function  $S(\mathcal{C}_i)$  to be  $+1$  when the orientation of a closed loop is outward and  $-1$  if the orientation is inward.

After each loop is labelled either ‘outward’ or ‘inward’, the area enclosed by each of the  $\mathcal{C}_i$  in  $\tilde{\Lambda}$  is easily calculated using a polygonal version of Green’s theorem. The line segments in a loop  $\mathcal{C}_i$  define a set of points in the plane, which are ordered by construction. These points can be mapped onto three-dimensional (3D) vectors  $\mathbf{a}_j$ , where the first two components are the  $x$  and  $y$  coordinates, respectively, the last component is zero, and  $j$  is an index. Let the set of these vectors be ordered according to the ordering imposed by  $\mathcal{C}_i$ . If there are  $\tilde{n} - 1$  distinct points which define the loop, then we require  $j = 0, \dots, \tilde{n}$  with  $\mathbf{a}_{\tilde{n}} = \mathbf{a}_0$ . The area of  $\mathcal{C}_i$  is given by

$$A(\mathcal{C}_i) = \left| \sum_{j=0}^{\tilde{n}-1} \mathbf{a}_j \times \mathbf{a}_{j+1} \right|, \quad (4.5)$$

where the  $\times$ -symbol indicates the cross-product and the vertical bars the norm of the vector obtained by summation. It can be shown that Eq. (4.5) is only valid when there are no self intersections, which is why these needed to be eliminated first. The surface area excluded from the interface by the presence of the particle is now approximated

$$\tilde{S}_{12} = \sum_i S(\mathcal{C}_i) A(\mathcal{C}_i). \quad (4.6)$$

The approximate contact-line length  $\tilde{L}_i$  can be obtained by summation of the length of the line segments that have the label  $P_i$ .

In summary, we presented a method that can be used to determine the surface areas and contact-line length(s) required to establish the free energy of adsorption for an arbitrary nonconvex contact-angle-patterned colloid in contact with a flat interface.

## 4.4 Interfacial Adsorption of a Truncated Cube

In this section we apply our generalized algorithm to study a specific contact-angle-patterned particle, namely a truncated nanocube, also see Fig. 4.3. These type of particles have recently been synthesized [89, 93] and investigations of their self-assembly on a liquid-liquid interface are under way [164]. As an initial step towards understanding the experimentally observed behaviour, we apply our simple model to this system and investigate the way in which such a particle adsorbs. This analysis should be seen as a proof of principle for the generalized triangular-tessellation technique, not as an attempt to rigorously quantify the physics behind the adsorption of these particles at an interface.

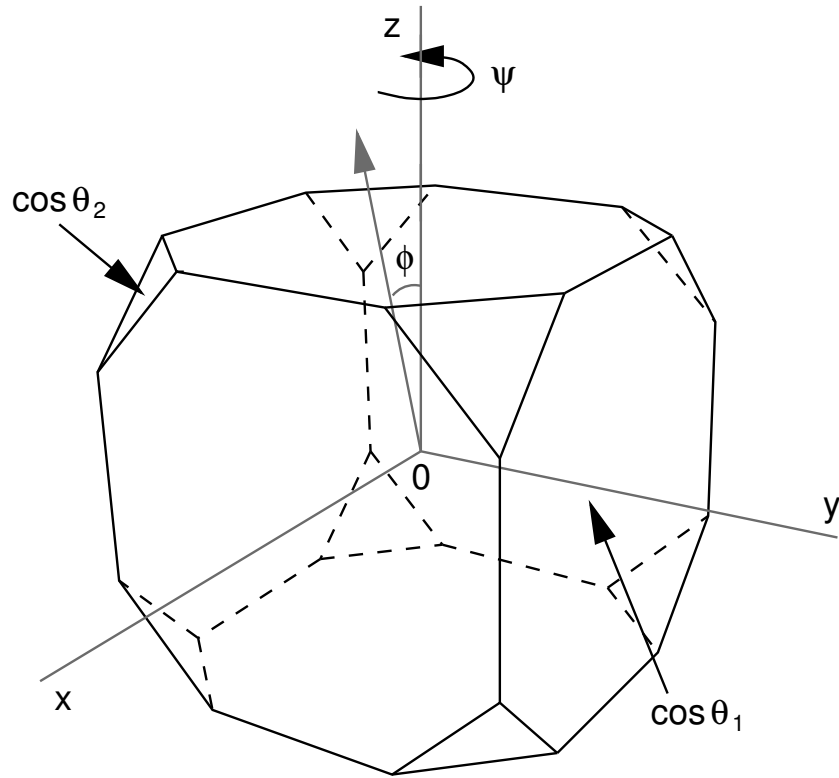


**Figure 4.3:** A sketch of the initial configuration of a contact-angle-patterned truncated cube, with truncation parameter  $s = 0.25$ . The orientation of the particle is specified by two angles: the polar angle  $\phi$ , which gives a rotation in the  $xz$ -plane with respect to the  $z$ -axis, and the azimuthal angle  $\psi$ , which gives the rotation around the  $z$ -axis. The octagonal faces can have a three-phase contact angle that differs from that of the triangular faces, as indicated by the labels  $\cos\theta_1$  and  $\cos\theta_2$ , with  $\theta_1$  and  $\theta_2$  the respective contact angles. The position of the flat liquid-liquid interface (not shown here for clarity) is given by the height  $z$ , which is measured with respect to the origin.

#### 4.4.1 The Truncated Cube Model

In our model the truncated cube initially has its octagonal faces axis-aligned and it is centred on the origin. The level of truncation can be described by the parameter  $s \in [0, 1/2]$ . The set of vertices of the truncated cube in its initial configuration is given by

$$\{\mathbf{v}(s)\} = \frac{1}{\left(1 - \frac{4}{3}s^3\right)^{(1/3)}} \mathcal{P}_D \left( \left( \pm \left( \frac{1}{2} - s \right), \pm \frac{1}{2}, \pm \frac{1}{2} \right)^T \right), \quad (4.7)$$

where  $\mathcal{P}_D$  is a permutation operation that generates all permutations of each element in the set of 8 vertices spanned by the  $\pm$ -operations. By letting  $\mathcal{P}_D$  act we obtain 48 vertices. Subsequently deletion of all duplicates reduces this set to the desired total of 24 vertices. The ‘ $T$ ’ indicates transposition. The prefactor ensures that the truncated cube is normalized to unit volume.

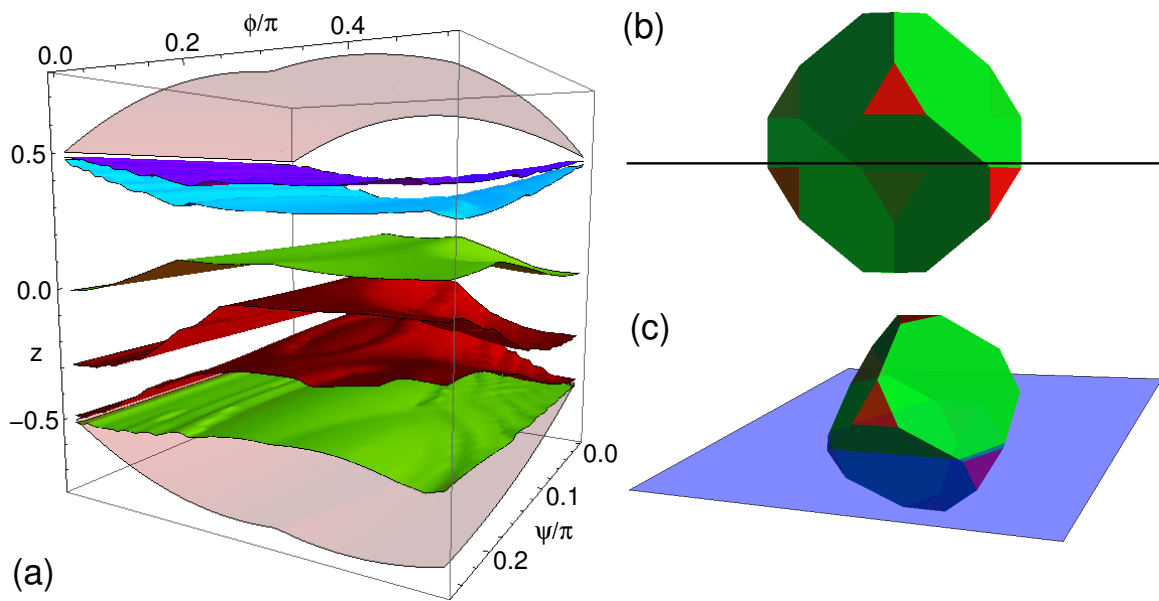
The orientation of a truncated cube is given by two angles. The azimuthal angle  $\psi$  applies a rotation around the  $z$ -axis. This is followed by a rotation in the  $xz$ -plane of  $\phi$  radians around the origin w.r.t. the  $z$ -axis in a counter-clockwise manner,  $\phi$  is referred to as the polar angle. It can be shown that these two rotations are sufficient to generate all possible orientations of a truncated cube. Due to symmetry properties of the particle, we can restrict ourselves to  $\phi \in [0, \pi/2]$  and  $\psi \in [0, \pi/4]$ . The height of the interface with respect to the origin, which is located at the centre of the particle, is denoted by  $z$ . We assume that the wetting properties of the different facets are given by  $\cos\theta_1$  for the octagonal facets and  $\cos\theta_2$  for the triangular facets, with  $\theta_1$  and  $\theta_2$  the respective contact angles.

#### 4.4.2 The Free Energy of Adsorption

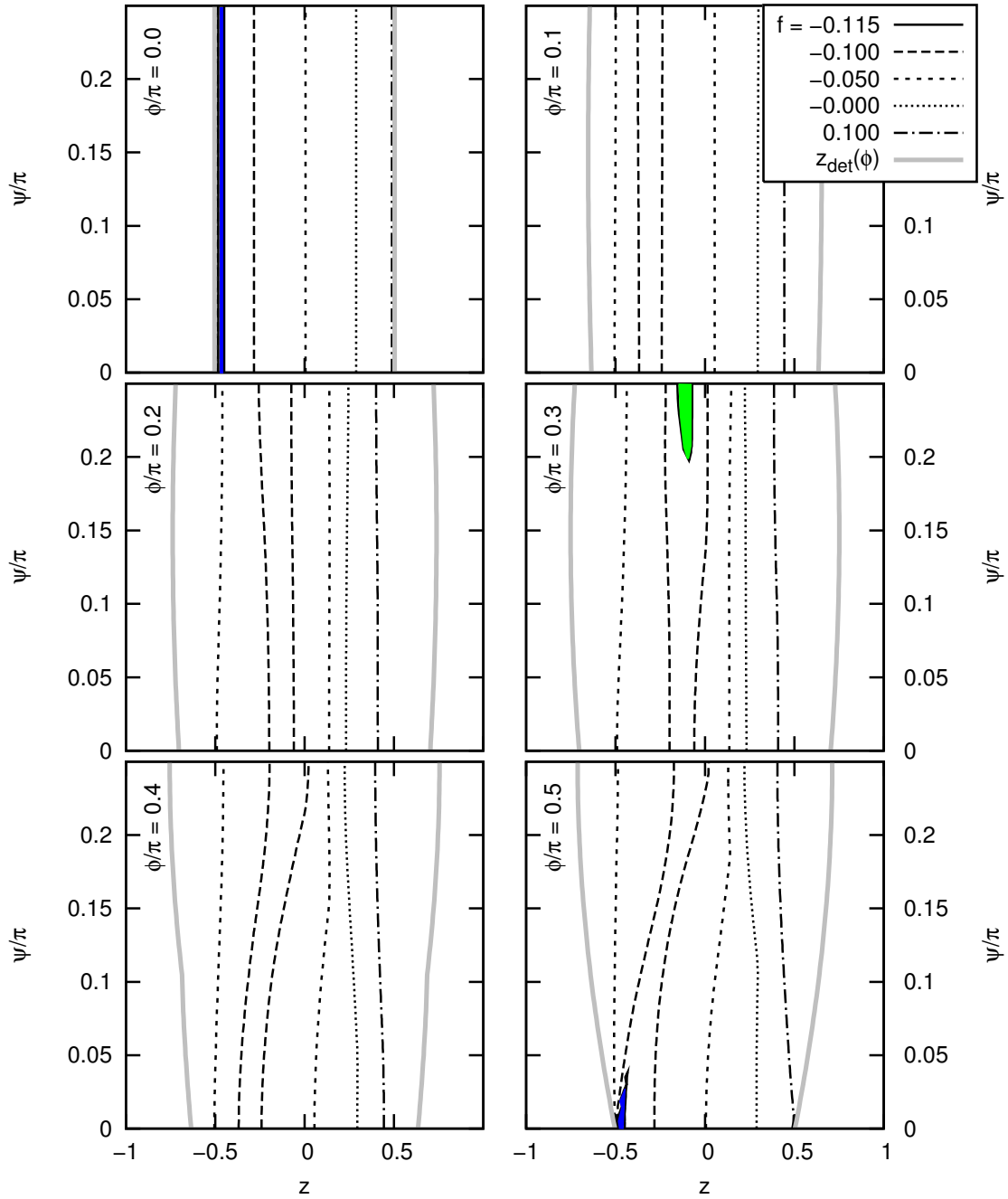
By varying  $z$ ,  $\phi$ , and  $\psi$  for fixed values of  $\cos\theta_1$  and  $\cos\theta_2$  and computing the reduced free energy  $f$  using our numerical technique, we could determine a four-dimensional (4D) free-energy landscape; three parameter coordinates and one coordinate for the function value. For several conveniently chosen (symmetric) configurations and several surface patterns we analytically verified the accuracy of our triangular-tessellation technique. The correspondence between the analytic and numerical results was within the numerical precision of our algorithm, which is very high, because we only required a 56 relatively large triangles to ‘approximate’ the shape of the truncated cube. This correspondence gives confidence that our technique can be used to handle general surface-patterned particles as well. In the following we restrict ourselves to investigate two levels of truncation  $s = 0.25$  and  $s = 0$ . All results were established using 50 nonequidistant grid points in  $z$ ,  $\phi$ , and  $\psi$ , respectively.

Figure 4.4 shows the free-energy landscape and equilibrium configurations for a truncated nanocube with  $\cos\theta_1 = -0.25$ ,  $\cos\theta_2 = -0.25$ , and  $\tau^* = 0$ , i.e., the particle has homogeneous surface properties. Note that we do not require any knowledge about the surface tension of the interface  $\gamma_{12}$  in the theory of Eq. (4.4). Figure 4.5 shows cross sections of the landscape in Fig. 4.4a parallel to the  $z\psi$ -plane.

There are two (meta)stable minima in the free energy for this system. The absolute minimum (green, middle-right Fig. 4.5) corresponds to the configuration shown in Fig. 4.4(b,c). A relatively large piece of the interface is excluded, thereby lowering the free energy, but this comes at the price of a large contact area with the unfavoured medium. The metastable minimum for  $\phi = 0$  (blue, top-left Fig. 4.5) corresponds to the particle being almost completely immersed in the favoured medium and it only excludes one of its octagonal facets from the interface. The free energy of this configuration is nearly identical to that of the absolute minimum, but based on our results it is favourable to exclude a larger amount of interfacial surface area for this particular system. Finally, there appears to be a third minimum (blue, bottom-right Fig. 4.5). The presence of this minimum can be explained by the fact that configurations with  $\phi = 0$  and  $\psi \in [0, \pi/4]$  are essentially the same as the configuration with  $\phi = \pi/2$  and  $\psi = 0$  due to the symmetry properties of the truncated cube. We therefore again find the metastable minimum. The small size of the region around  $\phi = \pi/2$  and  $\psi = 0$  where the configurations are similar to those around  $\phi = 0$  and  $\psi \in [0, \pi/4]$  also explains the serrated nature of the  $f = -0.115$  contour



**Figure 4.4:** The reduced free energy of adsorption  $f$  for a truncated cube with contact-angle surface patterning and its equilibrium position. The parameters for this system are  $s = 0.25$ ,  $\cos\theta_1 = -0.25$ ,  $\cos\theta_2 = -0.25$ , and  $\tau^* = 0$ . (a) Three-dimensional (3D) contour plot of  $f$  as a function of the height  $z$ , the polar angle  $\phi$ , and the azimuthal angle  $\psi$ . From red to blue the free-energy contours are  $f = -0.1$ ,  $-0.05$ ,  $0.05$ , and  $0.1$ , respectively. Two red translucent surfaces bound the adsorption region. (b,c) Two views of the equilibrium configuration achieved for this particular parameter set. The particle is intersected by the interface in such a way that three of the triangular faces are close to touching the interface and the largest part of the particle is immersed in the top medium.



**Figure 4.5:** A two-dimensional (2D) contour representation of the free energy  $f$  in Fig. 4.4a as a function of  $z$  and  $\psi$ . We chose slightly different contours here to give better insight into the properties of the landscape. The thick grey curves show the boundaries to the adsorption region. The minimum free energy is given by  $f \approx -0.116$ . There are three regions in this landscape where  $f < -0.115$ , indicated using blue and green. The absolute minimum is located in the green region and corresponds to the configuration in Fig. 4.4(b,c).

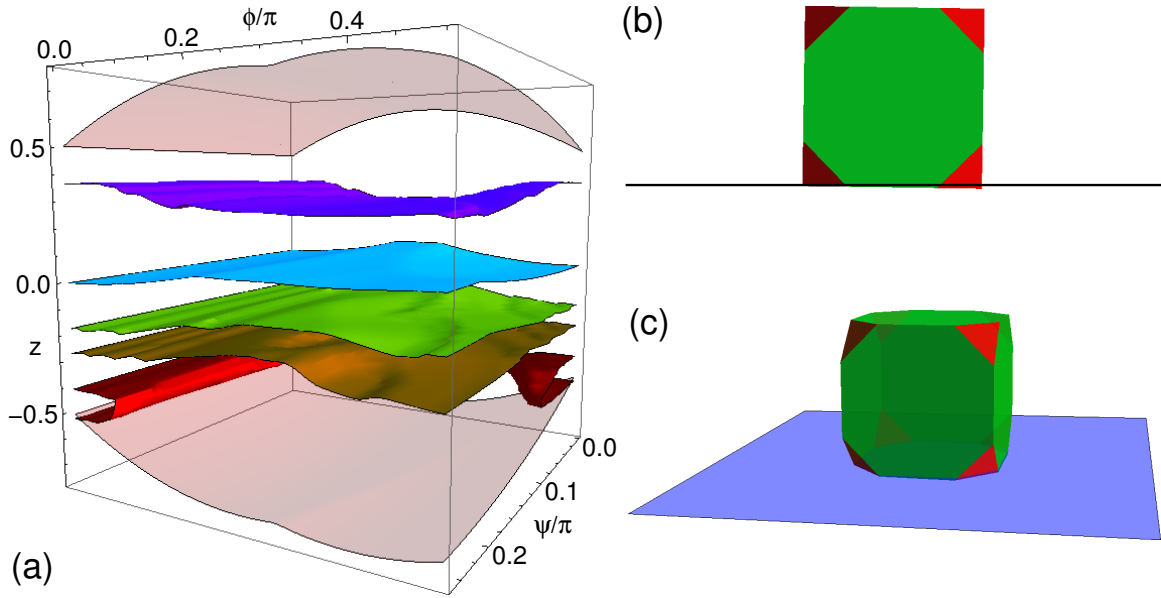


**Figure 4.6:** A representation of the reduced free energy  $f$  and the equilibrium position for a truncated nanocube with  $s = 0.25$ ,  $\cos \theta_1 = -0.8$ ,  $\cos \theta_2 = 0.0$ , and  $\tau^* = 0$ . (a) 3D contour plot of  $f$  as a function  $z$ ,  $\phi$ , and  $\psi$ . From red to blue the free-energy contours are  $f = -0.01, 0.05, 0.1, 0.2$ , and  $0.4$ , respectively. The two red translucent surfaces bound the adsorption region. (b,c) Two views of the equilibrium configuration achieved for this particular parameter set. The particle is almost completely immersed in the top medium.

in the bottom-right panel, since there is increased numerical uncertainty associated with such a small feature.

We also considered the set of parameters,  $s = 0.25$ ,  $\cos \theta_1 = -0.8$ ,  $\cos \theta_2 = 0$ , and  $\tau^* = 0$  for which the particle is contact-angle patterned. We obtained a different free-energy landscape, see Figs. 4.6a and 4.7, for which there is only one minimum, corresponding to the equilibrium configuration shown in Fig. 4.6b. The change in adsorption behaviour between the two systems we considered here is exclusively determined by the properties of the surfaces and media that are in contact. The quality of our results for these systems gave us confidence in applying our technique for other choices of the contact angle pattern as well. In the next section we therefore examine the dependence of the equilibrium configuration on  $\cos \theta_1$  and  $\cos \theta_2$ .

### 4.4.3 Equilibrium Adsorption Configurations

We considered an equidistant grid for  $\cos \theta_i \in [-1, 1]$  ( $i = 1, 2$ ) using 20 points, where we assumed  $s = 0.25$  and  $\tau^* = 0$ . For each of the contact-angle combinations we employed our triangular-tessellation technique to determine the free energy of adsorption  $f$  and from that we obtained the associated equilibrium configuration. In analysing these equilibrium configurations, we observed that they can be divided into three groups. Members in a group have a small spread around an average configuration, and the distance between the groups in  $(z, \phi, \psi)$  is large, i.e., they are disjoint. In Fig. 4.8 we show three configurations

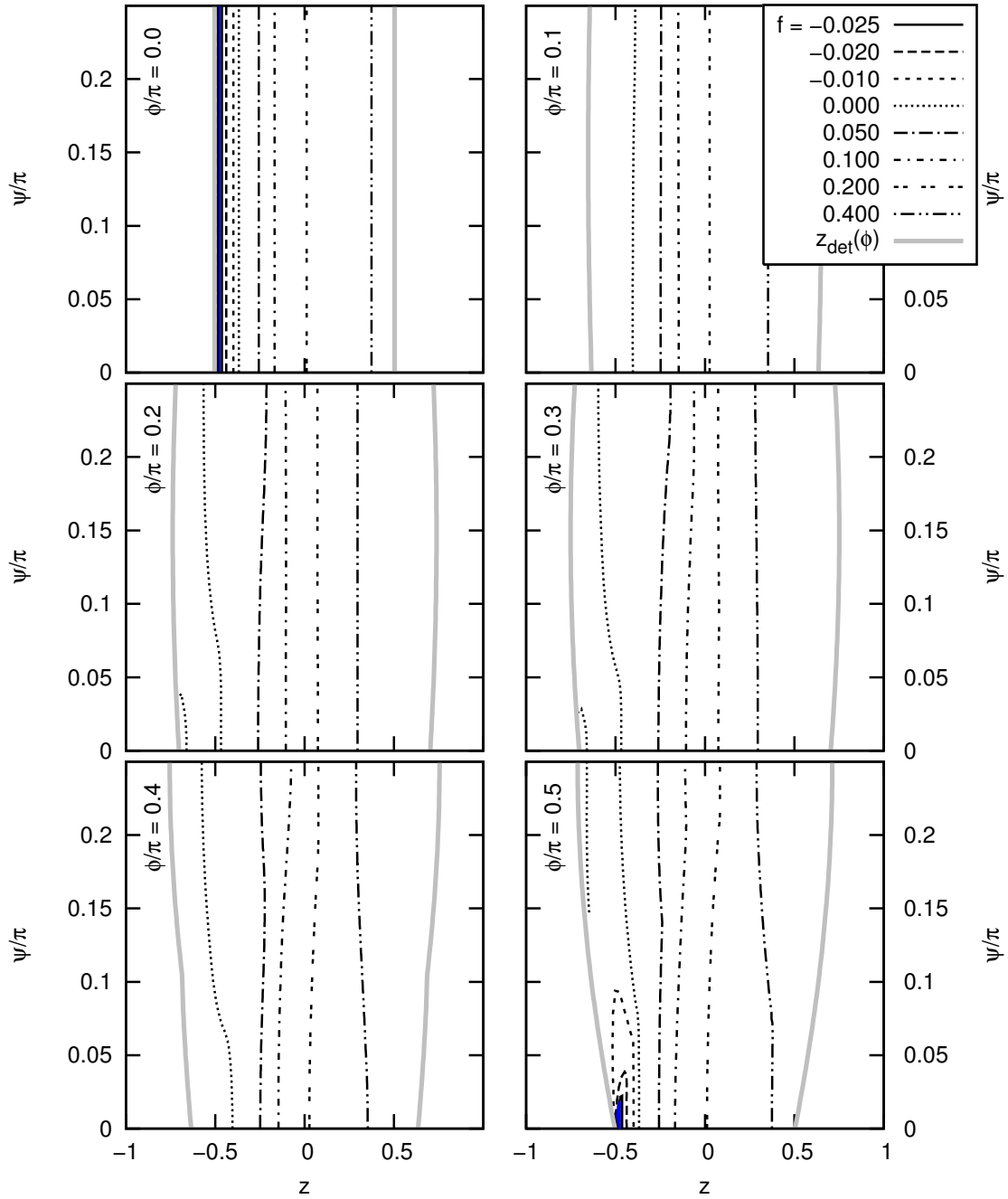


**Figure 4.7:** Various equi- $\phi$  sections corresponding to the system in Fig. 4.6. The slices of the landscape in Fig. 4.6a give a 2D contour representation of the free energy  $f$  as a function of  $\psi$  and  $z$ . Again we chose slightly different contours. The thick grey lines form the boundaries to the adsorption region. The minimum free energy is given by  $f \approx -0.026$ . There are now two regions in this landscape where  $f < -0.025$  occurs, indicated using blue. The absolute minimum, see Fig. 4.4(b,c), is assumed in both blue regions as explained in the text.

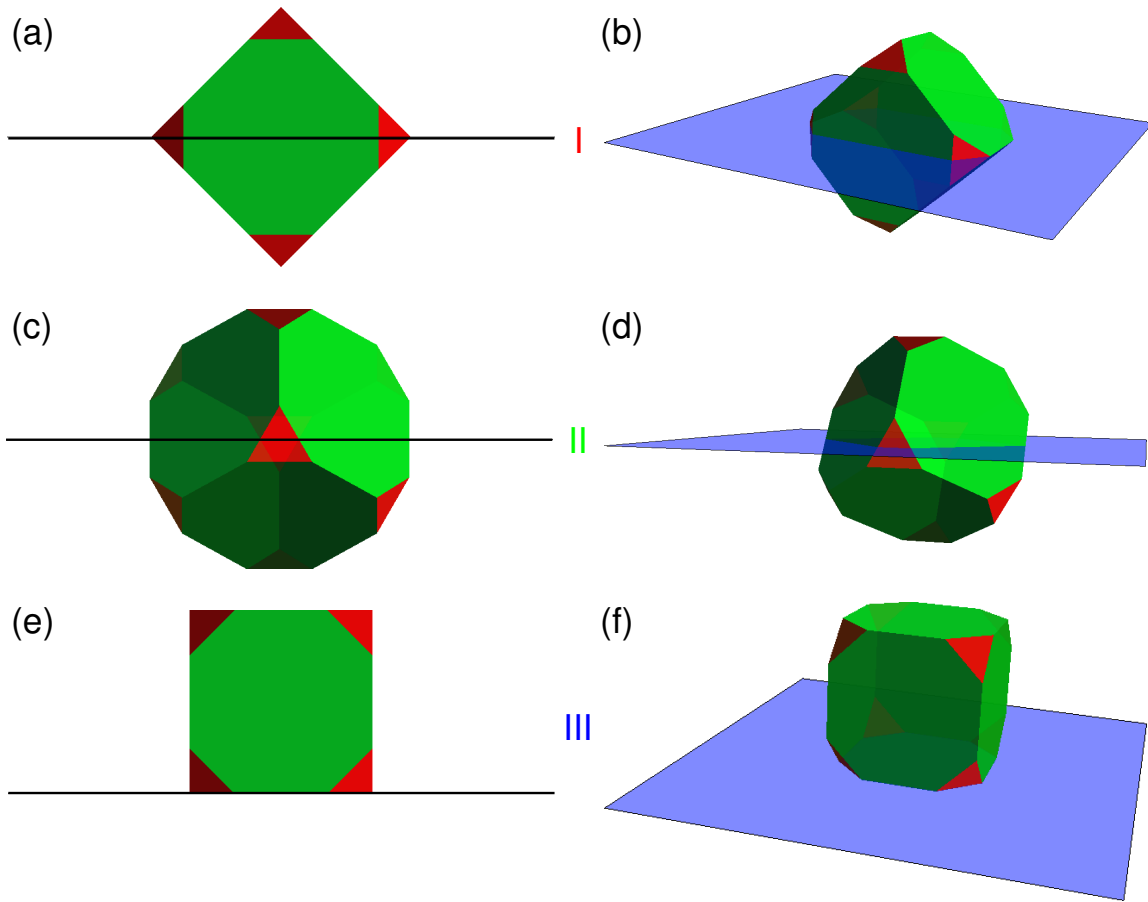


**Figure 4.8:** Visual representations of the three archetypal equilibrium adsorption configurations of a truncated cube ( $s = 0.25$ ) that are encountered by varying both  $\cos\theta_1$  and  $\cos\theta_2$  between  $-1$  and  $1$  ( $\tau^* = 0$ ). (a,b) The red ‘I’ configuration corresponds to the truncated cube having two opposing face diagonals and two associated opposing ribs flush with the interface. (c,d) The green ‘II’ configuration corresponds to the interface bisecting the particle in two of its triangular facets. (e,f) The blue ‘III’ configuration corresponds to one of the octagonal faces being flush with the interface.

that are representative of the three groups we found. The extent to which we take this archetypal property is exemplified by comparing Fig. 4.4b and configuration I from Fig. 4.8. The orientation in these two cases is very similar, the height of adsorption is however slightly different. To further illustrate the idea of these preferential configurations we also used the associated colour coding to indicate the minima in Figs. 4.5 and 4.7.

Figure 4.9 shows the equilibrium configurations obtained as a function of the two contact angles. We used the symmetry properties of the system to reduce the parameter space to  $\cos\theta_1 \in [0, 1]$  and  $\cos\theta_2 \in [-1, 1]$ . Most of the configurations we obtained can be assigned to one of the three representative states in Fig. 4.8. The relatively sharp division of these configurations into three areas is related to the disjoint nature of the grouping of the equilibrium configurations and shows that the members of these groups share properties with regards to the surface patterning. The contact angle of the octagonal

faces plays a dominant role in determining the particle's equilibrium configuration. This is to be expected, because the surface-area ratio of the triangular to the octagonal faces is 0.062.

In light of the results in Fig. 4.9, the presence of free-energy minima associated with configuration II and III for  $\cos \theta_1 = \cos \theta_2 = -0.25$ , see Figs. 4.4a and 4.5, can be explained by the close proximity of this parameter choice to the boundary between the respective regions. There are no metastable minima in the free energy for  $\cos \theta_1 = -0.8$  and  $\cos \theta_2 = 0.0$ , see Figs. 4.6a and 4.7, because this choice puts the system deep inside region III.

#### 4.4.4 Comparison to the Adsorption of a Cube

To give a reference frame for our results, we also studied regular cubes ( $s = 0$ ). Note that a cube only has one surface property in our model, which is specified by  $\cos \theta_1$ . We found *only two* equilibrium configurations upon varying the contact angle, i.e., all points in the respective groups fall on top of each other. Figure 4.10 shows this result and the associated equilibrium configurations. From Fig. 4.9 it becomes clear that for a truncated cube with homogeneous surface properties a new configuration appears with respect to the two configurations found for the cube. This new configuration can therefore be directly related to the truncation. Moreover, truncation appears to destabilize the equilibrium configurations, i.e., they are less sharply defined since the points in the three equilibrium-configuration groups have a spread. Keeping the change induced by truncation in mind, it becomes even more clear that the influence of  $\cos \theta_2$  is not very significant for  $s = 0.25$ . The only effect seems to be a slight increase/decrease in the sizes of the various regions.

In conclusion, we showed that we can determine the free energy of adsorption at a flat interface for a contact-angle surface-patterned particle by making use of the generalized triangular-tessellation technique. The research in this section is more a proof of principle than an attempt to establish a model for and rigorously analyse experimental systems. One key element that requires further investigation is the effect of interfacial deformation, which is expected to be very relevant in describing the behaviour of these sharp-edged particles in experiments. It would be interesting to see to what extent our observations may be recovered in a more elaborate model, but this goes beyond the scope of the current investigation.

## 4.5 Nonconvex Shapes and Confocal Microscopy

In this section we show that our generalized triangular-tessellation technique can be used to determine the cross section of a plane with a nonconvex particle. Together with the result in Section 4.4, this illustrates that our algorithm is in principle capable of determining the surface areas and contact-line length(s) required to establish the free energy of adsorption for a nonconvex contact-angle-patterned particle using our simple model. We choose *not* to study the free energy here, since for highly nonconvex faceted particles the assumption of negligible interfacial deformation is undoubtedly flawed. However, as mentioned in Section 2.4 the ability of our technique to determine cross-sectional shapes

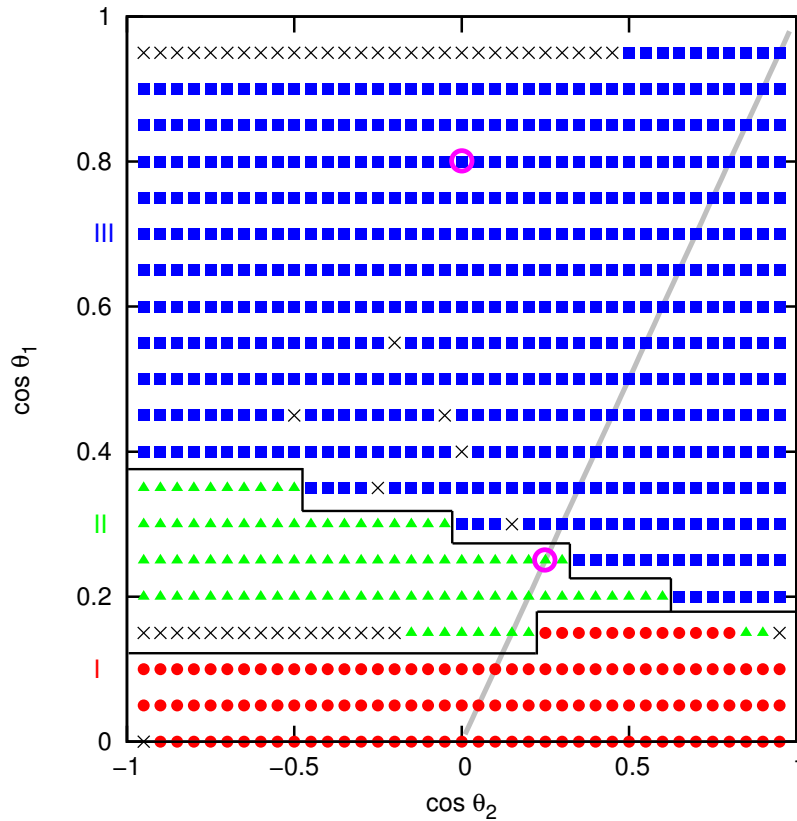


**Figure 4.9:** A visual representation of the equilibrium adsorption configurations as a function of  $\cos \theta_1$  and  $\cos \theta_2$  for a contact-angle-patterned truncated cube with truncation parameter  $s = 0.25$  and line tension  $\tau^* = 0$ . We used symmetry properties to reduce the domain. Red circles, green triangles, and blue squares indicate the configurations which can be assigned to groups I, II, and III, respectively, also see Fig. 4.8. Black crosses indicate the configurations which fall outside of these groups. The three groups of configurations also correspond to three connected areas in parameter space. We roughly indicate the boundaries between these areas using black lines. Two magenta circles give the location of systems equivalent to those considered in Figs. 4.4 and 4.6, respectively. The thick grey line indicates the systems for which the particle has a homogeneous contact angle ‘pattern’.

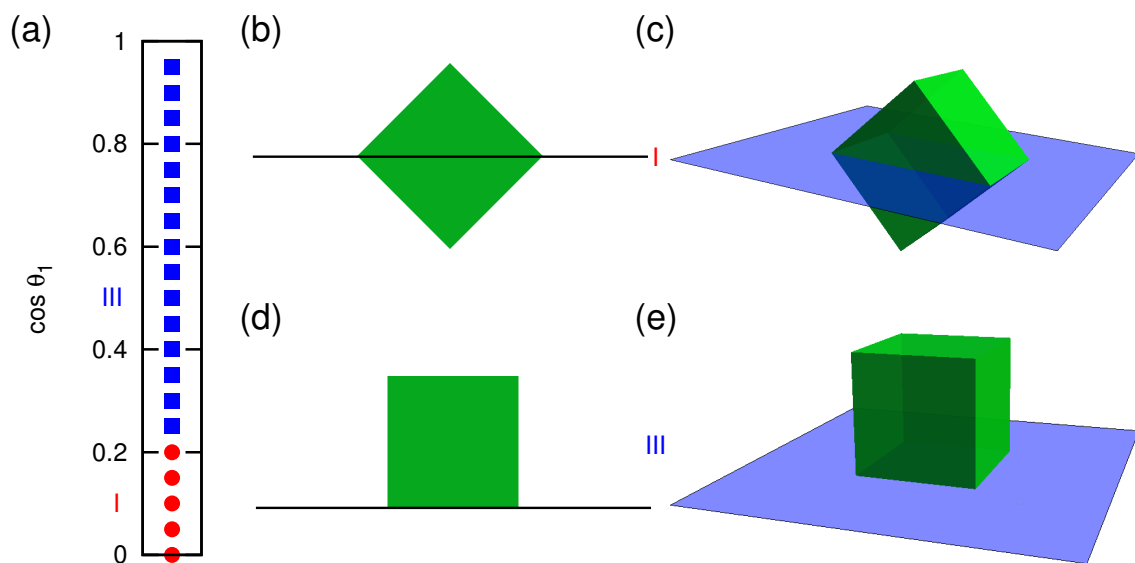


**Figure 4.10:** (a) The equilibrium adsorption configurations for a cube as a function of  $\cos \theta_1 \in [-1, 1]$ . We used symmetry properties to reduce the domain to  $\cos \theta_1 \in [0, 1]$ . Red circles indicate the systems that are in configuration ‘I’ and blue squares the systems that are in configuration ‘III’. The labelling is similar to that used in Fig. 4.9 to show the relation between these two particles. (b,c) The red ‘I’ configuration corresponds to the cube having two opposing face diagonals and two associated opposing ribs flush with the interface. (d,e) The cube in the blue ‘III’ configuration has one face flush with the interface, but is otherwise immersed in the favoured medium.

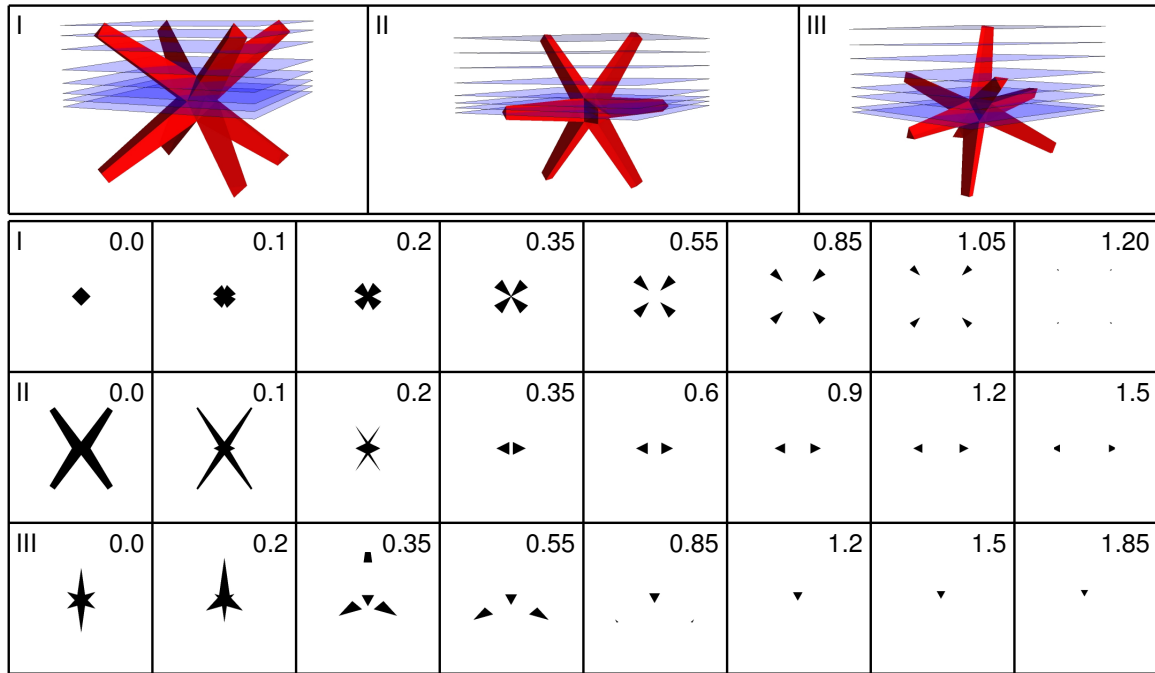


**Figure 4.11:** A sample of the cross sections that result from plane-octapod intersection. The top row gives three orientations of the octapod, labelled I, II, and III. The octapod (red) is intersected by various horizontal planes (blue, transparent). The bottom three rows give the different silhouettes that correspond to the intersections above. The orientation label can be found in the top-left corner of the leftmost panel. The height  $z$  is indicated in the top-right corner of each panel in the row. The projection of the octapod's centre of rotation is located in the middle of the panels.

for complex particles may be used to help understand two-dimensional (2D) confocal-microscopy data and to verify the quality of particle-tracking algorithms.

We considered an octapod-shaped nanocrystal [54], also see Chapter 7. This is an ideal candidate to demonstrate our technique on, because of its highly nonconvex nature, despite it being too small for conventional confocal microscopy. However, confocal microscopes capable of imaging on such length scales are being developed [244, 245]. The so-called octapods have an octahedral core on which eight tapered pods are grown. We approximated their shape according to the model given in Section 7.3.1. Figure 4.11 shows three orientations of the octapod model intersected by several conveniently chosen horizontal planes and the cross-sectional shape of these intersections. We scaled the model to unit volume and the value of the height  $z$  at which the plane intersects the octapod model is indicated in the associated reduced units. We obtained a variety of convex, nonconvex, and disjoint cross-sectional areas for these three configurations and we verified that these indeed correspond to the actual intersection.

We do not show that our method can also handle inclusions, e.g., the situation sketched in Fig. 4.2, since these do not occur for this model. However, we confirmed that these can also be handled by our algorithm. Moreover, we determined using analytic techniques that the surface areas and contact-line lengths predicted by our triangular-tessellation

method were indeed correct for several highly symmetric configurations. We have thus shown that our extended algorithm has the desired functionality.

## 4.6 Towards Interfacial Deformation

In this section we study the relatively simple case of the adsorption of a single colloidal sphere at a liquid-liquid interface to show the changes in the free energy of adsorption by going from a model that assumes an undeformed interface to model that allows the interface to deform. We only allow deformation that is induced by the requirement that along the three-phase contact line the contact angle is correct. To that end, we *closely* follow the approach outlined in Ref. [153].

We first consider a single colloidal sphere adsorbed at an interface that does not deform to give a frame of reference for the deformed-interface results. This is also the approximation used throughout this thesis to analyse interfacial adsorption. The free energy of adsorption  $F$  for such a system can be written as

$$\frac{F(\Delta h)}{\pi\gamma_{12}a^2} = \begin{cases} (1 + \cos\theta)^2 & \Delta h/a < -1 - \cos\theta \\ (\Delta h/a)^2 & -1 - \cos\theta \leq \Delta h/a \leq 1 - \cos\theta \\ (1 - \cos\theta)^2 & \Delta h/a > 1 - \cos\theta \end{cases}, \quad (4.8)$$

using the approach outlined in Chapter 2. Here  $\Delta h$  measures the particle's position with respect to the reference point. This reference point ( $\Delta h = 0$ ) is shown in Fig. 4.12 and corresponds to the colloid being adsorbed at a depth  $z = -a \cos\theta$  with respect to the interface, with  $z = 0$  the location of the interface. That is, the colloid is adsorbed in its equilibrium position. The height of the interface with respect to the colloid's centre is given by  $h = -z$  and for the reference state we therefore have  $h = a \cos\theta$ . This is the same result as obtained by Pieranski [129]. The free-energy profile of Eq. 4.8 is a parabola as long as there is contact with the interface, also see Fig. 4.14.

We now consider a system where the interface is allowed to deform, see Fig. 4.13. The reference point is given by the configuration in Fig. 4.12. The amount by which the interface is deformed can be quantified by the radially symmetric function  $u(r)$ , which measures the height of the interface w.r.t. the reference interface ( $z = 0$ ), as a function of the radial distance  $r$ . The value of  $r$  for which the interface makes contact with the colloid is given by  $r_0$ . The free energy can be subdivided in the following way:

$$F = F_{\text{contact}} + F_{\text{meniscus}} + F_{\text{volume}}, \quad (4.9)$$

where  $F_{\text{contact}}$  is the contribution that comes from the colloid being in contact with the two media,  $F_{\text{meniscus}}$  gives the free energy related to the colloid penetrating the interface and the interface being stretched by the deformation, and  $F_{\text{volume}}$  takes into account the force of gravity acting on the fluids. We consider a system for which there are no forces acting on the particle, such as gravity, and no forces acting across the interface, e.g., a force induced by osmotic pressure due to an ion concentration mismatch.

It is relatively easy to show, following Ref. [153], that the free energy associated with colloid-medium contact is given by

$$F_{\text{contact}} \approx \pi\gamma_{12} \left( (u(a \sin\theta) - \Delta h)^2 + (r_0^2 - a^2 \sin^2\theta) \right), \quad (4.10)$$

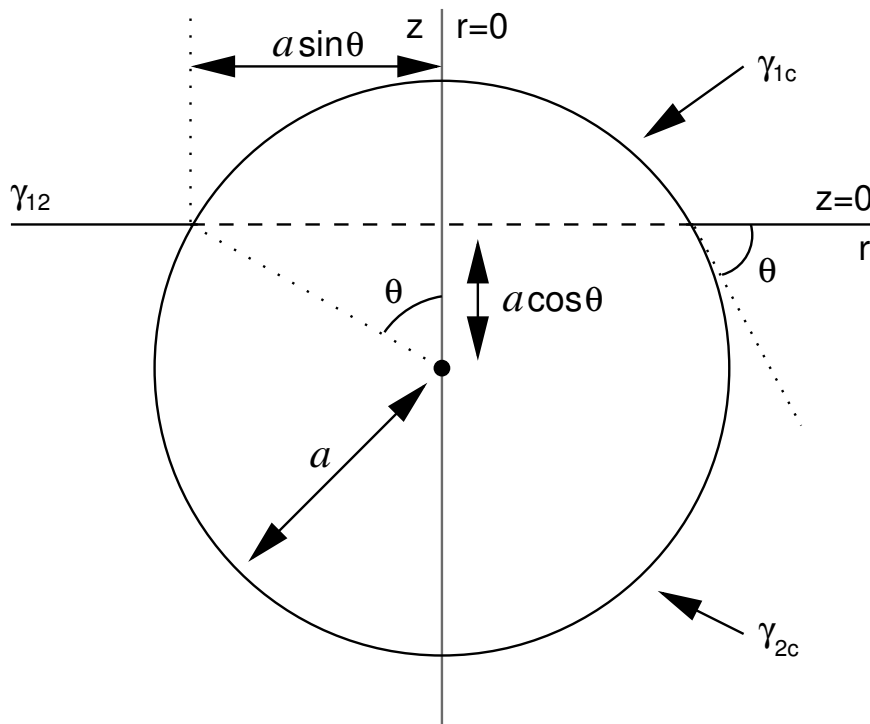


**Figure 4.12:** The reference point for the study of the influence of interfacial deformation on the free energy of adsorption for a spherical colloid. This reference state also corresponds to the equilibrium configuration for a system where the interface does not deform. The radius of the particle is given by  $a$ , the three-phase contact angle by  $\theta$ , the colloid-medium surface tensions by  $\gamma_{1c}$  and  $\gamma_{2c}$ , respectively, and the interfacial surface tension by  $\gamma_{12}$ . The interface is located at  $z = 0$  and the colloid's centre is at a depth  $z = -a \cos \theta$  with respect to the interface, or conversely the interface is at a height  $h = a \cos \theta$  with respect to the colloid's centre. The figure is rotationally symmetric around the  $z$ -axis and radial distance is measured by  $r$ .

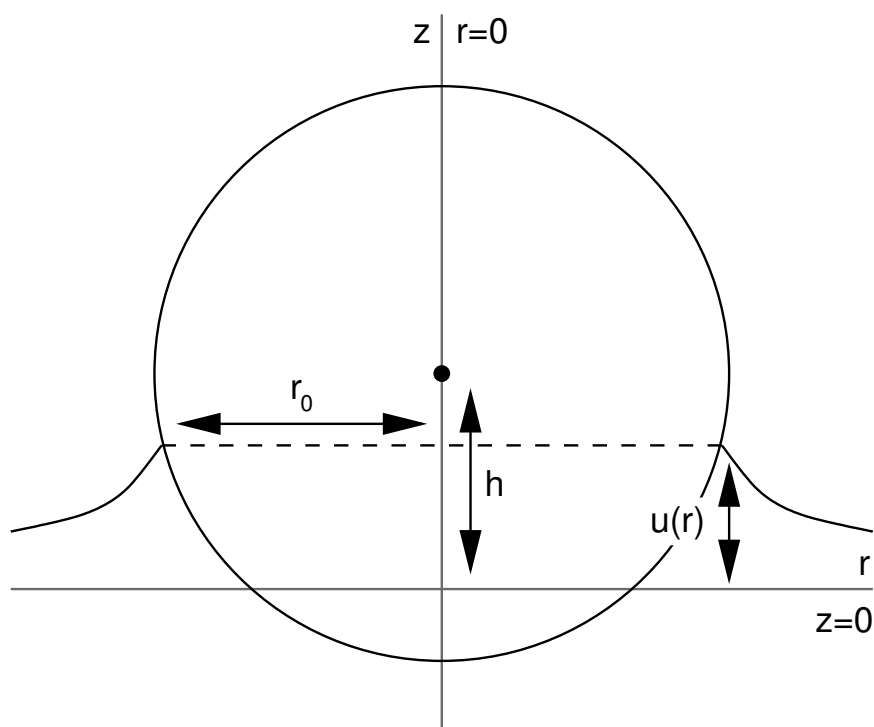


**Figure 4.13:** A sketch of a configuration for which the interface is deformed. The function  $u(r)$  measures the height of the interface with respect to the  $z = 0$ . The position of the interface with respect to the colloid's centre (in the reference state) is denoted by  $h$ . The value of  $r$  for which the interface makes contact with the particle is given by  $r_0$ .

with  $\Delta h = h - a \cos \theta$ . This approximation is valid when  $du/dr \ll 1$ . The contribution to the change in meniscus area  $F_{\text{meniscus}}$  can be approximated by

$$F_{\text{meniscus}} \approx \pi \gamma_{12} (a^2 \sin^2 \theta - r_0^2) + \pi \gamma_{12} \int_{a \sin \theta}^{\infty} r \left( \frac{du(r)}{dr} \right)^2 dr, \quad (4.11)$$

again using Ref. [153]. To determine  $F_{\text{volume}}$  we introduce the capillary length

$$\lambda = \sqrt{\frac{\gamma_{12}}{(\rho_2 - \rho_1)g}}, \quad (4.12)$$

with  $\rho_2 > \rho_1$  the mass densities of the two media and  $g$  the constant of gravitational acceleration, such that

$$F_{\text{volume}} \approx \pi \gamma_{12} \int_{a \sin \theta}^{\infty} r \frac{u^2(r)}{\lambda^2} dr. \quad (4.13)$$

By combining the three relations, Eqs. (4.10), (4.11), and (4.13), we obtain an expression for the free energy

$$F \approx \pi \gamma_{12} \left( \int_{a \sin \theta}^{\infty} r \left[ \left( \frac{du(r)}{dr} \right)^2 + \frac{u^2(r)}{\lambda^2} \right] + (u(a \sin \theta) - \Delta h)^2 \right) dr. \quad (4.14)$$

Functional minimization with respect to the interfacial profile  $u(r)$  for  $r > a \sin \theta$  leads to the following second-order ordinary differential equation

$$\frac{d^2 u}{dr^2} + \frac{1}{r} \frac{du}{dr} - \frac{1}{\lambda^2} u = 0. \quad (4.15)$$

Minimization with respect to  $u(a \sin \theta)$  leads to the first boundary condition

$$u'(a \sin \theta) = \frac{u(a \sin \theta) - \Delta h}{a \sin \theta}, \quad (4.16)$$

where the prime denotes the derivative w.r.t.  $r$ . The second boundary condition is that  $u(r \uparrow \infty) \rightarrow 0$ , i.e., the interface is asymptotically flat. The solution to the differential equation in Eq. (4.15) with these two boundary conditions can now be written as

$$u(r) = \frac{\lambda}{a \sin \theta} \frac{(\Delta h - K_0(a \sin \theta / \lambda))}{K_1(a \sin \theta / \lambda)} K_0(r / \lambda), \quad (4.17)$$

where  $K_0$  and  $K_1$  are the zeroth and first modified Bessel functions of the second kind [246]. When this relation is inserted in Eq. (4.14), we obtain that the free energy is again quadratic in  $\Delta h$ , but with different prefactors.

Figure 4.14 shows the free-energy profile we obtained for  $\cos \theta = 2/3$  and  $\lambda = 100a$ . This is a physically reasonable choice for  $\lambda$  since colloids are roughly  $1 \mu\text{m}$  in size and typical capillary lengths are in the order of a millimetre. In the absence of forces acting on the particle and across the interface the equilibrium configuration is the same as that of the undeformed interface model. This is not surprising since for a sphere the contact angle between the colloid and the interface is correct in this configuration. Moreover, any

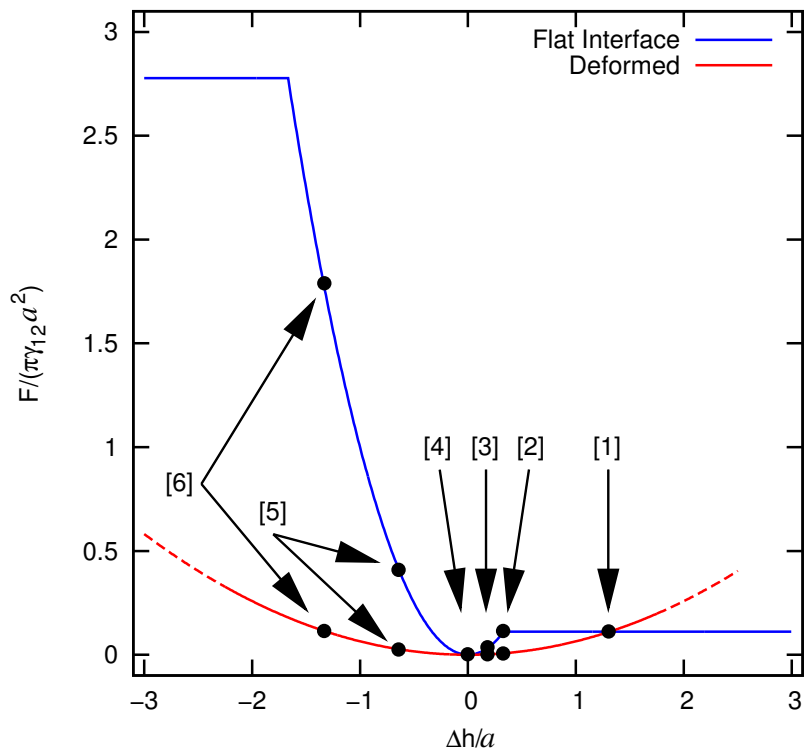


**Figure 4.14:** The reduced free energy of adsorption  $F/(\pi\gamma_{12}a^2)$  as a function of the height difference  $\Delta h$  with respect to the equilibrium position of a spherical colloid with radius  $a$ . The blue curve gives the result for the undeformed-interface model: a parabolic free energy when the particle is adsorbed, and two flat pieces when the particle does not touch the interface. The difference in height between the two flat pieces is determined by the contact angle we use here:  $\cos\theta = 2/3$ . The red curve shows the free energy for the model which takes interfacial deformation into account, the capillary length is given by  $\lambda = 100a$ . The dashed lines roughly indicate regions where the model breaks down, see the text. The location of the dots and corresponding numbers between brackets refer to the visual representations in Fig. 4.15.

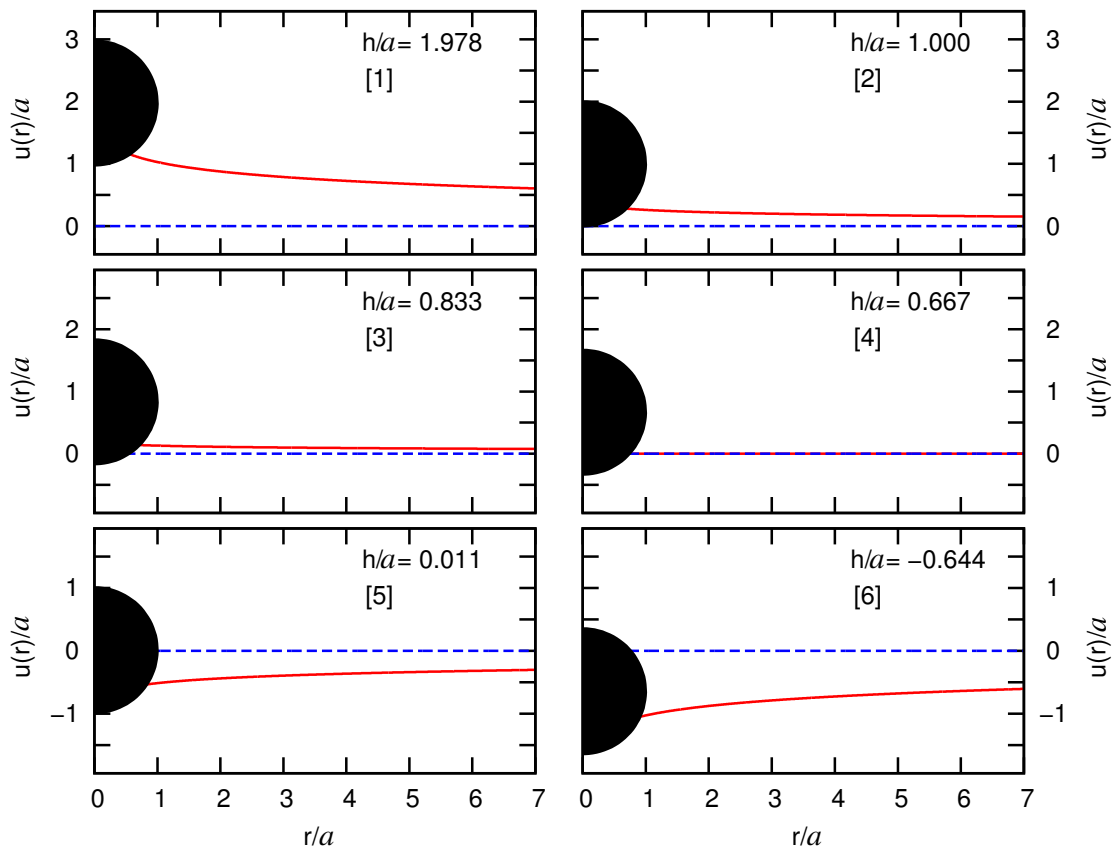


**Figure 4.15:** Several snapshots of a spherical colloid (black silhouette) at an interface. The contact angle is given by  $\cos \theta = 2/3$  and the capillary length by  $\lambda = 100a$ . We show the interfacial profile  $u(r)$  as a function of the radial distance from the origin  $r$ , for both the undeformed- (blue, dashed) and deformed-interface (red, solid) model. The height of adsorption  $h$  is given in the top-left corner and the corresponding number in Fig. 4.14 is given under it.

deformation of the interface with respect to this state would only lead to an increase in interfacial surface area, which gives a corresponding increase of the free energy.

By allowing the interface to deform the free-energy profiles become substantially wider with respect to the undeformed-interface model. We used dashed lines for certain values of  $\Delta h$  in Fig. 4.14 to roughly indicate where our deformed-interface model breaks down. For  $\Delta h \ll a$  the assumption that  $du/dr \ll 1$  is eventually violated when the particle moves deeper into the bottom medium, also see Fig. 4.15, which shows several snapshots of the colloid and the interface for the numbered sites in Fig. 4.14. In a model that incorporates interfacial curvature to a higher order approximation a liquid bridge will form. For sufficiently positive values of  $\Delta h$  we encounter a different problem: there is hysteresis, as we will explain in the following.

A colloid completely immersed in the top medium ( $\Delta h \gg a$ ) experiences the free energy of the blue curve (Fig. 4.14), which has a constant value. When the colloid reaches point 1 from ( $\Delta h \gg a$ ) the undeformed-interface configuration becomes metastable. However, the particle can only cross over to the free energy of the red curve, if it comes into contact with the interface. As long as the particle is not in contact with the interface it experiences the constant free energy associated with the blue curve, within the confines of the model. See Ref. [157] for a more realistic description of this phenomenology, in which capillary-wave fluctuations are considered. For  $\Delta h = 0$  the particle is penalized for moving away from the equilibrium configuration according to the free energy of the red curve. Upon reaching point 1, the deformed state becomes metastable. However, only when the interface de-wets the particle does it experience the constant free energy of complete immersion in the top medium. This is what we referred to when we mentioned that there is hysteresis in the system. We used dashes in Fig. 4.14, since our model does not account for capillary fluctuations and we could therefore not determine where the deformed free-energy branch terminates.

Summarizing, we showed that there is a significant difference between the free energy of adsorption associated with a model that does and with a model that does *not* take deformation of the interface into account. In light of this, the relevance of the results in Chapters 2 and 3 to experimental systems requires further investigation, but such a study goes beyond the scope of this thesis.

## 4.7 Conclusion and Outlook

In this chapter we generalized the triangular-tessellation technique from Chapter 2 to determine the surface areas and contact-line length(s) associated with the adsorption of an arbitrary nonconvex surface-patterned colloid at a flat interface. We demonstrated that our extended technique has the proper functionality by considering two systems.

Truncated nanocubes, for which the triangular and octagonal facets have distinct wetting properties, were studied to demonstrate that contact-angle surface-patterned particles can be handled by our method. Using our technique we examined the properties of the interfacial adsorption of truncated cubes within the confines of a simple undeformed-interface model. We found that there are three types of adsorption that can occur for truncated cubes and two for cubes. Our investigation marks the starting point of a the-

oretical study into the behaviour of similarly shaped colloids at a liquid-liquid interface, which is aimed at elucidating recent experimental observations [164, 242]. However, to give a proper description of the experimental systems our simple model has to be substantially extended. This we leave for future study.

Using a model for an octapod-shaped nanocrystal we showed that our triangular-tessellation technique is also capable of handling nonconvex particles. This, together with our observations for the patterned nanocubes, illustrates that the generalized technique can be applied to arbitrary surface-patterned particles.

Finally, we examined, using the methods of Ref. [153], the consequence of incorporating interfacial deformation into our model for the simple case of a spherical particle adsorbing to a liquid-liquid interface. We found that there is a richness in behaviour that is not captured by our undeformed-interface model even for such a simple shape. However, our results and approaches can be built upon in future studies to achieve better insight into the complex problem of interfacial adsorption.



---

## The Floppy-Box Monte Carlo Algorithm

---

In this chapter we introduce the floppy-box Monte Carlo (FBMC) method [L. Filion *et al.*, Phys. Rev. Lett. **103**, 188302 (2009)] to predict crystal-structure candidates. The algorithm is described in detail to ensure that it can be straightforwardly implemented on the basis of this text. The way in which hard-particle interactions are handled in a FBMC simulation is given special attention, as (soft) short-range and semi-long-range interactions can be treated in an analogous way. We also discuss two types of algorithm, the method of separating axes and a triangular-tessellation based technique. These can be combined with the FBMC method to enable crystal-structure prediction for systems comprised of highly shape-anisotropic particles. Finally, we comment on the process of crystal-structure prediction itself, which requires the FBMC algorithm to be applied many times to a particular system, and the choices that can be made in this regard.

## 5.1 Introduction

The prediction of crystal structures for atomic, colloidal, and nanoparticle systems, based only on knowledge of the interactions between particles, is of primary importance to guiding the development of new materials. This problem has received a lot of attention over the past few decades [165], but there are still many unanswered questions concerning the efficient prediction of crystal structures. Commonly used techniques rely on simulated annealing [177, 178], genetic algorithms [179, 180], or Monte Carlo (MC) basin hopping [181]. However, these methods do not work well for systems that have a large entropic contribution to the free energy. Hard-particle systems pose a particular problem, since the entropy is the only factor that imposes the crystal structure for a fixed pressure, temperature, and particle shape. These entropy-driven systems can in principle be studied using an ergodicity search algorithm [182] or a metadynamics method [183], but both methods have their limitations.

Interest in the subject of crystal-structure prediction has intensified over the past few years due to the remarkable advancements made in colloid and nanoparticle synthesis [82, 83]. Not only can spherical particles be synthesized with a high level of precision and reproducibility, but also a wide variety of convex (faceted) shapes, such as cubes [84–86], octahedra [89, 90, 247], tetrahedra [91, 92, 248], and many more [33, 93–96]. Perhaps most remarkable of all is the level of control that has been attained over the synthesis of nonconvex, irregular, and even punctured particles. Branched colloids and nanocrystals such as octapods [54, 78, 99–101] and tetrapods [102, 103] have been created, as well as other nonconvex shapes, e.g., nanostars [104–106, 247] and colloidal caps [107–109]. Moreover, there is a better understanding of the way to achieve phase behaviour that is dominated by entropic contributions in experimental systems [70–73].

To address the problem of crystal-structure prediction at finite pressures, for systems that are mostly entropy driven, the method of floppy-box Monte Carlo (FBMC) was recently introduced [75]. It is a technique that is similar in approach to the metadynamics simulation [183], but it uses compression from the fluid and Monte Carlo (MC) sampling to determine candidate structures. The FBMC technique was used to great effect on a wide variety of systems consisting of, for instance: spheres that interact via a combination of hard and attractive pair potentials, binary mixtures of hard spheres, and star polymers which have semi-long-range soft interactions [75]. Truly long-range dipole-dipole interactions, for which Ewald Sums were employed to determine the total energy of the system, were also considered [75]. Moreover, the FBMC algorithm was applied to determine a lower limit to the packing fraction of the densest configuration for highly shape-anisotropic solids [249], also see Chapter 6. This use of the FBMC technique connects the field of materials science with fields as diverse as discrete geometry, number theory and computer science [184, 186, 250–252]. We only briefly go into this here and leave the discussion of the recent developments in analysing densest packings for Chapter 6. The FBMC technique led to the discovery of a wide variety of new crystal structures [75, 171, 249] and it has proven itself to be a remarkably efficient and robust method.

In this chapter we describe the elements required to set up a FBMC crystal-structure-prediction algorithm, as implemented in Refs. [75, 249]. We assume only basic familiarity with thermodynamics and simulation techniques, such that this text can be used as a

self-explanatory recipe. In Section 5.2 we discuss the components that define a FBMC simulation. This is followed by an introduction of the MC trial moves and acceptance rules that we employ in Section 5.3. Section 5.4 presents a way to efficiently check for overlaps in the system, which is based on minimizing the number of periodic images that have to be taken into account. This, as we will show in Section 5.4, is a nontrivial problem due to the size of the box in comparison to the range of the interaction between the particles. Two types of hard-particle overlap routines are explained in Section 5.5, by which simulations of (nonconvex) irregular faceted particles can be performed. The technique of lattice reduction, which is essential to prevent unphysical distortions of the simulation box, is introduced in Section 5.6. We briefly comment on soft interactions and external fields in Section 5.7, before we examine the way to use the FBMC algorithm to allow for efficient crystal-structure prediction in Section 5.8. We conclude with a discussion of the properties of the algorithm, a brief comparison to other hard-particle algorithms developed to predict the dense structures, and an outlook in Section 5.9.

## 5.2 Characterisation of the Method

The FBMC algorithm is an isothermal-isobaric  $NPT$  ensemble Monte Carlo (MC) simulation. There are three properties that turn an ordinary  $NPT$  MC simulation into a tool for crystal structure prediction. (I) The number of particles  $N$  is small, typically  $N < 12$ . (II) The three vectors that span the simulation box are allowed to vary independently of each other in both their length and orientation. This is the origin of the term *floppy box*, which was adopted to emphasize that the box does not have a fixed shape. It is a variable-box-shape method, which is in common use in computational studies of colloids [183, 253]. However, by the adjective ‘floppy-box’ (MC) we refer to the whole of the technique to predict crystal structures, rather than just the fact that the box shape is variable. We shall use this distinction explicitly when referring to FBMC and regular variable-box-shape simulations throughout this thesis. Note that an  $NPT$  variable-box-shape simulation is essentially an isothermal-isotension simulation [253], for which a special form of the imposed stress tensor is used. This tensor only has diagonal elements, which are all the same and are directly proportional to the pressure, i.e., according to the hydrostatic-pressure assumption. We therefore prefer the wording ‘isothermal-isobaric’ or ‘ $NPT$ ’ ensemble. (III) To predict crystal structures the  $NPT$  part of the simulation is preceded by a compression from a dilute phase (gas or liquid), which is accomplished by increasing the pressure to drive the system towards higher densities. FBMC has a fourth ‘defining property’, which does not have anything to do with the algorithm itself, rather it pertains to the implementation. (IV) To effectively predict crystal structures it is necessary to perform FBMC simulations for the same system many times with different random seeds, initial conditions, compression paths, etc.

The first two properties - that the number of particles is small and that the box can deform - essentially allow the box to act as a *unit cell* for the crystal structures we are interested in. The crystal structure is strongly imposed by the periodic boundary conditions. That is, the effect of periodicity is far more pronounced than for simulations with  $N \gg 10$  particles, where the goal is to minimize such finite-size effects. Fast and efficient

exploration of crystal-structure candidates is made possible by choosing the method of compression (III) and the way in which the algorithm is repeatedly applied (IV). There is, however, a computational bottleneck that has to be overcome for any FBMC simulation to obtain such fast and efficient sampling: determining the number of periodic images that has to be checked. A particle in the unit cell of a crystal (simulation box) interacts with its neighbours, which are its own periodic images in the FBMC method. For instance, a single particle in a cubic unit cell is surrounded by a layer of 26 neighbours, followed by another layer that contains 98 (secondary) neighbours, etc. If a particle has an interaction range larger than the dimensions of the box, which is typical for FBMC simulations, it will notice the particles in one or more adjacent layers. When the particle is translated or rotated, the interaction between it and all these neighbours/images has to be checked to determine whether the move is accepted or rejected. Even worse, the number of relevant image layers may have increased when the box is deformed. Each additional layer that has to be considered increases the number of interaction computations quadratically, which quickly leads to unreasonable computational overhead even for simple interaction potentials. However, it is often not necessary to check all images in a layer, e.g., a sphere centred in a cubic box with a diameter slightly larger than the box length can only interact with 6 of the 27 images in the next layer. As we will show, determining a small, yet sufficient number of images to be taken into account, is not straightforward in general, especially for very deformed boxes. In the following we explain the procedure to obtain these images in a fast way. We shall first discuss the case where there are only pairwise hard-core interactions in a system of shape-anisotropic particles, before discussing the particles with soft-interactions.

### 5.3 The Ensemble and Monte Carlo Moves

We assume that the system of interest consists of  $N$  particles at positions  $\mathbf{r}_j \in \mathbb{R}^3$  and of which the orientation is specified by orientation vectors  $\mathbf{q}_j \in \mathbb{Q}$ , where  $j$  is an index and runs from 1 to  $N$ . The particles are contained in a box spanned by the three box vectors  $\mathbf{v}_i \in \mathbb{R}^3$ , with  $i = 1, 2, 3$ . In this description the vertices of the box are given with respect to a standard Cartesian coordinate frame and one of them is located at the origin. The set of  $\mathbf{r}_j$  gives the location of the particles' centre of rotation, also with respect to this coordinate frame. The orientation of the  $j$ -th particle is obtained by applying the rotation matrix generated by  $\mathbf{q}_j$  to a predetermined initial orientation [253]. Let the volume of the  $j$ -th particle be given by  $V_j > 0$ . The packing fraction is then  $\phi = (1/V) \sum_j V_j$ , with  $V \equiv |\mathbf{v}_1 \cdot (\mathbf{v}_2 \times \mathbf{v}_3)|$  the volume of the system. Each particle has an outscribed sphere, of which the centre is located at the rotation point  $\mathbf{r}_j$  and the radius is given by  $R_{O,j}$ . Note that this sphere does not necessarily satisfy the mathematical definition of the *minimum* outscribed sphere. The radius of the largest outscribed sphere is denoted  $R_O = \max_j R_{O,j}$ . Finally,  $U$  gives the total energy of the system, which implicitly depends on the sets  $\mathbf{v}^3 \equiv \{\mathbf{v}_i\}$ ,  $\mathbf{r}^N \equiv \{\mathbf{r}_j\}$ , and  $\mathbf{q}^N \equiv \{\mathbf{q}_j\}$ , i.e.,  $U \equiv U(\mathbf{v}^3, \mathbf{r}^N, \mathbf{q}^N)$ . For a system with only hard-particle interactions  $U$  assumes two values:  $\beta U = 0$ , when there are no overlaps, and  $\beta U = \infty$ , when there are overlaps.

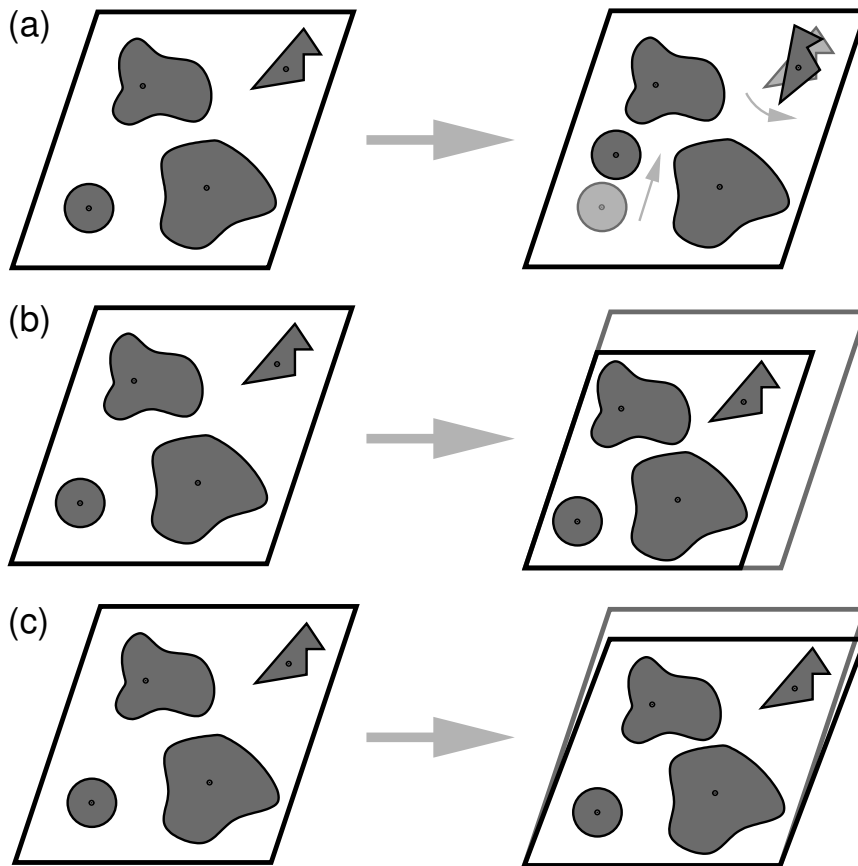


**Figure 5.1:** A two-dimensional (2D) representation of the 4 types of Monte Carlo (MC) trial moves that we consider for the floppy-box Monte Carlo (FBMC) simulations. (a) Translation and rotation of the particles. (b) Uniform scaling of the box. (c) Box deformation.

For a FBMC simulation we consider 4 types of trial moves to sample phase space: translation and rotation of the particles and scaling and deformation of the box, see Fig. 5.1. These moves must satisfy the acceptance criterion for detailed balance in the  $NPT$  ensemble, which is based on the Metropolis algorithm [253, 254]. We write the probability of a move to be accepted as  $\text{acc}(o \rightarrow n)$ , where ‘ $o$ ’ and ‘ $n$ ’ are the labels for the old and new state, respectively. Translation, rotation, and scaling moves are performed according to Ref. [253], where we apply Ref. [255] to construct the random perturbation of the quaternions. The acceptance criterion for these moves is given by

$$\text{acc}(o \rightarrow n) = \min \left( 1, \exp \left[ -\beta (U_n - U_o + P (V_n - V_o)) + (N + 1) \log \left( \frac{V_n}{V_o} \right) \right] \right), \quad (5.1)$$

where the subscripts indicate the new and old values,  $P$  is the pressure, and  $V$  is the volume of the system, as before. Here, we assume logarithmic steps in  $V$  for the scaling moves, hence the natural logarithm in Eq. (5.1) is preceded by the factor  $(N + 1)$  [253]. For the deformation moves we select one element of one of the box vectors at random. This element is perturbed by a small number, which is chosen from a uniform probability distribution over an interval symmetric around zero. These moves also satisfy detailed

balance for the  $NPT$  ensemble, when the acceptance rule

$$\text{acc}(o \rightarrow n) = \min \left( 1, \exp \left[ -\beta (U_n - U_o + P (V_n - V_o)) + N \log \left( \frac{V_n}{V_o} \right) \right] \right), \quad (5.2)$$

is used [253]. It is easy to verify that Eq. (5.2) holds for this type of move using properties of the cross- and dot-product to show that the deformations described above allow for perturbations of the volume that scale linearly with the perturbation of the box vectors.

We introduced two types of moves that change the volume of the box - scaling and deformation - because we found that the combination of the two typically led to faster equilibration and exploration of phase space than using deformation moves only. The scaling moves essentially create space in the system for deformations to be more readily accepted at high volume fractions. The order in which we apply these moves is chosen at random and satisfies the following probability distribution. For  $N = 1$  particles we only require deformation and scaling moves, but sampling is sped up by also allowing rotation moves. We do *not* make any assumptions concerning the orientation of the box here. A commonly used choice for variable-box-shape simulations is to have one of the box vectors along the  $x$ -axis, another vector in the positive part of the  $xy$ -plane, and the third in the  $z > 0$  half space. However, this choice *necessitates* the use of rotation moves for  $N = 1$  in order to fully explore phase space. We found that roughly 70% rotation, 15% scaling, and 15% deformation trial moves yields relatively efficient sampling. For  $N \geq 2$  we typically used 35% translation, 35% rotation, 15% scaling, and 15% deformation trial moves. The ratio assigned to the volume moves may appear to be somewhat high, when compared to typical ( $N \gg 10$ ) MC simulations, for which they are usually applied with probability  $\sim 1/N \ll 1$ . However, these values are not unreasonable, since there are only a few particles in the box and deformation plays an important role in sampling possible structures.

## 5.4 Construction of the Image-Lists

In the following we do not make any additional assumptions on the composition of the system other than the ones specified in Section 5.3: mixtures of highly shape-anisotropic particles are allowed. When there are only hard-particle interactions in the system, the acceptance criteria of Eqs. (5.1) and (5.2) are substantially simplified. Translation and rotation moves are always accepted when they do not result in overlaps. However, as explained before, checking for overlaps even in the simplest of systems can be time consuming due to the strong influence of periodicity. For scaling and deformation moves it is even more expensive, since the minimum number of periodic images that has to be taken into account also needs to be redetermined. We therefore first verify that such a move is not rejected on the basis of the pressure/volume part of  $\text{acc}(o \rightarrow n)$  [Eqs. (5.1) and (5.2)] before checking for overlaps. It is also convenient to use the packing fraction  $\phi$  as an early out at high densities, since  $\phi \leq 1$  must always hold.

In order to check for overlaps, as well as perform the various moves, it is convenient to introduce a set of scaled coordinates in analogy to the procedure outlined in Ref. [253]. Let  $\mathbf{s}_j \in [0, 1)^3$ , with  $j = 1, \dots, N$  an index, denote the scaled position coordinates of

the particles. There is a bijective function that relates these scaled coordinates to the positions of the particles in the box, i.e.,  $M : [0, 1]^3 \rightarrow \mathbb{R}^3$ ,  $\mathbf{r}_j = M\mathbf{s}_j$ . Here  $M$  is the matrix generated by the box vectors:  $M = (\mathbf{v}_1\mathbf{v}_2\mathbf{v}_3)$ , where it is understood that the box vectors are the columns of the matrix. This function is bijective when the volume of the box  $V > 0$ , since this implies that  $\det(M) \neq 0$ . The scaled coordinate frame allows us to determine the number of periodic images of the box that we need to check for overlaps in order to confirm that there are no overlaps in the entire system. Here we use the fact that checking for overlaps in the entire system is equivalent to checking for overlaps between a particle in the box and

- (i) another particle in the box,
- (ii) its own periodic images, and
- (iii) other particles' periodic images,

for all particles in the box. It is efficient to first carry out step (i) for all particles, making sure not to double check, then step (ii) for all particles, and finally step (iii). For  $N = 1$  the algorithm reduces to step (ii). It is computationally favourable to only check for overlaps between a particle and a minimum number of periodic images. However, obtaining this minimum number of images should not go at the expense of the overall speed of the algorithm, since volume changes occur frequently. We therefore construct the lists of images as follows.

Recall that the largest outscribed-sphere radius is given by  $R_O$ . When any two particles/images are a distance of  $2R_O$  apart, they do not overlap. However, it is difficult to determine how many layers of images we need to take into account in each direction such that every image-point inside this sphere is considered. To establish this number for the self-image check [step (ii)], we may assume, without loss of generality, that the particle in the box is located in the origin. We pick a plane that goes through the origin and that is orthogonal to the vector  $\mathbf{v}_1 + \mathbf{v}_2 + \mathbf{v}_3$ , to bisect the sphere of radius  $2R_O$ , see Fig. 5.2a. By choosing the plane orthogonal to the sum of the box vectors we can (usually) avoid it intersecting image points. We only consider images that are on one side of the plane or that lie in it. This is justified because of point-symmetry, as can be easily understood by considering Fig. 5.2a. Take any one of the green points in Fig. 5.2a and mirror it in the origin. This image interacts with the particle in the origin in the same way as the particle in the origin interacts with the image located at the original (green) point, because the orientation of all images is the same. That is to say, the periodicity allows us to translate the entire crystal by the distance vector between the two points and this translated structure coincides with the original. We therefore have to check only one of the two point-symmetric possibilities.

A sufficiently large list of self-images is constructed by considering a cube with vertices  $\mathbf{c}_n = 2R_O(\pm\hat{\mathbf{x}} \pm \hat{\mathbf{y}} \pm \hat{\mathbf{z}})$  with  $n = 1, \dots, 8$  and  $\hat{\mathbf{x}}$ ,  $\hat{\mathbf{y}}$ , and  $\hat{\mathbf{z}}$  the Cartesian unit vectors. This cube envelops the sphere at the origin with radius  $2R_O$ , see Fig. 5.2a. By applying the inverse matrix  $M^{-1}$  to the eight  $\mathbf{c}_n$  vertices of the cube we obtain 8 vertices that span a parallelepiped (Fig. 5.2b), say  $\mathbf{p}_n = M^{-1}\mathbf{c}_n$ . Using the vertices  $\mathbf{p}_n$  the upper bounds to the number of images that need to be checked in each direction can be constructed:

$$N_1 = \lceil \max_n (\mathbf{p}_n \cdot \hat{\mathbf{x}}) \rceil; N_2 = \lceil \max_n (\mathbf{p}_n \cdot \hat{\mathbf{y}}) \rceil; N_3 = \lceil \max_n (\mathbf{p}_n \cdot \hat{\mathbf{z}}) \rceil, \quad (5.3)$$

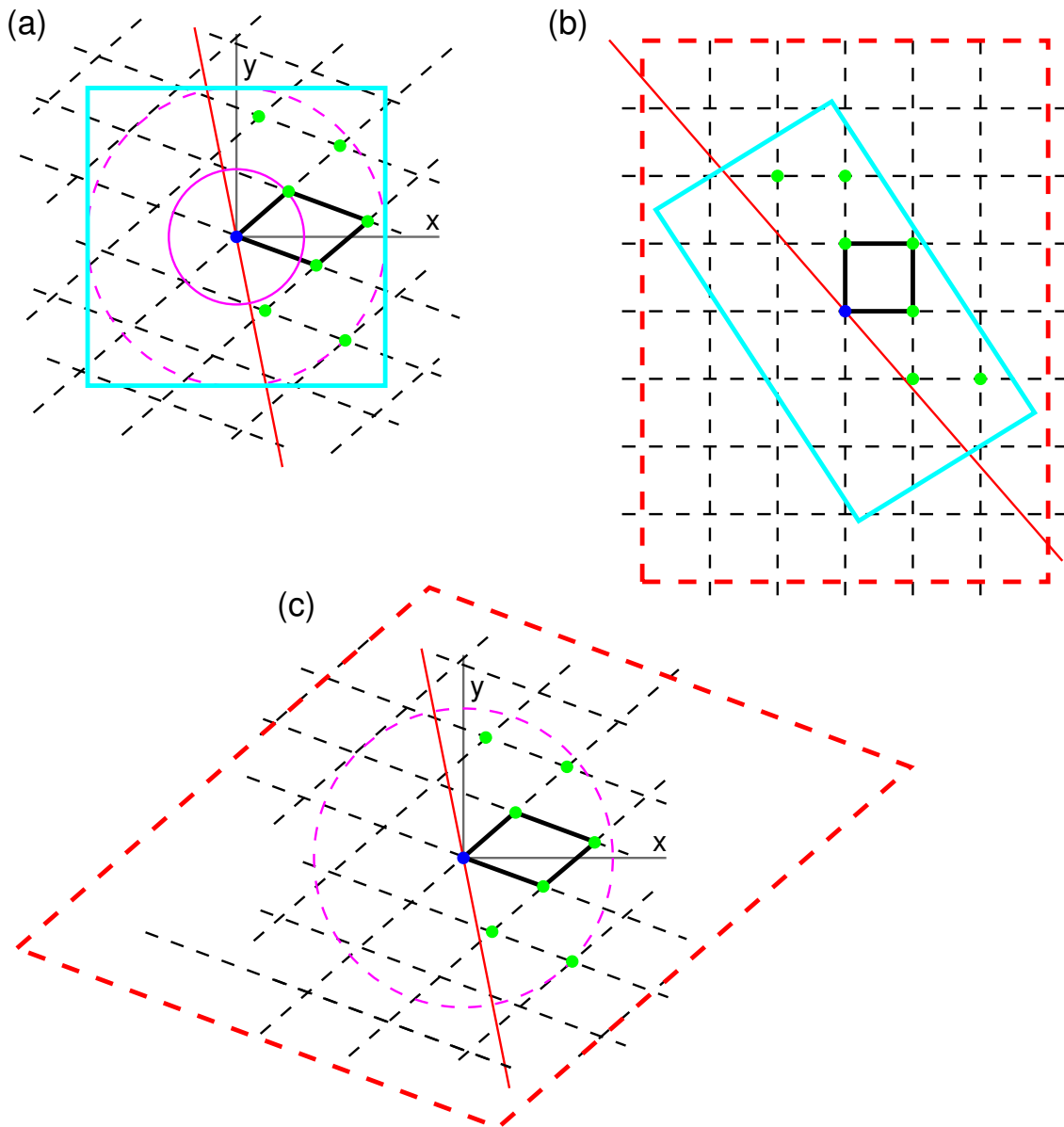


**Figure 5.2:** The construction of the self-image list in two dimensions; the three-dimensional (3D) case is analogous. (a) The simulation box (black parallelogram), the particle's position (blue dot), the coordinate frame (grey lines), the periodic images (dashed black lines), the outscribed circle of radius  $R_O$  (solid magenta), and double-radius circle (dashed magenta). The solid red line indicates the point-symmetry axis: all images relevant for the overlap check are indicated with green dots. An axis-aligned cyan square envelops the  $2R_O$  circle. (b) In the scaled coordinate frame a bounding rectangle  $[-N_1, N_1] \times [-N_2, N_2]$  (dashed red line) can be constructed. (c) The red bounding rectangle can be mapped back to the original frame and gives an upper bound to the number of images that have to be checked in each direction.

respectively, where  $\lceil \cdot \rceil$  indicates the ceiling function. Since the parallelepiped is symmetric around the origin the positions of the relevant images in the scaled coordinate frame are located in the rectangle  $[-N_1, N_1] \times [-N_2, N_2] \times [-N_3, N_3]$  (Fig. 5.2b). For images that

fall outside of this rectangle we can be certain that they do not overlap with the particle in the origin. Using the matrix  $M$  we may now establish the equivalent set of images in the regular coordinate frame  $P_{\text{im}} = \{i\mathbf{v}_1 + j\mathbf{v}_2 + k\mathbf{v}_3\}$ , with  $i = -N_1, \dots, N_1$ ;  $j = -N_2, \dots, N_2$ ;  $k = -N_3, \dots, N_3$ ; and  $i + j + k \neq 0$ , see Fig. 5.2c.

The list  $P_{\text{im}}$  can contain many elements which are irrelevant to the overlap check - i.e., points which fall outside of the hemisphere with radius  $2R_O$  - when the box becomes strongly deformed or the particle has an ‘odd’ shape. We employ the following steps to remove these images. Using the dot-product of a vector in  $P_{\text{im}}$  with the normal of the point-symmetry plane we can efficiently eliminate all images that are not on the right side of this sphere-bisecting plane. Points that have a distance to the origin greater than  $2R_O$  are also removed from the list by simply calculating the length of the position vector. Inscribed-sphere checks between the particle in the origin and a particle at a lattice-site in the reduced set of images  $\tilde{P}_{\text{im}}$  are used to confirm that there are no situations where two particles clearly overlap, before switching to a more computationally expensive overlap algorithm. Here we employ a ‘concentric approach’ to check for overlaps. That is, we first consider all images for which  $|i| + |j| + |k| = 1$ , followed by the set of images for which  $|i| + |j| + |k| = 2$ , etc. If there are overlaps it is far more likely that they are encountered close to the original particle, rather than further away. If there are no overlaps detected in the entire system - having checked steps (i), (ii), and (iii) - the reduced list is accepted and can be used to check for overlaps until an attempted volume move (scaling or deformation) requires a new self-image list to be constructed.

Checking for overlaps between a particle in the box and another particle’s images [step (iii)] is a simple matter of extending the above reduced self-image list. We add 1 layer of images in the positive  $\mathbf{v}_i$  directions to the set  $\tilde{P}_{\text{im}}$ . It is easily understood that it is sufficient to check up to this range in periodic images. The list  $\tilde{P}_{\text{im}}$  already contained all relevant image points with a distance  $2R_O$  and the distance added by considering two particles in the box is at most one box length in each  $\mathbf{v}_i$  direction. The fact that the problem is no longer point symmetric is overcome by checking one particle with another particle’s images and vice versa.

## 5.5 Hard-Particle Overlap Algorithms

In this section we briefly discuss two hard-particle overlap algorithms, the method of separating axes and a triangular-tessellation-based technique, which can be used in combination with the FBMC technique to study crystal structures for faceted (nonconvex) particles. These algorithms were recently employed to great effect in Refs. [54, 249]. The two routines are predominantly used in computer-game and engineering applications [218–220]. However, such methods have gained popularity in the physics and mathematics communities and show great promise for future studies, especially with the emergence of the graphics card as a powerful platform for particle simulations and image processing [256–258]. Moreover, there has been a marked increase in the ability to synthesize a stunning array of faceted (nonconvex) particles [78, 99, 102–106, 247], as well as the level of control with which such particles can be prepared [54]. This has led to particu-

lar interest from materials science in these overlap algorithms to perform simulations on nanoparticle and colloid systems [167, 169, 172–174, 259, 260].

### 5.5.1 The Method of Separating Axes

The method of separating axes is an overlap algorithm that can be applied to convex particles. This technique is based on the (Hahn-Banach) separating-hyperplane theorem for convex sets in Euclidean space [261]. The theorem implies that for two disjoint convex sets there exists a plane between these sets that does not intersect either. That is, one of the particles is in one of the halfspaces defined by the separating plane and the other particle is in the opposite halfspace, respectively. Any axis orthogonal to the separating plane is referred to as a *separating axis*, because orthogonal projections of the convex sets onto this axis are disjoint, also see Fig. 5.3. The problem of determining if two objects overlap can therefore be reduced to finding a separating axis: if there is such an axis, the objects do not overlap; if there is no such axis, they do. The procedure to find a separating axis for two arbitrary convex particles cannot be performed in a finite time, since an infinite number of directions may result in a possible separating axis. However, it can be shown that for two convex three-dimensional (3D) polyhedra, only a finite number of directions has to be checked [261]. This makes it possible to turn the separating-hyperplane theorem into an efficient algorithm.

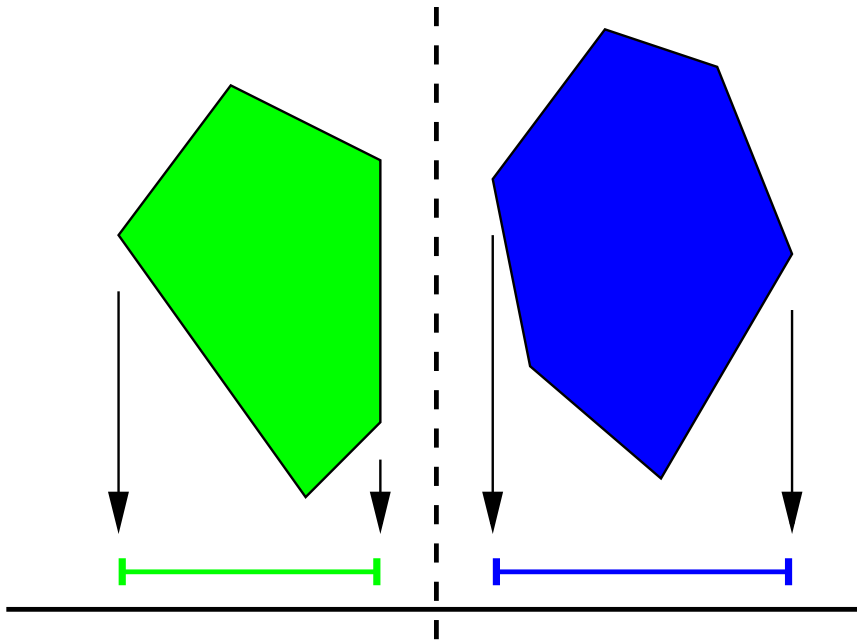


**Figure 5.3:** A 2D representation of method of separating axes. We consider two disjoint convex polygons. The dashed vertical line indicates a possible separating plane for these particles, and the solid horizontal line an associated separating axis. Note that the projection of the particles on the separating axis results in disjoint domains, as indicated by the arrows and line segments.

Only the set of vectors normal to the faces of the two polyhedra and the set of vectors generated by cross-products between two edges, one from each polyhedron, have to be

checked for separation. The way in which to perform such checks efficiently is described in great detail for 3D polyhedral particles, as well as for two-dimensional (2D) polygons, in Ref. [262]. One minor addition to the overlap routine of Ref. [262] should be made, when applying it in a FBMC simulation close to the maximum packing fraction. At these high densities it is possible that two particles come together in such a way that the cross-product of two of their respective edges becomes very small. This leads to numerical instabilities in the algorithm proposed in Ref. [262]. Such instabilities can result in a separating axis being identified, despite the particles interpenetrating. We found that normalizing the cross-product vector eliminates the problem for all the systems we considered.

### 5.5.2 Triangular-Tessellation-Based Overlap Algorithms

The method of separating axes described above has the advantage that it is very easy to implement, can be applied without modification to a wide class of particles, and is also computationally efficient. However, due to the algorithm's dependence on the separating-hyperplane theorem it cannot be extended to handle nonconvex particles.

Checking for overlaps between nonconvex particles can be made possible by approximating the shape of a particle with a collection of spheres or rods [263–266]. The respective overlap algorithms are simple and efficient enough to justify the use of spheres and rods as building blocks for larger objects. Such approximations give exact results in the case of, e.g., dumbbells, which consist of two interpenetrating spheres. However, a prohibitive number of spheres or rods may be required to give a decent approximation, especially when an object contains both drastic changes in curvature and large flat parts. Only recently were the first attempts made to study systems that contain relatively complex curved particles. For bowls [176] an overlap algorithm was devised unique to this shape. Nonconvex shapes with sharp edges and smooth surfaces, such as superdisks [175] and caps [176], have also come under investigation. Moreover, Ref. [267] introduced a general method to handle collision detection for smooth (nonconvex) objects in Molecular Dynamics simulations. Unfortunately, none of the above methods are particularly suited to study nonconvex faceted particles.

Simple nonconvex polyhedral (faceted) particles may be broken up into convex constituents, for which the method of separating axes can be employed. However, an alternative to this type of partitioning exists, which is better suited to study more complex faceted shapes. In computer-game and engineering applications the surface of the objects is defined usually by a polygonal mesh [218]. Two particles overlap when there is an intersection between a pair of polygons in the respective meshes. Such intersections are easily determined on a polygon-by-polygon basis, because of a polygon's simple shape, which also makes polygons ideally suited to describe objects. The algorithms employed to search for overlaps are often specifically designed to handle highly irregular objects and are typically very general in their setup. Moreover, they can usually be straightforwardly implemented, and ordinarily a lot of effort has been put into their optimization. An example of such optimization is the use of an oriented-bounding-box-tree (OBB-tree) [268] for high-polygon models. An OBB-tree essentially breaks up the model into smaller pieces

in a very efficient way. The tree allows the polygon-based overlap routine to be applied solely to parts of the model that are in close proximity.

Due to our familiarity with approximating the surface of an object with triangles, so-called triangular tessellation, also see Chapters 2 - 4, we decided to base our overlap algorithm for nonconvex hard particles on the *Robust and Accurate Polygon Interference Detection* (RAPID) library [218]. The RAPID library is designed specifically to quickly determine if there are triangle intersections; it employs an OBB-tree for larger objects and is easy to set up. See Refs. [219, 220] for some alternative overlap-detection libraries. The procedure of performing an overlap check is as follows. Particles are tessellated with triangles, according to the method of Chapter 2, to generate simulation models. This triangular tessellation is exact for polyhedral particles, i.e., the shape is approximated perfectly. These models are passed to the RAPID library. To perform an overlap check we only need to input two position vectors and two rotation matrices in the relevant RAPID subroutine. This subroutine returns a Boolean value that specifies whether there are triangle intersections or not. We found RAPID to be extremely stable, even for FBMC simulations in the high-pressure dense-packed limit, where the numerical stability of any algorithm is put to the test. Unlike the method of separating axes inclusions may occur, when there is a substantial size difference between particles, since the triangular-tessellation-based algorithm only considers the surface area of a particle. We can use an inscribed-sphere check to reject trial moves that result in an inclusion. The RAPID algorithm also allows for interior and even disconnected triangles to be added to a model [218] that can be used to further prevent inclusions, when the gap between a particle and its inscribed sphere is too wide.

## 5.6 Unphysical Distortions and Lattice Reduction

In the above discussion, we did not take into consideration that by allowing the box to deform, especially when compressing from a dilute phase, it may become very distorted. That is to say, the box can become very flat or elongated, when the angles between the lattice vectors become large or small. This slows down our algorithm, since an enormous number of periodic images needs to be taken into consideration in order to determine whether a move is accepted or not. Moreover, the overly distorted shape of the box can interfere with the sampling of crystal-structure candidates, i.e., it induces artificial preferential directions in the system. For a flat box the particles tend to line up into columns, which results in an unphysical contribution to the entropy, since the particles only interact with periodic images in one direction. At high pressures/densities the box cannot easily move back to a more orthorhombic shape, because the (isotropic) pressure induces a stronger cumulative force acting on the larger faces of the box, thereby squeezing it flat. To improve the efficiency of the FBMC algorithm and to prevent unphysical distortions of the unit cell we require lattice reduction.

Lattice reduction is the process by which a set of basis vectors for a lattice is replaced by an equivalent set of basis vectors, which are shorter and more orthogonal. That is to say the surface-to-volume ratio of the box is minimized. In Ref. [179] an algorithm is proposed to accomplish this lattice reduction in a three-dimensional (3D) system. We

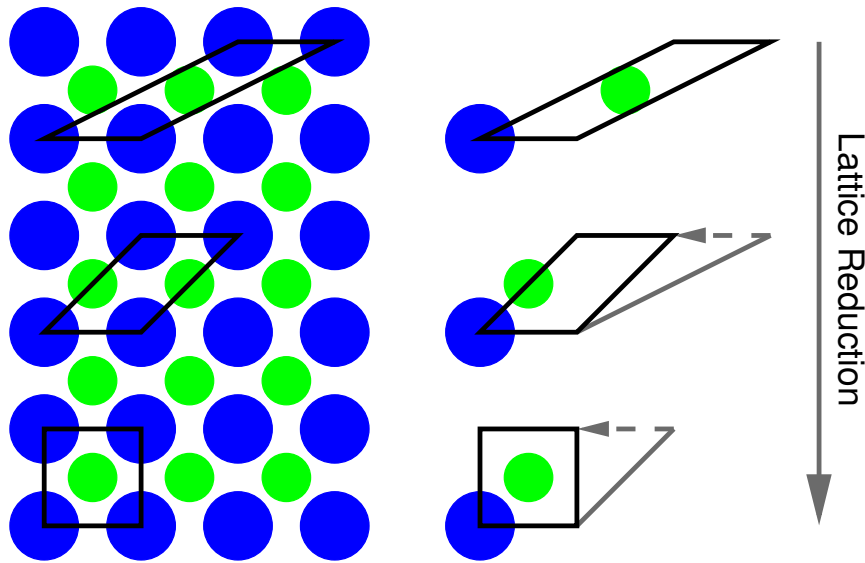


**Figure 5.4:** Illustration of the lattice-reduction procedure. A 2D binary crystal of disks is shown, as well as three possible unit cells for this crystal. From top to bottom the lattice vectors of the unit cells become more orthogonal and shorter. The lattice vector that is modified is shown in grey. The one by which it is reduced, is indicated using a dashed grey arrow. The lattice-reduced unit cell has a square geometry.

modify this algorithm as follows. We measure the distortion of the simulation box using the function

$$\mathcal{C}(\mathbf{v}_1, \mathbf{v}_2, \mathbf{v}_3) = \frac{1}{9} \frac{(|\mathbf{v}_1| + |\mathbf{v}_2| + |\mathbf{v}_3|)(|\mathbf{v}_1 \times \mathbf{v}_2| + |\mathbf{v}_1 \times \mathbf{v}_3| + |\mathbf{v}_2 \times \mathbf{v}_3|)}{\mathbf{v}_1 \cdot (\mathbf{v}_2 \times \mathbf{v}_3)}, \quad (5.4)$$

with  $|\cdot|$  the vector norm. This function is obtained by multiplying the average box-vector length with the size of the box's surface, dividing by the total volume of the box, and normalizing this quantity such that  $\mathcal{C} = 1$  for a cube. It can be shown that  $\mathcal{C} > 1$ , when the box is not cubic. We empirically established a criterion for lattice reduction: if  $\mathcal{C} \lesssim 1.5$  the box is sufficiently orthorhombic and we do *not* perform lattice reduction, although this number may be tweaked to better suit a particular system. When  $\mathcal{C} > 1.5$ , we follow Ref. [179] and generate a set of 12 lattice combinations:

$$\begin{aligned} & \{\mathbf{v}_1 \pm \mathbf{v}_2, \mathbf{v}_2, \mathbf{v}_3\}, \quad \{\mathbf{v}_1 \pm \mathbf{v}_3, \mathbf{v}_2, \mathbf{v}_3\}, \\ & \{\mathbf{v}_1, \mathbf{v}_2 \pm \mathbf{v}_1, \mathbf{v}_3\}, \quad \{\mathbf{v}_1, \mathbf{v}_2 \pm \mathbf{v}_3, \mathbf{v}_3\}, \\ & \{\mathbf{v}_1, \mathbf{v}_2, \mathbf{v}_3 \pm \mathbf{v}_1\}, \quad \{\mathbf{v}_1, \mathbf{v}_2, \mathbf{v}_3 \pm \mathbf{v}_2\}. \end{aligned} \quad (5.5)$$

We calculate the surface area for each of these potentially more orthorhombic boxes and select the one with the smallest surface area. For this new box another set of 12 combinations is constructed according to Eq. (5.5) and the procedure is repeated. This process is terminated when the smallest surface area among these 12 candidates is greater than the surface area of the box in the previous iteration. See Fig. 5.4 for an illustration of the procedure. Full lattice reduction is always accomplished within a finite number

of steps, but it is prudent to impose a cut-off at roughly 10 iterations. We found that convergence for this algorithm is fast, typically taking no more than 3 to 5 iterations, for boxes with  $1.5 \lesssim \mathcal{C} \lesssim 10$ . When the fully lattice-reduced box is found the particles are placed back in the box. Note that the number of particles in the box is preserved under lattice reduction. We did *not* implement the constraint of Ref. [75] on the angles that the box vectors can make with each other. The lattice-reduction procedure removes any unwanted deformations efficiently and an angular constraint might bias the simulation for particles with a highly anisotropic shape.

## 5.7 Soft Interactions and External Fields

Hard-particle FBMC simulations, for which a suitable overlap routine is chosen, can be performed using the above combination of acceptance criteria, image-list generation, and lattice reduction. Introducing soft interactions into the system requires extending the above approach as follows. The method of truncation and tail correction described in Ref. [253] is employed to determine the contribution to the system's total energy for short-range and semi-long-range interaction potentials. That is, soft interactions which decay faster than  $r^{-3}$ , with  $r$  the inter-particle distance. Here we assume a radially symmetric cut-off distance of  $R_C$ , which allows us to construct similar image lists as for the hard-particle interaction. A version of the FBMC method was also successfully applied to systems with long-range interaction potentials [75], for which Ewald Sums [253, 269] are required to compute the energy contribution. Interaction with an external field can also be easily introduced, since such a term only couples to the particles in the box in the expression for the total energy. It depends on the specifics of the system whether it is advantageous to first consider acceptance of the scaling and deformation moves on the hard-particle part of  $\text{acc}(o \rightarrow n)$  or on the soft-interaction part.

## 5.8 Compression and Crystal Structure Prediction

In order to successfully predict crystal structures we apply the following procedure, also see Chapter 6 for some examples. Systems are prepared in a dilute phase, for which the particles are not in contact, at a low pressure. What constitutes a 'low pressure' is strongly dependent on the system, but can easily be ascertained by a few trial runs. In order to obtain the pressure  $P$  of interest, the initial pressure is increased over a number of Monte Carlo cycles, where one cycle is understood to be one (translation, rotation, volume) trial move per particle. A slow increase of the pressure, for instance, according to a geometric series of pressure steps, can be applied to allow the system to sample more ways in which to 'crystallize', in the hope that it chooses the optimal structure. If a slow increase of the pressure is used, we typically find that the FBMC simulation only has to be performed a small number of times in order to obtain a good understanding of the possible crystal structures that can be found at the pressure of interest, say 25 to 100 compression runs. It is also possible to compress the system by rapidly increasing the pressure. In this case, effective sampling of crystal structures usually necessitates a larger set of compression runs than for the slower pressure increase, since there is less

time for the system to explore different orientations before it becomes jammed in a (local) minimum of the crystal-structure free energy. Both slow and fast compression runs should be followed by a period of equilibration at the desired pressure to allow the system to settle in its (locally) optimal structure. When the fluctuations in the system are relatively large, it can be useful to follow this equilibration with a production run during which, for instance, the lattice vectors, particle positions, and particle orientations are averaged to obtain a representative crystal-structure candidate.

Increasing and decreasing the pressure several times around the  $P$  value of interest can prove useful in helping the system to cross free-energy barriers, thereby improving the chance of finding the global minimum in the free energy. Allowing the MC step size to adjust to predetermined acceptance ratios during the compression and equilibration part of the simulation also improves the results of the FBMC algorithm. We typically employ an acceptance ratio of 25% for translations and rotations, and a ratio of 10% for scaling and deformation moves. The set of crystal-structure candidates that is obtained by slow and/or fast compression, can be analysed using a combination of software packages [270] and manually going through crystal-structure databases [271, 272]. For a binary mixture of hard spheres this approach allowed the crystal structures of the candidates to be determined [75]. However, establishing the structure of a numerically obtained result is highly nontrivial in general. Moreover, a description of a system by its molecular equivalent [75, 174, 260, 272], is not always adequate or possible for nonspherical particles, also see Ref. [249] and Chapter 6. Finally, we note that the frequency with which structures are observed in the FBMC runs can give some insight into which of the structures we find is stable [75], but only free-energy calculations can give a definitive answer.

## 5.9 Discussion and Outlook

Summarizing, we described in detail the way in which a floppy-box Monte Carlo (FBMC) simulation [75], which allows for the prediction of crystal-structure candidates at finite pressure, can be set up. We also discussed two types of overlap algorithm, the method of separating axes and a triangular-tessellation based technique, by which hard-particle simulations for (nonconvex) faceted objects can be performed. When these overlap routines are combined with the FBMC algorithm, a powerful simulation technique is obtained with many applications to colloid research, as well as mathematical problems of a more fundamental nature. We briefly go into these here and discuss these in more detail in Chapter 6.

The FBMC algorithm can be used to establish a lower bound to the packing fraction of the densest configuration of shape-anisotropic (nonconvex) objects [249]. Currently several techniques exist to estimate this lower bound numerically [166, 167, 169, 249, 260, 273, 274]. The FBMC method is similar to the adaptive-shrinking-cell (ASC) method of Refs. [166, 167], since both allow for a sequential search of configurational space and lattice space using a Metropolis based Monte Carlo (MC) procedure. However, FBMC uses a lattice-reduction technique [179] to avoid unphysical distortions of the unit cell, whereas the ASC algorithm employs a symmetric strain tensor. In addition, FBMC drives the systems towards its densest configuration by employing a (gradual) pressure

increase according to a  $NPT$ -MC simulation, whereas ASC drives compression using the negative packing fraction as the basis of its Metropolis acceptance rule. The method used in Refs. [169, 260], likely amounts to a different implementation of the principles that underlie the FBMC algorithm, whereas the technique of Refs. [273, 274] constitutes a completely different means of determining densest packings. The latter is based on a divide-and-conquer approach to achieve simultaneous satisfaction of multiple constraint equations. It goes beyond the scope of this thesis to determine which of these techniques is most suited to achieve densest-packed structures.

Of the aforementioned crystal-structure prediction algorithms FBMC has the advantage that it can be used to explore suboptimal packings in accordance with the statistical  $NPT$ -ensemble at finite pressures. This is particularly relevant, since densest-packed candidate crystal structure need not be thermodynamically stable at all pressures for which the system crystallizes [54, 171–173]. It is important to realize that there are strong finite-size effects for the prediction of candidates at finite pressure. The pressure  $P$  at which we perform the FBMC simulations only sets a range from which we sample crystal structures. Large fluctuations in  $PV/k_B T$ , where  $P$  is the pressure,  $V$  is the volume,  $k_B$  is Boltzmann’s constant, and  $T$  is the temperature, are to be expected in general due to the small number of particles considered. The extent of these fluctuations may be probed by studying the density fluctuations that occur during a FBMC simulation and this can give some insight into coarseness of the result. The presence of large fluctuations likely prevents mesophases with a small pressure range of stability to be discovered using our method. However, such mesophases can often be determined by melting a higher density crystal, which may be obtained using the FBMC technique, in an  $N \gg 10$  simulation [171].

Due to the level of fluctuations that is expected, the FBMC algorithm allows some flexibility in the precision to which soft-interaction terms are taken into account. For example, it is possible to ignore small cut-off corrections without incurring a large error, since this type of correction can be absorbed as a (small) pressure change in the acceptance rules. In this sense the FBMC technique is quite robust, but by the same token it is not a priori capable of attaining a high degree of accuracy at finite pressures. The ability of the technique to predict plastic-crystal phases has to be investigated further in the near future. Despite these minor concerns, the FBMC technique has proven itself an extremely useful and effective tool to predict crystal-structure candidates for colloids and nanoparticles, as well as dense regular packings of irregular nonconvex solids.

## 5.10 Acknowledgements

It is a pleasure to thank Dr. Laura Filion for proofreading this chapter. Her suggestions have greatly improved the quality of the text and the explanation of floppy-box Monte Carlo algorithm. I would also like to thank Dr. Matthieu Marechal, who helped me to set up my first crystal-structure-prediction algorithm. Finally, I wish to extend my gratitude towards Tristan Hartskeerl, who introduced me to the polygon-based overlap detection and with whom I collaborated to perform an initial study of the behaviour of highly shape-anisotropic particles.

---

## Dense Regular Packings of Irregular Nonconvex Particles

---

In this chapter we employ the floppy-box Monte Carlo technique introduced in Chapter 5 to analyse regular packings of odd-shaped bodies. Our interest stems from a materials-science perspective, as well as from a mathematical perspective. We examine the densest-known (regular) structures for 17 irregular nonconvex shapes and we confirm several mathematical conjectures for the packings of a large set of 142 convex polyhedra. We also extend upon these conjectures and prove that we have obtained the densest packings for rhombicuboctahedra and rhombic enneacontrahedra. Moreover, we improve the value of the densest-known packing of enneagons and truncated tetrahedra. For the colloid and nanoparticle aspect of our investigation we consider a family of truncated cubes, which interpolates between a cube and an octahedron. We obtain a fascinating richness in the structures that are achieved for the various levels of truncation. Finally, we apply our dense-packing result to determine the equation of state for a system of octahedra and we examine the properties of the different phases.

## 6.1 Introduction

As mentioned in Chapter 5 the synthesis of colloids and nanoparticles has advanced tremendously over the last decade [82, 83]. Currently it is not only possible to synthesize spherical particles with a high level of precision and reproducibility, but also a wide variety of convex faceted shapes, e.g., [84, 89, 93], as well as nonconvex, irregular, and even punctured particles, e.g., [54, 78, 102, 103, 106, 107, 109]. The experimental study of the self-assembly of such particles into dense phases and regular structures [275–277] has raised questions on how to model such systems using simulations. Several techniques were developed to perform simulations on dense phases of convex particles [166, 167, 169, 172, 173]. Interestingly, in studying these dense configurations materials-science research interfaces with fields as diverse as discrete geometry, number theory and computer science [184, 186, 250–252]. The computational power of modern desktop PCs makes it possible to analyse longstanding mathematical problems on the dense packing of solids in a numerical way, as well as assist in the proof of mathematical theorems, e.g., the proof of the Kepler conjecture [184, 186]. This is an additional driving force in the development of tools that allow dense packings to be predicted numerically. The discovery of tetrahedron packings which achieve a packing fraction greater than that of spheres [167, 169, 259, 278], is a particularly good example of the importance of simulation-based approaches to geometry. Despite this strong interest in packings, the properties of dense structures comprised of irregular and nonconvex solids have hardly been investigated. This can be explained by the fact that the overlap algorithm for such particles is often difficult to implement. Only recently were the first attempts made to study such systems, namely for superdisks [175] and bowls [176].

To analyse dense regular structures, we use the floppy-box Monte Carlo (FBMC) algorithm to predict candidate crystal structures, see Chapter 5 and Refs. [75, 176, 249]. When this predictive technique is combined with a triangular-tessellation-based overlap algorithm [218, 249] a powerful tool is obtained, which allows us to study the densely packed configurations of irregular nonconvex particles. In this chapter we demonstrate the general applicability of this method. We apply it to determine the densest-known packing of 142 convex polyhedra and 17 irregular shapes, also see Refs. [249, 279] and Appendix B. This set includes a few models that contain a huge number of triangles, e.g., the cap, the Stanford bunny, and the hammerhead shark, with 3,850, 3,756, and 5,116 triangles, respectively. These models allow us to gauge the efficiency of the algorithm, in Section 6.2. In Section 6.3, we discuss the mathematical insights gained by analysing the dense regular packings of these 159 polyhedral particles. This analysis is followed by a proof that the FBMC results achieve the densest packing for rhombicuboctahedra and rhombic enneacuboctahedra in Section 6.4. We also construct a denser packing for regular enneagons (9-gons) in Section 6.5. In Section 6.6, we introduce a family of truncated cubes and investigate the crystal structures that its members can form. We obtain a stunning richness in the structure as a function of the level of truncation. We conclude with an analysis of the equation of state for octahedra and a discussion of the phase behaviour of these particles in Section 6.7.



## 6.2 Method: Accuracy, Efficiency, and Applications

All particle models for the 159 (irregular) polyhedra considered in the following sections were obtained from particle databases [280–282] or were created to resemble existing nanoparticles and colloids [54, 102, 106, 109]. These triangular-tessellation models are given in Ref. [279]. We applied the FBMC technique described in Chapter 5 to these particles and we used the following strategy for the compression. Systems of tessellated particles were prepared in a dilute phase, typically with packing fraction  $\phi \approx 0.001$ . By increasing the reduced pressure  $p \equiv PV_M/k_B T$  from  $p = 1$  to  $p \approx 10^5$  in 100 steps over 50,000 Monte Carlo (MC) cycles, according to a geometric series of increases, we compressed the system to a high-density crystalline state. Here  $P$  is the pressure,  $V_M$  is the volume of a particle model,  $k_B$  is Boltzmann’s constant,  $T$  is the temperature, and one cycle is understood to be one trial move per particle. We typically applied this compression a total of 25 times for each number of particles in the unit cell  $N$  ( $N = 1, \dots, 6$ ) and for each shape and select the densest packing among these. These 6 packings (per shape) were allowed to equilibrate for  $10^6$  cycles at  $p \approx 10^6$ , to obtain a maximally compressed state. Finally, we compared the results and determined the lowest value of  $N$  for which the densest packing is achieved and what the lower bound to the packing fraction of the densest packing  $\phi_{LB}$  is.

The method was typically quite fast with simulations taking minutes to hours on a modern desktop PC. We observed that for the initial 50,000 MC cycles of compression the algorithm exhibits linear scaling in the number of triangles and moves. We disregarded the final compression run of  $10^6$  MC cycles, since this part only serves to achieve a high decimal accuracy, while the structure no longer changes significantly. Let  $N_T$  be the number of triangles of a specific model,  $N_C = 50,000$  the number of MC cycles, and let  $t$  be the total run time of the simulation in seconds. We obtained

$$\frac{t}{(NN_C)(NN_T)} = \mathcal{C}, \quad (6.1)$$

with  $\mathcal{C}$  a constant that depends only on the model and the way in which the system is compressed. The algorithm thus scales linearly with the total number of triangles times the total number of attempted moves. The value of  $\mathcal{C}$  differs per model, because some models ‘crystallized’ more easily than others. For the 159 models we studied, we found the mean value of this constant to be  $\langle \mathcal{C} \rangle \approx 70 \mu\text{s}$  on a modern 2.0 GHz desktop computer system. The median value is  $\langle \mathcal{C} \rangle_M \approx 40 \mu\text{s}$ , with only 27 models exceeding  $\mathcal{C} = 100 \mu\text{s}$ . Even for the aforementioned high-triangle models the time scales are accessible, the total run length of the simulations, including the final  $10^6$  cycles of equilibration, did not exceed 175 hours, mostly due to the advanced overlap algorithm that we employed. For more information on the overlap algorithm and its benchmarking we refer to Ref. [218].

We showed that our FBMC method yields sufficiently accurate results by considering the 5 Platonic and 13 Archimedean solids, for which we found excellent agreement with Refs. [169, 252, 283]. We typically obtained a very narrow distribution of crystal-structure candidates, which had a packing fraction close to that of the densest-known configuration, typically within 1%. The densest of these candidates was further compressed and this usually resulted in a packing fraction that only deviated from the literature value  $\phi_{LB}$  by

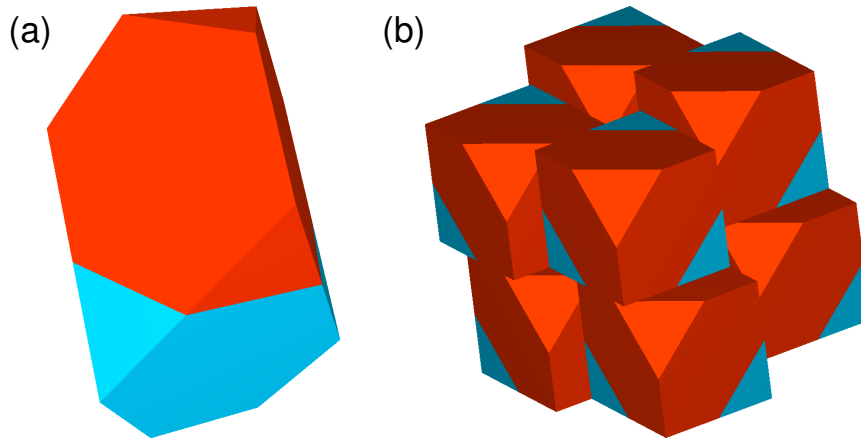


**Figure 6.1:** The dense dimer crystal structure for truncated tetrahedra that we obtained by the FBMC technique and which achieves a packing fraction  $\phi_{\text{LB}} = 0.988\dots$  (a) The dimer formed by two truncated tetrahedra (blue and red). (b) A piece of the crystal structure generated by this unit cell, only 7 periodic images are shown. The viewpoint is such that the dimers in this crystal are pointing out of the paper, with the top triangle [as given in (a)] facing the reader.

an absolute amount of 0.002. Upon analysing our results for the Archimedean solids, we discovered a new crystal structure for truncated tetrahedra, namely a dimer lattice with  $\phi_{\text{LB}} = 0.988\dots$ ; also see Fig. 6.1, Appendix B, and Refs. [249, 279]. This is not only mathematically interesting [283], but also relevant to the study of nanoparticle systems [260], since truncated tetrahedra have recently been synthesized [91, 93]. After verifying the accuracy of our method, we used it to study 17 nonconvex (irregular) shapes, some of which even contain holes. Our results for these shapes give confidence in the applicability of our method to nonconvex objects in general. Figure 6.2 shows representations of the shape and predicted crystal structure for 4 of the nonconvex particles we considered. Such candidate crystal structures can be used in simulations of larger systems or in theoretical studies to determine their stability by free-energy calculation, e.g., see Ref. [171]. We will come back to this in Section 6.7, in which we consider simulations of the phase behaviour of octahedra.

A nonconvex irregular particle that we considered in more detail is the colloidal cap, see Fig. 6.2a, which shows the model that was used. This model was derived by minimizing the Hamiltonian that describes the bending and in-plane stretching elasticity terms that govern the collapse of a shell under an external isotropic pressure using Surface Evolver [109, 284]. The cap (model) contains 3,850 triangles. When we applied our technique to this model, we obtained crystal structures similar to the ones found - also using the FBMC technique - for a much simpler bowl-shaped model [176]: columnar, braided, and inverse braided phases, see Appendix B. Figure 6.2b shows a braided configuration. Support is thus provided for the idea that the simple bowl shape of Ref. [176] captures the essential shape-related physics of these systems. We were unable to map our results directly onto the phase diagram of Ref. [176], because the substantial difference in the shape of the interior of the caps prevented us from assigning an appropriate

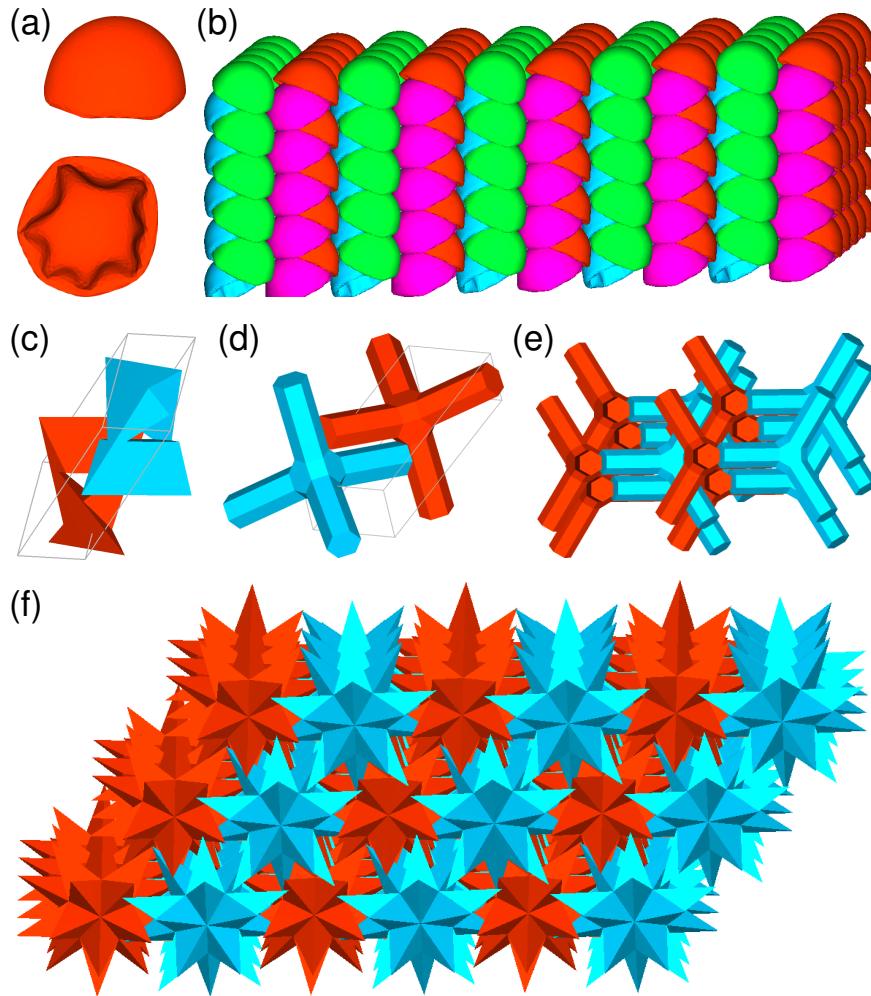


**Figure 6.2:** Four nonconvex shapes and three of their densest-known crystal structures. (a) Side and bottom view of our model (3,850 triangles) for a colloidal cap. (b) A piece of the double-braided structure formed by these caps. There are four particles in the unit cell, i.e., the structure can be decomposed into quadrimeric building blocks. Each particle in the unit cell is indicated with a different colour. (c) The centrosymmetric dimer formed by two Szilassi polyhedra (red, blue) in relation to the unit cell (grey box) predicted using the FBMC technique. We do not show the crystal this unit cell generates, since it is difficult to make out individual particles in it even when they are colour coded. (d) A centrosymmetric tetrapod dimer (red, blue) in relation to the unit cell (grey box) of the associated structure. (e) A piece of the crystal this unit cell generates. (f) The densest-known packing for great stellated dodecahedra, again the structure is a dimer lattice as indicated by the use of red and blue.

$L/\sigma$  [176] value. Nevertheless, this result is very encouraging as it gives an example of the usefulness of our method to the study of physically relevant systems.

Another physical system we studied in great detail is that of octapod-shaped nanocrystals dispersed in a liquid [54]. In Ref. [54] and Chapter 7 we analyse the hierarchical self-assembly of these so-called octapods into interlocking chains and three-dimensional (3D) super structures, which is caused by the hard-core repulsions and van-der-Waals attrac-

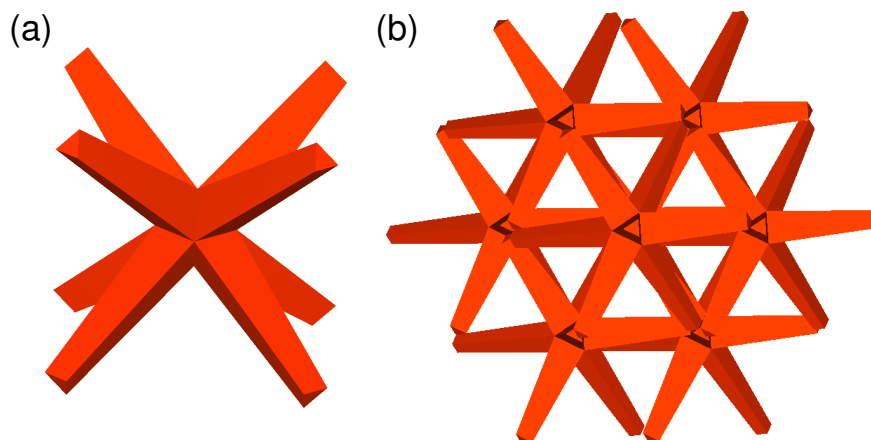


**Figure 6.3:** A crystal-structure candidate obtained for octapod-shaped particles, with short-ranged square well interactions between the tips of the pods. (a) The hard-particle part of the model used in this simulation. (b) A part of a candidate crystal structure that has a simple cubic morphology. Note that the octapods touch each other at the tips.

tions between the octapods. We managed to reproduce the interlocking-chain formation at high dilutions using an empirical model for octapod-octapod interactions, which incorporates an octapod-shaped hard core, a Lennard-Jones potential, and square-well attractions. Figure 6.3 shows an example (simple cubic) candidate crystal structure obtained by our FBMC method for a system of octapods with a less complicated interaction potential. The centroids of the tips are attracted to each other according to a short-ranged, a radius of half the tip length, yet deep ( $4 k_B T$ ) square-well interaction. Although simulations on octapods proved technically challenging, we showed that the method described in Chapter 5 allows for a complicated hard-particle interaction to be supplemented with soft potentials to more accurately model experimental systems.

### 6.3 General Properties of Convex Polyhedra

Over the course of our investigation we obtained several exciting and remarkable results on the packing of faceted particles, which we summarize in this paragraph. We refer the reader to Appendix B and Ref. [279] for additional information and the data which supports our claims, respectively.

- We extended the verification of Ulam’s conjecture [187], which states that all (non-spherical) convex particles can achieve a monodisperse space-filling packing that is denser than that of spheres, to the first 8 regular prisms and antiprisms, the 92 Johnson solids, and the 13 Catalan solids, see Fig. 6.4. For regular  $n$ -prisms and  $n$ -antiprisms, where  $n$  indicates the number of edges of the base polygon, the verification of Ulam’s conjecture may be further extended to  $n = \infty$ . For regular prisms this follows from the analysis of the lower bound to the packing fraction of regular  $n$ -gons [250, 251] and the columnar way in which these prisms stack. The estimate for antiprisms is based on determining the outscribed-cylinder volume. The particle

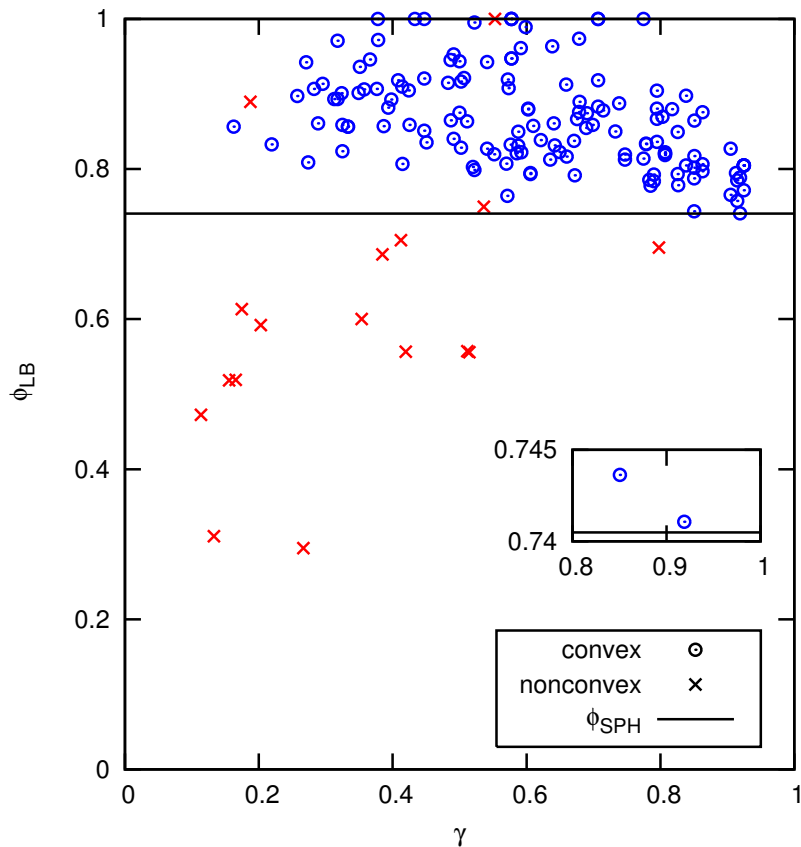


**Figure 6.4:** The maximum packing fraction  $\phi_{LB}$  we obtained using the FBMC technique as a function of the sphericity  $\gamma$  for the 142 convex (circles, blue) and 17 nonconvex (crosses, red) shapes we investigated. Also see Tables B.1 - B.15 for the numerical values of these data points. Note that particles with a sphericity of  $\gamma > 0.8$  tend to group closer to the packing fraction of spheres ( $\phi_{SPH} = \pi/\sqrt{18}$ , solid line), however, even for  $\gamma > 0.8$  there is significant spread in the  $\phi_{LB}$  values. Therefore, we conclude that there is no clear relation between  $\gamma$  and  $\phi_{LB}$ . Using the line  $\phi_{SPH}$  and the inset, we show that all 142 convex particles satisfy Ulam’s conjecture.

volume divided by this cylinder volume, times the hard-disc packing fraction  $\pi/\sqrt{12}$  gives a lower bound to the 3D packing fraction of antiprisms. From this estimate it follows that it is sufficient to check up to  $n = 7$  numerically. For all  $n > 7$  we have  $\pi/\sqrt{18} < \phi_{LB}$  by our outscribed-cylinder construction.

- Our results showed that there is no clear dependence between the sphericity  $\gamma$ , the ratio of the largest inscribed- and smallest outscribed-sphere radius, and the densest-known packing fraction  $\phi_{LB}$ . At least not in the  $\gamma$ -regime we analysed. The construction of  $\gamma$  is explained in Appendix B. Figure 6.4, which shows our value for  $\phi_{LB}$  as a function of  $\gamma$ , gives a visual representation of this result.
- We confirmed for 49 convex centrosymmetric particles that their densest-known lattice packing is a Bravais-lattice structure, in accordance with the conjecture of

Ref. [167]. Centrosymmetry is understood here to imply that there is an inversion point to the symmetry group that is associated to the particle's shape.

- Our data also supports the conjecture of Ref. [166] that convex, congruent solids without central symmetry do not *necessarily* achieve their densest packing in a non-Bravais structure. In general noncentrosymmetric particles pack densest in a non-Bravais structure, however, there are indications that some particles do not obey this 'rule'. A possible example is the snub cube (Fig. 6.5c) that achieved  $\phi_{\text{LB}} = 0.787\dots$  for  $N = 1$  particle in the unit cell (Bravais lattice). We confirmed this using an extended sample set to achieve greater numerical accuracy, see Appendix B. This result may be an indication that in three dimensions central symmetry is not as strong a prerequisite for the densest regular packing to be a Bravais structure as it is in two dimensions [285]. However, our result constitutes only a possible counter example, not a full mathematical proof. Nevertheless, the snub cube is not the only particle for which we observed this phenomenon, e.g., the snub dodecahedron and the metabigyrate rhombicosidodecahedron probably achieve their densest packing for  $N = 1$  as well. For the snub cube and snub dodecahedron this possibility was already alluded to in Refs. [166, 286].
- Many noncentrosymmetric particles, both convex and nonconvex, were found to form a centrosymmetric compound which achieves the densest regular packing. For noncentrosymmetric particles the arrangement of the particles in the crystal may be such that there is a Bravais sublattice with the same group of particles associated to each of its lattice sites. If the shape of this group is centrosymmetric we say that the particles pack densest by forming a centrosymmetric compound. For example, truncated tetrahedra (Fig. 6.1a), (anti)prisms ( $n < 11$ ), Szilassi polyhedra (Fig. 6.2c), and our tetrapod model (Fig. 6.2d), form centrosymmetric dimers and tetrahedra form centrosymmetric quadrumers [169].
- Remarkably, it appears that some noncentrosymmetric particles, e.g., the gyrate rhombicosidodecahedron and the tetrapod model, have a noncentrosymmetric  $N = 1$  packing and an  $N = 2$  centrosymmetric dimer packing that achieve (nearly) the same packing fraction.

## 6.4 Analytic Construction of Two Densest Packings

In this section we prove that the densest-packed configurations for rhombicuboctahedra  $\phi_{\text{LB}} = (4/3)(4\sqrt{2} - 5)$  and for rhombic enneacuboctahedra  $\phi_{\text{LB}} = 16 - 34/\sqrt{5}$  are given by the Bravais-lattice structures we obtained using the FBMC technique.

### 6.4.1 Rhombicuboctahedra

A rhombicuboctahedron (RCH, Fig. 6.5a) can be specified by the vertex coordinates

$$\left( i \left( \frac{1}{2} + \frac{p}{\sqrt{2}} \right), j \left( \frac{1}{2} + \frac{q}{\sqrt{2}} \right), k \left( \frac{1}{2} + \frac{r}{\sqrt{2}} \right) \right), \quad (6.2)$$

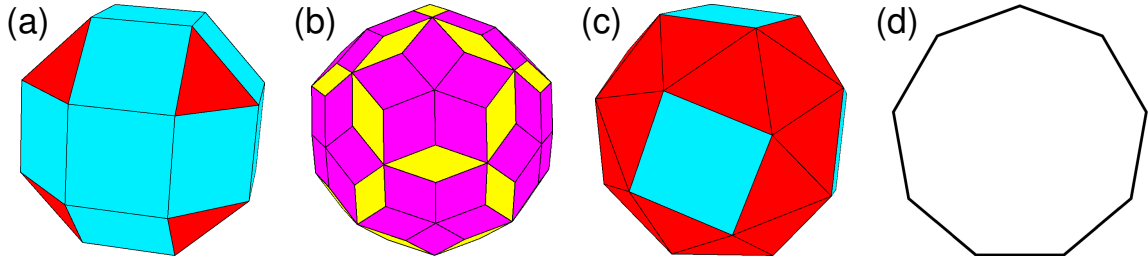


**Figure 6.5:** Four representations of convex particles for which interesting results were obtained. (a) Rhombicuboctahedron. (b) Rhombic enneacontrahedron. For both of these particles we showed that the densest packing is a Bravais-lattice packing. (c) The snub cube, which is *not* centrally symmetric, yet it appears to achieve its densest-known packing in a Bravais lattice. (d) An enneagon, for which we constructed a denser packing than was previously known.

where  $i, j$ , and  $k \in \{-1, 1\}$  and  $p, q$ , and  $r \in \{0, 1\}$ , with  $p + q + r = 1$ . This gives a list of 24 vertices centred on the origin, which span a RCH with volume  $V_M = 4 + 10\sqrt{2}/3$ . For the orientation imposed by this set of vertices, the three vectors that describe a (potential) unit cell which realizes the densest packing are given by

$$\mathbf{v}_0 = \left(1 + \frac{1}{\sqrt{2}}, -1 - \frac{1}{\sqrt{2}}, 0\right); \quad (6.3)$$

$$\mathbf{v}_1 = \left(1 + \frac{1}{\sqrt{2}}, 0, -1 - \frac{1}{\sqrt{2}}\right); \quad (6.4)$$

$$\mathbf{v}_2 = \left(0, 1 + \frac{1}{\sqrt{2}}, 1 + \frac{1}{\sqrt{2}}\right). \quad (6.5)$$

Checking for overlaps in this configuration is a simple matter of verifying that there are no overlaps for an appropriate number of nearest neighbours, i.e., the algebraic equivalent of the FBMC image-list-based overlap routine introduced in Chapter 5. The volume of the unit cell is given by  $|\mathbf{v}_0 \cdot (\mathbf{v}_1 \times \mathbf{v}_2)| = 5 + 7/\sqrt{2}$ . Therefore, the packing fraction is

$$\phi_{\text{LB}} = \frac{4 + 10\sqrt{2}/3}{5 + 7/\sqrt{2}} = \frac{4}{3} (4\sqrt{2} - 5), \quad (6.6)$$

which gives a lower bound to the packing fraction  $\phi_D$  of the densest configuration. We determined the minimum face-to-point distance for all 26 faces of the RCH, which leads to a set of 26 constrained equations. The maximum inscribed sphere can be obtained using constrained minimization on this set of equations. Its radius is  $R_I = 1/2 + 1/\sqrt{2}$  and its centre coincides with that of the RCH. This results in the following upper-bound estimate, according to Ref. [167], for  $\phi_D$ :

$$\phi_{\text{LB}} \leq \phi_D \leq \phi_{\text{UB}} \equiv \frac{V_M}{4\sqrt{2}R_I^3} = \frac{4 + 10\sqrt{2}/3}{4\sqrt{2} (1/2 + 1/\sqrt{2})^3} = \frac{4}{3} (4\sqrt{2} - 5). \quad (6.7)$$

This upper bound is incorrectly listed as  $\phi_{\text{UB}} = 1$  in Ref. [167]. We have thus proven that the maximum packing fraction is obtained, since  $\phi_{\text{UB}} = \phi_D = \phi_{\text{LB}}$ . Here it should be

noted that this proof is conditionally dependent on the proof of Ref. [184], which shows that spheres pack densest with packing fraction  $\pi/\sqrt{18}$ , via the proof for the upper-bound criterion of Ref. [167].

## 6.4.2 Rhombic Enneacontrahedra

We consider the rhombic enneacontrahedron (RECH, Fig. 6.5b) that is specified by the 92 vertices listed in Tables B.17 - B.19. These vertices span a RECH with volume

$$V_M = \frac{20}{3} \sqrt{43 + \frac{56\sqrt{5}}{3}}. \quad (6.8)$$

For the orientation of this RECH, the three vectors that describe a (potential) unit cell which realizes the densest packing are given by

$$\mathbf{v}_0 = \left( -\frac{5}{6}(2 + \sqrt{5}), \frac{1}{2}\sqrt{\frac{5}{3}}, \frac{1}{3}(5 + 2\sqrt{5}) \right); \quad (6.9)$$

$$\mathbf{v}_1 = \left( -\frac{5}{12}(1 + \sqrt{5}), \sqrt{\frac{235}{24} + \frac{35\sqrt{5}}{8}}, \frac{1}{6}(5 + \sqrt{5}) \right); \quad (6.10)$$

$$\mathbf{v}_2 = \left( \frac{1}{12}(25 + 13\sqrt{5}), \frac{5 + \sqrt{5}}{4\sqrt{3}}, \frac{1}{6}(5 + \sqrt{5}) \right). \quad (6.11)$$

Checking for overlaps in this configuration is again a simple matter. The volume of the unit cell is given by

$$|\mathbf{v}_0 \cdot (\mathbf{v}_1 \times \mathbf{v}_2)| = \frac{10(20 + 9\sqrt{5})}{3\sqrt{3}}. \quad (6.12)$$

This gives the lower bound  $\phi_{\text{LB}} = 16 - 34/\sqrt{5}$ . By determining the set of 90 face-to-point constrained equations, it is easily shown using constrained minimization that the centre of the maximum inscribed sphere coincides with the RECH's centre and that the radius of this sphere is given by

$$R_{\text{I}} = \sqrt{\frac{35}{12} + \frac{5\sqrt{5}}{4}}. \quad (6.13)$$

The upper bound to the packing fraction is therefore  $\phi_{\text{UB}} \equiv V_M/(4\sqrt{2}R_{\text{I}}^3) = 16 - 34/\sqrt{5} = \phi_{\text{LB}}$ . We have thus proven that the maximum packing is obtained.

Interestingly, it now is possible to construct two additional upper bounds to the packing fraction of the densest configuration for a given species of particle, which are based on the largest inscribed RCH and RECH, respectively. The proof follows the same line of argument as used in Ref. [167] for the construction of a sphere-based upper bound. The disadvantage of these estimates over the inscribed-sphere one is that determining the largest inscribed RCH and RECH is significantly more challenging than obtaining the largest inscribed sphere.

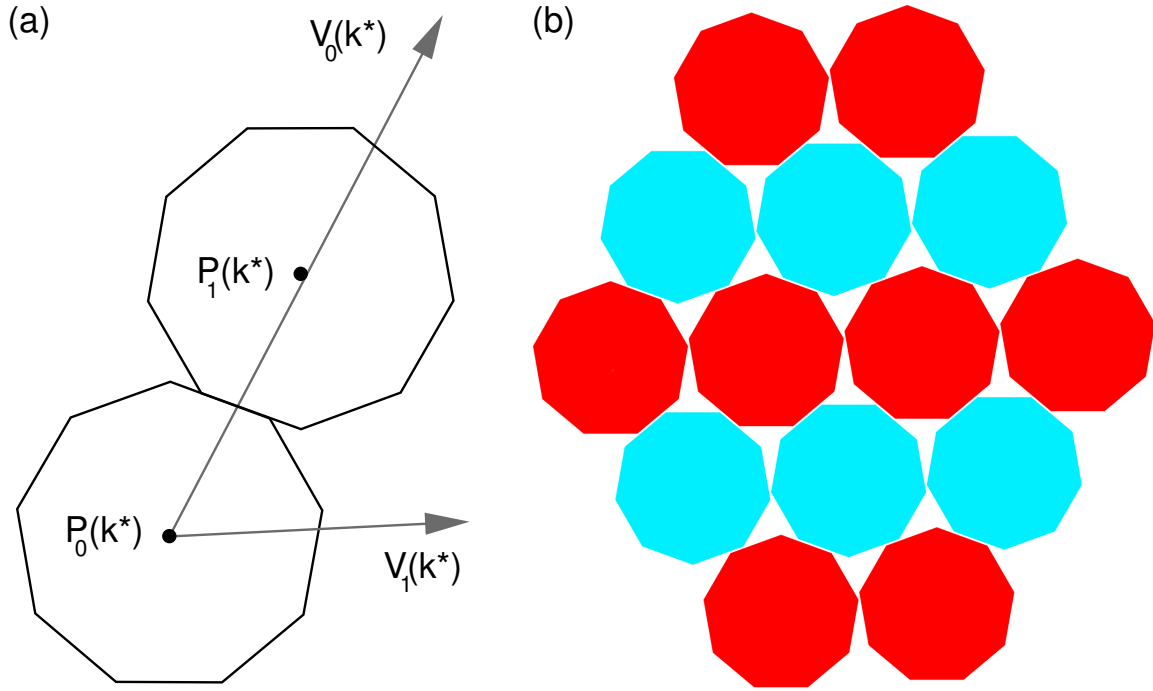


**Figure 6.6:** The new denser-packing crystal structure for enneagons. (a) The vectors  $V_0(k^*)$  and  $V_1(k^*)$  that span the unit cell in relation to the position  $[P_0(k^*)$  and  $P_1(k^*)]$  of the  $N = 2$  enneagons in it. We also show the outline of both enneagons to indicate their orientation with respect to each other. (b) A piece of the dimer crystal structure the unit cell generates. The two orientations of the enneagons are indicated with red and blue, respectively.

## 6.5 Denser-Packing Crystal Structure for Enneagons

By extension of our result for the 9-prism, we obtained a new two-dimensional (2D) packing (Fig. 6.6b) with  $\phi_{\text{lb}} = 0.901\dots$  for the regular Enneagon (Fig. 6.5d) that surpasses the packing fraction  $\phi_{\text{LB}} = 0.897\dots$  of the old structure [251] by roughly 0.04. In this section we describe the construction of our new 2D crystal. An enneagon is defined here to have a centre-to-tip distance of 1. It is centred on the origin of a Cartesian coordinate system with its tips mirror-symmetrically distributed around the  $y$ -axis and one tip located on the positive  $y$ -axis, i.e., it has the orientation shown in Fig. 6.5d. To describe the crystal structure we require three 2D vector parametrizations

$$\mathbf{p}_1(q) = \left( q \left( \sin \frac{\pi}{9} - \frac{\sqrt{3}}{2} \right) + 2 \cos \frac{\pi}{9} \sin \frac{2\pi}{9}, \frac{1}{4} \left( q \left( 2 - 4 \cos \frac{\pi}{9} \right) - \csc \frac{\pi}{18} \right) \right); \quad (6.14)$$

$$\mathbf{p}_2(r) = \left( 2 \cos \frac{\pi}{9} \sin \frac{\pi}{9} - r \sin \frac{2\pi}{9}, 2 \cos^2 \frac{\pi}{9} + r \left( 1 - \cos \frac{2\pi}{9} \right) \right); \quad (6.15)$$

$$\mathbf{p}_3(s) = \left( s \left( \sin \frac{\pi}{9} - \frac{\sqrt{3}}{2} \right) + 2 \cos \frac{\pi}{9} \sin \frac{2\pi}{9}, -\frac{1}{4} \left( s \left( 2 - 4 \cos \frac{\pi}{9} \right) - \csc \frac{\pi}{18} \right) \right), \quad (6.16)$$

with  $q$ ,  $r$ , and  $s \in [-1, 1]$ . We employ these to specify the lattice vectors of the unit cell and positions of the enneagons in it. We eliminate two of the variables ( $r$ ,  $s$ ) in such a

way that different enneagons in the structure (i) have some of their edges and corners touch and (ii) have these edges slide over each other upon varying the third variable ( $q$ ). To that end we introduce the relations

$$\begin{aligned}
T(k, l) = & \frac{\csc \frac{2\pi}{9}}{4 \left( \cos \frac{2\pi}{9} - 1 \right)} \cdot \\
& \left[ \sqrt{3}(k+l) \left( \cos \frac{2\pi}{9} - 1 \right) + 2(k+l) \sin \frac{\pi}{9} \right. \\
& - 8 \sin \frac{\pi}{9} \cos \frac{\pi}{9} - (k+l) \sin \frac{\pi}{9} \cos \frac{2\pi}{9} + (l-k) \sin \frac{2\pi}{9} \\
& + 8 \sin \frac{\pi}{9} \cos \frac{\pi}{9} \cos \frac{2\pi}{9} - 2(l-k) \sin \frac{2\pi}{9} \cos \frac{\pi}{9} \\
& \left. + 8 \sin \frac{2\pi}{9} \cos \frac{\pi}{9} - 8 \sin \frac{2\pi}{9} \cos \frac{\pi}{9} \cos \frac{2\pi}{9} \right]; \tag{6.17}
\end{aligned}$$

$$\begin{aligned}
U(k) = & \left[ \sqrt{3}k + 2 \cos \frac{\pi}{18} - k \cos \frac{\pi}{18} - \sqrt{3}k \cos \frac{\pi}{9} + 2k \cos \frac{\pi}{18} \cos \frac{\pi}{9} \right. \\
& + \sqrt{3}k \sin \frac{\pi}{18} - k \sin \frac{\pi}{9} + 4 \sin \frac{\pi}{18} \cos \frac{\pi}{18} - 2k \sin \frac{\pi}{18} \sin \frac{\pi}{9} \\
& \left. - 4 \sin \frac{2\pi}{9} \cos \frac{\pi}{9} - 8 \sin \frac{\pi}{18} \sin \frac{2\pi}{9} \cos \frac{\pi}{9} \right]; \tag{6.18}
\end{aligned}$$

$$\begin{aligned}
V(k) = & \left[ \sin \frac{\pi}{9} + 2 \sin \frac{\pi}{18} \sin \frac{\pi}{9} - \cos \frac{\pi}{18} \right. \\
& \left. - \sqrt{3} \left( \sin \frac{\pi}{18} + \cos \frac{\pi}{9} \right) + 2 \cos \frac{\pi}{18} \cos \frac{\pi}{9} \right]; \tag{6.19}
\end{aligned}$$

$$W(k) = \frac{U(k)}{V(k)}, \tag{6.20}$$

with  $k$  and  $l \in [-1, 1]$ . Using  $T(k, l)$  and  $W(k)$ , we may write

$$\mathbf{P}_0(k) = (0, 0); \tag{6.21}$$

$$\mathbf{P}_1(k) = \mathbf{p}_2(T(k, W(k))); \tag{6.22}$$

$$\mathbf{V}_0(k) = \mathbf{p}_3(W(k)) + \mathbf{p}_2(T(k, W(k))); \tag{6.23}$$

$$\mathbf{V}_1(k) = \mathbf{p}_1(k) + \mathbf{p}_3(W(k)), \tag{6.24}$$

where the  $\mathbf{P}_i$  ( $i \in \{0, 1\}$ ) give the position of the enneagons in the unit cell ( $N = 2$ ), which has lattice vectors  $\mathbf{V}_j$  ( $j \in \{0, 1\}$ ). The enneagon at  $\mathbf{P}_0$  has the same orientation as the base enneagon defined above and the one at  $\mathbf{P}_1$  is rotated by  $\pi$  with respect to the base enneagon, also see Fig. 6.6a which shows this configuration for the densest-known packing. By determining the value of  $k$ , say  $k^*$ , for which the volume fraction  $F_v$  associated to this structure is maximized,

$$F_v(k) = \frac{18 \sin \frac{\pi}{9} \cos \frac{\pi}{9}}{|\mathbf{V}_{0,x}(k)\mathbf{V}_{1,y}(k) - \mathbf{V}_{0,y}(k)\mathbf{V}_{1,x}(k)|}, \tag{6.25}$$

we obtain the desired crystal. For this structure the following holds

$$k^* = 0.334782056761309\dots, \quad (6.26)$$

$$F_v(k^*) = 0.901030078420934\dots = \phi_{\text{LB}}, \quad (6.27)$$

$$\mathbf{P}_0(k^*) = (0, 0), \quad (6.28)$$

$$\mathbf{P}_1(k^*) = (0.8471436672437109\dots, 1.691664920976177\dots), \quad (6.29)$$

$$\mathbf{V}_0(k^*) = (1.7675368645589482\dots, 3.372726522382239\dots), \quad (6.30)$$

$$\mathbf{V}_1(k^*) = (1.9530111855752121\dots, 0.094167780690677\dots). \quad (6.31)$$

An analytic expression for  $k^*$  can also be derived, but it is too cumbersome (spanning several pages) to reproduce here. Moreover, using the steps outlined above, it should be relatively straightforward to obtain the analytical result. Note that we confirmed that the density of at least one of the packings in Ref. [251] can be improved upon by large scale reorganizations. Also note that this configuration forms a centrosymmetric-dimer lattice.

## 6.6 A Family of Truncated Cubes

In this section we introduce a family of truncated cubes, which interpolates between a cube and an octahedron. We are interested in these systems, because such truncated particles have recently been synthesized [84–86, 93, 94, 247], in particular the entire family can be generated using one silver nanoparticle synthesis [89, 90, 287, 288]. Here, we study the densest regular packing of these truncated cubes and we analyse the dependency of the crystal structure on the level of truncation. We only consider hard particles, but our results may be extended to include soft interactions as explained before. A truncated cube is completely specified by the level of truncation  $s \in [0, 1]$  and the volume of the particle. Its vertices may be written as

$$\{\mathbf{v}(s)\} = \begin{cases} \frac{1}{\left(1 - \frac{4}{3}s^3\right)^{(1/3)}} \mathcal{P}_D \left( \left( \pm \left( \frac{1}{2} - s \right), \pm \frac{1}{2}, \pm \frac{1}{2} \right)^T \right) & s \in \left[0, \frac{1}{2}\right] \\ \frac{1}{\left(\frac{4}{3} - 4\lambda^3\right)^{(1/3)}} \mathcal{P}_D \left( \left( \pm(1 - \lambda), \pm\lambda, 0 \right)^T \right) & \lambda \equiv 1 - s \in \left[0, \frac{1}{2}\right] \end{cases}, \quad (6.32)$$

where  $\mathcal{P}_D$  is a permutation operation that generates all permutations of each element in the sets of 8 and 4 vertices spanned by the  $\pm$ -operations, respectively. All duplicate vertices are removed after letting  $\mathcal{P}_D$  act. The ‘ $T$ ’ indicates transposition. The prefactors ensure that the truncated cubes are normalized to unit volume. Figure 6.7a shows 5 of the shapes that may be obtained by varying  $s$ . Several Platonic and Archimedean solids are members of this family:  $s = 1$  a cube,  $s = (2 - \sqrt{2})/2$  a truncated cube,  $s = 1/2$  a cuboctahedron,  $s = 2/3$  a truncated octahedron, and  $s = 0$  an octahedron.

Using the FBMC technique in combination with a separating-axis-based overlap algorithm, see Chapter 5, we obtained the packing fraction  $\phi$  of the (densest-known) crystal structures as a function of  $s$ . For 1,000 equidistant points in  $s \in [0, 1]$  we prepared systems of truncated particles in a dilute phase, typically with packing fraction  $\phi \approx 0.001$ . We increased the reduced pressure in 100 steps according to a geometric series from  $p = 1$

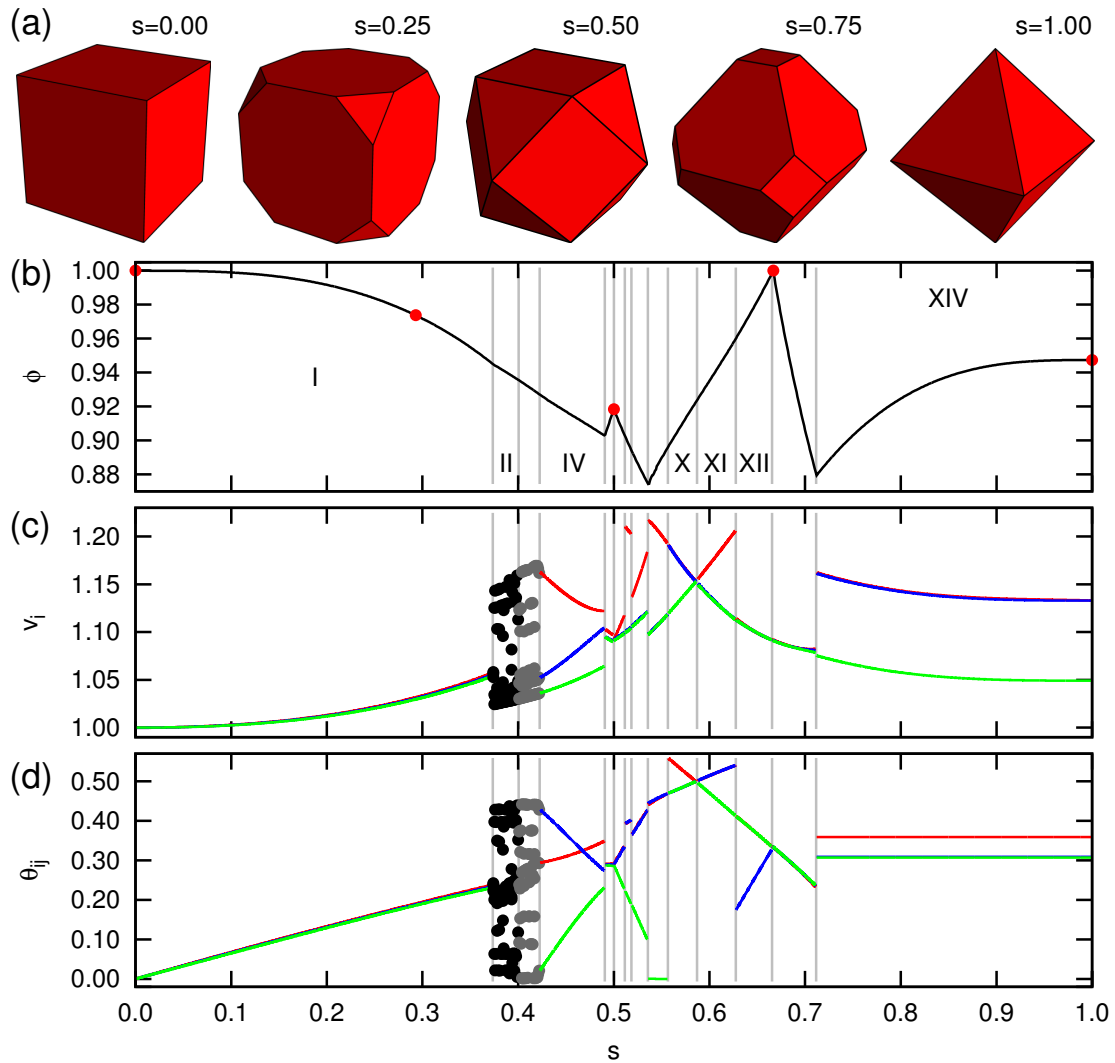


**Figure 6.7:** The denset-packing for a family of truncated cubes, which interpolates between a cube and an octahedron. (a) Visual representations of several members of this family with the corresponding truncation parameter  $s$  listed at the top. (b) The packing fraction  $\phi$  as a function of  $s$  for the denset-known crystal structure. The red dots show the location of several members of the Platonic and Archimedean solids. Grey vertical lines partition the  $s$ -domain into pieces with a ‘different’ crystal structure. Roman numerals are added to some of these areas to identify them; the enumeration is continued from left to right for the regions in which no number could be placed. (c) The length  $v_i$  ( $i = 1, 2$ , and  $3$ ) of the three vectors which span the unit cell, indicated in red, green, and blue. Not every line is clearly visible, since there is some overlap. In the region where the grey and black dots are used (II and III), there appears to be degeneracy in the crystal structures. (d) The cosine of the angles  $\theta_{ij}$  ( $i < j = 1, 2$ , and  $3$ ) between the three vectors that span the unit cell as a function of  $s$ .

to  $p \approx 10^5$  over  $4 \cdot 10^6$  Monte Carlo (MC) cycles in order to compress these systems to a high-density crystalline state. This pressure increase is typically applied a total of 1,000 times for  $N = 1$  particles in the unit cell and for each shape. We restricted ourselves to

$N = 1$  particles in the unit cell, because the truncated cubes are all centrosymmetric. We only considered  $N = 2, \dots, 6$  for 14 conveniently chosen values of  $s$ , located in the centre of the regions indicated in Fig. 6.7, as will be justified shortly. For these  $N > 1$  systems we obtained roughly same value of  $\phi$  and also the same crystal structures. The densest crystal-structure candidate was selected and allowed to compress further for another  $10^6$  MC cycles at  $p = 10^6$  to achieve 5 decimals of precision in  $\phi$ . In practice these final cycles of compression did not improve the packing fraction substantially. Figure 6.7b shows  $\phi$  as a function of  $s$ . Note that the packing fraction ‘curve’ is continuous, but has discontinuities in its first derivative. To double check our result, we considered another set of FBMC runs. We used several of the 1,000 densely-packed crystals as our initial configuration and we varied  $s$  around these points at high pressure to study the evolution of their structure. Steps of  $10^{-5}$  in  $s$  were used and for each step the system is expanded to remove any overlaps, before re-compressing it at  $p \approx 10^5$ . The packing fractions we obtained showed reasonable correspondence with our original result, but this correspondence failed for a transition between two crystal structures. The consecutive method would often become stuck in the lower density structure that corresponded to morphology of the crystal phase it came from.

The unit cell with  $N = 1$  truncated cubes can be specified by three vectors  $\mathbf{v}_i$  ( $i = 1, 2, 3$ ) that are implicitly  $s$  dependent. The structure spanned by these three vectors can also be described by the length  $v_i = |\mathbf{v}_i|$  of the vectors and the angles  $\theta_{ij}$  ( $i < j = 1, 2, 3$ ) between them. Note that we ignore the orientation of the particle with respect to the unit cell here. In order to give an unbiased comparison of the different vectors we used lattice reduction [179] to ensure that for each unit cell the surface to volume ratio is minimal. These results are shown in Fig. 6.7(c,d). By analysing the  $v_i$  and  $\theta_{ij}$ , as well as the location of the kinks in the  $\phi$ -curve, we were able to partition the  $s \in [0, 1]$  domain into 14 distinct pieces. This is the reason behind our choice of 14 verification points for  $N > 1$  simulations. In Figs. 6.8 and 6.9 the crystal structure in the centre of each of these 14 regions is shown. There is a strong difference between the domains  $s < 1/2$  and  $s > 1/2$ . Geometrically the cuboctahedron ( $s = 1/2$ ) is the transition point between shapes which have a more truncated-cube-like nature and shapes which have a more truncated-octahedron-like nature. It is therefore not surprising that the crystal structures in the two regions ( $s < 1/2$  and  $s > 1/2$ ) appear to have a deformed cubic symmetry and a body-centred symmetry, respectively. We illustrate this in Figs. 6.8 and 6.9 where we show the most orthorhombic unit cell:  $N = 1$  for  $s < 1/2$  and  $N = 2$  for  $s > 1/2$ . A more remarkable result is the stability of the Minkowski crystal [289], which is the densest-packed Bravais-lattice structure for octahedra [252], under variations in  $s$ . For all  $s \in [0.71, 1]$  find a Minkowski structure in the dense-packed limit, which can be inferred from the horizontal  $\cos \theta_{ij}$  lines in Fig. 6.7d. The scaled length of the vectors  $v_i \phi^{-1/3}$  is also constant on this domain.

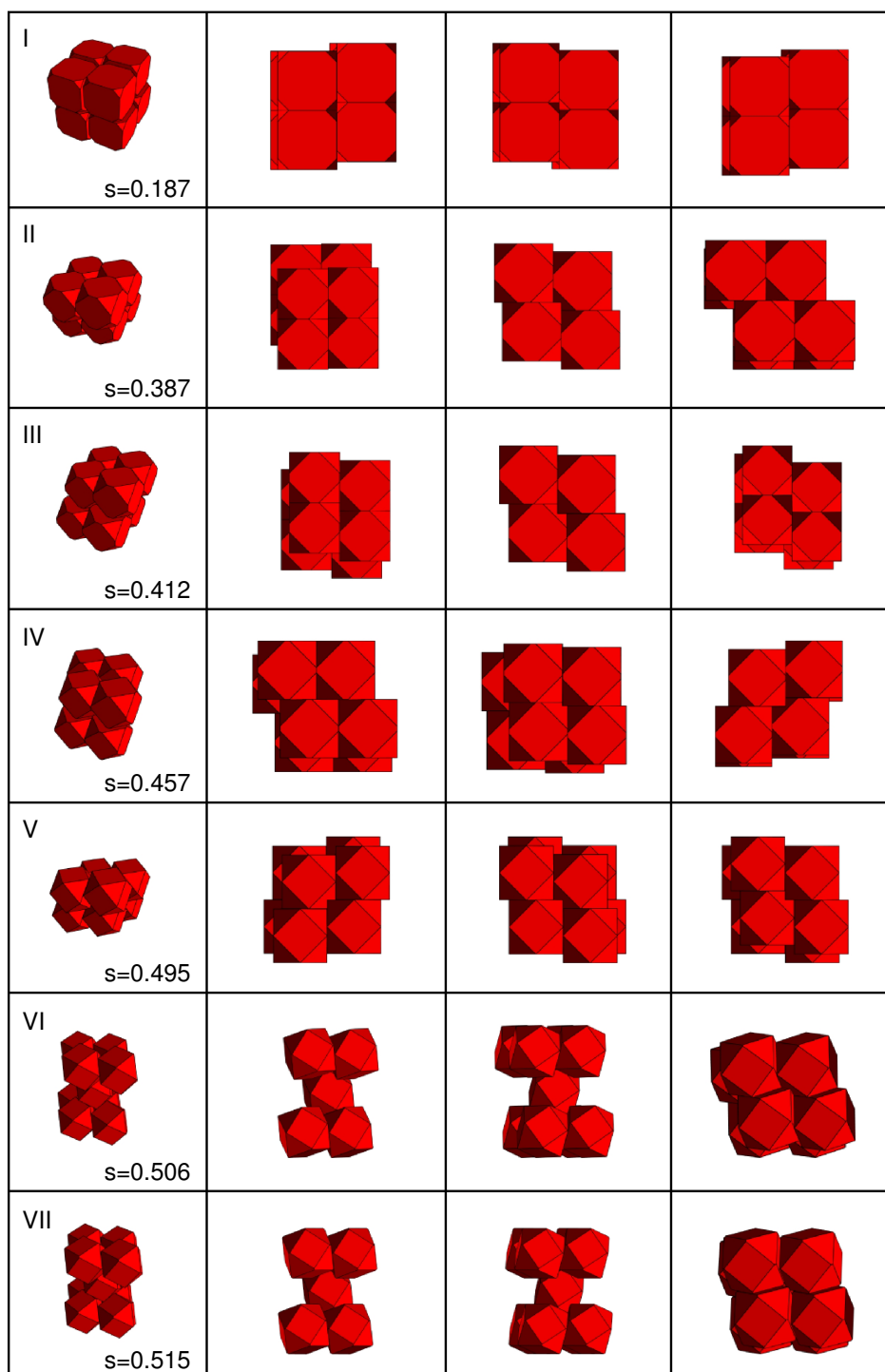


**Figure 6.8:** Visual representations of the crystal structures obtained for the first 7 regions in Fig. 6.7. From left to right each entry (row) contains a bird's eye view, the front view, the side view, and the top view of this structure. The Roman numeral in the top-left corner gives the relevant domain in Fig. 6.7. The truncation parameter  $s$  for these structures is given in the bottom-right corner.

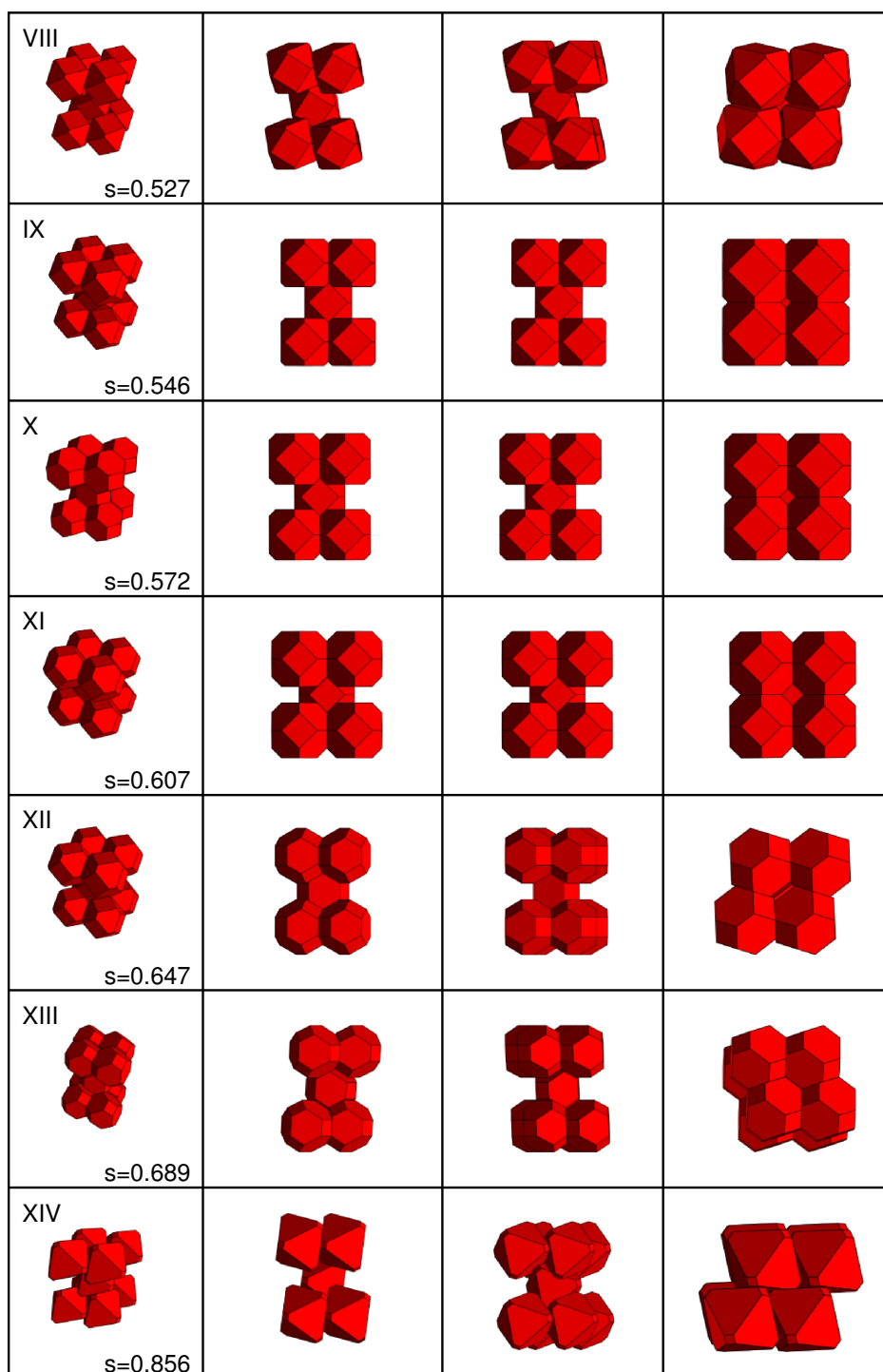


**Figure 6.9:** Visual representations of the crystal structures obtained for the last 7 regions in Fig. 6.7. From left to right each entry (row) contains a bird's eye view, the front view, the side view, and the top view of this structure. The Roman numeral in the top-left corner gives the relevant domain in Fig. 6.7. The truncation parameter  $s$  for these structures is given in the bottom-right corner.

Let us now examine the crystal structures in the 14 regions identified by the discontinuities in the vectors of the unit cell. In literature it has become commonplace to assign atomic equivalents to structures observed in simulations or experiments. For example, this was done for binary mixtures of spheres [74, 75], a family of truncated tetrahedra [260], several faceted particles [174], and systems of nanoparticles [40, 49]. We attempted to follow suit by determining the symmetry group of the structures in 6.8 and 6.9 using *FindSym* [270] and by subsequently assigning an atomic equivalent [272]. However, we found that a description in terms of atomic equivalents inadequately captures the richness in crystal structure, since particle orientation is not taken into account. Moreover, for many of our structures we were unable to determine a nontrivial space group using *FindSym*. We therefore resorted to visual analysis and we used this to group the 14 regions in Fig. 6.7 based on similarities between the respective structures.

- **I** In this region ( $s \in [0.00, 0.37]$ ) we obtained a continuous and uniform distortion of the simple cubic structure for cubes. For  $s = 0$  the particles form a simple cubic (sc) crystal, which has the same morphology as  $\alpha\text{Po}$  ( $\alpha$ -Polonium) [272]. The uniformly distorted simple cubic (udsc) structure we found for  $s > 0$  is similar to that of  $\beta\text{Po}$  [272]. We verified this distorted quality for values as low as  $s = 10^{-5}$ .
- **II & III** For these two regions ( $s \in [0.37, 0.40]$  and  $s \in [0.40, 0.42]$ ) we found that there is a degeneracy in the crystal-structure candidates that achieve the densest-known packing. Although certain structures appear favoured over others, there is no clear relation between  $\phi$  and  $s$ . The observed degeneracy can be explained by considering Fig. 6.10, which shows one of the crystal structures in region II. The truncated cubes arrange in a distorted simple cubic lattice, where the particles form columns. These columns are interlocked in a diagonal way, see Fig. 6.10(c,e), which fixes the structure in two directions, but leaves freedom of motion in the third. There appears to be a continuous degeneracy between systems where sheets consisting of diagonally-interlocked columns slide up or down (in the direction of the columns) with respect to each other. This degeneracy may prove to strongly influence the phase behaviour at intermediate to high pressures. We refer to these structures as mono-interlocking distorted simple cubic (mi-dsc) crystals.
- **IV** For this region ( $s \in [0.42, 0.49]$ ) we find a distorted simple cubic (dsc) phase that is interlocking in two directions: a bi-interlocking dsc (bi-dsc) phase. For each instance of interlocking two degrees of translational motion are frozen out. This implies that the bi-dsc structure is completely fixed, which is confirmed by the unicity of the  $v_i$  and  $\theta_{ij}$  results in Fig. 6.7(c,d).
- **V** In this region ( $s \in [0.49, 0.50]$ ) we observed a tri-interlocking dsc (ti-dsc) phase. At the time of this writing it is unclear whether the transition between the various interlocking (mi-, bi-, and ti-) dsc phases is continuous or not. The discontinuities in the parameters  $\phi$ ,  $v_i$  and  $\theta_{ij}$  as a function of  $s$  appear to imply that it is not.
- **VI - VIII** Here ( $s \in [0.50, 0.51]$ ,  $[0.51, 0.52]$ , and  $[0.52, 0.54]$ ) we found structures that are best described by a distorted body-centred tetragonal (dbct) structure. The truncated cubes in these crystals are not aligned with the axes of the unit cell.

It is unclear to what extent structures in regions VI, VII, and VIII are the same. The smooth flow of the  $\phi$ -curve (Fig. 6.7b) appears to imply continuity, but the jumps in the values of  $v_i$  and  $\theta_{ij}$  [Fig. 6.7(c,d)] suggest otherwise.

- **IX - XI** These structures ( $s \in [0.54, 0.56]$ ,  $[0.56, 0.59]$ , and  $[0.59, 0.63]$ ) have a body-centred tetragonal (bct) morphology, for which the particles are aligned with the lattice vectors of the unit cell. It is surprising that the structures in region XII exhibit a dbct morphology, since regions IX - XII share the same smooth piece of  $\phi$ -curve, see Fig. 6.7b. This leads us to conclude that a smooth dependence of  $\phi$  on  $s$  is *not* indicative of uniformity in crystal structure. The strong similarity between the crystal structures in regions IX - XI and the apparent smooth transition between structures from region IX to X and from X to XI, also leads us to conclude that discontinuities in the properties of unit cell are not indicative of discontinuities in the properties of the crystal structure.
- **XII & XIII** These two dbct structures ( $s \in [0.63, 0.67]$  and  $s \in [0.67, 0.71]$ ) are different from the dbct structures in regions VI - VIII, since the particles appear to be aligned with the lattice vectors of the unit cell. Moreover, crystals in region XIII are unusual, since there are large ‘voids’ in the structure. That is, for all other structures we found that the largest facets of a particle are always in contact with a facet of another particle. This is not the case in region XIII, because there is a substantial gap between some of the hexagonal facets.
- **XIV** The Minkowski crystal of region XIV ( $s \in [0.71, 1.00]$ ) is also peculiar. It is the only structure which does not undergo some form of reorganization upon varying the level of truncation. It is worthwhile to study the origin of this apparent stability, which sharply contrasts with the immediate distortion found around  $s = 0$ . However, this goes beyond the scope of the current investigation.

Summarizing, we studied the densest-known packings for a family of truncated cubes, which interpolates between a cube and an octahedron. Even for such a simple system there is a wealth of different structures, with interesting properties, that can be achieved by varying only one parameter. The dense-packed crystal structures that we found may be used to determine the crystal branch of the equation of state, which in turn can be used to establish the phase diagram for this family of truncated cubes, in analogy to the work of Refs. [171, 260]. Such a phase diagram [290] will lead to better understanding of experimental systems [287] and the way in which the phase behaviour of cubes is influenced by slight shape changes. The latter is of particular fundamental importance since it was recently shown that for hard cubes there is an unusually high vacancy concentration at coexistence pressures [291], and questions have been raised to what extent this high vacancy concentration is present for almost cubic shapes [263, 292]. Our truncated cube model has the advantage that levels of truncation very close to  $s = 0$  may be studied with relative ease, whereas other models, e.g., the superball model [168, 170, 171], suffer from numerical problems in the convergence of the overlap algorithm close to the cube limit.

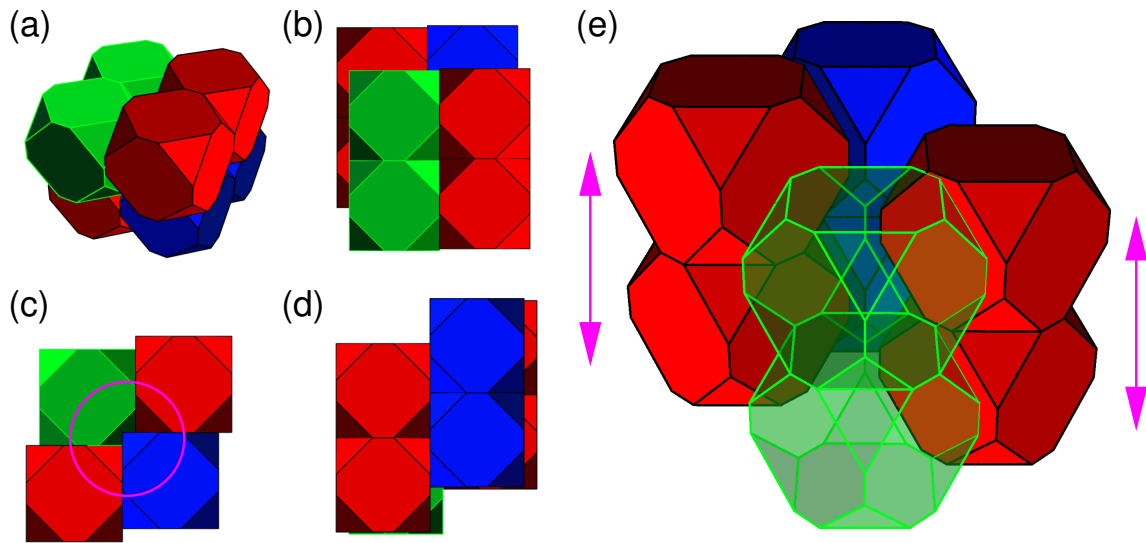


**Figure 6.10:** A visual representation of the crystal structure degeneracy that occurs in regions II and III of Fig. 6.7. Here we take a structure from region II, also see Fig. 6.8, and colour coded pairs of truncated cubes, for which the octahedral faces are aligned. (a-d) The viewpoints of Fig. 6.8. In (c) we use a magenta circle to indicate that the blue column is interlocking with the green column in a diagonal way. This property, together with the dense-packing condition prevents lateral motion in the plane normal to the column's direction. (e) The two red columns are *not* interlocking with the blue and green column, allowing for freedom of motion in the direction of the magenta arrows. The green column has been made translucent to better illustrate the properties of this crystal structure.

## 6.7 The Phase Behaviour of Hard Octahedra

In this paragraph we discuss the way in which a phase diagram can be determined using our results. We confine ourselves to a system of hard octahedra ( $s = 1$ ) and we focus on determining the equation of state (EOS) and analysing the phase behaviour. The EOS gives pressure as a function of the density of the system, or equivalently the reduced pressure  $p = PV_M/k_B T$  as a function the packing fraction  $\phi$ . We only briefly comment on the free-energy calculation required to establish the coexistence densities, since we were only indirectly involved with this part of the research.

We determined the EOS using isothermal-isobaric ( $NPT$ ) Monte Carlo (MC) simulations and system sizes of 1,458 octahedra, see Fig. 6.11a. The liquid branch of the EOS was established using a cubic-box simulation, which is allowed since there is no long-range order in the liquid phase. We considered  $p \in [0.5, 13.5]$  with equidistant steps of 0.5, using  $0.5 \cdot 10^6$  MC cycles of equilibration and  $1.5 \cdot 10^6$  MC cycles of production to obtain 2 decimals of precision in  $\phi$ . We did not observe crystallization from the fluid phase upon increasing the pressure. This can be explained by the fact that the Minkowski crystal does not fit in a cubic box. Even in variable-box-shape simulations, for which the box vectors change freely and independently of each other to accommodate noncubic crystal

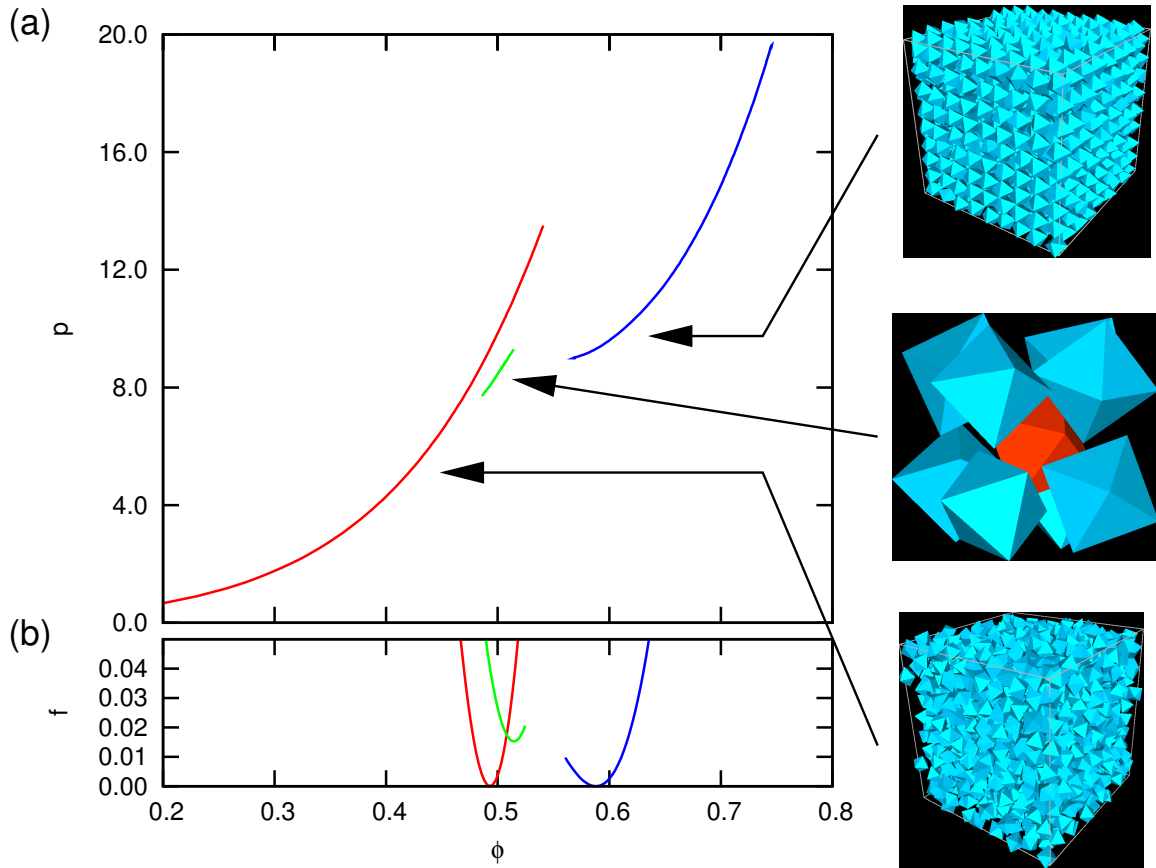


**Figure 6.11:** The equation of state (EOS) and free energy of the phases obtained for a system of hard octahedra. (a) The reduced pressure  $p = PV_M/k_B T$  as a function of the packing fraction  $\phi$ . The liquid branch is indicated in red, the body-centred cubic (bcc) rotator (plastic crystal) phase is indicated in green, and the Minkowski crystal phase is indicated in blue. The nature of these phases is illustrated by the insets which show snapshots of the simulation box in the liquid and crystal branch for the values of  $\phi$  indicated by the arrows. The bcc nature of the rotator phase is visualized by showing a part of the simulation box that contains one unit cell. The central particle is coloured red and the surrounding 8 octahedra are shown in blue. (b) The reduced and scaled free energy  $f$ , defined in Eq. (6.33), for the three phases as determined in Ref. [171] using the above equation of state. There is coexistence between the liquid and crystal phases: the  $f$ -axis acts as a common tangent. The plastic crystal is metastable with respect to these two phases since its free energy is greater than zero for all values of  $\phi$ .

structures, we did not observe crystallization. Our systems were probably too small to find liquid-crystal phase coexistence or nucleation of the crystal from the liquid.

The crystal branch of the EOS for this system was obtained by melting the Minkowski crystal. We arranged the 1,458 particles in the simulation box in the body-centred manner indicated in Fig. 6.9 (region XIV). This body-centred construction ensured that the simulation box is as orthorhombic as possible in order to minimize finite-size effects. Such finite-size effects are more pronounced for the  $N = 1$  Minkowski structure, since the corresponding simulation box is far more distorted. We were able to determine the crystal

branch of the EOS with a precision of at least two decimals in  $\phi$ , by employing an equilibration of  $0.9 \cdot 10^6$  cycles and a production of  $2.0 \cdot 10^6$  cycles, for  $p \in [9, 19.5]$  with steps of 0.05 for  $p < 9.5$  and steps of 0.25 otherwise. We used variable-box-shape *NPT* MC simulations to allow for a full exploration of phase space. For pressures  $p \lesssim 9$  we observed that the crystal phase melted into a plastic crystal (rotator) phase that has a body-centred cubic (bcc) structure, as can be seen in Fig. 6.11a. Our result [171] constitutes the first time that such a structure was reported for a system of hard particles.

We determined the rotator branch of the EOS by using the same number of equilibration and production cycles as for the crystal phase to achieve  $\phi$ -values with two or more decimals of precision. We studied  $p \in [7.7, 9.3]$  with a distance between  $p$  points of roughly 0.05 to map out the full rotator phase, including the part where there is hysteresis with respect to the crystal branch. Because of the bcc morphology of the rotator phase, regular *NPT* cubic-box simulations could be performed. The advantage of these simulations is that they are computationally faster than the variable-box-shape simulations and that they preserve the bcc structure more easily. Variable-box-shape simulations were used at several pressures to confirm that the morphology of the rotator phase is indeed bcc throughout. At high pressure ( $p \approx 11$ ) variable-box-shape simulations showed crystallization from the rotator phase into the Minkowski crystal. Note that the rotator phase has a very liquid-like pressure-density dependence, see Fig. 6.11a. This, to the best of our knowledge, has not been observed for any other plastic crystal. The cause of this liquid-like behaviour remains to be clarified.

The fact that no crystallization into the bcc rotator phase was observed from the liquid branch upon increasing the pressure, as well as the fact that the crystal branch always appears to melt into the rotator phase upon decreasing the pressure, raised questions with regards to the stability of this phase. These questions were addressed by determining the free energy. To that end the method of Widom-insertion [253] combined with thermodynamic integration [253] was applied to determine the free energy  $F$  as a function of  $\phi$  in the liquid branch [171]. For the crystal and rotator phase Einstein-integration [253] and the procedure of Ref. [293], to take the rotational degrees of freedom into account, were employed.

In order to perform an Einstein integration a suitable Einstein crystal is required. We therefore studied the  $\phi$ -dependence of the morphology of the crystal structure, by performing variable-box-shape *NPT* simulations to average the box vectors for 7 pressures in the crystal phase. We used  $1.0 \cdot 10^6$  cycles of equilibration and  $2.5 \cdot 10^6$  cycles of production for a box containing 512 particles in the  $N = 1$  representation of the Minkowski crystal to accomplish this. The properties of the averaged unit cell, which can be determined from the averaged box vectors, are shown in Fig. 6.12. The system accommodates for lower pressures by uniform scaling of the Minkowski lattice vectors only. Within the numerical uncertainty of our result, we did not observe a continuous deformation from the Minkowski crystal to the lattice of the bcc rotator phase. We also confirmed, as we will discuss shortly, that the average position and orientation of the particles is same as that of the densely-packed Minkowski crystal.

Our result allowed us to use a scaled Minkowski crystal as the Einstein crystal for the free-energy calculation. A similar approach was followed for the bcc rotator phase. Using the free energies we were able to construct a common tangent between the liquid

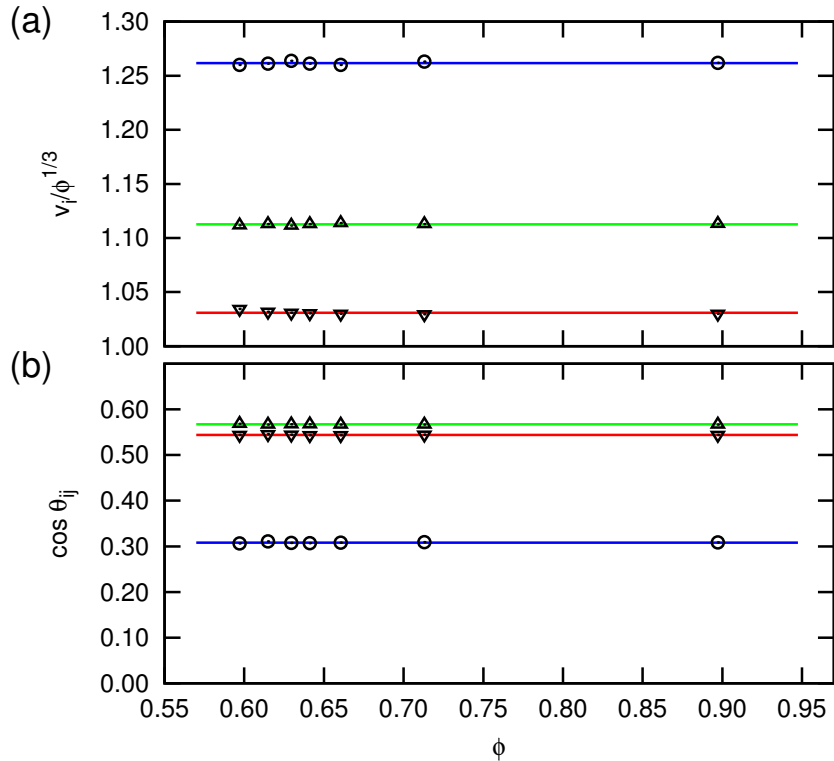


**Figure 6.12:** The dependence of the morphology of the crystal phase on the packing fraction  $\phi$  for hard octahedra. (a) The length  $v_i$  ( $i = 1, 2, 3$ ) of the three vectors that span the unit cell, which is scaled according to the volume fraction of the system. The points for which we determined the structure are indicated by the symbols and a horizontal line is fitted through these points. The lines are drawn from  $\phi \approx 0.57$  to  $\phi = 18/19$  the minimum and maximum packing fractions for the crystal phase of octahedra, respectively. (b) The cosine of the angles  $\theta_{ij}$  ( $i < j = 1, 2,$  and  $3$ ) between the three vectors that span the unit cell as a function of  $\phi$ . Again a horizontal line may be fitted to this data. These results show that the Minkowski crystal structure is preserved along the entire crystal branch.

and crystal branch and establish the phase-coexistence region. Figure 6.11b shows this common tangent. Here we introduced a scaled and reduced free energy

$$f = \frac{1}{k_B T} \left( \frac{F}{V} - V_M \phi \mu_c + P_c \right), \quad (6.33)$$

with  $F/V$  the free energy per unit of volume for the system,  $V_M$  the volume of the particle, and  $\mu_c$  and  $P_c$  the chemical potential and pressure at bulk coexistence, respectively. This scaling ensures that the common tangent between two coexisting phases is given by the line  $f = 0$ . The coexistence packing fractions are  $\phi = 0.492\dots$  and  $\phi = 0.588\dots$  for the liquid and crystal, respectively. The representation in Fig. 6.11b also allows us to visually indicate that the rotator phase is metastable with respect to the liquid and crystal phases. Its  $f$ -curve assumes its minimum for  $f \approx 0.015 > 0$ . The free energy difference per particle at the bulk coexistence pressure is however very small ( $F/N \approx 10^{-2}$ ). This may explain

why we always observed a two-stage melting from the crystal to the liquid via the rotator phase.

Let us return to the averaging of the particle coordinates. We performed regular *NVT* simulations to determine the average position and orientation for the 512 particles in the box. The volume in the *NVT* simulations is based on the pressures studied before. We again used  $1.0 \cdot 10^6$  cycles of equilibration and  $2.5 \cdot 10^6$  cycles of production. This allowed us to confirm that the particles indeed obeyed the Minkowski crystal structure with only a uniformly increased lattice spacing, i.e., the crystal fits nicely the simulation box. The results of the orientational averaging are, however, more interesting. Here we used the following strategy for averaging. The vectors which describe the orientation can be mapped on a unit sphere. For each particle, we added all sampled unit vectors, divided the resulting sum vector by number of sampling moments, and renormalized this result to obtain the averaged orientation vector. It can be shown that this way of averaging is acceptable for vectors that are confined to the unit sphere, when there is a small spread (solid angle) in the vectors being averaged [294, 295]. If this is not the case, the proper way to average is according to the Frobenius norm [294], which is algorithmically more complicated to implement.

For a system with sufficiently limited movement ( $\phi = 0.71$ ) this averaging method gives good results and reveals the cubic nature of the particle's rotational symmetry group, see Fig. 6.13(a,b). At low pressures our method breaks down. Figure 6.13(c,d) shows the distribution of the 512 averaged orientations for a packing fraction of  $\phi = 0.64$ . We obtained 6 circles that intersect in the 8 orientational points associated to the Minkowski structure. This result can be explained as follows. The particle orientations are the same as those of the Minkowski crystal, but the particles can flip between equivalent orientations in the octahedron's rotational symmetry group for  $\phi = 0.64$ . Because we initially did not consider averaging the orientations modulo the octahedron's symmetry group, we obtained averaged vectors that are 'in between' the orientation the particle was in before flipping and the orientation it has flipped to. Only 6 circles are formed, which implies that the flipping of the particles obeys certain rules, the points outside of the circles we account to multiple flips. We found that a particle only flips to one of the 3 closest equivalent orientations, i.e., it only rotates by an angle  $\pi/2$ . Further analysis of our results also revealed that this flipping only occurs in pairs: when one particle flips its orientation, one of its neighbours flips at the same time.

At even lower pressures, see Fig. 6.13(e,f) for results at a packing fraction of  $\phi = 0.61$ , the occurrence of flipping becomes more frequent, since there are far more point on the circles and we kept the number of production cycles and the number of particles the same. Also multi-flips begin to become more prevalent throughout the system. This flipping is likely a precursor to the full rotational freedom in the bcc plastic-crystal phase. We confirmed that, when we average the orientation modulo the octahedron's symmetry group, we retrieve the expected Minkowski-crystal orientations for the seven packing fraction we considered. Only the deviation from this average orientation increased with decreasing  $\phi$ .

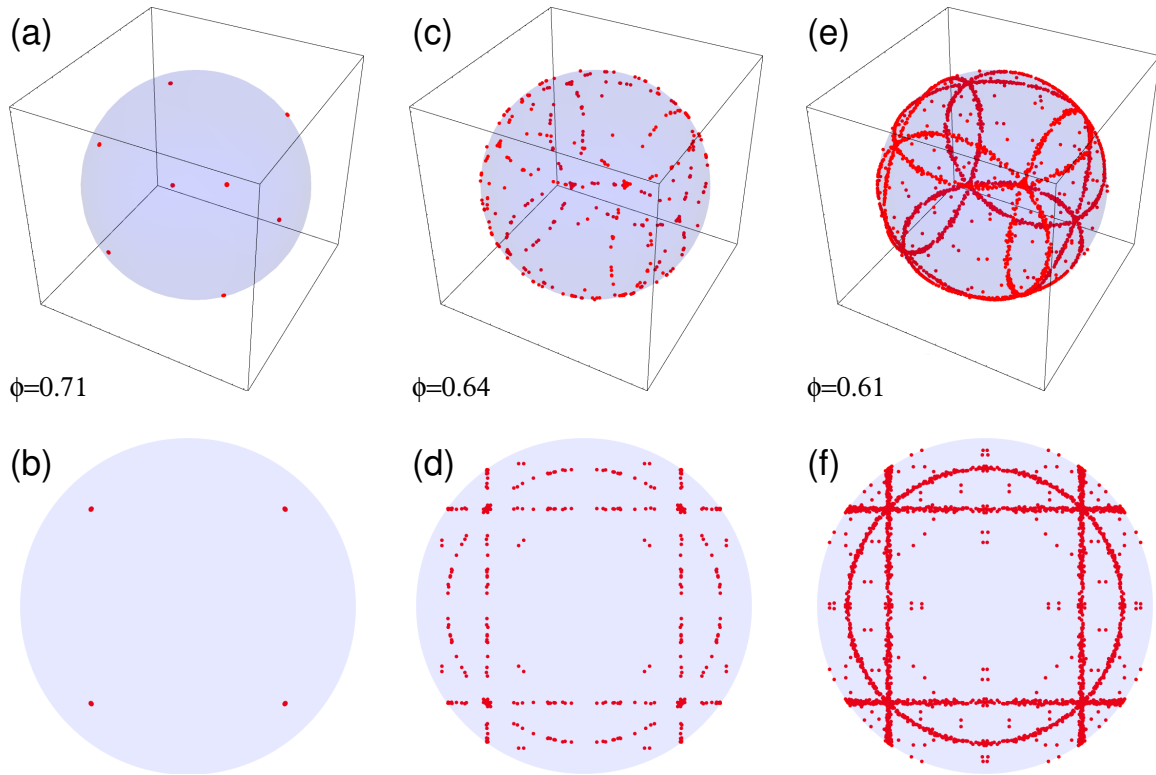


**Figure 6.13:** The distribution of the (incorrectly) averaged orientation vectors in the crystal phase. Any orientation is described by eight (equivalent) points on the unit sphere, which map out the rotational symmetry group of the octahedron. That is to say, there are eight rotations which take the octahedron into itself. (a) For  $\phi = 0.71$  all particles have the same average orientation - only 8 groups of points can be seen - as indicated by red points in a bird's eye view. (b) A side view which shows that the clusters are only slightly ellipsoidal, indicative of a small orientational spread. (c,d) For  $\phi = 0.64$  our averaging leads to a distribution which is confined to 6 circles that intersect in the original 8 points corresponding to the orientation in the densest-packed crystal. This behaviour becomes more pronounced with decreasing  $\phi$  as is illustrated by (e,f) for  $\phi = 0.61$ .

## 6.8 Conclusion and Outlook

We employed the combination of the floppy-box Monte Carlo (FBMC) technique and a triangular-tessellation-based overlap algorithm introduced in Chapter 5 to determine dense regular packings of irregular, nonconvex, and punctured objects. By establishing high-density crystal structures for 142 convex and 17 nonconvex shapes, we managed to improve upon the literature value for the packing fraction of a huge number of solids. We also confirmed and extended upon existing conjectures for the densest packing of convex solids. Using our numerical technique we discovered the densest-packed configurations for rhombicuboctahedra and rhombic enneacontrahedra. The analytic construction, by which we prove that the observed configurations indeed pack densest, constitutes a remarkable result, because it has historically [186] been exceedingly difficult to verify that a given arrangement of objects is the densest possible packing. Moreover, our result allows for

the construction of two new upper bounds to the packing fraction of the densest configuration of any shape. Finally, we discovered denser packings of enneagons and truncated tetrahedra, for which the particles form centrosymmetric-dimers.

In this chapter we also studied a family of truncated cubes, which interpolates between a cube and an octahedron. These truncated cubes have recently been synthesized [89, 90, 287, 288] and we believe that our results may be recovered in experimental systems. A wealth of different structures is achieved for this simple system by varying only one parameter, namely the level of truncation. We found that the members of this family can be grouped according to the crystal structure they form at high pressure. There are particles that formed a (distorted) simple cubic structure and there are particles that formed a structure with a (distorted) body-centred tetragonal morphology. Some of the crystals we obtained possess unusual properties. For instance, the Minkowski crystal, which is associated with the densest packing of octahedra, appeared to be very stable with respect to truncation. There are also levels of truncation for which the crystals showed degeneracies in their structure. Such degeneracies may be important to the formation of three-dimensional materials with two dimensional order.

To further illustrate the usefulness of our methods to condensed-matter research we also determined the phase diagram for hard octahedra. We observed three phases for these particles: a liquid, a body-centred cubic (bcc) plastic crystal, and a Minkowski crystal. Our result constitutes the first time that a bcc plastic crystal (rotator phase) was reported for a system of hard particles. Using free-energy calculations [171] it was shown that the rotator phase is metastable with respect to the coexistence between the liquid and crystal phases. In analysing the phase behaviour of hard octahedra we took a first step towards understanding the behaviour of similarly-shaped nanoparticles [89, 90, 247, 287, 288], for which the behaviour is typically also governed by short- and/or long-ranged interactions.

We showed that the methods introduced in Chapter 5 can be used to study previously inaccessible nanoparticle and colloid systems over a range of pressures and volume fractions. Our triangular-tessellation approach allowed us to approximate the shape of such particles with greater precision and the FBMC technique's ability to predict crystal-structure candidates is of paramount importance to establishing their phase behaviour. Moreover, we showed the potential of our methods to aid in the analysis of complex mathematical problems concerning the packing of shapes. This investigation therefore marks the starting point of a far more extensive investigation of complex shape-anisotropic objects than was previously considered feasible.

## 6.9 Acknowledgements

It is a pleasure to thank Anjan Gantapara for the fruitful collaboration on the truncated-cube project, his hard work and in particular his free-energy calculations have been instrumental in obtaining the results presented for octahedra. I would also like to thank Ran Ni for useful discussions on the results obtained for the family of truncated cubes and the phase behaviour of octahedra.



---

## Hierarchical Self-Assembly of Octapod-Shaped Nanoparticles

---

In this chapter we analyse the recently observed hierarchical self-assembly of octapod-shaped nanocrystals (octapods) into three-dimensional superstructures [K. Miszta *et al.*, *Nature Materials* **10**, 872 (2011)], using the methods developed in Chapters 5 and 6. We devise a simulation model with simple empirical interaction potentials that is capable of reproducing the initial chain-formation step of the self-assembly. A Hamaker-de-Boer-type integration is used to obtain the van-der-Waals interactions between octapods dispersed in a liquid and justifies elements of our empirical model. The theoretical calculation, together with the experimental and simulation results, allows us to formulate a mechanism that explains the observed self-assembly in terms of the solvent-dependence and directionality of the octapod-octapod interactions. Our approach shows the great potential of our approach to study self-assembly in other experimental systems containing anisotropic nanoparticles.

## 7.1 Introduction

Over the past few years significant progress has been made in the ability to realize self-assembly of man-made nanoscale units into macroscopic superstructures [32, 34–54, 60, 61]. The quest to control this process is inspired by the richness in structure that self-organization brings about in nature [57, 58]. A limited number of (relatively simple) building blocks can lead to a spectacular variety in the materials that are formed by the numerous ways in which these building blocks self-assemble in a hierarchical way [55, 56, 59, 62, 63]. Unfortunately, man-made self-assembled structures consisting of inorganic nanocrystals are still at an elementary level. This is due to limited control over the fabrication of these nanocrystals, specifically with regard to the complexity of the shapes and interaction potentials with which we are currently able to endow these building blocks.

Recently, the hierarchical self-assembly of complex inorganic nanocrystals (octapods) into high-quality macroscopic objects was observed [54]. Octapods [54, 78, 99] are branched colloidal nanocrystals consisting of a CdSe octahedral core, on which eight CdS pods are grown. These particles were found to self-assemble into interlocking chains in the apolar solvent toluene. Such chains could subsequently self-assemble into a 3D superstructure by the addition of the polar solvent acetonitrile. This remarkable result was made possible by an improved control over the synthesis of the octapods, which resulted in samples that were sufficiently monodisperse in size and shape to conduct self-assembly studies on [54]. It was shown that obtaining large structures comprised of complex inorganic building blocks, which are of interest to, for instance, the semi-conductor industry, is possible.

In this chapter we focus our theoretical and simulation study on the observed hierarchical self-assembly of octapods. In Section 7.2 we describe the experimental investigation performed in the group of Prof. dr. Liberato Manna to put our contribution into context. In Section 7.3 we consider simulations using a simple empirical model for the octapod-octapod interactions in toluene, by which we are able to reproduce the initial interlocking-chain formation step of the hierarchical self-assembly. In Section 7.4 we introduce a theoretical model for the van-der-Waals (vdW) interactions between octapods suspended in a liquid and we discuss its consequences. The vdW forces that we obtain give insight into the solvent-dependent nature of the hierarchical mechanism, as well as the directionality observed in the interlocking-chain formation step and the subsequent aggregation of these chains into the 3D superstructures. Finally, in Section 7.5 we combine the simulation, theoretical, and experimental results and propose a model which we believe to explain the observed self-assembly.

## 7.2 Experimental Results

In this section we discuss the experimental findings for the behaviour of octapods dispersed in an (a)polar liquid, see Ref. [54] for more information. We focus only on the elements relevant to the simulation and theoretical studies in the following sections. The Manna group recently developed a synthesis technique to create octapod-shaped nanocrystals, in which eight CdS ‘pods’ are grown from a central region made of CdSe [54, 78, 99], with unprecedented shape homogeneity and monodispersity. Figure 7.1a shows a 3D tomo-

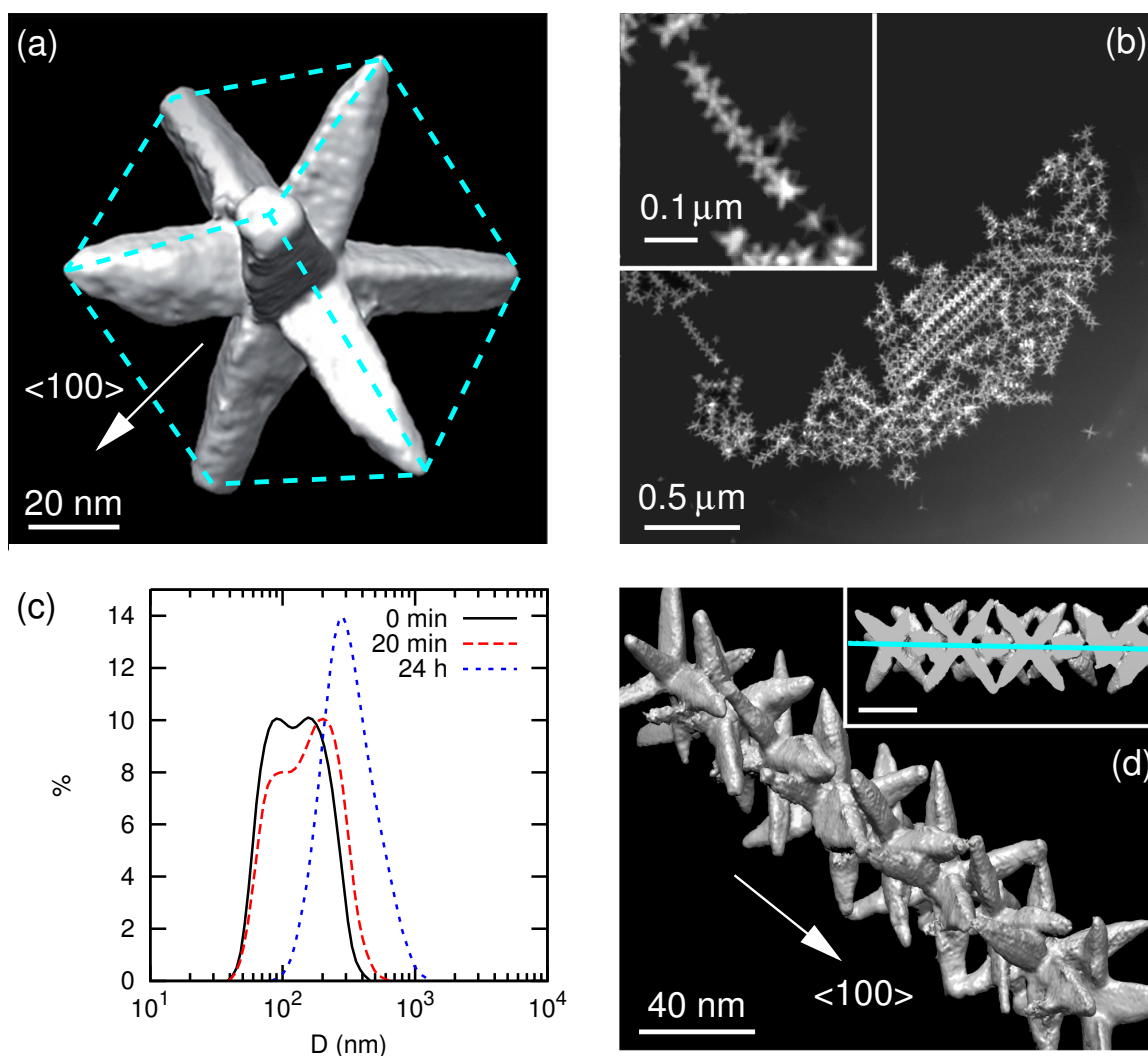


**Figure 7.1:** (a) Three-dimensional (3D) tomographical reconstruction of a single eight-fold branched nanocrystal (octapod) used in the self-assembly experiments of Ref. [54]. The dashed lines show the cubic nature of the particle's symmetry group. (b) An STEM image of the vitrified dispersion reveals the presence of chains of octapods after 24 hours of ageing, which are approximately  $4 \mu\text{m}$  in length. The inset shows a magnified view of a single chain. (c) Curves obtained by DLS give the cluster-size distribution at different ageing times. Here  $D$  is the size of the aggregates and the vertical axis gives the percentage frequency (%). The DLS measurements show a time-dependent evolution of the cluster size and confirm the formation of aggregates. (d) A single chain of octapods reconstructed by performing a 3D tomographical analysis on a sample similar to that in (b). From this reconstruction the interlocking nature of the chain becomes clear. The octapods are properly aligned on the chain axis. This is illustrated by the cut-through in the inset, where the cyan line indicates the axis.

graphical reconstruction of one of these so-called octapods. The octapods were coated with hydrophobic surfactant molecules and therefore they favourably interacted with hydrophobic solvents, i.e., apolar or moderately polar solvents. When the octapods were suspended in chloroform they remained stable and separated in solution, as confirmed in Ref. [54] by both Dynamic Light Scattering (DLS) and cryo-Scanning Transmission Electron Microscopy (cryo-STEM). For octapods dissolved in toluene, slow aggregation on a time scale of a few hours was observed. This aggregation could be followed by DLS (Fig. 7.1c) and by cryo-STEM, see Fig. 7.1b, which shows an image of an aliquot taken after 24 hours of ageing. Most of the octapods had arranged into chain-like structures and only a few isolated particles remained. Further investigation using STEM and tomographical reconstruction revealed that the octapods in the chains are ‘interlocking’ with their neighbours (Fig. 7.1d and inset). No other types of chains or structures were found in toluene. Henceforth, we shall refer to these chains as *interlocking chains*.

The addition of the highly polar acetonitrile to a chloroform-based suspension of octapods or a freshly prepared toluene-based suspension led to rapid precipitation, resulting in disordered aggregates of octapods. A different type of precipitate was formed when acetonitrile was added to an aged suspension of octapods in toluene. This suspension had been sufficiently aged to allow almost all octapods to assemble into interlocking chains. The precipitate obtained by the addition of acetonitrile to this suspension consisted of micron-sized 3D superstructures of octapods, together with a fraction of isolated linear chains (Fig. 7.2a). The fraction of chains consisted of longer and straighter chains than those observed in pure toluene, suggesting that they were stiffer [54]. The morphology and internal structure of the ordered 3D clusters led us to conclude that they had formed by aggregation of the linear chains rather than via clustering of individual octapods. This was further confirmed by the fact that occasionally entire chains of octapods were missing (Fig. 7.2b). Moreover, the nearest-neighbour configuration along one of the principal directions of the crystal had the interlocking property of the chains (Fig. 7.2c). The structure could be described by a tetragonal unit cell, with the  $c$ -direction parallel to the chain axis (Fig. 7.2d). Note that the arms of two neighbouring octapods in adjacent chains were in close contact, we refer to this as the *pod-pod* configuration.

## 7.3 Monte Carlo Simulations of Octapods

In this section we consider the simulations that we performed to gain an understanding of the experimental results. We refer the reader to Chapter 5 for a more detailed explanation of some of the techniques that we used: floppy-box Monte Carlo (FBMC) simulations [75, 249], isothermal-isobaric ( $NPT$ ) Monte Carlo (MC) simulations, and isothermal-isochoric ( $NVT$ ) MC simulations.

### 7.3.1 Hard Octapods

We first considered a hard-particle model (Fig. 7.3a) in order to verify that interlocking chains and superstructures do not form by excluded-volume interactions only. This also allowed us to test the speed and efficiency of the various simulations. We based the shape



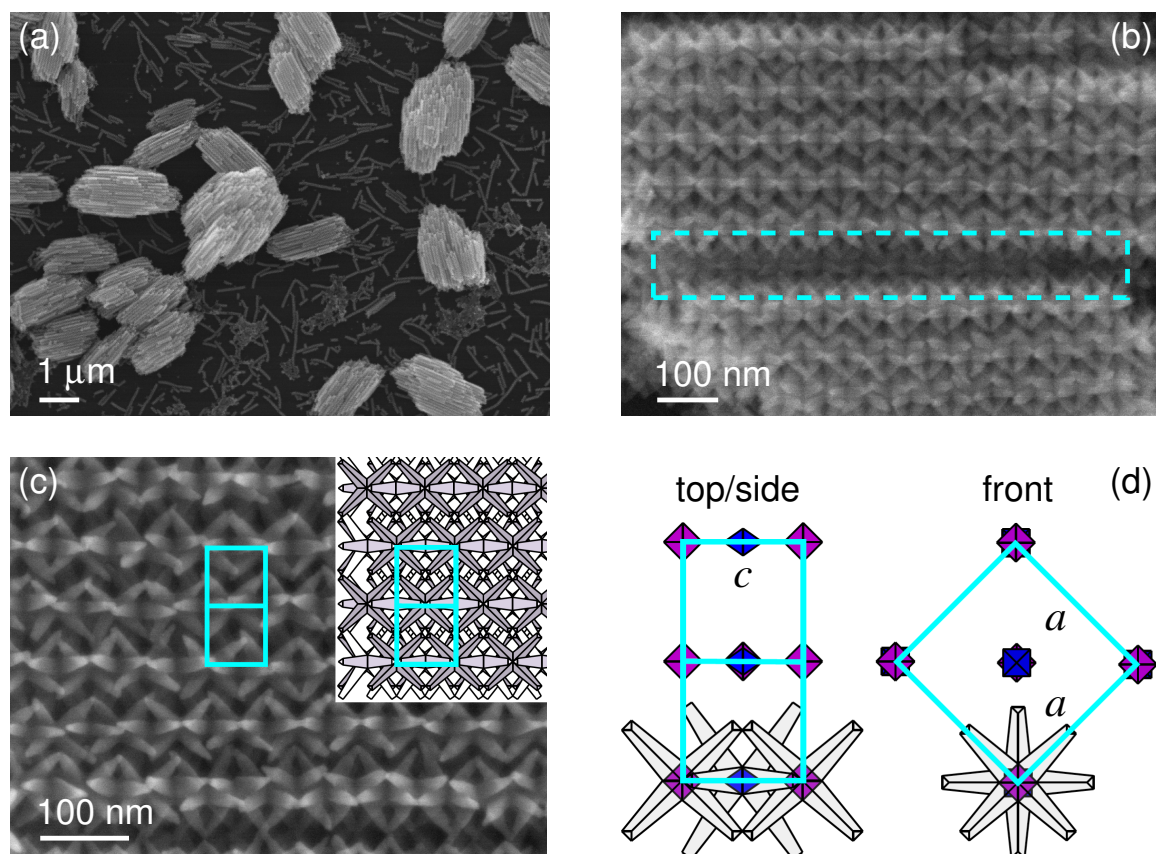


**Figure 7.2:** (a) Scanning Electron Microscopy shows that 3D clusters approximately  $2 \mu\text{m}$  in length have formed after the addition of the highly polar acetonitrile to an aged toluene-based suspension containing mostly chains. (b) The clusters have a regular (crystalline) structure, which is achieved by the ordered packing of the interlocking chains. This is further illustrated by the cyan box, which marks the spot of a defect in the superstructure, where a chain is missing. The defect also reveals the layer underneath. (c) A close-up of the structure showing the arrangement of the octapods: a crystal with a tetragonal unit cell. The inset shows a sketch of the structure using the 3D models that were employed in the simulation studies. (d) A representation of the tetragonal unit cell, seen here from the top/side and the front, with  $c \approx 70 \text{ nm}$  and  $a \approx c\sqrt{2}$ . The chains are oriented along the  $c$ -axis. The blue and magenta octahedra represent the cores of the octapods and the colour also serves to indicate the orientation of the particles.

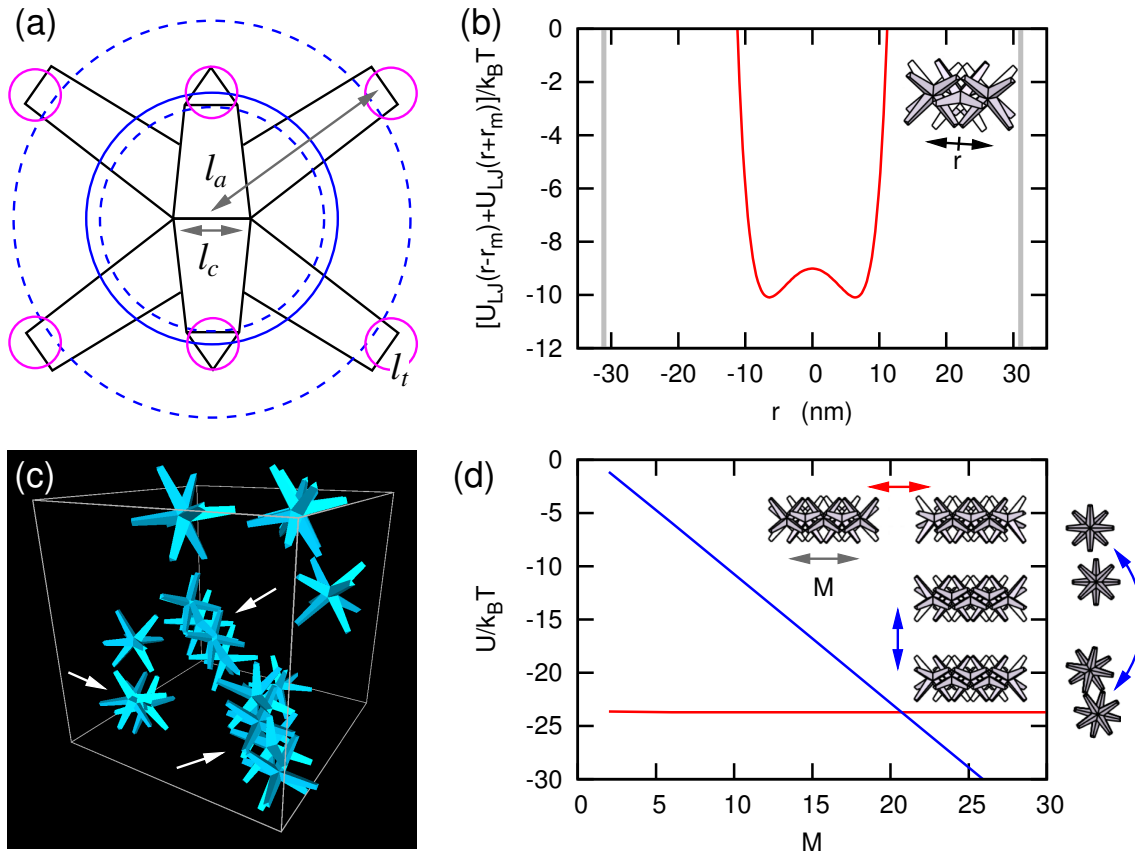


**Figure 7.3:** (a) Two-dimensional (2D) projection of the octapod model used in our simulations. The core edge length is given by  $l_c$ , the tip edge length by  $l_t$ , and the pod length by  $l_a$ . The range of the tip-tip square-well (SW, magenta) interaction and the core-core Lennard-Jones (LJ, blue) interaction is also shown. The dashed blue circles indicate  $U_{LJ}(r) = -1 k_B T$ , and the solid blue circle indicates  $r_m$  [ $U_{LJ}(r_m) \approx -8 k_B T$ ;  $U_{LJ}$  is minimal]. (b) The interaction strength (in  $k_B T$ ) experienced by an octapod in the interlocking configuration, as a function of the distance  $r$ . This distance is measured along the chain axis from the centre ( $r = 0$ ) of the cage formed by two octapods. The grey vertical lines indicate for which  $r$  the octapod comes into contact with its neighbours. (c) A snapshot of a simulation box containing 16 octapods at a volume fraction of  $\phi \approx 0.01$ . Several of the octapods have formed interlocking chains, indicated with white arrows. (d) The aggregation energy  $U$  (at contact) as a function of the number of octapods  $M$  in an interlocking chain for on-end attachment (red) and side-by-side aggregation (blue). The energetically favoured side-by-side contact is shown to the right.

of the model for the octapods used in simulations on the tomography results shown in Fig. 7.1a. The following quantities define the shape and size of the octapod model, also see Fig. 7.3a, which shows this model and indicates various length scales. The edge length of the octahedral core is given by  $l_c = 22$  nm, the edge length of the triangular tip of a pod by  $l_t = 15$  nm, and the length of a pod by  $l_a = 62$  nm, which is measured from the centre of the octapod to the centroid of the triangular tip. In this model we do not account for the increase in the width of this inorganic nanocrystal caused by the presence of a capping layer, which one could consider a soft-potential effect.

For the FBMC crystal-structure-prediction simulations we compressed a system of octapods - over 1000 trials with varying compression rates - from a dilute-gas phase to a high-density state for  $N = 1, \dots, 6$ , with  $N$  the number of particles in the unit cell. We found several high-density crystal structures, none of which corresponded to the experimentally observed crystal. The hard-particle model's inability to form 3D superstructures was further confirmed by performing regular  $NVT$  MC simulations at high volume fractions  $\phi \approx 0.2$ , as well as regular  $NPT$  MC simulations at pressures for which the system 'crystallizes'. Only irregular clusters of octapods were found. Also, for gas-phase  $NPT$  and  $NVT$  simulation studies with  $\phi \approx 0.01$ , we did not observe any chain-like structures forming spontaneously. We therefore conclude that the hard-particle model is not suited to describe the hierarchical self-assembly. This was to be expected on the basis of the experimental results, since the initial chain-formation step and the dilution at which this occurs, are indicative of a system driven by attractive interactions.

### 7.3.2 Attractive Interactions

For the next phase of our investigation, we focused on reproducing the experimentally observed chain formation in toluene at low volume fractions, which is an important step in the superstructure self-assembly process. We studied a variety of simple soft potentials, which we added to our hard-particle model, in order to determine a combination that produces the experimental structures. Here we were restricted to very basic potential types and small system sizes due to computational difficulties. We achieved formation of chains in the dilute phase using a model for which there are attractions between the octahedral cores of the particles and also attractions between the tips of the pods.

One model we found to give good results employs a Lennard-Jones (LJ) interaction  $U_{LJ}(r)$  between the cores and a square-well (SW) interaction  $U_{SW}(r)$  between the centroids of the tips. Figure 7.3a shows a representation of the LJ and SW interaction potentials in relation to the hard-particle model. The LJ interaction is given by

$$U_{LJ}(r) = \epsilon_l \left\{ \left( \frac{r_m}{r} \right)^{12} - 2 \left( \frac{r_m}{r} \right)^6 \right\}, \quad (7.1)$$

with  $r$  the centre-to-centre distance between two octapods,  $r_m \approx l_a/\sqrt{3}$  the location of the minimum, and  $\epsilon_l \approx 8 k_B T$  the well depth, where  $k_B$  is Boltzmann's constant and  $T$  is the temperature. The value of  $r_m$  was chosen such that in an interlocking chain configuration, each octapod is located in the double-well potential of the 'cage' formed by its two neighbouring octapods, provided it is not on the end of the chain. Figure 7.3b shows this effect and the associated double-well potential. To ensure that the tips of the

octapods (with the same orientation) touch in the interlocking configuration a spherically symmetric SW interaction was implemented

$$U_{\text{SW}}(r) = \begin{cases} -\epsilon_s & : r < \sigma \\ 0 & : r > \sigma \end{cases} \quad (7.2)$$

with  $r$  the centroid-to-centroid distance between the triangular tips of the pods,  $\sigma \approx l_t/2$  the range of the interaction, and  $\epsilon_s \approx 4 k_B T$  the well depth.

### 7.3.3 Self-Assembly into Interlocking Chains

Using the above LJ-SW empirical model in  $NVT$  MC simulations we observed the formation of chains containing as many as 5 octapods in the interlocking configuration for dilute systems with  $\phi \approx 0.01$ . Figure 7.3c shows a snapshot of an  $NVT$  simulation box containing 16 particles, most of which have formed interlocking-chain segments. Two segments of length four and one dimer can be observed. For the dilute systems all particles eventually became part of a chain through on-end attachment. Small changes in the model did not interfere with the formation of chains, although the ease of formation and the stability of the chains varied significantly when the depth of either interaction potential was changed by  $1 k_B T$ . The well-depth used in both the LJ and the SW potentials was required to achieve spontaneous formation of relatively stable chains at low densities  $\phi \approx 0.01$ , also see Fig. 7.1b. For higher densities, both branching and noninterlocking trimer formation were observed. Clustering of the chains into structures with greater hierarchy, such as sheets or crystals was, however, not observed.

Figure 7.3d shows the on-end lengthening and the side-by-side aggregation interaction energy as a function of the number of octapods  $M$  in the two chains coming together. The interaction energy was determined by theoretical calculation, since simulations of these long chains, using  $2M$  octapods that are free to move, proved prohibitive. Our results show that chain lengths exceeding  $M = 20$  octapods are required to make on-end lengthening of the chain energetically less favourable than side-by-side assembly. For the LJ-SW model the energetically favoured side-by-side aggregation of chains did not yield the experimentally observed pod-pod morphology. Instead, we found a configuration where the chains touch at the tips, see the representation in Fig. 7.3d. This was confirmed by  $NVT$  MC (and limited FBMC) simulations of rigid pre-assembled chains that did not allow movement of the octapods in the chain or detachment from the chain.

By performing FBMC simulations we were able to probe the high density structures that our LJ-SW models can form more readily than by ordinary  $NPT$  and  $NVT$  simulations. We observed a variety of crystal structures, which *did not* possess the chain-like morphology. For the most part, configurations where the tips of the pods are in close proximity to one another were found, e.g., structures similar to the one in Fig. 6.3. These configurations differed from the experimentally observed 3D superstructure because they either did not possess the interlocking property, or if they did, the interlocking rows did not come together in the pod-pod configuration. On occasion, however, we did find structures similar to those observed in the experiments, possessing both the interlocking and the pod-pod configuration. We attribute these occurrences to an increased probability of

interlocking aggregation taking place, when compressing from the fluid phase, due to the core-core attractions.

Summarizing, we established an empirical simulation model capable of reproducing the experimentally observed formation of interlocking chains in the dilute fluid phase. We accounted for the shape of the octapods using a triangular-tessellation-based overlap algorithm [249] and the model used Lennard-Jones attractions between the cores of the octapods and square-well attractions between the tips of the octapods to achieve octapod self-assembly. However, our model did not appear to capture the subsequent step of the chains aggregating into 3D superstructures with the desired morphology.

### 7.3.4 Opportunities for Improvement

For dilute systems,  $\phi \approx 0.01$ , cluster moves could have been employed to accelerate the exploration of phase space. We did not pursue this here for the following reasons. Cluster moves only facilitate the initial on-end lengthening and sideways aggregation of the chains. However, when these chains come in close proximity of one another, the largest contribution to the sampling of phase space comes from single particle translations or rotations. We would therefore again be limited by the computational efficiency of our method. That is, the number of individual octapods required to simulate several long chains with this type of LJ-SW interaction is prohibitive. The stiff pre-assembled chains we used to compute the on-end lengthening and side-by-side aggregation energy, reduce the freedom of motion of the particles and thereby the number of overlap checks and energy calculation that have to be performed. This compromise between computational efficiency and the area of phase space that can be sampled allowed us to perform simulations for long chains on a time scale that is accessible. However, the relevance of the results obtained for this system to the system where the octapods are free to move is questionable. Another reason why we did not consider cluster moves is that at higher packing fractions,  $\phi \approx 0.2$ , the nonconvex nature of the octapods makes it difficult to identify clusters and to move such clusters, since the octapods can form a kind of ‘brier patch’ through which single particles cannot easily pass, let alone clusters. On the basis of our simulation results, we cannot exclude that these dense systems were kinetically arrested, but it is unlikely that the use of cluster moves would have been able to overcome any such arrest. Currently, a new (more coarse) model is being considered in the group of Prof. dr. Marjolein Dijkstra [266], by which the computational efficiency may be improved. This model consists of four spherocylinders which intersect in their respective centres and span a cube. Since the hard-particle overlap routine is sped up significantly with respect to the triangular-tessellation model, bigger and more complex systems may be considered.

## 7.4 Van-der-Waals Interactions between Octapods

In this section we examine the van-der-Waals (vdW) interactions between solvated octapods to ascertain the extent to which these interactions can explain the experimentally observed self-assembly. We start by describing the method used to determine the vdW interactions. This is followed by a discussion of the properties of the media in which

the octapods are suspended and the effect the medium has on the strength of the vdW interaction. We also examine the steric repulsion between the octapods that is brought about by the capping layer that covers these particles. Finally, we show the orientational dependence of the vdW interaction between two octapods in toluene.

### 7.4.1 Numerical Integration of the Dispersion Forces

Calculating the vdW interactions between two octapods is extremely complicated, due to the geometry of the particle and the high dimensionality of the parameter space which can be explored. Our approach to this problem is as follows. The nonretarded vdW interaction between two octapods is given by  $U_{\text{vdW}}(\mathbf{r}, \mathbf{u}, \mathbf{v})$ ,  $U_{\text{vdW}}$  for short, where  $\mathbf{r}$  denotes the position of the centre of one of the octapods (octapod 1) with respect to the centre of the other (octapod 2) and the quaternions  $\mathbf{u}$  and  $\mathbf{v}$  specify the orientation of octapods 1 and 2, respectively. Using a Hamaker-de-Boer-type integration [69] of the inter-atomic dispersion forces the vdW interaction can be approximated by

$$U_{\text{vdW}}(\mathbf{r}, \mathbf{u}, \mathbf{v}) = C\rho_1\rho_2 \int_{O_1} \int_{O_2} |\boldsymbol{\tau}_1 - \boldsymbol{\tau}_2|^{-6} d\boldsymbol{\tau}_2 d\boldsymbol{\tau}_1, \quad (7.3)$$

with  $|\cdot|$  the Euclidean vector norm,  $C$  the London constant associated with the octapod-medium-octapod dispersion interaction, and  $\rho_i$  the number density of atoms in the  $i$ -th octapod ( $i = 1, 2$ ). The integration boundaries  $O_i$  are implicitly dependent on  $\mathbf{r}$ ,  $\mathbf{u}$ , and  $\mathbf{v}$ . Our model assumes homogeneous density distributions  $\rho_i$  and a spatially constant value of  $C$ . The London constant  $C$  is related to the Hamaker constant  $A$  for the octapod-medium-octapod interaction according to  $A = 2\pi C\rho_1\rho_2$ .

Analytic evaluation the integrals in Eq. (7.3) is impractical due to the complex shape of the octapod even for the most symmetric of configurations. We therefore resort to a numerical method. It proves useful split the integration in Eq. (7.3) into two parts and consider a convenient reference frame. Without loss of generality we can place octapod 1 in the origin, such that its pods are oriented along the  $(\pm 1, \pm 1, \pm 1)$  vectors. The vdW potential of this single octapod in the origin is given by

$$U_{\text{vdW,pnt}}(\mathbf{R}) = \frac{A}{\pi^2\rho_2} \int_{O_1} |\boldsymbol{\tau}_1 - \mathbf{R}|^{-6} d\boldsymbol{\tau}_1, \quad (7.4)$$

where  $O_1$  is understood to be appropriately translated and rotated to place the octapod in the origin with the proper orientation. The vdW interaction between the two octapods can be written in terms of this potential as

$$U_{\text{vdW}}(\mathbf{r}, \mathbf{u}, \mathbf{v}) = \rho_2 \int_{O_2} U_{\text{vdW,pnt}}(\boldsymbol{\tau}_2) d\boldsymbol{\tau}_2, \quad (7.5)$$

where  $O_2$  is subject to the same transformation operation as  $O_1$  to preserve the configuration of interest. By tabulating the potential of Eq. (7.4) we can determine the vdW interaction for a given configuration using Eq. (7.5) in a computationally reasonable time.

In our analysis we exploited the symmetry of the octapod and we therefore tabulated Eq. (7.4) for only one octant of the Cartesian coordinate frame over a cubic grid ( $\mathbf{R}$ -grid) with a 0.5 nm lattice spacing up to a distance of 180 nm from the origin. We were

able to determine this potential landscape in roughly 4 days using 20 modern 2.0 GHz desktop PCs. Carefully tailoring the number of integration points on the octapod allowed us to obtain convergence to within 5% of the actual value of  $U_{\text{vdW,pnt}}(\mathbf{R})$  per  $\mathbf{R}$ -grid point. We required approximately 10 points per nm in each direction on the octapod - replacing the integral in Eq. (7.4) by a summation over these points - to achieve this level of convergence. The deviation from the actual value of  $U_{\text{vdW,pnt}}(\mathbf{R})$  was determined by comparing our results to results obtained using higher precision numerical integration for a limited number of points, both close to the octapod and farther away from it. The high precision integration took roughly four hours per  $\mathbf{R}$ -point, thereby making it impractical to apply it for the entire  $\mathbf{R}$ -grid within a reasonable amount of time. The point density used in the tabulated potential is necessary to obtain a decent approximation for  $U_{\text{vdW}}$  when the octapods are in close proximity. Note that a range of 180 nm in the  $\mathbf{R}$ -grid does not allow for a very large separation of the octapods, which themselves are 124 nm in diameter. We were, however, limited to this range due to time constraints and round-off errors, which became appreciable for large  $|\mathbf{R}|$ .

To determine  $U_{\text{vdW}}$  for a given configuration, we approximated octapod 2 using a group of points ( $O_2$ -grid, approximately 10 points per nm in each direction) which had the correct position and orientation with respect octapod 1. We summed  $U_{\text{vdW,pnt}}$  over the  $O_2$ -points to obtain  $U_{\text{vdW}}$ . Since the  $O_2$ -grid did not coincide with the  $\mathbf{R}$ -grid we used a trilinear interpolation to obtain the relevant values. We managed to achieve a fractional deviation of around 0.15 from the actual value of  $U_{\text{vdW}}$  for configurations where the octapods were within 3 to 6 nm of contact. We determined this value by fitting a higher order interpolation to the potential and integrating that with high precision for several configurations, accounting for the 5% deviation already present in the potential landscape. The relatively high deviation at close separations is a result of an underestimation of  $U_{\text{vdW}}$ , due to a systematic property of the trilinear interpolation. The level of deviation was, however, acceptable and better accuracies could be achieved for greater separations.

It took around 30 minutes to evaluate Eq. (7.5) using the precalculated  $\mathbf{R}$ -grid for a single configuration on a modern 2.0 GHz desktop computer with 2 GB of random-access memory (RAM). Because the tabulated potential of Eq. (7.4) was too large to store in RAM, roughly 5 GB of data, we implemented a piecewise strategy: retrieving a portion of the  $\mathbf{R}$ -grid from the hard drive, integrating all relevant  $O_2$ -points over that, and repeating this until all  $O_2$ -points had been considered. We believe that substantially faster integration and better convergence is possible by making more conscientious choices with regards to the tabulation of Eq. (7.4) and the interpolation/integration techniques, but for the purposes of our investigation the current approach sufficed.

## 7.4.2 Hamaker Constants and Steric Repulsion

To determine the value of the vdW interaction for the experimental systems, we required the Hamaker constant of the octapod-medium-octapod interaction for the three media used: chloroform, toluene, and toluene-acetonitrile. CdSe and CdS have an equal Hamaker constant (over vacuum)  $A_{\text{CdSe}} = A_{\text{CdS}} = 11.0 \cdot 10^{-20}$  J [296, 297]. That of toluene over vacuum is given by  $A_{\text{tol}} = 5.4 \cdot 10^{-20}$  J [298]. The Hamaker constant of CdSe/CdS over toluene is therefore  $A_{\text{oto}} = (\sqrt{11.0} - \sqrt{5.4})^2 \cdot 10^{-20}$  J =  $9.9 \cdot 10^{-21}$  J, where we applied

the combining relations of Ref. [69]. For chloroform we obtained  $A_{\text{oco}} = 7.9 \cdot 10^{-21}$  J, because the Hamaker constant over vacuum for chloroform is given by  $A_{\text{chl}} = 5.9 \cdot 10^{-20}$  J, according to Lifshitz theory [69] and the values in Ref. [299]. Finally, for the toluene-acetonitrile mixture we obtained  $A_{\text{oa0}} = 1.5 \cdot 10^{-20}$  J, since  $A_{\text{ace}} = 4.2 \cdot 10^{-20}$  J over vacuum [300] and we have an 80% acetonitrile to 20% toluene solution (by volume), for which we used the theory of Ref. [301]. We assumed that impurities and the presence of the capping layer do not strongly affect the vdW interaction and we therefore considered these CdSe/CdS-based Hamaker constants to be representative for the octapod-medium-octapod values. The large difference between  $A_{\text{oa0}}$ ,  $A_{\text{oto}}$ , and  $A_{\text{oco}}$  results in a proportional difference in the strength of the vdW forces between the octapods in the three solvents, since  $U_{\text{vdW}}$  is linear in the Hamaker constant [see Eq. (7.5)].

There are short-ranged repulsive interactions between the octapods when the surfaces of these particles are in close proximity to each other. These steric repulsions are caused by a loss of configurational entropy resulting from volume restriction of the molecules in the two overlapping capping layers, due to interdigitation. For the octapods the capping layer consisted of octadecylphosphonic acid (ODPA) molecules [54], which have a length of  $H = 2.5$  nm [302]. Therefore, we assumed that steric effects only occur when the surfaces of two octapods are within  $2H = 5.0$  nm of each other. The steric repulsion dominates over the vdW attraction in a good solvent for the ODPA molecules, which prevents the octapods from aggregating. In a poor solvent the repulsion is reduced and the octapods can aggregate. To determine steric interactions the Alexander-de Gennes model [69] is often employed. However, for our system we did not feel justified in using this model, since there are too many unknowns with respect to the properties of the capping layer. For instance, we did not know the affinity (covering density) of the ODPA for the different crystal facets of the octapod. Moreover, the behaviour of the molecules near the edges joining the various facets was not well understood. To (in some way) take the steric repulsion into account in our model for octapod interactions and to ensure a fair comparison of the different media, we specified that the combined vdW and steric repulsion interaction assumes its minimum at  $1.5H$  and that the depth of this minimum is given by  $U_{\text{vdW}}$ . We chose  $r = 1.5H$  because steric repulsion is unlikely to dominate the vdW force at  $r = 2H$ , but will almost certainly dominate at  $r = H$ ; based on simple estimates using the theory in Ref. [69] for spherical particles and typical values of the surfactant covering in nanoparticle systems [49].

### 7.4.3 Van-der-Waals Interactions in Toluene

Given an initial orientation  $\mathbf{u}$  and  $\mathbf{v}$  of the two octapods and an initial  $\mathbf{r}$ , say  $\mathbf{r}_0$ , for which the octapods touch, we determined the distance dependence of the vdW interaction using the method explained in Section 7.4.1, the Hamaker constants of Section 7.4.2, and the following expression

$$U_{\text{vdW}}(r) \equiv U_{\text{vdW}} \left( \mathbf{r}_0 + r \frac{\mathbf{r}_0}{|\mathbf{r}_0|}, \mathbf{u}, \mathbf{v} \right), \quad (7.6)$$

with  $r$  the separation between the surfaces of the octapods. Because of the large configurational space that is associated to two octapods interacting and the computational limits of our method, we restricted ourselves to 7 configurations for which we computed

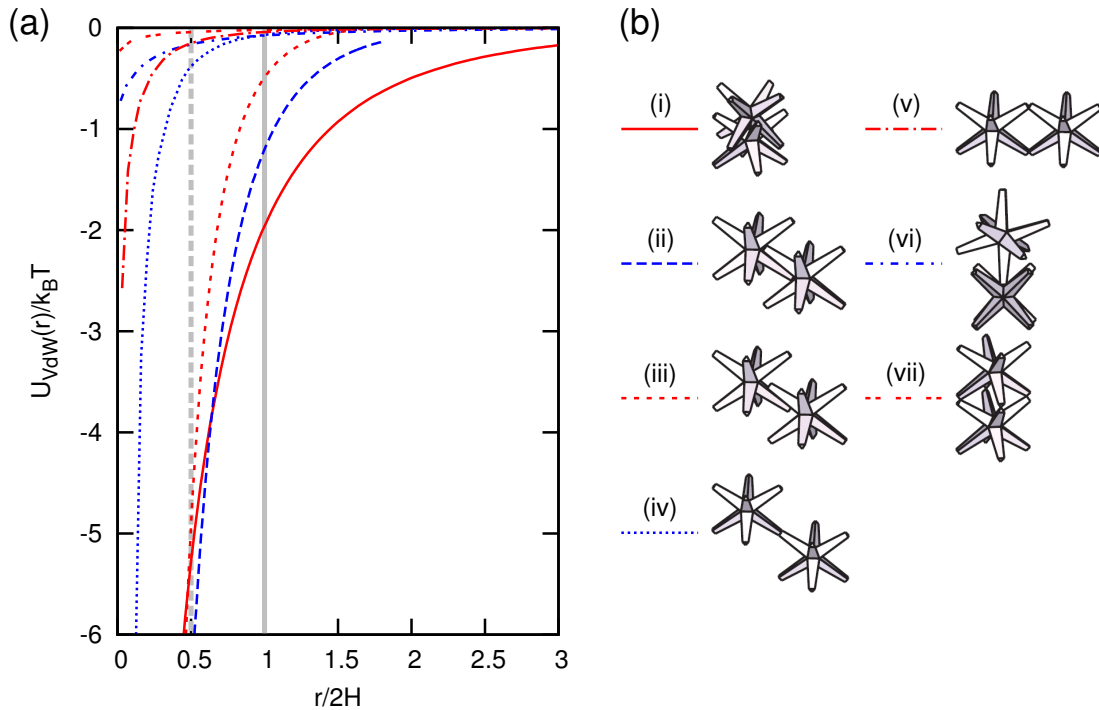


**Figure 7.4:** (a) The nonretarded vdW interaction strength  $U_{\text{vdW}}$  in toluene in terms of the thermal energy  $k_{\text{B}}T$  as a function of the distance  $r$  between the octapods for 7 configurations. The distance is measured from contact between the octapods ( $r = 0$ ) and is expressed in terms of  $2H$ , with  $H = 2.5$  nm is the length of a fully extended octadecylphosphonic acid (ODPA) molecule. The dashed grey line indicates  $r = H$  and the solid grey line  $r = 2H$ . (b) The 7 configurations at contact are shown schematically and are labelled with Roman numerals to which we reference in the text.

$U_{\text{vdW}}(r)$  on an equidistant  $r$ -grid using 200 points starting from  $r = 0$  with steps of 0.30 nm.

Figure 7.4 shows our results for 7 configurations in toluene, the results for chloroform and the toluene-acetonitrile mixture can be obtained by vertical scaling of these curves. We chose these particular configurations because they were either observed in the experiments (i), (ii), (iii), and (vii), or because we believed that they might give similar interaction strengths as the experimentally observed configurations (iv), (v), and (vi). The difference between configurations (ii) and (iii) is that for the former the pods are along each other as far as possible, whereas for the latter another octapod can be symmetrically fitted in the ‘V-structure’ formed by two pods at a separation of  $1.5H$ .

The interlocking (i) and pod-pod (ii,iii) configuration appear to be the only configurations which have a substantial vdW interaction, when compared to the thermal energy  $k_{\text{B}}T$ . Configuration (i) achieves a well depth of around  $-3 k_{\text{B}}T$  at  $r = 1.5H$  and configurations (ii,iii) achieve  $-2.5 k_{\text{B}}T$  and  $-1.5 k_{\text{B}}T$  at  $r = 1.5H$ , respectively. We conjecture that in toluene configuration (i) is the only one that is stable, since the interaction strength of configurations (ii,iii) is lower and  $U_{\text{vdW}}$  also decays much faster. In fact, for short distances (ii,iii)  $U_{\text{vdW}}(r) \propto r^{-14}$  to  $U_{\text{vdW}}(r) \propto r^{-18}$  depending on the separation, whereas

$U_{\text{vdW}}(r) \propto r^{-6}$  for configuration (i). In addition, configurations (ii,iii) are probably more efficiently passivated by steric repulsion, since the contact area for  $r = 1.5H$  is much greater.

We verified that there is sufficient interaction strength between the octapods to stabilize the interlocking chains in toluene. That is, the distance between the surfaces of the octapods in the chain is roughly  $2.5H$ , which would seemingly result in a far lower vdW binding energy than the  $3 k_{\text{B}}T$  that we predicted for  $1.5H$  of separation. However, superimposing the vdW interactions of the two neighbouring octapods that form a cage around an octapod in the interlocking configuration (see Fig. 7.3b for an example of this caging) leads to significant binding energy. The central octapod typically experiences a vdW binding energy of between 2 and  $5 k_{\text{B}}T$ , depending on exact shape of the cage and the position of the octapod within it.

#### 7.4.4 Relation to the Simulation Model

In this section we briefly compare the vdW interactions that we found using the Hamaker-de-Boer formalism to the soft interactions that we employed to achieve chain formation in our simulations, see Section 7.3.2. An essential element for the chain self-assembly in simulations was the use of core-core Lennard-Jones (LJ) attractions. Our calculations showed that there are indeed relatively strong attractions between the core regions of the octapods in toluene. We consider this further (indirect) evidence that the vdW interactions are responsible for the initial self-assembly step in toluene. However, the square-well tip-tip attractions, which ensured that the tips of the octapods (with the same orientation) touched in the interlocking chain, could not be explained by our results. It is possible that the steric repulsion between the tips of the octapods is far lower than we assumed in our model, because the ODPa surface coverage is lower at the tip, but this is merely speculation. Another possibility is that tip-tip interactions are unnecessary. The octapod and capping layer combination may be described better by an effectively more voluminous simulation model. The model we used had rather slender pods, which only accounted for the CdS part of the octapod and not for the presence of the capping layer, see Section 7.3.1. The added width of the capping layer could substantially reduce the freedom of motion in the interlocking configuration and might thereby naturally impose close proximity of the tips due to geometrical constraints. Adjusting our simulation model according to the insights gained by our vdW calculations is, however, left for future studies.

### 7.5 Mechanism for the Hierarchical Self-Assembly

By combining the experimental, theoretical, and simulation results we can now formulate a mechanism for the hierarchical self-assembly of the octapods and explain the experimental observations.

The strength of the vdW attractions between the octapods in chloroform is reduced by 20% with respect to the values in toluene. Moreover, chloroform is a better solvent for the capping molecules, which likely improves the steric repulsion. The combination of these



effects may well be sufficient to prevent aggregation of octapods into larger structures for this solvent, in agreement with the experimental observations.

In toluene the vdW attractions are sufficiently strong to allow for self-assembly into interlocking chains. The formation of chains can be further explained by considering the peculiar geometry of the octapods. In forming a dimer each octapod can approach another octapod from eight possible equivalent directions. However, once a dimer is formed, a third octapod can join and form a stable trimer only by adding to one of the two ends of the chain, any other side is too sterically hindered by the pods of the other octapods in the dimer. Furthermore, the interlocking configuration at the ends is the only one which is capable of supporting attachment in toluene. The same holds for formation of longer chains, realized either by addition of individual octapods or by gluing of octapod oligomers. The interaction strength in toluene is however insufficient to support the chain lengths required to achieve stable side-by-side aggregation. That is, only linear chains may be formed in toluene. This dimer formation and subsequent chain lengthening is shown in the sketch of Fig. 7.5a.

The addition of acetonitrile, a strongly polar solvent, to an aged suspension of octapods in toluene containing mostly chains, has two effects. First, the effective thickness of the capping layer around each octapod can shrink, because acetonitrile is a poor solvent for its ligands. Second, the increased polarity of the toluene-acetonitrile mixture boosts the vdW interaction strength, see Fig. 7.5b. Within the confines of our model this has several consequences, in agreement with the experimental findings. (i) Octapods in pre-existing chains bind more strongly, thereby stiffening these chains. (ii) Chain-chain interactions become stronger, initially resulting in lengthening of the chains. This is followed by side-by-side aggregation, when the chains are of sufficient length to make such aggregation energetically preferential. (iii) The side-by-side aggregation favours the pod-pod due to deep vdW minimum that is associated with it. A schematic of steps (ii) and (iii) is given in Fig. 7.5c to clarify this process. The addition of acetonitrile therefore ultimately yields large, ordered 3D structures with the morphology observed in experiments. These superstructures precipitate when they have grown to sufficient size.

## 7.6 Conclusion and Outlook

In this chapter we considered the hierarchical self-assembly of branched octapod-shaped nanocrystals, which were suspended in a liquid, into the interlocking chains and three-dimensional (3D) superstructures observed in experiments [54], using simulations and theory. Our simulation studies showed that attractions between the cores of the octapods are essential in obtaining interlocking chains at low volume fractions. The origin of these attractions was considered using a theoretical calculation of the van-der-Waals (vdW) interaction between two octapods, which is based on the Hamaker-de-Boer formalism. Our analysis also showed that the vdW attractions between the pods of an octapod can explain the morphology of the 3D superstructure and revealed the role that the suspending medium plays in the hierarchical process. Based on our simulation and theoretical work we have thus demonstrated that the observed self-assembly is predominantly driven by

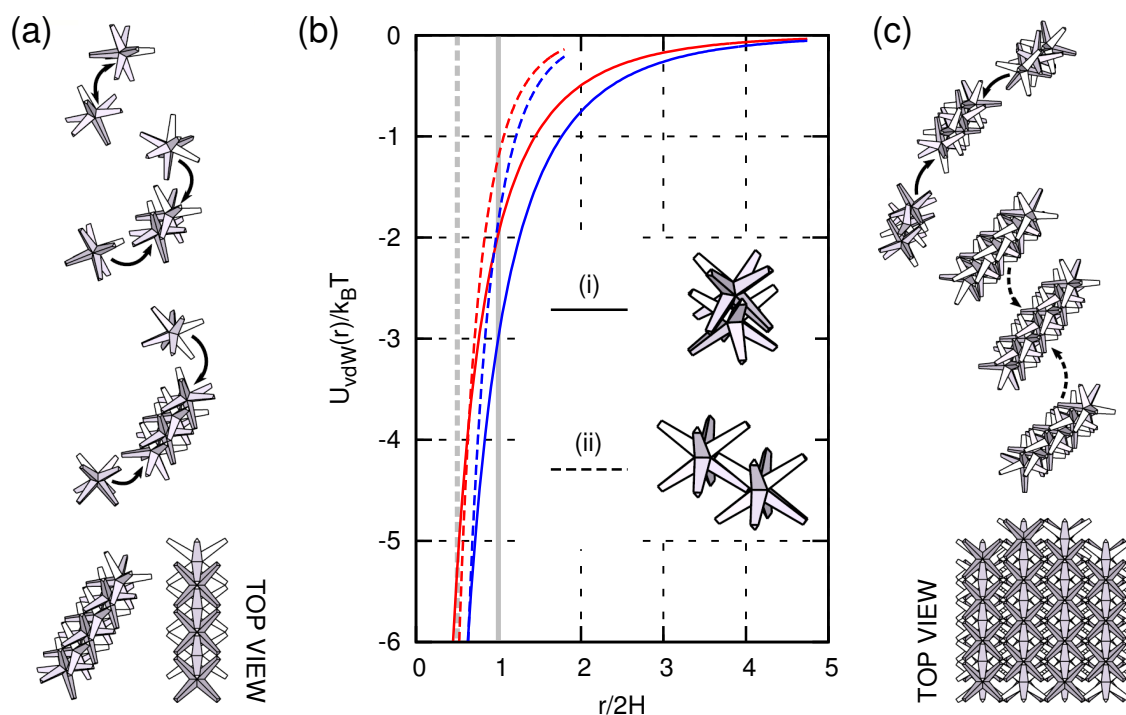


**Figure 7.5:** (a) In toluene chains are grown by interlocking of octapods [configuration (i)]. (b) The red curves give the vdW strength  $U_{vdW}$  (in  $k_B T$ ) as a function of the separation  $r$  between two octapod surfaces for a pure toluene solvent and the blue curves are for a 20/80% by volume toluene/acetonitrile mixture. The gray vertical lines mark the steric hindrance, see Section 7.4.2. The interlocking configuration between two octapods achieves sufficient vdW attraction [full curve, or (i)] to result in the formation of chains in toluene. The interaction-strength increase for the pod-pod configuration [dashed curve, or (ii)] by the addition of acetonitrile explains the morphology of the three-dimensional (3D) superstructure the chains self-assemble into. (c) The addition of acetonitrile to an aged toluene sample (containing mostly chains) initially leads to chain growth by on-end interlocking of smaller chains [configuration (i)]. This is followed by side-by-side assembly of chains into the 3D superstructure according to the pod-pod interaction [configuration (ii)] between octapods belonging to different chains, when the chains reach sufficient length to support such aggregation.

the complex anisotropic shape of the octapods, through the directionality of the hard-core repulsions and the van-der-Waals (vdW) attractions this shape brings about.

A natural step for further investigation is to improve upon our simulation model with the knowledge obtained from our theoretical vdW analysis. It is our hope that an improved model will capture superstructure formation, a step in the hierarchical self-assembly that we did not manage to reproduce. The use of a simpler model for the shape of the octapod, based on a spherocylinder approximation [266], may prove essential in obtaining the computational efficiency required to perform such complicated simulations. Another point that requires further study is the possibility of an electrostatic component to the octapod interactions. Electrostatic interactions in polar media can be quite strong due to the relatively low ionic screening, despite the fact that only a few charge groups can dissociate in such solvents. We did not take these effects into account, because the mechanisms based on vdW interactions appear to explain the main steps of the self-assembly process, but it would be preferable to show that this is justified.

The theoretical and simulation procedures described in this chapter for octapods show great promise for the analysis of other experimental systems that achieve (hierarchical) self-assembly. It is our hope that our methods will not just be limited to describing the behaviour in experiments, but that in the near future they can be built upon to obtain a predictive tool which may be used to guide experimental studies.

## 7.7 Acknowledgements

It is a pleasure to thank Prof. dr. Liberato Manna, Dr. Giovanni Bertoni, Karol Miszta, Dr. Dirk Dorfs, Dr. Rosaria Brescia, Sergio Marras, Dr. Luca Ceseracciu, and Prof. dr. Roberto Cingolani of the Istituto Italiano di Tecnologia, where the study of the hierarchical self-assembly of the octapods was initiated and all experiments were performed, for the fruitful collaboration on this project. I would in particular like to thank Giovanni Bertoni and Liberato Manna for the long discussions on the properties of the experimental system, which proved crucial to guiding the simulation and theoretical investigation.



---

## Electrostatic Interactions between Janus particles

---

In this chapter we study the ionic screening of charged spherical Janus particles using primitive-model Monte Carlo simulations for a wide variety of parameters. We introduce a method to compare these results to the predictions of nonlinear Poisson-Boltzmann theory. Using this method and the large set of parameters studied, we are able to probe the range of validity of the Poisson-Boltzmann approximation. For homogeneously charged spheres this range of validity corresponds well to the range that was predicted by field-theoretical studies of homogeneously charged flat surfaces. Moreover, we find similar ranges for colloids with a Janus-type charge distribution. Our investigation therefore extends the field-theoretical result to charged spherical (Janus) particles. The techniques and parameters we introduce may be used in future studies of an even wider class of charge-patterned particles.

## 8.1 Introduction

Electrostatic interactions in suspensions of charged colloids are of paramount importance to the structure and phase behaviour of these systems [66, 76, 77, 191]. However, characterising the behaviour of such systems by theory or by simulations is difficult due to the long range of the Coulomb interactions between charged particles, which results in a complex many-body problem. The presence of mobile ions in the suspension causes the bare charge on the particles to be screened. That is, near a charged surface a diffuse layer of ions forms of which the excess charge is opposite to that of the surface, this structure is called the *double layer*. The presence of this double layer effectively reduces the range of colloid-colloid interactions, which is therefore screened.

Several theoretical models have been formulated to describe the phenomenon of screening. The Derjaguin Landau Verwey Overbeek (DLVO) [192, 193] is a classic linear screening theory that is applicable only in a limited parameter range, mostly for monovalent salts, high-polarity solvents, low surface charge, and high ionic strength. The nonlinear Poisson-Boltzmann (PB) approach [194, 195] extends this range, although analytic results are only possible for a limited number of systems. PB theory is based on a mean-field approximation that ignores ion-ion correlations, which is justified only at high temperatures, high dielectric constants, low ion valence, and low salt concentrations. Finally, in regimes where ion-ion correlations are important Strong-Coupling (SC) theory [196–198] may be applied. Several other approaches exist [303–311], including modifications of the traditional PB theory that account for finite-size ions, but, interesting as this may be, we will not go into these here.

In the computational field, both Monte Carlo (MC) and Molecular Dynamics (MD) techniques have been developed to analyse charged particles suspended in an electrolyte. Simulations are used to bridge the gap between the macroscopic phenomenology that is described well by theory and the smaller length scales, which often need to be considered on a more explicit level, relevant to many experiments. In *primitive-model* simulations ions are taken into account explicitly [199–204]. Ewald Sums [269] usually provide the basis for calculating the long-ranged Coulomb contribution to the total energy of a system with periodic boundary conditions. However, employing Ewald Sums is computationally expensive and the systems that can be studied in the primitive model are therefore small in size. When studying charged colloids suspended in an electrolyte it is desirable to coarse grain the system and use the much shorter ranged effective interactions between the particles instead of accounting for the ions explicitly. Most simulation studies therefore consider systems where the interactions between the colloids can be modelled by a DLVO pair potential [77, 205–208].

Even charge-patterned particles have been studied using the DLVO approximation by partitioning the surface charge over a finite number of point-Yukawa charges with different prefactors [190]. For charge-patterned particles this approximation still generally results in an expensive calculation of the pair interaction as a function of the separation and orientation. Moreover, it is known that the point-Yukawa description inadequately accounts for the hard core of the particle, i.e., it implicitly assumes that ions can penetrate the colloid. In Ref. [212] a correct, simple, and therefore computationally far more efficient DLVO-multipole approximation was derived for the effective interaction between



two charge-patterned particles. The multipole-based effective interactions have an enormous potential for use in simulation studies to explore the phase behaviour of previously inaccessible systems

In this chapter we investigate the range of applicability for nonlinear PB theory to accurately describe the behaviour of the ion density around charged heterogeneous particles. We are interested in this, because it allows us to quantify for which parameters the DLVO-multipole approximation of Ref. [212] may be applied in coarse-grained simulations, since this approximation was derived using PB theory. For this study we restrict ourselves to particles with a Janus-type charge pattern. The term *Janus* refers to the two-faced Roman god of doors and was introduced to describe colloid properties in 1988 [117]. A Janus particle [117–119] consists of two opposing parts (usually hemispheres) with different properties for the wetting, charge, chemical functionality, etc. The past decade has seen a marked increase in the ability to synthesize such Janus colloids [110–116] and of their use in self-assembly experiments. Many interesting structures were found [32, 190] and questions have been raised on how to approach simulations of such systems. With our study we aim to address some of these questions for charged Janus particles in an electrolyte, in much the same way as the pioneering simulation studies that probed the applicability of the regular DLVO/PB approximation for homogeneously charged particles [199, 201].

In Section 8.2 we introduce the methods by which we compute the ion density around charged Janus particles: primitive-model MC simulations (8.2.1) and nonlinear PB theory (8.2.2). We discuss the results of our investigation in Section 8.3, which is divided into four parts. In Section 8.3.1 we introduce the method, based on Fourier-Legendre (FL) mode decomposition, by which we compare the MC and PB results. This method is applied to a homogeneously charged particle in Section 8.3.2, in which we also investigate the relation to the field-theoretical results of Refs. [213, 214] for homogeneously charged flat surfaces. In Section 8.3.3 we extend our results to a Janus dipole and show that there is remarkable correspondence with the results for a homogeneously charged sphere. We consider a particle with a single charged hemisphere in Section 8.3.4. Finally, we discuss our findings, comment on the potential synergy between simulation methods and theoretical results, and present an outlook in Section 8.4.

## 8.2 Simulations and Theory

In the following we consider a system of spherical charge-patterned colloids with radius  $a$  suspended in an electrolyte. The colloid volume fraction is denoted by  $\eta$ . To simplify the calculations we study only one of these particles, which we locate at the centre of a volume  $V = 4\pi a^3/(3\eta)$ . We apply periodic boundary conditions to this volume to account for the fact that we are in principle interested in a system which contains many colloids. The particle's (heterogeneous) surface charge may be specified in Poisson-Boltzmann (PB) theory by a charge density  $q(\mathbf{r})$ , which is only nonzero when  $|\mathbf{r}| = a$  with  $\mathbf{r}$  the position w.r.t. the origin, or in Monte Carlo (MC) simulations by 100 point charges distributed over this surface. We studied three types of charge distribution. (i) A homogeneous surface charge of  $Ze$ , with  $Z > 0$  the number of charges and  $e$  the elementary charge. (ii) A perfectly

antisymmetric surface charge, with  $Ze/2$  and  $-Ze/2$  homogeneously distributed over the particle's upper and lower hemisphere, respectively. (iii) A homogeneously charged upper hemisphere with charge  $Ze$  and a completely uncharged lower hemisphere. Unless stated otherwise  $Z = 100$  throughout this chapter. The number of free monovalent ions  $N$  in the volume  $V$  is fixed, i.e., we are interested in an average ion concentration  $N/V$  for the system that we approximate by our one-colloid calculation. We only consider systems for which a monovalent salt is added to improve the screening effected by the counter ions to the particle's charge. The balance between the number of positive  $N_+$  and negative  $N_-$  ions ( $N = N_+ + N_-$ ) is such that the volume, and thereby the entire system, is charge neutral. For the monopole and charged hemisphere we require  $Z + N_+ - N_- = 0$  and for the Janus dipole  $N_+ = N_-$ . We assume that there is a perfect dielectric match between the colloid, the ions, and the medium to avoid any related boundary effects.

### 8.2.1 Ewald Sums and Monte Carlo Simulations

To study the systems described above by MC simulations we turn to the primitive model, for which the ions are represented by charged spheres and the suspending medium is treated as a dielectric continuum. To sample phase space Monte Carlo (MC) simulations are performed in the isothermal-isochoric (canonical,  $NVT$ ) ensemble. We consider a cubic simulation box of length  $L = 50d$ , with  $d$  the ion diameter. A spherical particle is located at the centre of the box (the origin). Periodic boundary conditions are imposed to emulate a system with a colloid volume fraction  $\eta$ . The particle's rotational symmetry axis is chosen parallel to one of the box's ribs for the Janus-type charge distributions. The charge sites on the colloid are chosen according to the optimal packing of 100 points on a sphere [312] to ensure that they are spaced as homogeneously as possible. The ion-ion pair potential is a combination of a Coulomb and a hard-particle interaction part:

$$\mathcal{U}_{\text{II}}(\mathbf{r}_i, \mathbf{r}_j) = \frac{q_i q_j e^2}{4\pi\epsilon_0\epsilon} \frac{1}{|\mathbf{r}_i - \mathbf{r}_j|} + \begin{cases} \infty & |\mathbf{r}_i - \mathbf{r}_j| \leq d \\ 0 & |\mathbf{r}_i - \mathbf{r}_j| > d \end{cases}, \quad (8.1)$$

with  $\mathbf{r}_i$  and  $\mathbf{r}_j$  the position of ions  $i$  and  $j$  with respect to colloid's centre, respectively. The function  $|\cdot|$  gives the Euclidean norm of a vector,  $q_i = \pm 1$  the sign of the  $i$ -th ion's charge,  $\epsilon_0$  the permittivity of vacuum, and  $\epsilon$  the relative dielectric constant of the medium, ions, and particle. The interaction between a charge site on the particle located at  $\mathbf{r}_i$ , with  $|\mathbf{r}_i| = d - a/2$ , and an ion located at  $\mathbf{r}_j$  is given by

$$\mathcal{U}_{\text{SI}}(\mathbf{r}_i, \mathbf{r}_j) = \frac{q_i q_j e^2}{4\pi\epsilon_0\epsilon} \frac{1}{|\mathbf{r}_i - \mathbf{r}_j|} + \begin{cases} \infty & |\mathbf{r}_j| \leq a + d/2 \\ 0 & |\mathbf{r}_j| > a + d/2 \end{cases}. \quad (8.2)$$

The coupling between periodicity and the (long-range) Coulomb interactions, Eqs. (8.1) and (8.2), is taken into account using Ewald Sums with conductive boundary conditions [253, 269]. The total electrostatic energy  $U_C$  of a particular configuration may be



written as

$$\begin{aligned} \frac{4\pi\epsilon_0\epsilon}{e^2}U_C &= \frac{1}{2L^3} \sum_{\mathbf{k}\neq\mathbf{0}} \left[ \frac{4\pi}{|\mathbf{k}|^2} \left| \sum_{j=1}^{\tilde{N}} q_j \exp(i\mathbf{k}\cdot\mathbf{r}_j) \right|^2 \exp\left(-\frac{|\mathbf{k}|^2}{4\gamma}\right) \right] \\ &\quad - \sqrt{\frac{\gamma}{\pi}} \sum_{i=1}^{\tilde{N}} q_i^2 + \frac{1}{2} \sum_{i\neq j}^{\tilde{N}} \frac{q_i q_j \operatorname{erfc}(\sqrt{\gamma}|\mathbf{r}_i - \mathbf{r}_j|)}{|\mathbf{r}_i - \mathbf{r}_j|}, \end{aligned} \quad (8.3)$$

where summation is over both the ions and the charge sites, i.e.,  $\tilde{N}$  is the total number of charges in the system, both free and fixed;  $\mathbf{k} \equiv (2\pi/L)\mathbf{l}$  is a Fourier space vector, with  $\mathbf{l} \in \mathbb{Z}^3$ ;  $\gamma$  is the Ewald convergence parameter [253]; and  $\operatorname{erfc}$  is the complementary error function. One can safely ignore the site-site interactions in Eq. (8.3), because this gives a constant contribution to the electrostatic energy  $U_C$ . The self-energy term also drops out of the energy difference, on which the acceptance criterion for the MC trial moves is based [253].

For our simulations we employ the following parameters. (i) Each run consists of 100,000 MC equilibration cycles, where 1 MC cycle is understood to be one trial (translation) move per free ion. (ii) This equilibration is followed by a production run of 250,000 MC cycles to determine the ensemble-averaged ion density profiles  $\rho_{\pm}(\mathbf{r})$ , with  $\mathbf{r}$  the position with respect to the centre of the colloid. (iii) The step size for the ion translational moves is in the range  $[0, 5d]$  and it is adjusted to yield an acceptance ratio of 0.25. (iv) For the Ewald Sums the real space cut-off radius for the third term in Eq. (8.3) is set to  $L/2.5$ , and we use  $\gamma = 0.03$  and  $|\mathbf{l}| < 6$ . This choice of Ewald parameters gives a reasonable approximation to the value of the electrostatic interaction energy. Doubling and halving the number of cycles for several runs showed that the MC parameters give sufficiently equilibrated results for most systems. A possible exception to the perceived equilibration is deep inside the strong-coupled regime, where ion-ion correlations play an important role, as we will explain in Section 8.3.1.

## 8.2.2 The Poisson-Boltzmann Approach

The spherical particle of radius  $a$  in a cubic box models a system with colloid volume fraction  $\eta = (4\pi/3)(a/L)^3$ . The equivalent system in PB theory is described using a spherical Wigner-Seitz (WS) cell model [195, 313–315], where the radius of the WS cell is given by

$$R = \left( \frac{3L^3}{4\pi} \right)^{1/3} = a\eta^{-1/3}, \quad (8.4)$$

and the colloid is located at the centre of the cell. The choice of  $R$  ensures that the volumes, and therefore the average density of colloids/ions is the same in both methods. PB theory is applied, in accordance with the procedure outlined in Refs. [209, 210, 212], to determine the dimensionfree electrostatic potential  $\phi(\mathbf{r})$  and the associated ion density profiles  $\rho_{\pm}(\mathbf{r})$  around the colloid. In our simulations the hard-particle interaction between the ions and the colloid prevent the ions from approaching the colloid's centre closer than a distance of  $a + d/2$ . We therefore assume the same spherical hard-core exclusion volume

for the point ions in PB theory. The colloid's surface charge density is given by  $q(\mathbf{r})$ , which is only nonzero when  $|\mathbf{r}| = a$ . The PB equation for this system may now be written as

$$\nabla^2 \phi(\mathbf{r}) = 4\pi\lambda_B q(\mathbf{r}) + \begin{cases} 0 & |\mathbf{r}| \leq a + d/2 \\ \kappa^2 \sinh(\phi(\mathbf{r})) & |\mathbf{r}| > a + d/2 \end{cases}, \quad (8.5)$$

where  $\kappa^2 = 8\pi\lambda_B\rho_s$  ( $\kappa^{-1}$  is the Debye screening length), with  $\rho_s$  the (yet unknown) bulk ion density and  $\lambda_B$  the Bjerrum length. The Bjerrum length is expressed in terms of measurable system properties ( $\epsilon, T$ ) as

$$\lambda_B = \frac{e^2}{4\pi\epsilon_0\epsilon k_B T}, \quad (8.6)$$

with  $k_B$  Boltzmann's constant and  $T$  the temperature. We impose the following boundary condition

$$\nabla\phi(\mathbf{r}) \cdot \hat{\mathbf{r}}|_{r=R} = 0, \quad (8.7)$$

with  $\hat{\mathbf{r}} \equiv \mathbf{r}/|\mathbf{r}|$ , on the edge of the spherical cell to ensure that the normal component of the electric field vanishes at the boundary, i.e., the WS cell is charge neutral. To solve Eq. (8.5) the charge density  $q(\mathbf{r})$  and the electrostatic potential  $\phi(\mathbf{r})$  are expanded as

$$q(\mathbf{r}) = \sum_{\ell} \sigma_{\ell} \delta(r - a) P_{\ell}(x); \quad (8.8)$$

$$\phi(\mathbf{r}) = \sum_{\ell} \phi_{\ell}(r) P_{\ell}(x), \quad (8.9)$$

with  $\sigma_{\ell}$  and  $\phi_{\ell}(r)$  the surface-charge and potential modes, respectively. Here  $r \equiv |\mathbf{r}|$  and  $x \equiv \mathbf{r} \cdot \hat{\mathbf{z}}$ , with  $\hat{\mathbf{z}}$  the orientation of the colloid's rotational symmetry axis. The  $P_{\ell}$  are  $\ell$ -th order Legendre polynomials. The nonlinear PB equation [Eq. (8.5)] is likewise expanded using Fourier-Legendre (FL) mode decomposition and Taylor expansion of the sinh term around the monopole potential  $\phi_0(r)$ . The higher-order expansion coefficients contain products of Legendre polynomials thereby inducing coupling between the various modes. These products must be rewritten as a sum of other Legendre polynomials [316] to solve for the separate modes using an iterative procedure. The mode coupling this induces necessitates the analysis of a significant number of multipoles even if, for example, only the dipole mode is of interest. See Refs. [209, 210, 212] for more information on the procedure of mode expansion to solve the PB equation for heterogeneously charged colloids.

It is important to note that the PB theory treats the screening ions in the grand-canonical ( $\mu VT$ ) ensemble. The MC simulations were performed in the canonical ensemble, where the number of ions is fixed, to allow for faster exploration of phase space. We fit the bulk ion concentration  $\rho_s$  in PB theory to ensure that the number of positive and negative ions in the WS cell corresponds to the number of ions in the MC simulation box. We consider this condition, coupled with the fact that we study the same colloid volume fraction  $\eta$  in both approaches, sufficient to justify comparison of the results in the two ensembles. The bulk ion concentration is fitted according to the criterion

$$N_{\pm} = N_{\pm, \text{PB}} \equiv \int \rho_{\pm, \text{PB}}(\mathbf{r}) d\mathbf{r}, \quad (8.10)$$

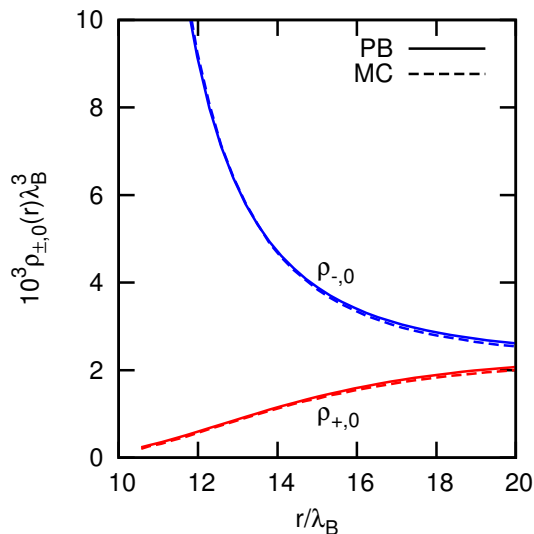


**Figure 8.1:** The monopole moments of the ion distribution  $\rho_{0,\pm}(r)$  as a function of the radial distance  $r$  from a homogeneously charged spherical colloid's centre. Here  $a = 10d$ ,  $\lambda_B = d$ ,  $N_+ = 250$ , and  $N_- = 350$ . The results derived by PB theory are indicated using solid curves and those obtained by MC simulations are indicated using dashed curves. All quantities are expressed in terms of the Bjerrum length  $\lambda_B$  in order to give dimensionfree results. We only show the monopole term, since the higher order modes are negligible.

where the integration is over the region  $|\mathbf{r}| \in [a + d/2, R]$ . One of the two equations is redundant, since solving for  $N_+$  is equivalent to solving for  $N_-$ . The appropriate bulk ion concentration  $\rho_s$ , which comes into the right-hand side of Eq. (8.10) via the dependence of  $\rho_{\pm,\text{PB}}(\mathbf{r})$  on this concentration, is established using an iterative procedure. All PB results presented in this chapter were obtained on an equidistant radial grid of 2,000 points for  $|\mathbf{r}| \in [a + d/2, R]$  by 5-th order Taylor expansion of  $\sinh(\cdot)$  using 6 multipole modes.

### 8.3 Ionic Screening of Janus Particles

In this section we describe our results for the comparison of ion density profiles obtained by MC simulations and by PB theory. A total of 99 systems were considered for each of the three charge-patterned colloids. We used three particle radii  $a = 5d$ ,  $10d$ , and  $15d$ . For every particle radius  $a$ , three salt concentrations were studied: 125, 250, and 375 monovalent cations and anions, respectively, were added to the counter ions already present in the system. This gives  $N_{\pm} = 175, 300, \text{ and } 425$  for the Janus dipole. For the homogeneously and hemispherically charged particle  $N_+ = 125, 250, \text{ and } 375$  when  $N_- = 225, 350, \text{ and } 475$ , respectively. We considered 11 Bjerrum lengths  $\lambda_B/d = 0.01, 0.05, 0.1, 0.25, 0.5, 1.0, 2.0, 4.0, 6.0, 8.0, \text{ and } 10.0$  for each  $a$  and  $N_{\pm}$  combination.

### 8.3.1 Method of Comparison

Figures 8.1, 8.2, and 8.3 show examples of our results for a typical set of parameters:  $a = 10d$ ,  $\lambda_B = d$ , and 250 added anions and cations, respectively. For the homogeneous charge distribution we only give the monopole term ( $\ell = 0$ , Fig. 8.1), since the ion profiles are spherically symmetric within the numerical uncertainty. The azimuthal average of the excess ion concentration  $[\rho_+(\mathbf{r}) - \rho_-(\mathbf{r})]$  is shown for the Janus dipole (Fig. 8.2a) and for the hemispherical surface charge (Fig. 8.3a) to give insight into the shape of the density profiles. The multipole-expanded ion-density profiles [Figs. 8.2(b-c) and 8.3(b-c)] further illustrate the level of correspondence between the MC and PB result for these two systems. Due to the antisymmetry of the problem  $\rho_{+,\ell}(r) = \rho_{-,\ell}(r)(-1)^\ell$  for the Janus dipole. All three systems are in the weak-coupling regime for the ion-ion interactions ( $\alpha \approx 0.06$ ), which explains the good agreement between both methods. Here we use the coupling-parameter  $\alpha$  introduced in Ref. [204], which is a measure for the degree of ion association, to quantify the extent to which strong-coupling effects occur. The definition of  $\alpha$  in terms of our variables reads

$$\alpha = 1 - \frac{1}{K\rho_s} \left( \sqrt{1 + 4K\rho_s} - 1 \right); \quad (8.11)$$

$$K = \frac{\pi}{2} \int_d^{\lambda_B} r^2 \exp\left(\frac{2\lambda_B}{r}\right) dr, \quad (8.12)$$

where the fitted value for  $\rho_s$  is used. In Ref. [204] it is shown that  $\alpha \lesssim 0.5$  implies that strong-coupling effects are not relevant.

The local dimensionfree charge density for the homogeneously charged colloid is  $y \equiv Z\lambda_B/(\kappa a)^2 = 4\pi\sigma\lambda_B/\kappa \approx 5.2$ . This charge density can be used as a nonlinearity parameter and  $y \approx 5.2$  implies that mode coupling occurs [212]. We will come back to this parameter in the context of heterogeneous surface charges later. For the Janus dipole we can clearly observe a nonlinear effect, namely  $\lim_{r \downarrow a} \rho_{\pm,0}(r) \neq \rho_s$ , despite the fact that the charge on the colloid has no intrinsic monopole component. Nonvanishing quadrupole ( $\ell = 2$ ) modes are also induced by mode coupling (nonlinearity).

In order to quantify the difference between results obtained by MC simulations and by PB theory we compare the difference in the distribution of ions in the double layer directly for each mode. To that end, we introduce the functions  $f_\ell$ , which can be applied to a general Janus particle with  $Z_U$  unit charges on the *upper* hemisphere and  $Z_L$  unit charges on the *lower* hemisphere, respectively:

$$f_\ell = \frac{4\pi}{|Z_U| + |Z_L|} \int_{a+d/2}^{L/2} r^2 |\rho_{\ell,\text{MC}}(r) - \rho_{\ell,\text{PB}}(r)| dr, \quad (8.13)$$

where  $\rho_\ell(r) = \rho_{+,\ell}(r) - \rho_{-,\ell}(r)$  gives the ion density difference (ion excess) and we use the labels MC and PB to indicate the origin of the respective profiles. Equation (8.13) has the property that all  $f_\ell$  are 0 when the two profiles are exactly the same and that at least one  $f_\ell > 0$  when they are not. Because we compare results for the cubic geometry of the simulation box to the spherical geometry of the WS cell in PB theory, the upper integration boundary is set to  $L/2 < R$ . In principle the difference in shape and associated boundary conditions imply that we consider the correspondence between a simple-cubic

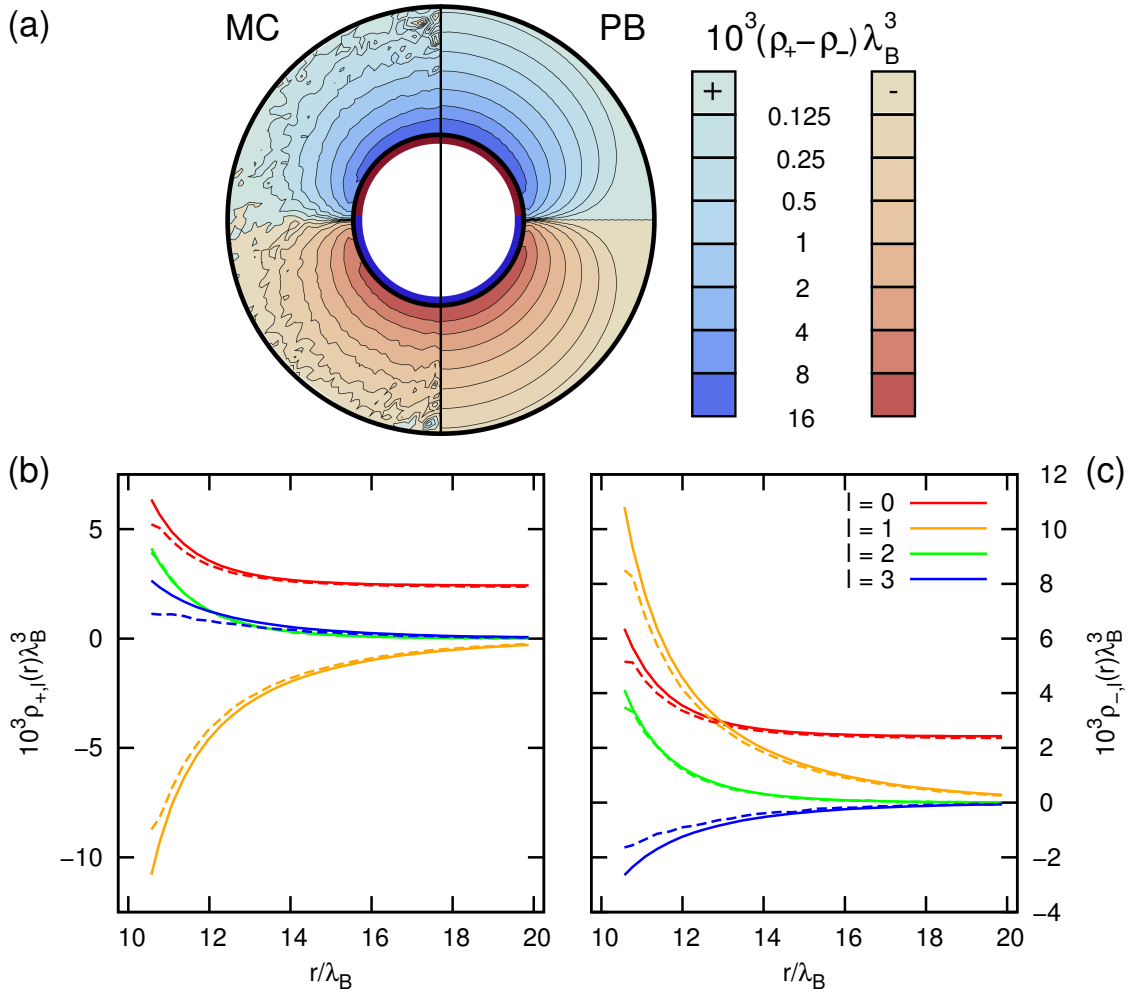


**Figure 8.2:** Ionic screening for a Janus-dipole. Here  $a = 10d$ ,  $\lambda_B = d$ , and  $N_{\pm} = 300$ . (a) Contour plot of the azimuthally averaged ion excess ( $\rho_+ - \rho_-$ ) for the Janus dipole: MC simulations (left) and PB theory (right). The two results are divided by a black vertical line and the radius of the colloid and  $r = L/2$  are indicated using thick black circles. The surface charge distribution inside the colloid is represented by a red and blue semicircle. (b,c) The first four FL modes for the colloid in (a). From red to blue the colours indicate the monopole ( $\ell = 0$ ) through octapole ( $\ell = 3$ ) contribution to the ion densities. The positive ion profiles  $\rho_{+,\ell}(r)$  are given in (b) and the negative ones  $\rho_{-,\ell}(r)$  in (c).

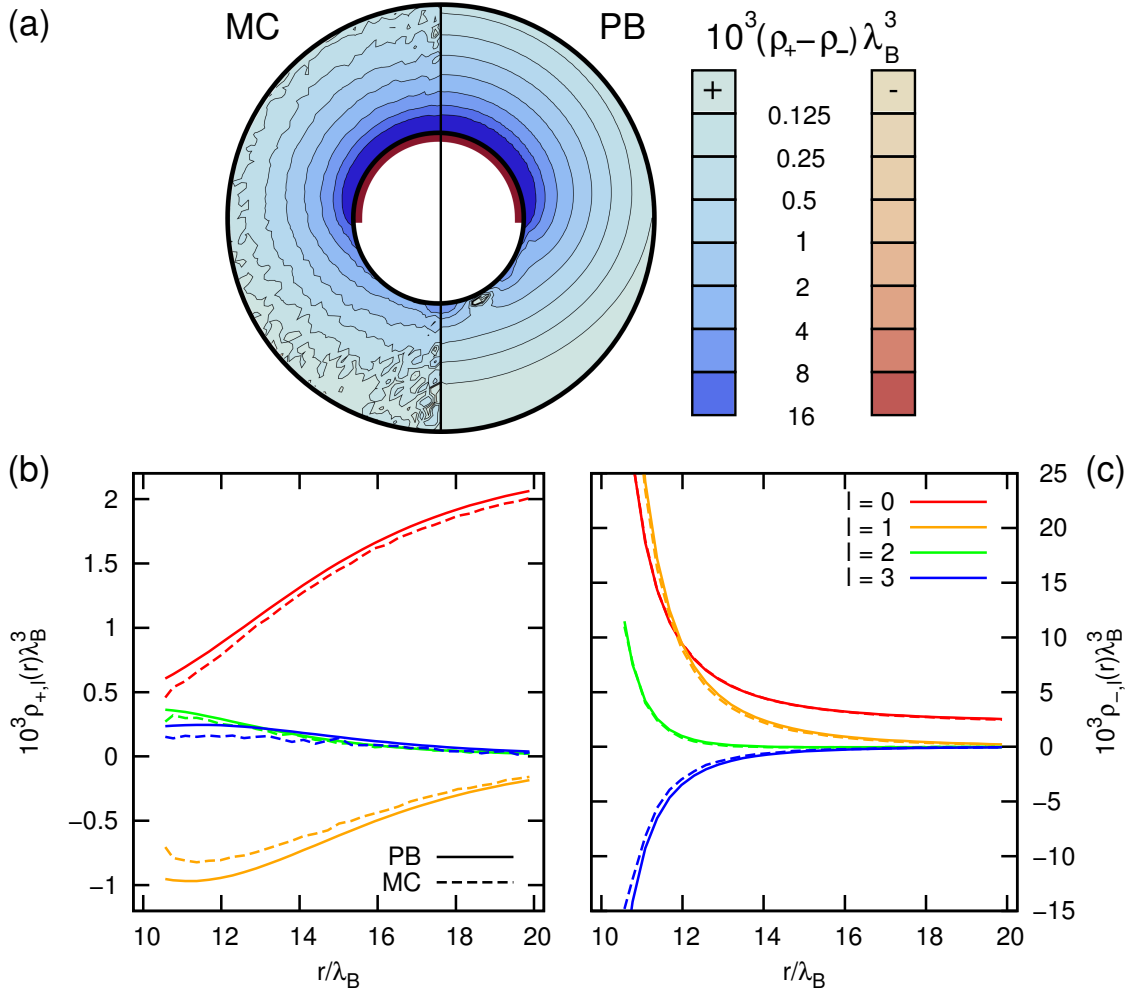


**Figure 8.3:** Ionic screening for a hemispherical charge distribution. Here  $a = 10d$ ,  $\lambda_B = d$ ,  $N_+ = 250$  and  $N_- = 350$ . (a) Contour plot of the azimuthally averaged ion excess ( $\rho_+ - \rho_-$ ) for the hemispherically charged colloid: MC simulations (left) and PB theory (right). The two results are divided by a black vertical line and the radius of the colloid and  $r = L/2$  are indicated using thick black circles. The surface charge distribution inside the colloid is represented by a red and blue semicircle. There is a numerical artefact near the bottom of the particle for the PB results, which can in principle be eliminated by considering a greater number of multipole modes. (b,c) The first four FL modes for the colloid in (a). From red to blue the colours indicate the monopole ( $\ell = 0$ ) through octapole ( $\ell = 3$ ) contribution to the ion densities. The positive ion profiles  $\rho_{+, \ell}(r)$  are given in (b) and the negative ones  $\rho_{-, \ell}(r)$  in (c).

crystal of colloids and a liquid of colloids at the same volume fraction. However, due to the separation of the particles and the level of ionic screening the results are virtually independent of the shape of the volume, when we compare up to  $r = L/2$ . This is the reason why we only considered systems with added salt.

The functions  $f_\ell$  are normalized by  $|Z_U| + |Z_L|$  such that for a homogeneously charged particle  $f_0 = 2$ , when there is a full discrepancy between the MC and PB results. Because the counter charge in the double layer should compensate for the net charge on a colloid, each  $|\rho_0(r)|$  separately will contribute at most  $|Z_U| + |Z_L|$ . When the two profiles do not overlap we obtain twice this number. An example of a strong mismatch between the MC and PB results is found deep in the strong-coupling regime where the MC method predicts a total condensation of counter ions in a very small region close to the surface, whilst PB theory predicts the counter charge to be located in a diffuse layer around the colloid of significant width. For higher order modes the value of  $f_\ell$  is bounded, but the range is not necessarily  $[0, 2]$ . We will come back to the effect of this in Section 8.3.4.

### 8.3.2 Homogeneously Charged Spherical Particles

To prove that the difference functions introduced in Eq. (8.13) give a useful description of the deviation between the MC and PB results, we investigated the property of the monopole term  $f_0$  for homogeneously charged spherical particles, see Fig. 8.4a. We compared the behaviour of  $f_0$  to field-theoretical predictions [213, 214], which were also aimed at establishing a range of validity for PB theory, and showed that there is a good correspondence between the two ranges.

In Refs. [213, 214] the parameter regimes were investigated, for which DH, PB, and SC theory give trustworthy results for the effective interaction between homogeneously charged flat surfaces, respectively. For these flat surfaces parameter space is partitioned into three pieces, see Fig. 8.4b. (I) A region where the Debye-Hückel (DH) approximation can be applied to the PB equation, the screening is linear. (II) A region where the charge of the surfaces becomes higher, the nonlinear PB equation [194, 195] has to be solved in order to determine the effective electrostatic interactions. (III) A region in which the ion-ion correlations close to the surface require the use of Strong-Coupling (SC) theory [196–198]. In Fig. 8.4 the parameters  $\kappa\mu = 2/y$  and  $\Xi = (y/2)\kappa\lambda_B$  represent parameter space in a ‘field-theoretical way’ (see Ref. [214]), with  $y$  the local dimensionfree charge density and  $\mu$  the Gouy-Chapmann length. The Gouy-Chapmann length must not be confused with the chemical potential, which is also usually denoted by  $\mu$ . In literature  $\Xi$  is often referred to as the electrostatic strong-coupling parameter, but we prefer to use the symbol throughout this text to avoid confusion with the ion-association coupling parameter  $\alpha$ . PB theory produces satisfactory results for low values of  $\Xi$ . Ref. [214] sets the value of  $(\Xi \approx 10) \equiv \Xi^*$  for the transition between the PB and SC regimes. The value of  $\kappa\mu$  is of minor importance when  $\Xi < \Xi^*$  as PB theory can be straightforwardly applied to the region where the DH approximation is used in the low-charge limit.

We define  $f_0^* = 0.1$  to be the value for which the transition between the PB-theory and SC-theory regimes occurs. This choice is based on a comparison of the MC and PB ion profiles for the 99 systems containing a homogeneously charged sphere that we investigated. There appears to be a relatively sharp transition in the agreement between

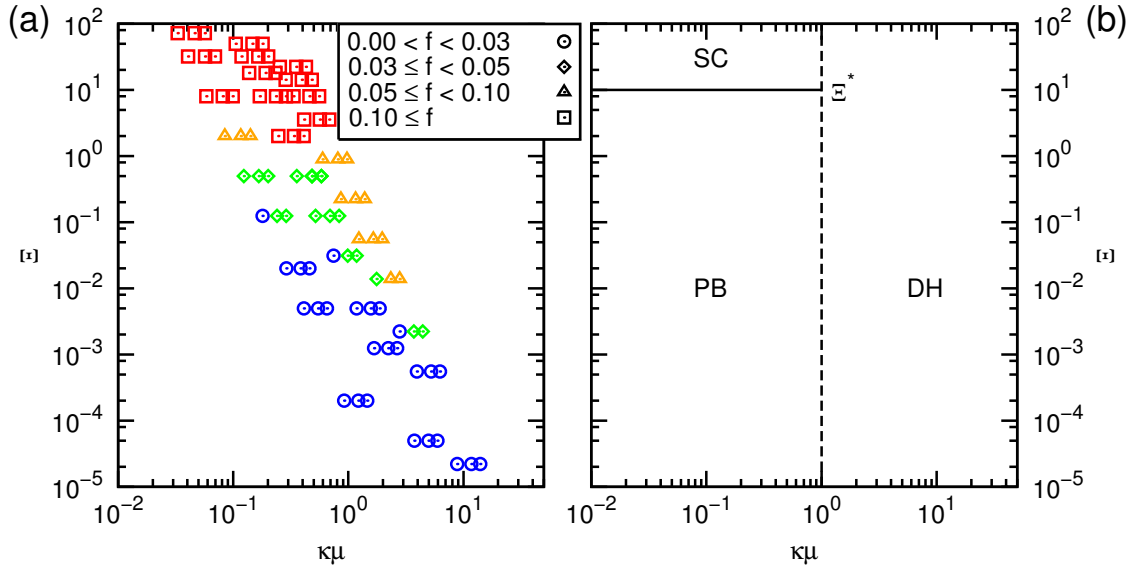


**Figure 8.4:** (a) Comparison of the data obtained by PB theory and by MC simulations according to the difference function  $f_0$  of Eq. (8.13), which quantifies the deviation in the distribution of charge in the ionic double layer. We show  $f_0$  as a function of  $\kappa\mu$ , the ratio of the Gouy-Chapmann and the Debye length, and  $\Xi$ , the strong-coupling parameter, for several of the systems we studied. The legend indicates to which values of  $f$  (only  $f_0$  is shown here) the symbols in the graph correspond. (b) The field-theoretical prediction of Refs. [213, 214] for homogeneously charged flat surfaces partitions parameter space into three regimes. Debye-Hückel (DH), Poisson-Boltzmann (PB), and Strong-Coupling (SC) approximations can be used to obtain acceptable results in the respective domains. The divides between the three regions are indicated using solid and dashed black lines and the value of the PB-SC divide is denoted by  $\Xi^* \approx 10$ .

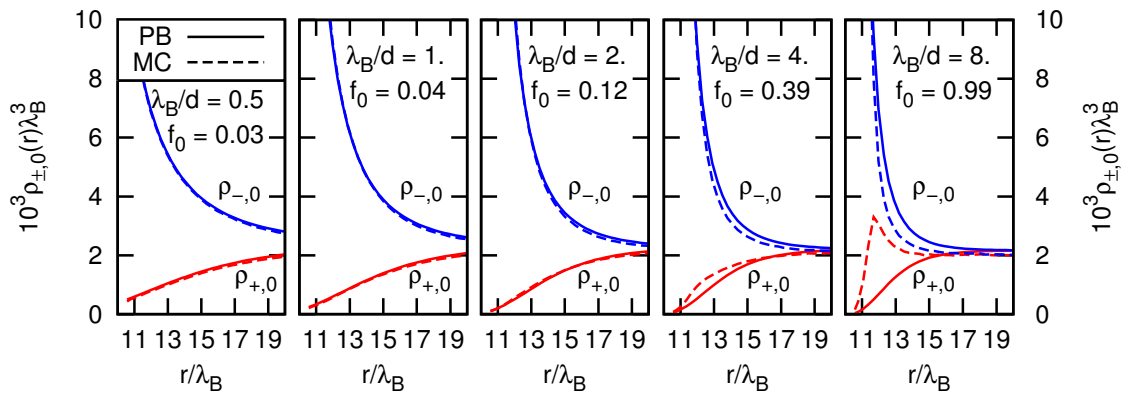


**Figure 8.5:** A series of 5 MC and PB ion density profiles  $\rho_{\pm,0}(r)$  for a homogeneously charged spherical colloid. Here  $a = 10d$ ,  $N_{\pm} = 250$ , and  $\lambda_B/d = 0.5, 1.0, 2.0, 4.0$ , and  $8.0$  (from left to right). The representation in each subgraph is similar to that of Fig. 8.1 and the value of  $\lambda_B$  and  $f_0$  are indicated in the top-right corner. The result for  $\lambda_B = 8d$  shows a very clear deviation in the behaviour of the ions according to PB theory and MC simulations, which can be explained by the fact that the ions experience strong coupling  $\alpha \approx 0.73$ .

the results around  $(f_0 \approx 0.1) \equiv f_0^*$ . This is illustrated in Fig. 8.5, which shows  $f_0$  for a series of systems with  $a = 10d$ ,  $N_{\pm} = 250$ , and 5 different values of  $\lambda_B$ . When  $f_0 < f_0^*$  PB theory gives accurate results and for  $f_0 > f_0^*$  SC theory should be considered. Based on the distribution of  $f_0$  values we obtained for our 99 systems, see Fig. 8.4a, and our value of  $f_0^*$ , we locate the PB-SC divide at  $\Xi^* \approx 1$ . Minor changes in the value of  $f_0^*$  do not significantly change the location of the PB-SC transition in parameter space. However, since what is considered an unacceptable level of the discrepancy between PB and MC results is dependent on the quantities/behaviour we are interested in, there is a measure of arbitrariness to our result. Nevertheless, our approach to this problem and our choice for  $f_0^*$  appears justified since we obtain a similar partitioning of parameter space as was found in Ref. [214], see Fig. 8.4b. This is to be expected for a homogeneously charged sphere, since there is only a geometrical difference with respect to a homogeneously charged plate, which for sufficiently large spheres can be considered small close to the sphere's surface. Our results show that even for relatively small spheres (compared to the size of the ions) there is qualitative agreement.

For completeness we comment on the accuracy of our MC result deep inside the strong-coupling regime. The MC results, also see Fig. 8.5, show that a layer of oppositely charged ions can form on the surface of the particle. The interaction between the charges (sites and ions) is such that the free ions effectively condensate on the particle, see Refs. [306, 311, 317–320] for a more comprehensive account of this phenomenology. The ions in the electrolyte experience similarly strong interactions and form Bjerrum pairs: dipole-like clusters of two oppositely charged ions that are closely bound due to the strong interaction energy [203, 204]. Since we only consider single particle MC trial moves, the formation of Bjerrum pairs interferes with the exploration of phase space in the strong-coupling limit. The clusters hardly move, because most single particle moves that would break up a cluster are rejected on the basis of the energy difference. This results in an ensemble average that is not representative of the system, when the Bjerrum-pair concentration is high ( $\alpha \gtrsim 0.5$ ) [204]. The problem can be overcome by introducing cluster and association-dissociation moves for the Bjerrum pairs to obtain the correct sampling [203, 204]. However, we do not believe that ion condensation and Bjerrum-pair formation will influence our result with regard to the location of  $\Xi^*$ , since these effects only start to play a role for  $\Xi \gg \Xi^*$ .

### 8.3.3 Janus-Dipole Charge Distributions

In this section we apply our method of comparison to higher order Fourier-Legendre (FL) modes of the ion density for the case of a Janus dipole. Figure 8.6 shows the deviation parameter  $f_\ell$  for the first four multipole moments ( $\ell = 0, 1, 2$ , and 3) for the large set of parameters we studied. To apply a representation similar to the one used in Ref. [213] for Janus particles, we introduce the following *modified* parameters:  $y_\Sigma = 2/(\kappa\mu_\Sigma) \equiv (|Z_U| + |Z_L|)\lambda_B/(\kappa a^2)$  and  $\Xi_\Sigma \equiv (y_\Sigma/2)\kappa\lambda_B$ . The sum of the absolute value of the charge on each hemisphere is used, rather than the total charge, which is zero in the case of a Janus dipole. For pure monopoles  $y_\Sigma$  and  $\Xi_\Sigma$  reduce to the original parameters  $y$  and  $\Xi$ . We prefer to express our results in terms of the dimensionfree (absolute) local charge density  $y_\Sigma$  rather than in terms of  $\kappa\mu = 2/y_\Sigma$ , since the former is a more natural quantity

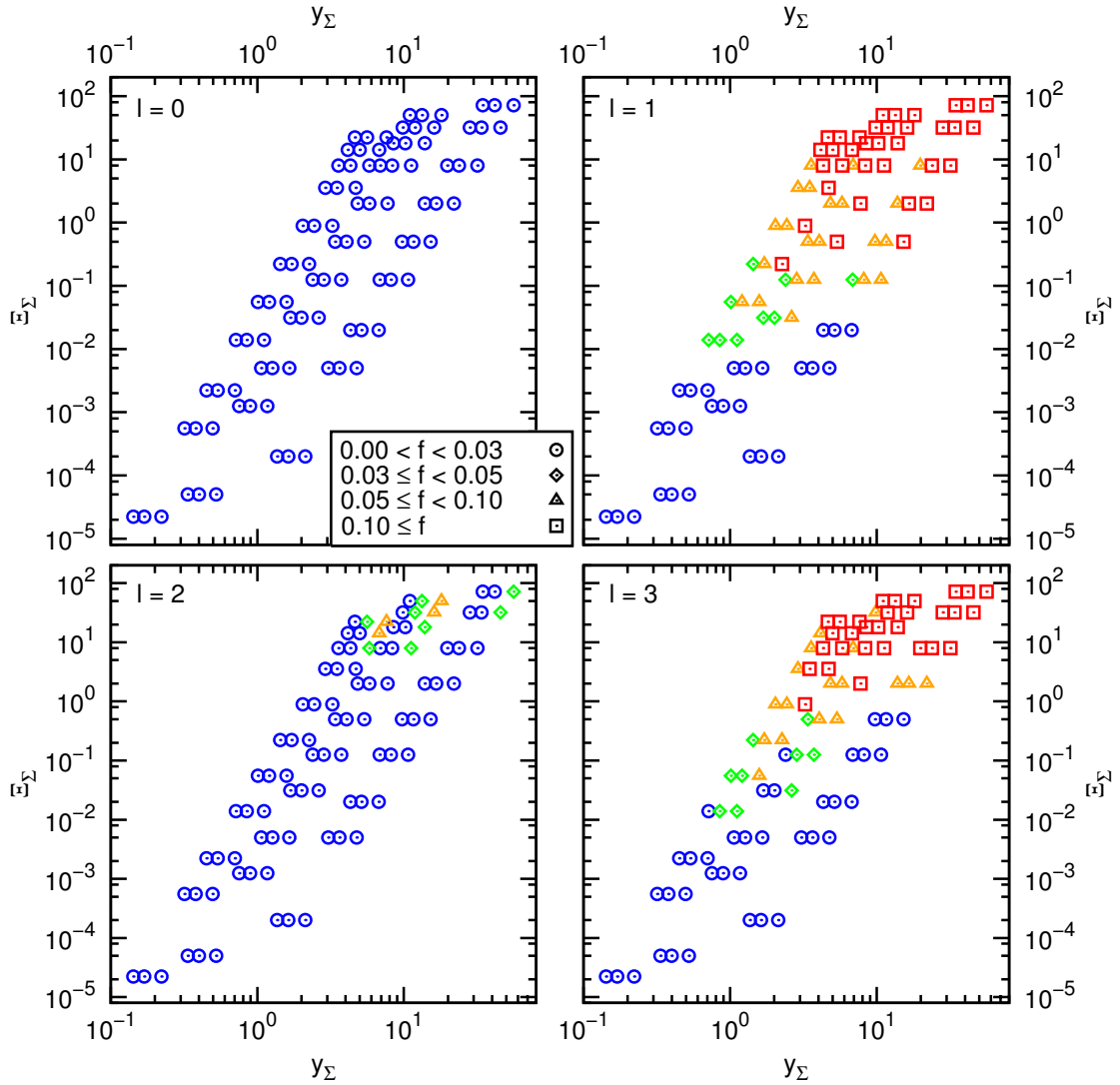


**Figure 8.6:** The deviation  $f_\ell$  in the double layer, determined using the MC simulations and PB theory, for a Janus dipole as a function of the modified charge density  $y_\Sigma$  and the modified strong-coupling parameter  $\Xi_\Sigma$ . The subgraphs show the results for the first four FL modes ( $\ell = 0, 1, 2, 3$ ), corresponding to the monopole, dipole, quadrupole, and octapole term, respectively.

for PB theory of colloid systems. The parameter  $\kappa\mu$  was used in Fig. 8.4 to illustrate the correspondence between our results and the partitioning given in Ref. [214].

The dipole mode  $\ell = 1$  is the first mode to contribute significantly to the double layer around the Janus dipole. For this dipole term we observe trends in the value of  $f_1$  (Fig. 8.6) as a function of  $\mathbf{y}$  and  $\Xi$  similar to those observed for the value of  $f_0$  corresponding to a homogeneously charged sphere (Fig. 8.4a). The property  $\rho_{+,\ell}(r) = \rho_{-,\ell}(r)(-1)^\ell$  ensures that there is no ion excess for the even modes in the PB theory. This implies that the functions  $f_\ell$  ( $\ell$  even) are not particularly suited to establish the difference in the double layer between the MC and PB results for these antisymmetric systems. That is, if we also obtain  $\rho_{+,\ell}(r) \approx \rho_{-,\ell}(r)$  with  $\ell$  even for the MC simulations, but  $\rho_{\pm,\ell,MC} \neq \rho_{\pm,\ell,PB}$ , this difference would not be picked up in  $f_\ell$ , since the comparison is based on the ion excess, which for both methods is zero. The monopole and quadrupole terms in Fig. 8.6 indeed show negligible discrepancy between the MC and PB result compared to the far greater mismatch that is observed for the odd modes. In essence, only the level of numerical noise on the MC data set is measured, which we find to be very acceptable.

Due to this ‘unfortunate shortcoming’ of our method we are forced to base our comparison of the PB and MC results on the odd FL modes only. However, analysis of our results shows that this is not unreasonable, since when there is correspondence between the odd modes, there also appears to be good correspondence between the even modes. This was to be expected due to the coupling between the different modes. The onset of a strong difference in the correspondence between the two results for the dipole mode occurs at  $f_1^* \approx 0.1$ , as is illustrated in Fig. 8.7, which shows the MC and PB ion profiles corresponding to the first four multipole modes for a Janus-dipole charge distribution. For the octapole ( $\ell = 3$ ) term the value of  $f_3^*$  for the accepted level of deviation appears to be slightly larger than 0.1, but on the strength of our results it is difficult to say this with certainty.

Based on the above observations a regime can be distinguished for the leading dipole term where PB theory yields accurate results for the charge profiles in the electric double layer ( $\Xi_\Sigma < \Xi_\Sigma^* \approx 1$ ). For the  $\ell = 1, \dots, 5$  modes ( $\ell = 5$  not shown here) the correspondence between MC and PB results is also sufficient when  $\Xi_\Sigma < \Xi_\Sigma^*$ . The modified parameter  $\Xi_\Sigma$  therefore appears useful to describe parameter space for dipolar Janus particles with regards to quantifying the region where PB theory can be used to describe the system.

### 8.3.4 Hemispherical Charge Distributions

Figure 8.8 shows the deviation  $f_\ell$  ( $\ell = 0, 1, 2, 3$ ) as a function of  $\mathbf{y}_\Sigma$  and  $\Xi_\Sigma$  for spherical particles with a hemispherical charge distribution. The value of  $f_\ell$  is larger for lower values of  $\Xi_\Sigma$  when  $\ell$  is odd, than for  $\ell$  is even. Analysis of the ion density multipole expansion, see Fig. 8.9 for a sample of the data obtained for the 99 systems we studied, reveals that for the even modes the level of deviation  $f_\ell^* \approx 0.1$  sets a rough upper bound to the applicability of PB theory. For the odd modes a value of  $f_\ell^* \approx 0.25$  appears to be more appropriate. At the time of this writing, it is unclear what causes this difference. We speculate the size of the range in which  $f_\ell$  assumes values for odd  $\ell$  may be substantially

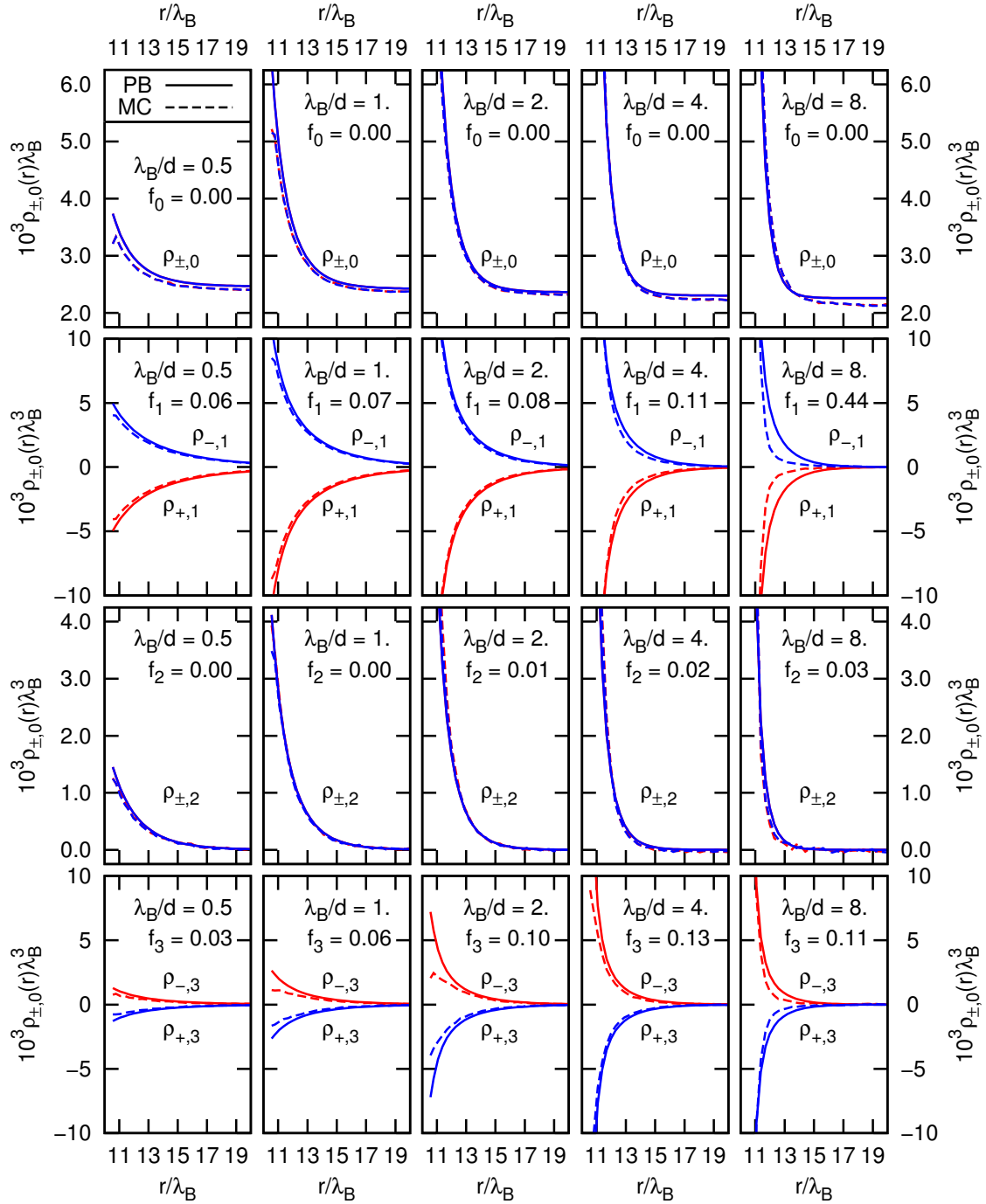


**Figure 8.7:** The analogue of the series representation in Fig. 8.5 for a Janus dipole. The PB results are represented by solid curves and the MC results by dashed curves. We use  $a = 10d$ ,  $N_{\pm} = 300$ , and  $\lambda_B/d = 0.5, 1.0, 2.0, 4.0,$  and  $8.0$  (from left to right). From top to bottom the  $\ell = 0, 1, 2,$  and  $3$ , multipole modes are shown, respectively.

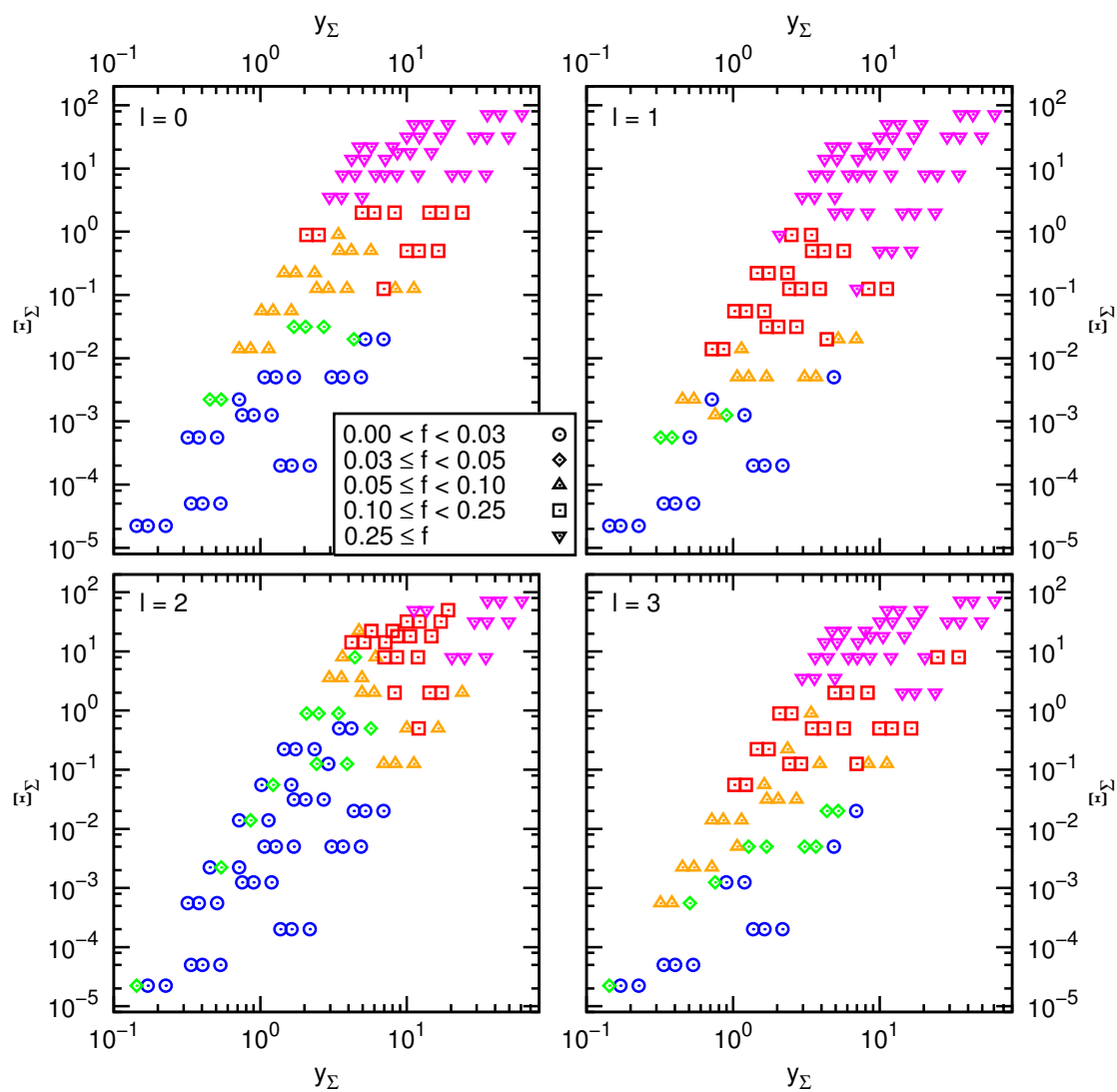


**Figure 8.8:** The deviation  $f_\ell$  in the double layer for a hemispherical charge distribution as a function of  $y_\Sigma$  and  $\Xi_\Sigma$ . The subgraphs show the results for the first four multipole modes ( $\ell = 0, 1, 2, 3$ ), respectively.

larger than for even  $\ell$ . There is an indication that the range for  $f_1$  is indeed larger than that for  $f_0 \in [0, 2]$ , since we obtained  $f_1 \approx 2.53$  for  $\lambda_B = 8d$ , see Fig. 8.9.

Note that the effects of strong coupling are far more apparent for the hemispherical charge distribution than for the other two distributions we considered. This can be explained by the fact that locally the surface charge density is twice as high, even though the total charge density is the same as that of the homogeneously charged sphere. In the MC simulations this is expressed by using 50 divalent charge sites on the upper hemisphere, instead of the monovalent sites used before, since we took the same 100-site distribution [312] for all three particles. With the boundaries  $f_\ell^* \approx 0.1$  and  $f_\ell^* \approx 0.25$  for  $\ell$  odd and even, respectively, we can locate the range of validity of the PB result in the region  $\Xi_\Sigma \lesssim 1$ . However, further investigation of these hemispherical results is warranted to give a good level of confidence in this result.

## 8.4 Conclusion and Outlook

In this chapter we studied the range in parameter space for which the nonlinear Poisson-Boltzmann (PB) theory of Refs. [209–212] accurately describes the behaviour of the ions around a Janus charge-patterned spherical colloid in an electrolyte. We used primitive-model Monte Carlo (MC) simulations to establish the ion density around such a charged particle for a huge set of parameters. By also computing the ion density for the same parameters [212] and comparing the two results we were able to establish a regime in which this PB theory gives a good approximation. This comparison is based on Fourier-Legendre (FL) decomposition of the MC ion density to determine the contribution of the monopole, dipole, quadrupole, . . . charge terms. The theoretical approach also relies on FL decomposition and this enables us to quantify the differences on a mode-by-mode basis.

For a homogeneously charged sphere we compared our range of validity for PB theory to the range found in Refs. [213, 214] for a system of homogeneously charged flat plates in an electrolyte. There is a remarkable correspondence between the two ranges, especially considering the small size of the colloids in relation to the size of the ions that we studied. For such small spheres a greater deviation with respect results of a flat-plate calculation could reasonably be expected. We were also able to show that the range in which the PB results accurately describes the ion density around a spherical Janus-dipole is similar to that found for the homogeneously charged sphere. For particles with a homogeneously charged hemisphere there is an indication that the regime in which PB theory can be applied matches the regimes found for the other particles, but our results are not sufficiently conclusive and further study is required.

Our analysis forms a first step towards obtaining a good understanding of the range in parameter space for which the PB approximation can be applied to describe the behaviour of heterogeneously charged colloids. This is, for instance, relevant to the study of such particles using simulations, where PB-theory-based effective interactions [212] can be used to study the phase behaviour of such particles in the right regime. However, a more extensive study is required to quantify the limitations of the theoretical approximation before we can follow such an approach. In this chapter we only considered the equilibrium



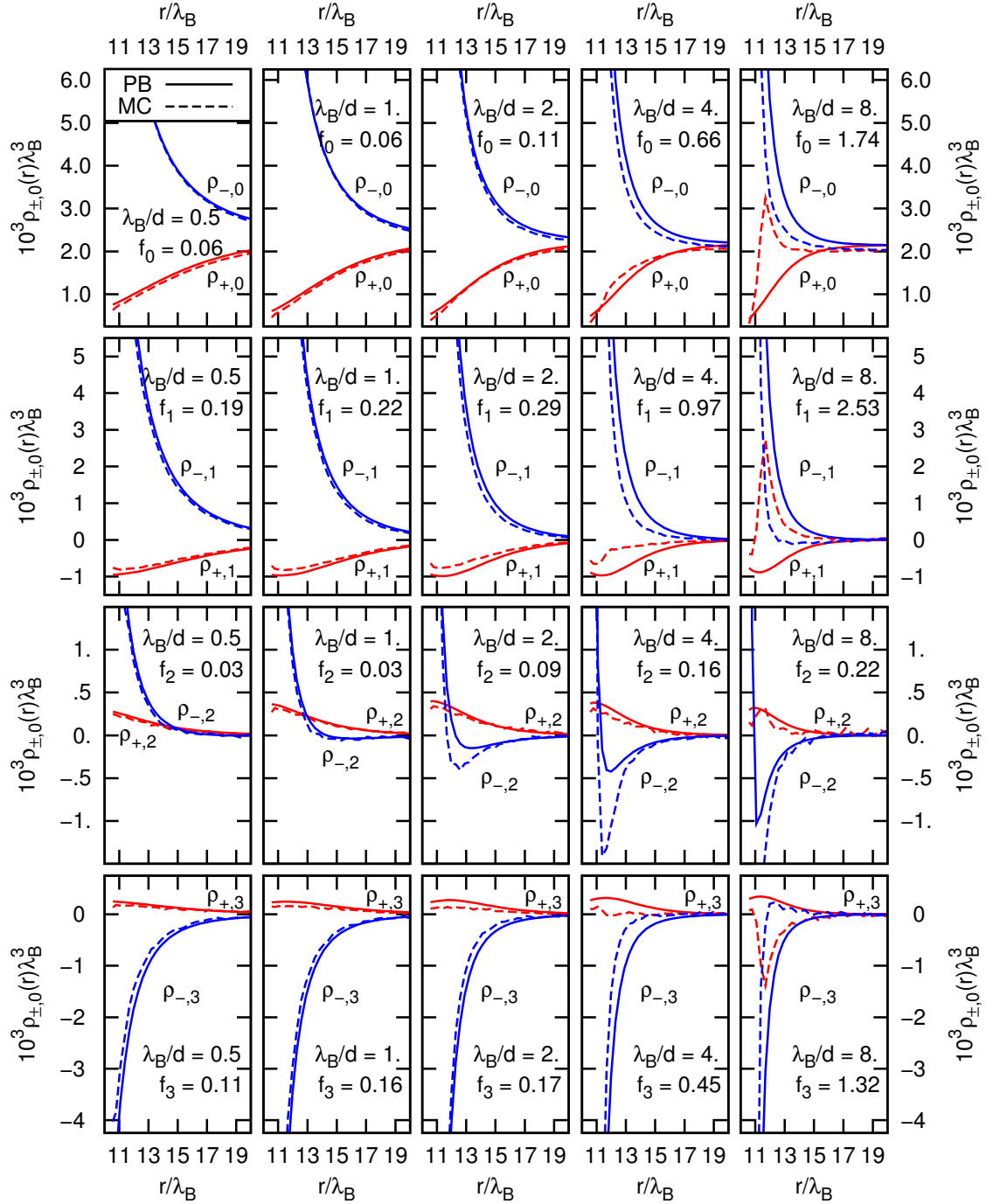


**Figure 8.9:** The analogue of the Fig. 8.7 for a spherical colloid with a homogeneously charged hemisphere:  $a = 10d$ ,  $N_+ = 250$ ,  $N_- = 350$ , and we consider a variety of  $\lambda_B/d = 0.5, 1.0, 2.0, 4.0,$  and  $8.0$  (from left to right). The PB results are indicated using solid curves and the MC results using dashed curves. From top to bottom we show the FL modes for the monopole ( $\ell = 0$ ), dipole ( $\ell = 1$ ), quadrupole ( $\ell = 2$ ), and octapole ( $\ell = 3$ ) term, respectively.

ion density profiles of stationary colloids. The rotational movement of mobile charge-patterned colloids can occur on time scales that would lead to an out-of-equilibrium double layer. What the effect of the out-of-equilibrium ion density is on the screening of the particle and how such effects should be incorporated into effective interaction potentials used in simulations, is left for future investigation.

## 8.5 Acknowledgements

It is a pleasure to thank Dr. Niels Boon, with whom I collaborated on this project, for his work on the theoretical calculations and the many fruitful discussions we had concerning the interpretation of our results and the means by which to compare these.



# A

---

## Analytic Expressions for the Free Energy of Adsorption

---

In this appendix we reproduce the semianalytic expressions for the free energy of adsorption of ellipsoids, cylinders, and spherocylinders, used in Chapter 2 to verify the accuracy of the triangular-tessellation method. We also consider the problem of determining a plane-particle cross section for prolate versions of these three particle species.

## A.1 Semianalytic Free-Energy Expressions

We consider the free energy of adsorption, Eq. (2.4), for ellipsoids, cylinders, and spherocylinders in an analytic way. In the following sections we reproduce the semianalytic expressions for the  $z$  and  $\phi$  dependence of the surface areas  $S$ ,  $S_1$ , and  $S_{12}$  and contact-line length  $L$  required to specify this free energy. We refer to Fig. 2.1 for a visual representation of the quantities and variables used here. To shorten the notation the dependence of the parametrizations on  $z$  and  $\phi$  is often implicit.

The following symmetry properties are employed to describe the system and speed up numerical calculations

$$S_2(z, \phi) = S - S_1(z, \phi); \quad (\text{A.1})$$

$$S_1(-z, \phi) = S - S_1(z, \phi); \quad (\text{A.2})$$

$$S_{12}(-z, \phi) = S_{12}(z, \phi); \quad (\text{A.3})$$

$$L(-z, \phi) = L(z, \phi). \quad (\text{A.4})$$

We can therefore restrict ourselves to define our expressions for the surface areas and contact-line length only on the  $(z, \phi)$ -domain

$$D = [0, \infty) \times [0, \pi/2]. \quad (\text{A.5})$$

It proves necessary to subdivide this domain into disjoint pieces to characterise the system, i.e.,  $S$ ,  $S_1$ ,  $S_{12}$ , and  $L$  only admit a piecewise description.

For all three particle species the numerical evaluation of one dimensional integrals is required to obtain the value of the free energy for a given  $z$  and  $\phi$ . In most cases, a simple equidistant trapezoidal integration algorithm can be used to achieve a high level of precision. However, for oblate spherocylinders the numerical evaluation of the integrals requires a more stable method, because of divergences in the integrands near the integration boundary points. For these particles we use Aitken's method [321] to obtain accurate and stable results.

## A.2 Ellipsoids

For an ellipsoidal particle the domain  $D$  can be partitioned into three subdomains, labelled  $D_{11}$ ,  $D_{12}$ , and  $D_2$ , such that  $D = D_{11} \cup D_{12} \cup D_2$ . These subdomains are

$$D_{11} = [0, p_1] \times [0, \pi/2]; \quad (\text{A.6})$$

$$D_{12} = [p_1, p_2] \times [0, \pi/2]; \quad (\text{A.7})$$

$$D_2 = [p_2, \infty) \times [0, \pi/2], \quad (\text{A.8})$$

where the boundaries are given by

$$p_1 = a \cos \phi; \quad (\text{A.9})$$

$$p_2 = \sqrt{a^2 \cos^2 \phi + b^2 \sin^2 \phi}. \quad (\text{A.10})$$

These boundaries correspond to a transition point in the integration domain and  $z_{\text{det}}(\phi)$ , respectively. The definition of a subdomain used here is slightly convoluted, since  $p_1$  and  $p_2$  depend on  $\phi$ . The notation  $[0, p_1] \times [0, \pi/2]$  is meant to imply that for a specific  $\phi \in [0, \pi/2]$  the  $z$ -domain is the line segment  $[0, p_1(\phi)]$ .

We introduce the following parameters, which are related to the boundary points of a plane-ellipsoid intersection,

$$x_{\pm} = \frac{-b^2 z \tan \phi \pm ab \sqrt{p_2^2 - z^2}}{(a^2 + b^2 \tan^2 \phi) \cos \phi}; \quad (\text{A.11})$$

$$y_{\pm} = \frac{a^2 z \pm ab \tan \phi \sqrt{p_2^2 - z^2}}{(a^2 + b^2 \tan^2 \phi) \cos \phi}. \quad (\text{A.12})$$

to determine the semiaxes of the corresponding cross section. The long semiaxis can be written as

$$a_{\text{cross}} = \frac{1}{2} \sqrt{(y_+ - y_-)^2 + (x_+ - x_-)^2}, \quad (\text{A.13})$$

and the short semi-axis is given by

$$b_{\text{cross}} = b \sqrt{1 - \left(\frac{y_+ + y_-}{2a}\right)^2 - \left(\frac{x_+ + x_-}{2b}\right)^2}. \quad (\text{A.14})$$

We also define the integration kernels and associated integral expressions required to describe the surface area of the particle above the interface

$$\mathcal{I}_1(\eta) = 2\pi ab \sqrt{1 - \left(1 - \left(\frac{b}{a}\right)^2\right) \eta^2}; \quad (\text{A.15})$$

$$\mathcal{I}_2(\eta) = \frac{\mathcal{I}_1(\eta)}{\pi} \arccos \left( \frac{z - a\eta \cos \phi}{b \sin \phi \sqrt{1 - \eta^2}} \right) \quad (\text{A.16})$$

$$\mathcal{J}_1 = \int_{(y_+/a)}^1 \mathcal{I}_1(\eta) d\eta; \quad (\text{A.17})$$

$$\mathcal{J}_2 = \int_{(y_-/a)}^{(y_+/a)} \mathcal{I}_2(\eta) d\eta. \quad (\text{A.18})$$

Using the above parametrizations we can now establish the surface areas and contact-line length required to give the free energy of adsorption. The total surface area of an ellipsoidal particle is given by

$$S = \int_{-1}^1 \mathcal{I}_1(\eta) d\eta, \quad (\text{A.19})$$

the surface area above the interface by

$$S_1(z, \phi) = \begin{cases} \mathcal{J}_1 + \mathcal{J}_2 & (z, \phi) \in D_{11} \\ \mathcal{J}_2 & (z, \phi) \in D_{12} \\ 0 & (z, \phi) \in D_2 \end{cases}, \quad (\text{A.20})$$

the cross-sectional surface area by

$$S_{12}(z, \phi) = \begin{cases} \pi a_{\text{cross}} b_{\text{cross}} & (z, \phi) \in D_{11} \cup D_{12} \\ 0 & (z, \phi) \in D_2 \end{cases}, \quad (\text{A.21})$$

and the contact-line length by

$$L(z, \phi) = \begin{cases} 4a_{\text{cross}} \int_0^{\pi/2} \sqrt{1 - \left( \frac{a_{\text{cross}}^2 - b_{\text{cross}}^2}{a_{\text{cross}}^2} \right) \sin^2 \psi} d\psi & (z, \phi) \in D_{11} \cup D_{12} \\ 0 & (z, \phi) \in D_2 \end{cases}. \quad (\text{A.22})$$

The above expressions hold for both oblate and prolate ellipsoidal particles.

### A.3 Cylinders

For cylinders it is necessary to distinguish between two regimes in polar angle, separated by  $\tilde{\phi} = \arctan(a/b)$ . The angle  $\tilde{\phi}$  arises naturally from the geometry of the cylinder: for  $\phi > \tilde{\phi}$  the interface cannot intersect the shaft of the cylinder without intersecting one of its caps. The domain is decomposed according to  $D = D_{11} \cup D_{12} \cup D_2 \cup D_3$ , with

$$D_{11} = [0, p_1] \times [0, \tilde{\phi}]; \quad (\text{A.23})$$

$$D_{12} = [0, p_1] \times [\tilde{\phi}, \pi/2]; \quad (\text{A.24})$$

$$D_2 = [p_1, p_2] \times [0, \pi/2]; \quad (\text{A.25})$$

$$D_3 = [p_2, \infty) \times [0, \pi/2], \quad (\text{A.26})$$

where the boundaries

$$p_1 = \begin{cases} a \cos \phi - b \sin \phi & \phi \in [0, \tilde{\phi}] \\ b \sin \phi - a \cos \phi & \phi \in [\tilde{\phi}, \pi/2] \end{cases}; \quad (\text{A.27})$$

$$p_2 = a \cos \phi + b \sin \phi, \quad (\text{A.28})$$

represent the position of the bottom point of the edge between the shaft and cap of a cylinder and  $z_{\text{det}}(\phi)$ , respectively.

We introduce the following parametrizations to shorten the notation for the surface areas and the contact-line length

$$q_{\pm} = \frac{z \pm a \cos \phi}{b \sin \phi}; \quad (\text{A.29})$$

$$u_{\pm} = \arccos q_{\pm} - q_{\pm} \sqrt{1 - q_{\pm}^2}; \quad (\text{A.30})$$

$$v_{\pm} = q_{\pm} \arccos q_{\pm} - \sqrt{1 - q_{\pm}^2}; \quad (\text{A.31})$$

$$w_{\pm} = b^2(u_{\pm} \pm 2v_{\pm} \tan \phi). \quad (\text{A.32})$$

The  $q_{\pm}$  specify the points of intersection between the interface and one of the cylinder's caps and  $u_{\pm}$ ,  $v_{\pm}$ , and  $w_{\pm}$  follow from the evaluation of surface integrals. The integration kernel

$$\mathcal{K}(\psi) = \frac{2b}{\cos \phi} \sqrt{1 - \sin^2 \phi \sin^2 \psi}, \quad (\text{A.33})$$

is used to determine the contact-line length. The above definitions lead to the following expressions for  $S$ ,  $S_1$ ,  $S_{12}$ , and  $L$ . The total surface area is given by

$$S = 2\pi b^2 + 4\pi ab, \quad (\text{A.34})$$

the surface area above the interface by

$$S_1(z, \phi) = \begin{cases} \pi b^2(1 - 2q_- \tan \phi) & (z, \phi) \in D_{11} \\ w_+ + w_- & (z, \phi) \in D_{12} \\ w_- & (z, \phi) \in D_2 \\ 0 & (z, \phi) \in D_3 \end{cases}, \quad (\text{A.35})$$

the area excluded from the interface by

$$S_{12}(z, \phi) = \begin{cases} \frac{\pi b^2}{\cos \phi} & (z, \phi) \in D_{11} \\ \frac{b^2(u_- - u_+)}{\cos \phi} & (z, \phi) \in D_{12} \\ \frac{b^2 u_-}{\cos \phi} & (z, \phi) \in D_2 \\ 0 & (z, \phi) \in D_3 \end{cases}, \quad (\text{A.36})$$

and contact-line length by

$$L(z, \phi) = \begin{cases} \int_{-\pi/2}^{\pi/2} \mathcal{K}(\psi) d\psi & (z, \phi) \in D_{11} \\ \int_{\arcsin q_-}^{\arcsin q_+} \mathcal{K}(\psi) d\psi + 2b\sqrt{1 - q_+^2} + 2b\sqrt{1 - q_-^2} & (z, \phi) \in D_{12} \\ \int_{\arcsin q_-}^{\pi/2} \mathcal{K}(\psi) d\psi + 2b\sqrt{1 - q_-^2} & (z, \phi) \in D_2 \\ 0 & (z, \phi) \in D_3 \end{cases}. \quad (\text{A.37})$$

The above expressions hold for both oblate and prolate cylindrical particles.

## A.4 Spherocylinders

For spherocylinders the geometrical problem of a flat interface intersecting a particle is even more complicated and we are therefore forced to split this section into two parts. In the first we consider prolate spherocylinders and in the second we consider oblate spherocylinders. Recall that our definition for the long semiaxis  $a$  of a prolate spherocylinder includes the hemispherical caps and that our definition for the semiaxis  $b$  of an oblate spherocylinder accounts for the particle's toroidal rim.

### A.4.1 Prolate Spherocylinders

For a prolate spherocylinder there are two polar-angle regimes, separated by the angle  $\tilde{\phi} = \arctan((a-b)/b)$ . The domain  $D$  may be written as  $D = D_{11} \cup D_{12} \cup D_2 \cup D_3 \cup D_4$ , with

$$D_{11} = [0, p_1] \times [0, \tilde{\phi}]; \quad (\text{A.38})$$

$$D_{12} = [0, p_1] \times [\tilde{\phi}, \pi/2]; \quad (\text{A.39})$$

$$D_2 = [p_1, p_2] \times [0, \pi/2]; \quad (\text{A.40})$$

$$D_3 = [p_2, p_3] \times [0, \pi/2]; \quad (\text{A.41})$$

$$D_4 = [p_3, \infty) \times [0, \pi/2], \quad (\text{A.42})$$

and

$$p_1 = \begin{cases} (a-b) \cos \phi - b \sin \phi & \phi \in [0, \tilde{\phi}] \\ b \sin \phi - (a-b) \cos \phi & \phi \in [\tilde{\phi}, \pi/2] \end{cases}; \quad (\text{A.43})$$

$$p_2 = (a-b) \cos \phi + b \sin \phi; \quad (\text{A.44})$$

$$p_3 = (a-b) \cos \phi + b. \quad (\text{A.45})$$

The three boundaries correspond to the position of the bottom and top of the edge between the particle's shaft and hemispherical cap, and  $z_{\text{det}}(\phi)$ , respectively.

We introduce the following parametrizations to shorten the notation for the surface areas and the contact-line length

$$q_{\pm} = \frac{z \pm (a-b) \cos \phi}{b \sin \phi}; \quad (\text{A.46})$$

$$s_{\pm} = \cos^2 \phi \sqrt{1 + (1 - q_{\pm}^2) \tan^2 \phi} \pm q_{\pm} \sin^2 \phi; \quad (\text{A.47})$$

$$t_{\pm} = \arcsin q_{\pm} + q_{\pm} \sqrt{1 - q_{\pm}^2}; \quad (\text{A.48})$$

$$u_{\pm} = \arccos q_{\pm} - q_{\pm} \sqrt{1 - q_{\pm}^2}; \quad (\text{A.49})$$

$$v_{\pm} = q_{\pm} \arccos q_{\pm} - \sqrt{1 - q_{\pm}^2}; \quad (\text{A.50})$$

$$w_{\pm} = q_{\pm} \cos \phi \sqrt{1 - q_{\pm}^2}; \quad (\text{A.51})$$

$$x_{\pm} = \sqrt{1 - q_{\pm}^2 \sin^2 \phi}; \quad (\text{A.52})$$

$$y_{\pm} = \arccos \left( \frac{q_{\pm} \cos \phi}{x_{\pm}} \right); \quad (\text{A.53})$$

$$\lambda_+ = x_+ y_+; \quad (\text{A.54})$$

$$\lambda_- = x_- (\pi - y_-); \quad (\text{A.55})$$

$$\mu_+ = y_+ (1 - q_+^2 \sin^2 \phi); \quad (\text{A.56})$$

$$\mu_- = (1 - q_-^2 \sin^2 \phi) (\pi - y_-). \quad (\text{A.57})$$

We also require the integration kernels

$$\mathcal{K}(\psi) = \frac{2b}{\cos \phi} \sqrt{1 - \sin^2 \phi \sin^2 \psi}; \quad (\text{A.58})$$

$$\mathcal{L}_{\pm}(h) = 2b^2 \arccos \left( \frac{(h \mp q_{\pm}) \tan \phi}{\sqrt{1 - h^2}} \right), \quad (\text{A.59})$$

to determine the following physical quantities, by which the free energy of adsorption can be specified. The total surface area is given by

$$S = 4\pi ab, \quad (\text{A.60})$$

the surface area above the interface by

$$S_1(z, \phi) = \begin{cases} 2\pi b^2(1 - q_- \tan \phi) & (z, \phi) \in D_{11} \\ \int_{-q_-}^{s_-} \mathcal{L}_-(h) dh - \int_{q_+}^{s_+} \mathcal{L}_+(h) dh + \\ \pi b^2(2 - q_+ - q_-) + 2b^2(v_+ - v_-) \tan \phi & (z, \phi) \in D_{12} \\ \int_{-q_-}^{s_-} \mathcal{L}_-(h) dh + \pi b^2(1 - q_-) - 2b^2 v_- \tan \phi & (z, \phi) \in D_2 \\ 2\pi b(p_3 - z) & (z, \phi) \in D_3 \\ 0 & (z, \phi) \in D_4 \end{cases}, \quad (\text{A.61})$$

the area excluded from the interface by

$$S_{12}(z, \phi) = \begin{cases} \frac{\pi b^2}{\cos(\phi)} & (z, \phi) \in D_{11} \\ \frac{b^2(t_+ - t_-)}{\cos(\phi)} + b^2(\mu_+ - w_+) + b^2(\mu_- + w_-) & (z, \phi) \in D_{12} \\ \frac{b^2 u_-}{\cos \phi} + b^2(\mu_- + w_-) & (z, \phi) \in D_2 \\ \pi b^2 x_-^2 & (z, \phi) \in D_3 \\ 0 & (z, \phi) \in D_4 \end{cases}, \quad (\text{A.62})$$

and the contact-line length by

$$L(z, \phi) = \begin{cases} \int_{-\pi/2}^{\pi/2} \mathcal{K}(\psi) d\psi & (z, \phi) \in D_{11} \\ \int_{\arcsin q_-}^{\arcsin q_+} \mathcal{K}(\psi) d\psi + 2b(\lambda_+ + \lambda_-) & (z, \phi) \in D_{12} \\ \int_{\arcsin q_-}^{\pi/2} \mathcal{K}(\psi) d\psi + 2b\lambda_- & (z, \phi) \in D_2 \\ 2\pi b x_- & (z, \phi) \in D_3 \\ 0 & (z, \phi) \in D_4 \end{cases} . \quad (\text{A.63})$$

Note the sign asymmetry in the integration boundaries of the  $\mathcal{L}_{\pm}$  integrals in Eq. (A.61). This asymmetry is induced by the  $\mp$ -sign in Eq. (A.59). Although the appearance of these asymmetries may seem counter intuitive, we extensively verified that these equations indeed hold.

### A.4.2 Oblate Spherocylinders

For oblate particles we find two polar-angle regimes, separated by  $\tilde{\phi} = \arctan(a/(b-a))$ . The domain  $D$  may be written as  $D = D_{11} \cup D_{12} \cup D_2 \cup D_3 \cup D_4$ , with

$$D_{11} = [0, p_1] \times [0, \tilde{\phi}]; \quad (\text{A.64})$$

$$D_{12} = [0, p_1] \times [\tilde{\phi}, \pi/2]; \quad (\text{A.65})$$

$$D_2 = [p_1, p_2] \times [0, \pi/2]; \quad (\text{A.66})$$

$$D_3 = [p_2, p_3] \times [0, \pi/2]; \quad (\text{A.67})$$

$$D_4 = [p_3, \infty) \times [0, \pi/2], \quad (\text{A.68})$$

and

$$p_1 = \begin{cases} a \cos \phi - (b-a) \sin \phi & \phi \in [0, \tilde{\phi}] \\ (b-a) \sin \phi - a \cos \phi & \phi \in [\tilde{\phi}, \pi/2] \end{cases}; \quad (\text{A.69})$$

$$p_2 = (b-a) \sin \phi + a \cos \phi; \quad (\text{A.70})$$

$$p_3 = (b-a) \sin \phi + a. \quad (\text{A.71})$$

The three boundaries give the top point of the lower circular edge between the toroidal rim and the cylindrical interior of the particle, the bottom point of the top circular edge, and  $z_{\text{det}}(\phi)$ , respectively.

To shorten the notation of the surface areas and contact-line length related to the adsorption of the particle at a flat interface we introduce the following variables and

functions

$$\begin{aligned} x_{\pm}^t &= \cos \phi (z - (b - a) \sin \phi) \\ &\quad \pm \sin \phi \sqrt{(a + z - (b - a) \sin \phi)(a - z + (b - a) \sin \phi)}; \end{aligned} \quad (\text{A.72})$$

$$\begin{aligned} x_{\pm}^b &= \cos \phi (z + (b - a) \sin \phi) \\ &\quad \pm \sin \phi \sqrt{(a + z + (b - a) \sin \phi)(a - z - (b - a) \sin \phi)}; \end{aligned} \quad (\text{A.73})$$

$$\mu_{\pm}^i = 2\pi a \left( a - x_{\pm}^i + (b - a) \arccos \left( \frac{x_{\pm}^i}{a} \right) \right); \quad (\text{A.74})$$

$$h(x) = z \sin \phi - \frac{x - z \cos \phi}{\tan \phi} \quad (\text{A.75})$$

$$\begin{aligned} k(x) &= (b - a)^2 \arccos \left( \frac{h(x)}{b - a} \right) \\ &\quad - h(x) \sqrt{(b - a)^2 - h^2(x)}. \end{aligned} \quad (\text{A.76})$$

$$r(x) = (b - a) + \sqrt{a^2 - x^2} \quad (\text{A.77})$$

$$w(x) = \sqrt{r^2(x) - h^2(x)}, \quad (\text{A.78})$$

where the  $i$  in Eq. (A.74) can be either ‘ $t$ ’ or ‘ $b$ ’, which stands for ‘top’ and ‘bottom’, respectively. We use a prime to denote the derivative with respect to  $x$ , e.g.,  $h'(x) \equiv \partial h(x)/\partial x$ , in the following integration kernels

$$\mathcal{N}_1(x) = \frac{2ar(x)}{\sqrt{a^2 - x^2}} \arccos \left( \frac{h(x)}{r(x)} \right); \quad (\text{A.79})$$

$$\mathcal{N}_2(x) = \frac{2w(x)}{\sin \phi}; \quad (\text{A.80})$$

$$\mathcal{N}_3(x) = 2\sqrt{1 + (h'(x))^2 + (w'(x))^2}. \quad (\text{A.81})$$

Using the above parametrizations, equations, and kernels the physical quantities relevant to the free energy of adsorption can be specified. The total surface area of the particle is given by

$$S = 2\pi \left( b^2 + (\pi - 2)ba - (\pi - 3)a^2 \right), \quad (\text{A.82})$$

the surface area above the interface by

$$S_1(z, \phi) = \begin{cases} \int_{x_-^t}^{x_+^b} \mathcal{N}_1(x) dx + \pi(b-a)^2 + \mu_+^b & (z, \phi) \in D_{11} \\ \int_{-a}^a \mathcal{N}_1(x) dx + k(a) + k(-a) & (z, \phi) \in D_{12} \\ \int_{x_-^t}^a \mathcal{N}_1(x) dx + k(a) & (z, \phi) \in D_2 \\ \int_{x_-^t}^{x_+^t} \mathcal{N}_1(x) dx & (z, \phi) \in D_3 \\ 0 & (z, \phi) \in D_4 \end{cases}, \quad (\text{A.83})$$

the area excluded from the interface by

$$S_{12}(z, \phi) = \begin{cases} \int_{x_-^t}^{x_+^b} \mathcal{N}_2(x) dx & (z, \phi) \in D_{11} \\ \int_{-a}^a \mathcal{N}_2(x) dx & (z, \phi) \in D_{12} \\ \int_{x_-^t}^a \mathcal{N}_2(x) dx & (z, \phi) \in D_2 \\ \int_{x_-^t}^{x_+^t} \mathcal{N}_2(x) dx & (z, \phi) \in D_3 \\ 0 & (z, \phi) \in D_4 \end{cases}, \quad (\text{A.84})$$

and the contact-line length by

$$L(z, \phi) = \begin{cases} \int_{x_-^t}^{x_+^b} \mathcal{N}_3(x) dx & (z, \phi) \in D_{11} \\ \int_{-a}^a \mathcal{N}_3(x) dx + 2w(a) + 2w(-a) & (z, \phi) \in D_{12} \\ \int_{x_-^t}^a \mathcal{N}_3(x) dx + 2w(a) & (z, \phi) \in D_2 \\ \int_{x_-^t}^{x_+^t} \mathcal{N}_3(x) dx & (z, \phi) \in D_3 \\ 0 & (z, \phi) \in D_4 \end{cases}. \quad (\text{A.85})$$

## A.5 Plane-Particle Intersection

In this section we give the parametrization of the cross sections that result from the intersection of a plane and a prolate ellipsoid, cylinder, or spherocylinder. As explained



in Section 2.4, these cross sections may be used to gain insight into two-dimensional confocal-microscopy data and to test the accuracy of particle-tracking algorithms. The symmetry properties of the particles allow us to only consider  $z > 0$  and  $\phi \in [0, \pi/2]$  to completely specify the solution to this geometrical problem.

### A.5.1 Ellipsoids

In this paragraph we introduce a parametrization of the intersection between a plane and a uniaxial ellipsoid. The following notations are used to simplify the expression for the cross section

$$B(\phi) = \cos \phi \sqrt{a^2 + b^2 \tan^2 \phi}; \quad (\text{A.86})$$

$$x_1(z, \phi) = b^2 z \tan \phi / \cos \phi; \quad (\text{A.87})$$

$$x_2(z, \phi) = \sqrt{a^2 b^2 (a^2 - z^2 / \cos^2 \phi + b^2 \tan^2 \phi)}; \quad (\text{A.88})$$

$$x_3(z, \phi) = a^2 + b^2 \tan^2 \phi; \quad (\text{A.89})$$

$$x_{\pm}(z, \phi) = -\frac{x_1(z, \phi) \mp x_2(z, \phi)}{x_3(z, \phi)}; \quad (\text{A.90})$$

$$y_{\pm}(x, z, \phi) = \pm b \sqrt{1 - (x/b)^2 - ((z/\cos \phi + x \tan \phi)/a)^2}; \quad (\text{A.91})$$

$$\zeta(x, z, \phi) = a \sqrt{1 - (x/b)^2 - (y_+(x, z, \phi)/b)^2}; \quad (\text{A.92})$$

$$\xi(x, z, \phi) = \frac{(z + x \sin \phi) \tan \phi}{|z/\cos \phi + x \tan \phi| \cos \phi}; \quad (\text{A.93})$$

$$\mu(x, z, \phi) = \zeta(x, z, \phi) \cdot \begin{cases} 1 & \xi(x, z, \phi) \geq 0 \\ -1 & \xi(x, z, \phi) < 0 \end{cases}; \quad (\text{A.94})$$

$$c(x, z, \phi) = (x \cos \phi + \mu(x, z, \phi) \sin \phi, y_{\pm}(x, z, \phi), z). \quad (\text{A.95})$$

Calculations were performed in a frame where the colloid is oriented along the  $z$ -axis and the plane is at an angle, which is inspired by the approach of Ref. [143]. By rotating this frame such that the colloid is at an angle and the plane is horizontal, we obtained the parametrization  $c(x, z, \phi)$ , which is used to specify boundary to the cross section

$$C(z, \phi) = \begin{cases} (x, \pm b \sqrt{1 - (z/b)^2 + (x/a)^2}, z) & z \in [0, b] \wedge \phi = \pi/2 \\ |x| \leq a \sqrt{1 - (z/b)^2} & \\ c(x, z, \phi) & \\ x \in [x_-(z, \phi), x_+(z, \phi)] & z \in [0, B(\phi)] \wedge \phi \in [0, \pi/2) \\ \emptyset & \text{else} \end{cases}, \quad (\text{A.96})$$

with  $\emptyset$  the empty set (no intersection). We put the vector-valued functions directly above their domain in the left column and we specify the range of applicability in the right column. It is implied that, in order to obtain the entire boundary, both the branches (resulting from the  $\pm$ -sign) of the parametrizations have to be evaluated. For  $\phi = \pi/2$  our description results in degeneracies in the frame of reference and we therefore treat it as a special case.

### A.5.2 Cylinders

For a prolate cylinder we introduce the following notations to describe the intersection with a horizontal plane

$$\tilde{\phi} = \arctan(a/b); \quad (\text{A.97})$$

$$B(\phi) = a \cos \phi + b \sin \phi; \quad (\text{A.98})$$

$$p_1(\phi) = a \cos \phi - b \sin \phi; \quad (\text{A.99})$$

$$p_{2,\pm}(z, \phi) = \pm a / \tan \phi - z / \sin \phi; \quad (\text{A.100})$$

$$B_0(z, \phi) = \begin{cases} -b & z \geq -p_1(\phi) \\ p_{2,-}(z, \phi) & z < -p_1(\phi) \end{cases}; \quad (\text{A.101})$$

$$B_1(z, \phi) = \begin{cases} b & z < p_1(\phi) \\ p_{2,+}(z, \phi) & z \geq p_1(\phi) \end{cases}; \quad (\text{A.102})$$

$$c(x, z, \phi) = \left( (x + z \sin \phi) / \cos \phi, \pm \sqrt{b^2 - x^2}, z \right). \quad (\text{A.103})$$

Note the similarity between these parameters and the ones presented in Section A.3. Using Eqs. (A.97) - (A.103) the boundary of the plane-shaft cross section is written as

$$S(z, \phi) = \begin{cases} \begin{array}{l} (x, \pm \sqrt{b^2 - z^2}, z) \\ x \in [-a, a] \end{array} & z \in [0, b] \wedge \phi = \pi/2 \\ \begin{array}{l} c(x, z, \phi) \\ x \in [B_0(z, \phi), B_1(z, \phi)] \end{array} & z \in [0, B(\phi)] \wedge \phi \in [0, \pi/2) \\ \emptyset & \text{else} \end{cases}. \quad (\text{A.104})$$

To specify the intersection of the cylinder's caps with the plane we require a relation that gives the relevant parametrizations and corresponding domains for all possible orientations

$$\tilde{c}(z, \phi) = \begin{cases} \begin{array}{l} \overline{(-(a + z \cos \phi) / \sin \phi, y_0, z) \cup ((a - z \cos \phi) / \sin \phi, y_1, z)} \\ y_0 \in [-\sqrt{b^2 - p_{2,-}^2(z, \phi)}, \sqrt{b^2 - p_{2,-}^2(z, \phi)}] \\ y_1 \in [-\sqrt{b^2 - p_{2,+}^2(z, \phi)}, \sqrt{b^2 - p_{2,+}^2(z, \phi)}] \end{array} & \begin{array}{l} z < -p_1(\phi) \\ \wedge \\ z > p_1(\phi) \end{array} \\ \begin{array}{l} \overline{(-(a + z \cos \phi) / \sin \phi, y_0, z)} \\ y_0 \in [-\sqrt{b^2 - p_{2,-}^2(z, \phi)}, \sqrt{b^2 - p_{2,-}^2(z, \phi)}] \end{array} & z < -p_1(\phi) \\ \begin{array}{l} \overline{((a - z \cos \phi) / \sin \phi, y_1, z)} \\ y_1 \in [-\sqrt{b^2 - p_{2,+}^2(z, \phi)}, \sqrt{b^2 - p_{2,+}^2(z, \phi)}] \end{array} & z > p_1(\phi) \end{cases}. \quad (\text{A.105})$$

The boundary to the plane-cap cross section(s) - there may be two depending on the particle's orientation - is given by

$$E(z, \phi) = \begin{cases} \begin{array}{l} \overline{(-a, y, z) \cup (a, y, z)} \\ y \in [-\sqrt{b^2 - z^2}, \sqrt{b^2 - z^2}] \end{array} & z \in [0, b] \wedge \phi = \pi/2 \\ \tilde{c}(z, \phi) & z \in [0, B(\phi)] \wedge \phi \in [0, \pi/2) \\ \emptyset & \text{else} \end{cases}, \quad (\text{A.106})$$

By combining Eqs. (A.104) and (A.106) we derive the expression for the full boundary to the cross section

$$C(z, \phi) = S(z, \phi) \cup E(z, \phi). \quad (\text{A.107})$$

### A.5.3 Spherocylinders

For a prolate spherocylinder we introduce the following notations to describe the intersection with a horizontal plane.

$$\tilde{\phi} = \arctan(a/b); \quad (\text{A.108})$$

$$B(\phi) = a \cos \phi + b; \quad (\text{A.109})$$

$$p_1(\phi) = a \cos \phi - b \sin \phi; \quad (\text{A.110})$$

$$p_{2,\pm}(z, \phi) = \pm a / \tan \phi - z / \sin \phi; \quad (\text{A.111})$$

$$B_0(z, \phi) = \begin{cases} -b & z \geq -p_1(\phi) \\ p_{2,-}(z, \phi) & z < -p_1(\phi) \end{cases}; \quad (\text{A.112})$$

$$B_1(z, \phi) = \begin{cases} b & z < p_1(\phi) \\ p_{2,+}(z, \phi) & z \geq p_1(\phi) \end{cases}; \quad (\text{A.113})$$

$$c(x, z, \phi) = \left( (x + z \sin \phi) / \cos \phi, \pm \sqrt{b^2 - x^2}, z \right). \quad (\text{A.114})$$

Note the similarity between these parameters and the ones presented in Section A.4. N.B. For convenience we use  $a$  to denote the halflength of the cylindrical part in this section. The total length of the spherocylinder is therefore  $2(a + b)$ . Using Eqs. (A.108 - A.114) the shaft-plane intersection is given by

$$S(z, \phi) = \begin{cases} \begin{array}{l} (x, \pm \sqrt{b^2 - x^2}, z) \\ x \in [-a, a] \end{array} & z \in [0, b] \wedge \phi = \pi/2 \\ \begin{array}{l} c(x, z, \phi) \\ x \in [B_0(z, \phi), B_1(z, \phi)] \end{array} & z \in [0, B(\phi)] \wedge \phi \in (0, \pi/2) \\ \begin{array}{l} (b \cos \eta, b \sin \eta, z) \\ \eta \in [0, 2\pi] \end{array} & z \in [0, a] \wedge \phi = 0 \\ \emptyset & \text{else} \end{cases}. \quad (\text{A.115})$$

For the plane-hemisphere intersection(s) we require additional expressions to simplify the notation of the boundary to the cross section

$$x_{0,b}(z, \phi) = \frac{-\cos^2 \phi \left( \sqrt{(b^2 - (z + a \cos \phi)^2) / \cos^2 \phi} + (z / \cos \phi + a) \tan \phi \right)}{z / \cos \phi + a}; \quad (\text{A.116})$$

$$x_{1,b}(z, \phi) = \begin{cases} \frac{-\cos^2 \phi \left( \sqrt{(b^2 - (z + a \cos \phi)^2) / \cos^2 \phi} - (z / \cos \phi + a) \tan \phi \right)}{z / \cos \phi + a} & z \in [-B(\phi), -a \cos \phi - b \sin \phi] \\ p_{2,-}(z, \phi) & z \notin [-B(\phi), -a \cos \phi - b \sin \phi] \end{cases}; \quad (\text{A.117})$$

$$x_{0,t}(z, \phi) = \begin{cases} \frac{-\cos^2 \phi \left( \sqrt{(b^2 - z^2) / \cos^2 \phi + 2az / \cos \phi - a^2} + (z / \cos \phi - a) \tan \phi \right)}{z / \cos \phi - a} & z \in [a \cos \phi + b \sin \phi, B(\phi)] \\ p_{2,+}(z, \phi) & z \notin [a \cos \phi + b \sin \phi, B(\phi)] \end{cases}; \quad (\text{A.118})$$

$$x_{1,t}(z, \phi) = \frac{\cos^2 \phi \left( \sqrt{(b^2 - z^2) / \cos^2 \phi + 2az / \cos \phi - a^2} - (z / \cos \phi - a) \tan \phi \right)}{z / \cos \phi - a}; \quad (\text{A.119})$$

$$y_{\pm,t}(x, z, \phi) = \pm b \sqrt{1 - (x/b)^2 - ((z / \cos \phi + x \tan \phi - a)/b)^2}; \quad (\text{A.120})$$

$$y_{\pm,b}(x, z, \phi) = \pm b \sqrt{1 - (x/b)^2 - ((z / \cos \phi + x \tan \phi + a)/b)^2}; \quad (\text{A.121})$$

$$\check{c}_{\pm,i}(x, z, \phi) = ((x + z \sin \phi) / \cos \phi, y_{\pm,i}(x, z, \phi), z). \quad (\text{A.122})$$

In Eq. (A.122) the parameter ‘ $i$ ’ can take the values ‘ $t$ ’ and ‘ $b$ ’. In analogy to the result for a cylinder we introduce a relation that gives the relevant parametrizations and corresponding domains

$$\tilde{c}(z, \phi) = \begin{cases} \tilde{c}_{+,b}(\xi_b, z, \phi) \cup \tilde{c}_{-,b}(\xi_b, z, \phi) \cup \tilde{c}_{+,t}(\xi_t, z, \phi) \cup \tilde{c}_{-,t}(\xi_t, z, \phi) & z < -p_1(\phi) \\ \xi_b \in [x_{0,b}(z, \phi), x_{1,b}(z, \phi)] & \wedge \\ \xi_t \in [x_{0,t}(z, \phi), x_{1,t}(z, \phi)] & z > p_1(\phi) \\ \tilde{c}_{+,b}(\xi_b, z, \phi) \cup \tilde{c}_{-,b}(\xi_b, z, \phi) & z < -p_1(\phi) \\ \xi_b \in [x_{0,b}(z, \phi), x_{1,b}(z, \phi)] & \\ \tilde{c}_{+,t}(\xi_t, z, \phi) \cup \tilde{c}_{-,t}(\xi_t, z, \phi) & z > p_1(\phi) \\ \xi_t \in [x_{0,t}(z, \phi), x_{1,t}(z, \phi)] & \end{cases}. \quad (\text{A.123})$$

The curves that result from the intersection(s) between the spherocylinder's hemispherical caps and the plane are given by

$$E(z, \phi) = \left\{ \begin{array}{ll} \begin{array}{l} (-a + \sqrt{b^2 - z^2} \cos(\pi - \eta), \sqrt{b^2 - z^2} \sin(\pi - \eta), z) \cup \\ (a + \sqrt{b^2 - z^2} \cos \eta, \sqrt{b^2 - z^2} \sin \eta, z) \\ \eta \in [-\pi/2, \pi/2] \end{array} & \begin{array}{l} z \in [0, b] \wedge \\ \phi = \pi/2 \end{array} \\ \\ \tilde{c}(z, \phi) & \begin{array}{l} z \in [0, B(\phi)] \wedge \\ \phi \in (0, \pi/2) \end{array} \\ \\ \begin{array}{l} (\sqrt{b^2 - (z - a)^2} \cos \eta, \sqrt{b^2 - (z - a)^2} \sin \eta, z) \\ \eta \in [0, 2\pi] \end{array} & \begin{array}{l} z \in [a, a + b] \wedge \\ \phi = 0 \end{array} \\ \\ \emptyset & \text{else} \end{array} \right. \quad (\text{A.124})$$

Using Eqs. (A.115) and (A.124) the expression for the full boundary to the cross section is obtained

$$C(z, \phi) = S(z, \phi) \cup E(z, \phi). \quad (\text{A.125})$$



# B

---

## Properties of Dense Regular Packings

---

In this appendix we present the data that we collected on the dense regular packing of solids, particle models, and miscellaneous shapes and to which we refer in Chapter 6.

## B.1 Tables of Packing Properties

In Tables B.1 - B.15 we consider 11 properties of dense regular packings for solids, particle models, and miscellaneous shapes. These results were established by analysing the crystal structures obtained by our combination of the floppy-box Monte Carlo (FBMC) technique [75] and a triangular-tessellation-based overlap routine, also see Chapters 5 and 6. The relevant crystal structures are given in our polyhedral database [279].

1. The *centrosymmetry* of the particle. For a centrosymmetric particle there is an inversion point to the symmetry group that is associated to its shape. This property is abbreviated ‘CS’ and we use the symbols ‘C’ and ‘NC’ to indicate centrosymmetric and noncentrosymmetric shapes.
2. The number of particles  $N$  in the unit cell for which densest-known regular packing is achieved.
3. The value of the packing fraction  $\phi_{\text{LB}}$  for the densest-known crystal structure. This value has been rounded down to 5 decimals.
4. The decomposition of the structure into *centrosymmetric compounds*. For a centrosymmetric particle it is hypothesized that the densest-packed regular structure is always a Bravais lattice [167]. For noncentrosymmetric particles the arrangement of the particles in the crystal may be such that there is a Bravais sublattice with the same group of particles associated to each of its lattice sites. If the shape of this group is centrosymmetric we say that the particles pack densest by forming a centrosymmetric compound. For example, the densest-known packing of tetrahedra admits a Bravais sublattice by grouping the particles into centrosymmetric quadrumers [169]. In our definition we allow the group/compound to consist of one particle to also account for the Bravais lattices formed by centrosymmetric particles. We use the abbreviation ‘CS<sub>c</sub>’ and specify whether or not a centrosymmetric compound may be formed by the symbols: ‘y’ for yes and ‘n’ for no. We use a dash ‘-’ when we did not consider this property for a particular particle.
5. The possibility of a *space-filling compound*. The regular structure we obtain using the FBMC method can have a packing fraction of 1 at most. When a structure achieves a packing fraction of 1, it is space filling. There are also structures with lower packing fractions, for which the voids between the particles can be filled using another regular polyhedron. Such packings therefore admit a space-filling compound. We abbreviate this property by ‘SF<sub>c</sub>’. If the compound consists of Platonic and/or Archimedean solids it is called a uniform partition of 3-space (three-dimensional space), or uniform partition for short. We use capitalized symbols ‘Y’, ‘N’, and ‘-’ to indicate the space-filling potential of a packing and to differentiate from the symbols used for CS<sub>c</sub>.
6. The inscribed-sphere upper bound to the packing fraction  $\phi_{\text{UB}}$ . We established the radius  $R_{\text{I}}$  of the *maximum* inscribed sphere using constrained optimization and



applied the procedure of Ref. [167] to arrive at this value:

$$\phi_{\text{UB}} = \min \left( 1, \frac{2\sqrt{2}\pi^2 R_{\text{I}}^3}{3V_{\text{M}}} \right), \quad (\text{B.1})$$

with  $V_{\text{M}}$  the volume of the particle. This value has been rounded up to 5 decimals.

7. The outscribed-sphere lower bound  $\phi_{\text{OS}}$  to the maximum packing fraction. We determined the radius  $R_{\text{O}}$  of the *minimum* outscribed sphere using constrained optimization and obtain

$$\phi_{\text{OS}} = \frac{V_{\text{M}}}{4\sqrt{2}R_{\text{I}}^3}. \quad (\text{B.2})$$

This value has been rounded down to 5 decimals.

8. The oriented-bounding-box lower bound  $\phi_{\text{OBB}}$  to the maximum packing fraction. We determine the volume  $V_{\text{OBB}}$  of *smallest* oriented bounding box using the method of Ref. [268] and obtain

$$\phi_{\text{OBB}} = \frac{V_{\text{M}}}{V_{\text{OBB}}}. \quad (\text{B.3})$$

This value has been rounded down to 5 decimals.

9. The *sphericity*  $\gamma \equiv R_{\text{I}}/R_{\text{O}} \in [0, 1]$ , defined in analogy to the asphericity parameter of Ref. [167], which is the reciprocal of  $\gamma$ .

We supplemented the simulation based material with literature results and we put references in the footnotes wherever appropriate - only for 29 out of 159 entries a literature result is known.

**Table B.1: Data for the Platonic solids.**

Code	CS	$N$	$\phi_{LB}$	$CS_c$	$SF_c$	name
		$\phi_{UB}$	$\phi_{OS}$	$\phi_{OBB}$	$\gamma$	
PS01	NC	4	0.85634 <sup>a</sup>	y	N	Tetrahedron
		1.00000	0.09072	0.33333	0.33333	
PS02	C	1	0.83635 <sup>b</sup>	y	N	Icosahedron
		0.89343	0.44833	0.51502	0.79465	
PS03	C	1	0.90450 <sup>b</sup>	y	N	Dodecahedron
		0.98116	0.49235	0.47745	0.79465	
PS04	C	1	0.94736 <sup>b</sup>	y	Y <sup>c</sup>	Octahedron
		1.00000	0.23570	0.56218	0.57734	
PS05	C	1	1.00000 <sup>b</sup>	y	Y <sup>c</sup>	Cube
		1.00000	0.27216	1.00000	0.57734	

<sup>a</sup>Ref. [169].

<sup>b</sup>Refs. [167, 252].

<sup>c</sup>Cubes are space filling [172, 322]. Octahedra and tetrahedra with equal edge lengths in a 1:2 ratio can form a uniform partition of 3-space [322].

<sup>d</sup>The following solids have a nanoparticle, colloid, or microscopic particle shape equivalent: tetrahedra [91, 92, 248], cubes [84–86, 89, 90], octahedra [89, 90, 247], dodecahedra [323] (microscopic), and icosahedra [91, 95, 96].

**Table B.2: Data for the Archimedean solids.**

Code	CS	$N$	$\phi_{\text{LB}}$	$\text{CS}_c$	$\text{SF}_c$	name
		$\phi_{\text{UB}}$	$\phi_{\text{OS}}$	$\phi_{\text{OBB}}$	$\gamma$	
AS01	NC	2	0.99519 <sup>a</sup>	y	Y <sup>d</sup>	
		1.00000	0.29718	0.41071	0.52223	Truncated Tetrahedron <sup>e</sup>
AS02	C	1	0.78498 <sup>b</sup>	y	N	
		0.83856	0.64230	0.51351	0.91495	Truncated Icosahedron
AS03	NC	1	0.78769 <sup>b</sup>	n <sup>c</sup>	N	
		0.93492	0.57484	0.66109	0.85033	Snub Cube <sup>f</sup>
AS04	NC	1	0.78864 <sup>b</sup>	n <sup>c</sup>	N	
		0.85547	0.66367	0.53018	0.91886	Snub Dodecahedron
AS05	C	1	0.80470 <sup>b</sup>	y	N	
		0.83596	0.66075	0.54747	0.92459	Rhombicosidodecahedron
AS06	C	1	0.82721 <sup>b</sup>	y	N	
		0.89731	0.66498	0.53395	0.90494	Truncated Icosidodecahedron
AS07	C	1	0.84937 <sup>b</sup>	y	N	
		1.00000	0.59356	0.74491	0.82594	Truncated Cuboctahedron
AS08	C	1	0.86472 <sup>b</sup>	y	N	
		0.93800	0.57737	0.50464	0.85064	Icosidodecahedron
AS09	C	1	0.87580 <sup>b</sup>	y	N	
		0.87580	0.56262	0.61928	0.86285	Rhombicuboctahedron <sup>g</sup>
AS10	C	1	0.89778 <sup>b</sup>	y	N	
		0.97387	0.57413	0.50032	0.83850	Truncated Dodecahedron
AS11	C	1	0.91836 <sup>b</sup>	y	N	
		1.00000	0.41666	0.83333	0.70710	Cuboctahedron
AS12	C	1	0.97374 <sup>b</sup>	y	Y <sup>d</sup>	
		1.00000	0.42712	0.96649	0.67859	Truncated Cube
AS13	C	1	1.00000 <sup>b</sup>	y	Y <sup>d</sup>	
		1.00000	0.50596	0.53333	0.77459	Truncated Octahedron

<sup>a</sup>Ref. [252].

<sup>b</sup>Refs. [260, 283].

<sup>c</sup>The snub cube and snub dodecahedron are *not* centrally symmetric, yet they achieve their densest packing in unit cell containing  $N = 1$  particles, *nor* do they form a centrosymmetric compound.

<sup>d</sup>Truncated tetrahedra and tetrahedra form a 2:6 space-filling compound with a 3:1 edge length ratio [283]. Cuboctahedra and octahedra form a 1:1 uniform partition of 3-space with 1:1 edge length ratio and truncated cubes and octahedra form a 1:1 uniform partition with edge length ratio 1:1 [322].

<sup>e</sup>For truncated tetrahedra we report a new dimer crystal structure with  $\phi_{\text{LB}} = 0.98854\dots$ , see Section B.2. The  $\phi_{\text{LB}}$  value in this table was obtained by analytic construction [260, 283].

<sup>f</sup>This result was established using 500 computer experiments for  $N = 1, \dots, 8$  with a slow pressure increase over  $4.5 \cdot 10^6$  MC cycles from  $p = 1$  to  $p = 1.2^{100}$  in 100 steps, followed by  $0.5 \cdot 10^6$  MC cycles of equilibration/production at that pressure. For each  $N$  and every run we obtained the Bravais lattice of Ref. [252] and the packing fraction deviated no more than 0.005 in absolute value from the literature value  $\phi_{\text{LB}} = 0.78769\dots$

<sup>g</sup>Rhombicuboctahedra achieve their densest packing in a crystal lattice, see Section 6.4.

<sup>h</sup>The following solids have a nanoparticle or colloid shape equivalent: truncated tetrahedra [91, 93], truncated cubes [89, 90, 93], truncated octahedra [94], and cuboctahedra [84, 89, 90].

**Table B.3: Data for the Catalan solids.**

Code	CS	$N$	$\phi_{LB}$	$CS_c$	$SF_c$	name
		$\phi_{UB}$	$\phi_{OS}$	$\phi_{OBB}$	$\gamma$	
CS01	C	1	0.77155	y	N	Deltoidal Hexecontahedron
		0.78287	0.61878	0.53980	0.92459	
CS02	C	1	0.79693	y	N	Deltoidal Icositetrahedron
		0.85134	0.54691	0.54525	0.86285	
CS03	C	1	0.79328	y	N	Disdyakis Dodecahedron
		0.81365	0.45844	0.54603	0.82594	
CS04	C	1	0.76549	y	N	Disdyakis Triacontahedron
		0.77313	0.57295	0.54354	0.90494	
CS05	NC	2	0.74107	n <sup>a</sup>	N	Pentagonal Hexecontahedron
		0.78283	0.60732	0.52603	0.91886	
CS06	NC	2	0.74363	n <sup>a</sup>	N	Pentagonal Icositetrahedron
		0.84856	0.52174	0.51407	0.85033	
CS07	C	1	0.75755	y	N	Pentakis Dodecahedron
		0.78799	0.60356	0.53419	0.91495	
CS08	C	1	1.00000	y	Y <sup>b</sup>	Rhombic Dodecahedron
		1.00000	0.35355	0.50000	0.70710	
CS09	C	1	0.80174	y	N	Rhombic Triacontahedron
		0.83462	0.51374	0.59016	0.85064	
CS10	C	1	0.87601	y	N	Small Triakis Octahedron
		0.93728	0.29289	0.63158	0.67859	
CS11	C	1	0.81401	y	N	Tetrakis Hexahedron
		0.87841	0.40824	0.55555	0.77459	
CS12	C	1	0.80479	y	N	Triakis Icosahedron
		0.81804	0.48227	0.55402	0.83850	
CS13	NC	2	0.79886	y	N	Triakis Tetrahedron
		1.00000	0.16329	0.59999	0.52223	

<sup>a</sup>Note that the pentagonal hexecontahedron and pentagonal icositetrahedron are *not* centrally symmetric, yet these particles do *not* achieve their densest-known packing by forming a centrosymmetric compound.

<sup>b</sup>Rhombic dodecahedra are space filling [172].

<sup>c</sup>The following solids have a nanoparticle or colloid shape equivalent: rhombic dodecahedra [33, 85, 86, 324] and possibly deltoidal icositetrahedra [325, 326].

**Table B.4: Data for the Johnson solids.**

Code	CS	$N$	$\phi_{LB}$	$CS_c$	$SF_c$	name
		$\phi_{UB}$	$\phi_{OS}$	$\phi_{OBB}$	$\gamma$	
JS01	NC	2	0.88745	-	-	Augmented Dodecahedron
		1.00000	0.41071	0.49624	0.73848	
JS02	NC	2	0.97192	-	-	Augmented Hexagonal Prism
		1.00000	0.21678	0.69255	0.37819	
JS03	NC	4	0.90463	-	-	Augmented Pentagonal Prism
		1.00000	0.21120	0.66082	0.42422	
JS04	NC	2	0.83264	-	-	Augmented Sphenocorona
		1.00000	0.26330	0.44643	0.57631	
JS05	NC	2	0.94527	-	-	Augmented Triangular Prism
		1.00000	0.18200	0.57321	0.48671	
JS06	NC	2	0.85704	-	-	Augmented Tridiminished Icosahedron
		1.00000	0.13072	0.28916	0.38646	
JS07	NC	2	0.96347	-	-	Augmented Truncated Cube
		1.00000	0.40619	0.85433	0.63827	
JS08	NC	1 <sup>a</sup>	0.87969	-	-	Augmented Truncated Dodecahedron
		1.00000	0.54646	0.51399	0.81740	
JS09	NC	2	0.90795	-	-	Augmented Truncated Tetrahedron
		1.00000	0.27695	0.57813	0.57344	
JS10	NC	2	0.90677	-	-	Biaugmented Pentagonal Prism
		1.00000	0.16543	0.56196	0.37650	
JS11	NC	2	0.91501	-	-	Biaugmented Triangular Prism
		1.00000	0.22322	0.60549	0.48294	
JS12	C	1	0.96102	y	-	Biaugmented Truncated Cube
		1.00000	0.36374	0.78361	0.59153	
JS13	NC	2	0.81863	-	-	Bigyrate Diminished Rhombicosidodecahedron
		1.00000	0.62385	0.58749	0.80687	
JS14	C	1	0.95273	-	-	Bilunabirotonda
		1.00000	0.19876	0.62377	0.49112	
JS15	NC	2	0.82232	-	-	Diminished Rhombicosidodecahedron
		1.00000	0.62385	0.57791	0.80687	

<sup>a</sup>Note that the augmented truncated dodecahedron is *not* centrally symmetric, yet it achieves its densest-known packing for  $N = 1$  particles in the unit cell.

**Table B.5: Data for the Johnson solids - continued.**

Code	CS	$N$	$\phi_{LB}$	$CS_c$	$SF_c$	name
		$\phi_{UB}$	$\phi_{OS}$	$\phi_{OBB}$	$\gamma$	
JS16	NC	2	0.85634	-	-	Dipyramid 3
		1.00000	0.07654	0.29003	0.33333	
JS17	NC	2	0.84024	-	-	Dipyramid 5
		1.00000	0.17317	0.32759	0.49112	
JS18	NC	2	0.85870	-	-	Disphenocingulum
		1.00000	0.37476	0.53256	0.69884	
JS19	NC	2	0.83541	-	-	Elongated Pentagonal Cupola
		1.00000	0.36461	0.65928	0.45045	
JS20	NC	2	0.83751	-	-	Elongated Pentagonal Dipyramid
		1.00000	0.38059	0.46158	0.67091	
JS21	C	1	0.79475	y	-	Elongated Pentagonal Gyrobicupola
		1.00000	0.44920	0.60407	0.60567	
JS22	C	1	0.81918	y	-	Elongated Pentagonal Gyrobirotunda
		1.00000	0.43524	0.57603	0.74693	
JS23	NC	2	0.78374	-	-	Elongated Pentagonal Gyrocupolarotunda
		1.00000	0.51299	0.58594	0.79010	
JS24	NC	2	0.79329	-	-	Elongated Pentagonal Orthobicupola
		1.00000	0.44920	0.60407	0.60567	
JS25	NC	2	0.81243	-	-	Elongated Pentagonal Orthobirotunda
		1.00000	0.43524	0.57603	0.74693	
JS26	NC	2	0.79266	-	-	Elongated Pentagonal Orthocupolarotunda
		1.00000	0.51299	0.58594	0.79010	
JS27	NC	2	0.86656	-	-	Elongated Pentagonal Pyramid
		1.00000	0.35743	0.53225	0.67555	
JS28	NC	2	0.81652	-	-	Elongated Pentagonal Rotunda
		1.00000	0.44260	0.61737	0.65993	
JS29	NC	2	0.85746	-	-	Elongated Square Cupola
		1.00000	0.43718	0.68054	0.61012	
JS30	C	1	0.90995	y	-	Elongated Square Dipyramid
		1.00000	0.14788	0.60947	0.41421	

**Table B.6: Data for the Johnson solids - continued.**

Code	CS	$N$	$\phi_{LB}$	$CS_c$	$SF_c$	name
		$\phi_{UB}$	$\phi_{OS}$	$\phi_{OBB}$	$\gamma$	
JS31	NC	2	0.80639	-	-	Elongated Square Gyrobicupola
		0.87580	0.56262	0.61928	0.86285	
JS32	NC	2	0.94371	-	-	Elongated Square Pyramid
		1.00000	0.21844	0.72385	0.49999	
JS33	NC	2	0.91258	-	-	Elongated Triangular Cupola
		1.00000	0.35441	0.60017	0.65935	
JS34	NC	2	0.83284	-	-	Elongated Triangular Dipyramid
		1.00000	0.05180	0.29326	0.21927	
JS35	C	1	0.87941	y	-	Elongated Triangular Gyrobicupola
		1.00000	0.29486	0.62703	0.60243	
JS36	NC	2	0.88043	-	-	Elongated Triangular Orthobicupola
		1.00000	0.29486	0.54326	0.60243	
JS37	NC	4	0.86089	-	-	Elongated Triangular Pyramid
		1.00000	0.09737	0.35016	0.28867	
JS38	NC	2	0.83325	-	-	Gyrate Bidiminished Rhombicosidodecahedron
		1.00000	0.58695	0.56431	0.77906	
JS39	NC	1 <sup>a</sup>	0.80470	-	-	Gyrate Rhombicosidodecahedron
		0.83596	0.66075	0.54302	0.92459	
JS40	NC	2	1.00000	-	Y <sup>b</sup>	Gyrobifastigium
		1.00000	0.15309	0.50000	0.43301	
JS41	NC	2	0.76412	-	-	Gyroelongated Pentagonal Bicutopola
		1.00000	0.42911	0.58293	0.57146	
JS42	NC	2	0.77761	-	-	Gyroelongated Pentagonal Birtunda
		0.94171	0.45641	0.55737	0.78549	
JS43	NC	4	0.80695	-	-	Gyroelongated Pentagonal Cupola
		1.00000	0.34161	0.63982	0.41448	
JS44	NC	2	0.78540	-	-	Gyroelongated Pentagonal Cupolarotunda
		1.00000	0.51719	0.56621	0.78342	

<sup>a</sup>Note that the gyrate rhombicosidodecahedron is *not* centrally symmetric, yet it achieves its densest-known packing for  $N = 1$  particles in the unit cell. However, the densest-known  $N = 2$  packing forms a centrosymmetric-dimer lattice, which achieves a packing fraction remarkably close to that of the  $N = 1$  packing.

<sup>b</sup>The gyrobifastigium is space filling [172].

**Table B.7: Data for the Johnson solids - continued.**

Code	CS	$N$	$\phi_{LB}$	$CS_c$	$SF_c$	name
		$\phi_{UB}$	$\phi_{OS}$	$\phi_{OBB}$	$\gamma$	
JS45	NC	2	0.86077	-	-	Gyroelongated Pentagonal Pyramid
		1.00000	0.38637	0.50959	0.64079	
JS46	NC	2	0.81250	-	-	Gyroelongated Pentagonal Rotunda
		1.00000	0.44203	0.59756	0.63546	
JS47	NC	2	0.77850	-	-	Gyroelongated Square Bicapola
		0.97994	0.55378	0.54574	0.82676	
JS48	NC	2	0.80712	-	-	Gyroelongated Square Cupola
		1.00000	0.42183	0.60324	0.56972	
JS49	NC	2	0.80261	-	-	Gyroelongated Square Dipyramid
		1.00000	0.17614	0.43129	0.51974	
JS50	NC	2	0.82236	-	-	Gyroelongated Square Pyramid
		1.00000	0.25752	0.45133	0.59228	
JS51	NC	4	0.79162	-	-	Gyroelongated Triangular Bicapola
		1.00000	0.32153	0.52112	0.67198	
JS52	NC	2	0.83145	-	-	Gyroelongated Triangular Cupola
		1.00000	0.37306	0.56343	0.64231	
JS53	NC	2	0.83853	-	-	Hebesphenomegacorona
		1.00000	0.36444	0.54634	0.62123	
JS54	NC	2	0.87796	-	-	Metabiaugmented Dodecahedron
		1.00000	0.38632	0.51502	0.71464	
JS55	NC	2	0.93602	-	-	Metabiaugmented Hexagonal Prism
		1.00000	0.18772	0.65039	0.35100	
JS56	NC	2	0.86978	-	-	Metabiaugmented Truncated Dodecahedron
		1.00000	0.53239	0.52766	0.80327	
JS57	NC	2	0.91942	-	-	Metabidiminished Icosahedron
		1.00000	0.32441	0.46065	0.57232	
JS58	NC	2	0.83373	-	-	Metabidiminished Rhombicosidodecahedron
		1.00000	0.58695	0.56431	0.77852	

**Table B.8: Data for the Johnson solids - continued.**

Code	CS	$N$	$\phi_{LB}$	$CS_c$	$SF_c$	name
		$\phi_{UB}$	$\phi_{OS}$	$\phi_{OBB}$	$\gamma$	
JS59	NC	1 <sup>a</sup>	0.80470	-	-	Metabigyrate Rhombicosidodecahedron
		0.83596	0.66075	0.54302	0.92459	
JS60	NC	1 <sup>a</sup>	0.82056	-	-	Metagyrate Diminished Rhombicosidodecahedron
		1.00000	0.62385	0.58749	0.80687	
JS61	C	1	0.88941	y	-	Parabiaugmented Dodecahedron
		1.00000	0.33173	0.51502	0.67926	
JS62	C	1	0.97102	y	-	Parabiaugmented Hexagonal Prism
		1.00000	0.13937	0.65778	0.31783	
JS63	C	1	0.88053	y	-	Parabiaugmented Truncated Dodecahedron
		1.00000	0.51540	0.52766	0.79465	
JS64	C	1	0.85486	y	-	Parabidiminished Rhombicosidodecahedron
		1.00000	0.58695	0.63661	0.68915	
JS65	C	1	0.80470	y	-	Parabigyrate Rhombicosidodecahedron
		0.83596	0.66075	0.55217	0.92459	
JS66	NC	1 <sup>b</sup>	0.82048	-	-	Paragyrate Diminished Rhombicosidodecahedron
		1.00000	0.62385	0.57791	0.80687	
JS67	NC	2	0.85648	-	-	Pentagonal Cupola
		1.00000	0.09698	0.44385	0.16245	
JS68	C	1	0.85891	y	-	Pentagonal Gyrobicupola
		1.00000	0.19397	0.44385	0.32491	
JS69	NC	2	0.84969	-	-	Pentagonal Gyrocupolarotunda
		1.00000	0.38567	0.48784	0.58777	
JS70	NC	2	0.82381	-	-	Pentagonal Orthobicupola
		1.00000	0.19397	0.44385	0.32491	
JS71	NC	2	0.81713	-	-	Pentagonal Orthobirotonda
		0.93800	0.57737	0.50464	0.85064	

<sup>a</sup>Note that the metabigyrate rhombicosidodecahedron and metagyrate diminished rhombicosidodecahedron are *not* centrally symmetric, yet they achieve their densest-known packing in unit cell containing  $N = 1$  particles.

<sup>b</sup>Note the paragyrate diminished rhombicosidodecahedron is *not* centrally symmetric, yet it achieves its densest-known packing for  $N = 1$  particles in the unit cell. However, the densest-known  $N = 2$  packing forms a centrosymmetric-dimer lattice, which achieves a packing fraction remarkably close to that of the  $N = 1$  packing.

**Table B.9: Data for the Johnson solids - continued.**

Code	CS	$N$	$\phi_{LB}$	$CS_c$	$SF_c$	name
		$\phi_{UB}$	$\phi_{OS}$	$\phi_{OBB}$	$\gamma$	
JS72	NC	2	0.83123	-	-	Pentagonal Orthocupolarotunda
		1.00000	0.38567	0.48784	0.58777	
JS73	NC	2	0.85874	-	-	Pentagonal Rotunda
		1.00000	0.28868	0.50464	0.42532	
JS74	NC	2	0.94582	-	-	Pyramid 4
		1.00000	0.11785	0.33333	0.36601	
JS75	NC	2	0.80887	-	-	Pyramid 5
		1.00000	0.08658	0.23032	0.27365	
JS76	NC	2	0.86477	-	-	Snub Disphenoid
		1.00000	0.18900	0.65970	0.48676	
JS77	NC	4	0.81981	-	-	Snub Square Antiprism
		1.00000	0.34434	0.52936	0.55150	
JS78	NC	2	0.82102	-	-	Sphenocorona
		1.00000	0.27733	0.44893	0.58532	
JS79	NC	2	0.85093	-	-	Sphenomegacorona
		1.00000	0.16304	0.39771	0.44699	
JS80	NC	2	0.94227	-	-	Square Cupola
		1.00000	0.15397	0.47140	0.27059	
JS81	NC	2	0.82692	-	-	Square Gyrobicupola
		1.00000	0.30795	0.47140	0.54119	
JS82	C	1	0.94249	y	-	Square Orthobicupola
		1.00000	0.30795	0.55228	0.54119	

**Table B.10: Data for the Johnson solids - continued.**

Code	CS	$N$	$\phi_{LB}$	$CS_c$	$SF_c$	name
		$\phi_{UB}$	$\phi_{OS}$	$\phi_{OBB}$	$\gamma$	
JS83	NC	2	0.91836	-	-	Triangular Cupola
		1.00000	0.20833	0.41666	0.40824	
JS84	NC	2	0.87496	-	-	Triangular Hebesphenorotunda
		1.00000	0.26151	0.47213	0.49999	
JS85	NC	2	0.88316	-	-	Triangular Orthobicupola
		1.00000	0.41666	0.52465	0.70710	
JS86	NC	2	0.87421	-	-	Triaugmented Dodecahedron
		1.00000	0.36090	0.52502	0.69033	
JS87	NC	2	0.89315	-	-	Triaugmented Hexagonal Prism
		1.00000	0.15008	0.49731	0.31783	
JS88	NC	2	0.82855	-	-	Triaugmented Triangular Prism
		1.00000	0.20411	0.42377	0.50211	
JS89	NC	2	0.86679	-	-	Triaugmented Truncated Dodecahedron
		1.00000	0.52875	0.53355	0.79465	
JS90	NC	2	0.91669	-	-	Tridiminished Icosahedron
		1.00000	0.26245	0.37267	0.50209	
JS91	NC	2	0.84993	-	-	Tridiminished Rhombicosidodecahedron
		1.00000	0.55005	0.52883	0.73251	
JS92	NC	2	0.80456	-	-	Trigyrate Rhombicosidodecahedron
		0.83596	0.66075	0.54302	0.92459	

**Table B.11: Data for regular prisms.**

Code	CS	$N$	$\phi_{LB}$	$CS_c$	$SF_c$	
		$\phi_{UB}$	$\phi_{OS}$	$\phi_{OBB}$	$\gamma$	name
RP03	NC	2	1.00000 <sup>a</sup>	y	Y <sup>c</sup>	
		1.00000	0.17181	0.50000	0.37796	Prism 3
RP04	C	1	1.00000 <sup>a</sup>	y	Y <sup>c</sup>	
		1.00000	0.27216	1.00000	0.57734	Cube
RP05	NC	2	0.92131 <sup>a</sup>	y	N	
		1.00000	0.31659	0.69098	0.50673	Prism 5
RP06	C	1	1.00000 <sup>a</sup>	y	Y <sup>c</sup>	
		1.00000	0.32863	0.75000	0.44721	Prism 6
RP07	NC	2	0.89269 <sup>a</sup>	y	N	
		1.00000	0.32407	0.73825	0.39803	Prism 7
RP08	C	1	0.90615 <sup>a</sup>	y	Y <sup>c</sup>	
		1.00000	0.31175	0.82842	0.35740	Prism 8
RP09	NC	2	0.90103 <sup>b</sup>	y	N	
		1.00000	0.29629	0.75712	0.32361	Prism 9
RP10	C	1	0.91371 <sup>a</sup>	y	N	
		1.00000	0.28003	0.77254	0.29524	Prism 10

<sup>a</sup>We used Ref. [251] to compare our results to the literature studies of two-dimensional (2D) regular polygons. See Table B.1 for more information on the cube.

<sup>b</sup>For regular enneaprisms (9-gonal base) we discovered a new packing, which also improves upon the result of Ref. [251] for the regular 9-gon (enneagon, nonagon), see Section 6.5.

<sup>c</sup>Cubes (square base), as well as regular tri- (triangular base) and hexaprisms (hexagonal base) are space filling [172, 322].

**Table B.12: Data for regular antiprisms.**

Code	CS	$N$	$\phi_{LB}$	$CS_c$	$SF_c$	name
		$\phi_{UB}$	$\phi_{OS}$	$\phi_{OBB}$	$\gamma$	
AP03	C	1	0.94736	y	Y	Octahedron <sup>a</sup>
		1.00000	0.23570	0.56218	0.57734	
AP04	NC	2	0.86343	y	N	Antiprism 4
		1.00000	0.30385	0.66666	0.51108	
AP05	C	1	0.92052	y	N	Antiprism 5
		1.00000	0.32441	0.67418	0.44721	
AP06	NC	2	0.88189	y	N	Antiprism 6
		1.00000	0.32114	0.73204	0.39331	
AP07	C	1	0.90137	y	N	Antiprism 7
		1.00000	0.30741	0.72740	0.34904	
AP08	NC	2	0.89332	y	N	Antiprism 8
		1.00000	0.28987	0.75526	0.31270	
AP09	C	1	0.90672	y	N	Antiprism 9
		1.00000	0.27164	0.75000	0.28264	
AP10	NC	2	0.89731	y	N	Antiprism 10
		1.00000	0.25411	0.76608	0.25750	

<sup>a</sup>See Table B.1 for more information on the octahedron.

**Table B.13: Data for several miscellaneous solids.**

Code	CS	$N$	$\phi_{LB}$	$CS_c$	$SF_c$	name
		$\phi_{UB}$	$\phi_{OS}$	$\phi_{OBB}$	$\gamma$	
MS01	C	1	0.98926	y	N	Dürer's Solid <sup>b</sup>
		1.00000	0.31151	0.60300	0.59880	
MS02	C	1	1.00000	y	Y <sup>a</sup>	Elongated Dodecahedron
		1.00000	0.31426	0.66666	0.57734	
MS03	C	1	0.79473	y	N	Rhombic Enneacontrahedron <sup>c</sup>
		0.79473	0.60457	0.54914	0.91286	
MS04	C	1	0.82280	y	N	Rhombic Icosahedron
		1.00000	0.34650	0.52786	0.64945	
MS05	NC	2	1.00000	y	Y <sup>a</sup>	Squashed Dodecahedron
		1.00000	0.35355	0.50000	0.70710	
MS06	NC	4	0.70503	n	N	Stanford Bunny <sup>d</sup>
		1.00000	0.13380	0.31616	0.41221	
MS07	NC	2	0.47242	y	N	Hammerhead Shark <sup>d</sup>
		1.00000	0.00853	0.06853	0.11355	

<sup>a</sup>The elongated dodecahedron and the squashed dodecahedron are space filling.

<sup>b</sup>Note that Dürer's solid is not the same as the dimer compound formed by truncated tetrahedra, also see Section B.2.

<sup>c</sup>For the rhombic enneacontrahedron we proved that the Bravais lattice we discovered achieves the densest packing, see Section 6.4.

<sup>d</sup>For the Stanford bunny [280] and the hammerhead shark [281] the number of triangles that comprise these models is very high, 3,756 and 5,116 triangles, respectively, however all quantities could be established with the appropriate accuracy.

**Table B.14: Data for nonconvex polyhedra.**

Code	CS	$N$	$\phi_{LB}$	$CS_c$	$SF_c$	name
		$\phi_{UB}$	$\phi_{OS}$	$\phi_{OBB}$	$\gamma$	
PH01	NC	2	0.61327	n	N	
		1.00000	0.04157	0.23149	0.17469	Császár Polyhedron
PH02	C	1	0.29477	y	N	
		1.00000	0.07659	0.06269	0.26640	Echidnahedron
PH03	C	1	1.00000	y	Y <sup>a</sup>	
		1.00000	0.22922	0.45845	0.55284	Escher's Solid
PH04	C	1	0.55728	y	N	
		1.00000	0.21644	0.20989	0.51160	Great Rhombictriacontrahedron
PH05	C	2	0.88967	n	N	
		1.00000	0.18806	0.18237	0.18759	Great Stellated Dodecahedron
PH06	C	1	0.74965	y	N	
		1.00000	0.34558	0.39699	0.53633	Jessen's Orthogonal Icosahedron
PH07	C	1	0.55602	y	N	
		1.00000	0.20643	0.20019	0.51455	Mathematica Spikey 1 <sup>b</sup>
PH08	C	1	0.59998	y	N	
		1.00000	0.14378	0.20246	0.35355	Rhombic Dodecahedron Stella- tion 2 <sup>c</sup>
PH09	C	2	0.55654	n	N	
		1.00000	0.19854	0.19253	0.41946	Rhombic Hexecontrahedron
PH10	C	2	0.69528	n	N	
		0.97719	0.49635	0.47293	0.79787	Small Triambic Icosahedron
PH11	NC	2	0.51913	y	N	
		1.00000	0.03637	0.13732	0.16538	Szilassi Polyhedron

<sup>a</sup>Escher's solid is space filling by construction.

<sup>b</sup>The number '1' in the name 'Mathematica spikey 1' refers to the first version of the Mathematica spikey, which was used as a logo for the first version of the Mathematica software package [327]. It is a cumulated icosahedron with cumulation ratio  $\sqrt{6}/3$ .

<sup>c</sup>The number '2' in the name 'rhombic dodecahedron stellation 2' refers to the fact that there are three stellations of the rhombic dodecahedron (four when including the original). This particular stellation is listed as number '2' in the Mathematica polyhedron database [282].

**Table B.15: Data for nonconvex nanoparticle and colloid models.**

Code	CS	$N$	$\phi_{LB}$	$CS_c$	$SF_c$	name
		$\phi_{UB}$	$\phi_{OS}$	$\phi_{OBB}$	$\gamma$	
PA01	NC	4	0.51850	n	N	Cap <sup>b</sup>
		1.00000	0.18253	0.27282	0.155754	
PA02	C	1	0.68615	y	N	Nanostar
		1.00000	0.09602	0.22903	0.38489	
PA03	C	1	0.31077	y	N	Octapod
		1.00000	0.02525	0.06681	0.13281	
PA04	NC	2 <sup>a</sup>	0.59207	y	N	Tetrapod
		1.00000	0.04864	0.10628	0.20303	

<sup>a</sup>The tetrapod model achieves its densest-known packing for  $N = 2$  particles in the unit cell, however, the  $N = 1$  the packing fraction is remarkably close to that value.

<sup>b</sup>Our cap model [109] is comprised of 3,850 triangles. Despite this model's complexity, all quantities could be established with the appropriate accuracy.

<sup>c</sup>The solids were modelled after the following nanoparticles and colloids: caps [107–109], nanostars [104–106, 247], octapods [54, 78, 99–101], and tetrapods [102, 103].

## B.2 Dimer Structure for Truncated Tetrahedra

For the system containing  $N = 2$  truncated tetrahedra we provide additional information on the composition of the dimer lattice that we obtained using our method. This lattice achieves a packing fraction  $\phi_{\text{LB}} = 0.988\dots$ . Table B.16 lists the position and orientation of the particles inside the unit cell, as well as the shape of the cell itself.

**Table B.16: Coordinates that define the dimer lattice of truncated tetrahedra.**

This table lists the 12 vertices  $\mathbf{v}$  corresponding to the truncated tetrahedron model used in our simulations. It also gives the three vectors  $\mathbf{u}_m$ , with  $m = 1, 2, 3$  an index, that span the unit cell; the two position vectors  $\mathbf{R}_i$ , with  $i = 1, 2$  the particle number, that indicate the location of the truncated tetrahedra with respect to the origin; and the two rotation matrices  $\mathbf{M}_i$ , that specify the rotation of the particles with respect to the initial configuration. The initial configuration is defined by the set of vertices  $\mathbf{v}$ . The volume enclosed by the particle's surface is unity. We provide all vector and matrix entries with 6 decimal precision. Rounding errors may lead to small overlaps of particles in the crystal generated using these coordinates.

	$v_x$	$v_y$	$v_z$	$v_x$	$v_y$	$v_z$
$\mathbf{v}$	0.621121	-0.358604	-0.439200	0.621121	0.358604	-0.439200
	0.828162	0.000000	0.146400	-0.414081	-0.717209	0.146400
	-0.621121	-0.358604	-0.439200	0.000000	-0.717209	-0.439200
	0.000000	0.717209	-0.439200	-0.621121	0.358604	-0.439200
	-0.414081	0.717209	0.146400	-0.207040	0.358604	0.732000
	-0.207040	-0.358604	0.732000	0.414081	0.000000	0.732000
	$u_x$	$u_y$	$u_z$	$R_x$	$R_y$	$R_z$
$\mathbf{u}_1, \mathbf{R}_1$	0.241977	0.928872	0.855892	0.000000	0.000000	0.000000
$\mathbf{u}_2, \mathbf{R}_2$	0.604353	-0.735843	0.832841	-0.073508	-0.001753	0.875316
$\mathbf{u}_3$	-1.053988	-0.200499	0.654313			
	$M_{xx}$	$M_{xy}$	$M_{xz}$	$M_{yx}$	$M_{yy}$	$M_{yz}$
$\mathbf{M}_1$	-0.892816	-0.442579	0.083685	-0.443985	0.896032	0.001996
$\mathbf{M}_2$	0.892816	-0.442579	-0.083685	0.443985	0.896032	-0.001996
	$M_{zx}$	$M_{zy}$	$M_{zz}$			
$\mathbf{M}_1$	-0.075867	-0.035373	-0.996490			
$\mathbf{M}_2$	0.075867	-0.035373	0.996490			

### B.3 Vertices of a Rhombic Enneacontrahedron

In this section the orientation of a rhombic enneacontrahedron (RECH) is specified by listing its 92 vertices in Tables B.17 - B.19. This orientation is used to prove that we obtained the densest packing of these particles in Section 6.4.

**Table B.17: The vertices of a rhombic enneacontrahedron.**

---



---

$\left(\frac{1}{3}(-5 - \sqrt{5}), 0, \frac{1}{3}(-7 + 2\sqrt{5})\right)$	$\left(\frac{1}{3}(-5 - \sqrt{5}), 0, \frac{2}{3}(-2 + \sqrt{5})\right)$
$\left(\frac{1}{6}(-7 - 3\sqrt{5}), -\sqrt{\frac{1}{6}(3 + \sqrt{5})}, \frac{2}{3}(-3 + \sqrt{5})\right)$	$\left(\frac{1}{6}(-7 - 3\sqrt{5}), -\sqrt{\frac{1}{6}(3 + \sqrt{5})}, -1 + \frac{2\sqrt{5}}{3}\right)$
$\left(\frac{1}{6}(-7 - 3\sqrt{5}), \sqrt{\frac{1}{6}(3 + \sqrt{5})}, \frac{2}{3}(-3 + \sqrt{5})\right)$	$\left(\frac{1}{6}(-7 - 3\sqrt{5}), \sqrt{\frac{1}{6}(3 + \sqrt{5})}, -1 + \frac{2\sqrt{5}}{3}\right)$
$\left(-\frac{2}{3}(1 + \sqrt{5}), 0, \frac{2}{3}(-1 + \sqrt{5})\right)$	$\left(\frac{1}{3}(-4 - \sqrt{5}), -\frac{1}{\sqrt{3}}, \frac{1}{3}(-7 + \sqrt{5})\right)$
$\left(\frac{1}{3}(-4 - \sqrt{5}), \frac{1}{\sqrt{3}}, \frac{1}{3}(-7 + \sqrt{5})\right)$	$\left(\frac{1}{6}(-5 - 3\sqrt{5}), -\sqrt{\frac{7}{6} + \frac{\sqrt{5}}{2}}, \frac{1}{3}(-6 + \sqrt{5})\right)$
$\left(\frac{1}{6}(-5 - 3\sqrt{5}), -\sqrt{\frac{7}{6} + \frac{\sqrt{5}}{2}}, \frac{1}{3}(-3 + \sqrt{5})\right)$	$\left(\frac{1}{6}(-5 - 3\sqrt{5}), \sqrt{\frac{1}{6}(7 + 3\sqrt{5})}, \frac{1}{3}(-6 + \sqrt{5})\right)$
$\left(\frac{1}{6}(-5 - 3\sqrt{5}), \sqrt{\frac{1}{6}(7 + 3\sqrt{5})}, \frac{1}{3}(-3 + \sqrt{5})\right)$	$\left(-1 - \frac{\sqrt{5}}{3}, 0, -\frac{7}{3}\right)$
$\left(\frac{1}{2}(-1 - \sqrt{5}), -\sqrt{\frac{1}{6}(3 + \sqrt{5})}, -2\right)$	$\left(\frac{1}{2}(-1 - \sqrt{5}), -\sqrt{\frac{1}{6}(3 + \sqrt{5})}, -1 + \sqrt{5}\right)$
$\left(\frac{1}{2}(-1 - \sqrt{5}), \sqrt{\frac{1}{6}(3 + \sqrt{5})}, -2\right)$	$\left(\frac{1}{2}(-1 - \sqrt{5}), \sqrt{\frac{1}{6}(3 + \sqrt{5})}, -1 + \sqrt{5}\right)$
$\left(\frac{1}{6}(-7 - \sqrt{5}), -\sqrt{\frac{7}{6} + \frac{\sqrt{5}}{2}}, \frac{2}{3}(-1 + \sqrt{5})\right)$	$\left(\frac{1}{6}(-7 - \sqrt{5}), \sqrt{\frac{1}{6}(7 + 3\sqrt{5})}, \frac{2}{3}(-1 + \sqrt{5})\right)$
$\left(-\frac{2\sqrt{5}}{3}, 0, -\frac{2}{3} + \sqrt{5}\right)$	$\left(\frac{1}{6}(-5 - \sqrt{5}), -\sqrt{\frac{5}{6}(3 + \sqrt{5})}, \frac{1}{3}(-5 + \sqrt{5})\right)$
$\left(\frac{1}{6}(-5 - \sqrt{5}), -\sqrt{\frac{5}{6}(3 + \sqrt{5})}, \frac{1}{3}(-2 + \sqrt{5})\right)$	$\left(\frac{1}{6}(-5 - \sqrt{5}), \sqrt{\frac{5}{6}(3 + \sqrt{5})}, \frac{1}{3}(-5 + \sqrt{5})\right)$
$\left(\frac{1}{6}(-5 - \sqrt{5}), \sqrt{\frac{5}{6}(3 + \sqrt{5})}, \frac{1}{3}(-2 + \sqrt{5})\right)$	$\left(\frac{1}{3}(-1 - \sqrt{5}), -\sqrt{\frac{2}{3}(3 + \sqrt{5})}, \frac{1}{3}(-7 + \sqrt{5})\right)$
$\left(\frac{1}{3}(-1 - \sqrt{5}), \sqrt{\frac{2}{3}(3 + \sqrt{5})}, \frac{1}{3}(-7 + \sqrt{5})\right)$	$\left(\frac{1}{6}(-3 - \sqrt{5}), -\sqrt{\frac{7}{6} + \frac{\sqrt{5}}{2}}, -\frac{2}{3} + \sqrt{5}\right)$

---



---

**Table B.18: The vertices of a rhombic enneacuboctahedron - continued.**

---



---

$\left(\frac{1}{6}(-3 - \sqrt{5}), -\sqrt{\frac{1}{6}(3 - \sqrt{5})}, -\frac{8}{3}\right)$ $\left(\frac{1}{6}(-3 - \sqrt{5}), \sqrt{\frac{1}{6}(7 + 3\sqrt{5})}, -\frac{2}{3} + \sqrt{5}\right)$ $\left(-\frac{\sqrt{5}}{3}, -\frac{1}{\sqrt{3}}, -\frac{1}{3} + \sqrt{5}\right)$ $\left(-\frac{\sqrt{5}}{3}, \sqrt{\frac{5}{3}}, -\frac{7}{3}\right)$ $\left(\frac{1}{6}(-1 - \sqrt{5}), \sqrt{\frac{5}{6}(3 + \sqrt{5})}, \frac{2}{3}(-1 + \sqrt{5})\right)$ $\left(-\frac{1}{3}, -\sqrt{3 + \frac{4\sqrt{5}}{3}}, \frac{1}{3}(-3 + \sqrt{5})\right)$ $\left(-\frac{1}{3}, \sqrt{3 + \frac{4\sqrt{5}}{3}}, \frac{1}{3}(-3 + \sqrt{5})\right)$ $\left(\frac{1}{6}(-3 + \sqrt{5}), \sqrt{\frac{1}{6}(3 + \sqrt{5})}, -\frac{1}{3} + \sqrt{5}\right)$ $\left(0, -\sqrt{\frac{2}{3}(3 + \sqrt{5})}, -1 + \sqrt{5}\right)$ $(0, 0, \sqrt{5})$ $\left(0, \sqrt{\frac{2}{3}(3 + \sqrt{5})}, -1 + \sqrt{5}\right)$ $\left(\frac{1}{6}(3 - \sqrt{5}), \sqrt{\frac{1}{6}(3 + \sqrt{5})}, -\frac{8}{3}\right)$ $\left(\frac{1}{3}, -\sqrt{3 + \frac{4\sqrt{5}}{3}}, -1 + \frac{2\sqrt{5}}{3}\right)$ $\left(\frac{1}{3}, \sqrt{3 + \frac{4\sqrt{5}}{3}}, -1 + \frac{2\sqrt{5}}{3}\right)$ $\left(\frac{1}{6}(1 + \sqrt{5}), \sqrt{\frac{5}{6}(3 + \sqrt{5})}, \frac{1}{3}(-7 + \sqrt{5})\right)$ $\left(\frac{\sqrt{5}}{3}, -\frac{1}{\sqrt{3}}, -\frac{8}{3}\right)$ $\left(\frac{\sqrt{5}}{3}, \sqrt{\frac{5}{3}}, -\frac{2}{3} + \sqrt{5}\right)$	$\left(\frac{1}{6}(-3 - \sqrt{5}), \sqrt{\frac{1}{6}(3 - \sqrt{5})}, -\frac{8}{3}\right)$ $\left(-\frac{\sqrt{5}}{3}, -\sqrt{\frac{5}{3}}, -\frac{7}{3}\right)$ $\left(-\frac{\sqrt{5}}{3}, \frac{1}{\sqrt{3}}, -\frac{1}{3} + \sqrt{5}\right)$ $\left(\frac{1}{6}(-1 - \sqrt{5}), -\sqrt{\frac{5}{6}(3 + \sqrt{5})}, \frac{2}{3}(-1 + \sqrt{5})\right)$ $\left(-\frac{1}{3}, -\sqrt{3 + \frac{4\sqrt{5}}{3}}, \frac{1}{3}(-6 + \sqrt{5})\right)$ $\left(-\frac{1}{3}, \sqrt{3 + \frac{4\sqrt{5}}{3}}, \frac{1}{3}(-6 + \sqrt{5})\right)$ $\left(\frac{1}{6}(-3 + \sqrt{5}), -\sqrt{\frac{1}{6}(3 + \sqrt{5})}, -\frac{1}{3} + \sqrt{5}\right)$ $\left(0, -\sqrt{\frac{2}{3}(3 + \sqrt{5})}, -2\right)$ $(0, 0, -3)$ $\left(0, \sqrt{\frac{2}{3}(3 + \sqrt{5})}, -2\right)$ $\left(\frac{1}{6}(3 - \sqrt{5}), -\sqrt{\frac{1}{6}(3 + \sqrt{5})}, -\frac{8}{3}\right)$ $\left(\frac{1}{3}, -\sqrt{3 + \frac{4\sqrt{5}}{3}}, \frac{2}{3}(-3 + \sqrt{5})\right)$ $\left(\frac{1}{3}, \sqrt{3 + \frac{4\sqrt{5}}{3}}, \frac{2}{3}(-3 + \sqrt{5})\right)$ $\left(\frac{1}{6}(1 + \sqrt{5}), -\sqrt{\frac{5}{6}(3 + \sqrt{5})}, \frac{1}{3}(-7 + \sqrt{5})\right)$ $\left(\frac{\sqrt{5}}{3}, -\sqrt{\frac{5}{3}}, -\frac{2}{3} + \sqrt{5}\right)$ $\left(\frac{\sqrt{5}}{3}, \frac{1}{\sqrt{3}}, -\frac{8}{3}\right)$ $\left(\frac{1}{6}(3 + \sqrt{5}), -\sqrt{\frac{7}{6} + \frac{\sqrt{5}}{2}}, -\frac{7}{3}\right)$
---	---

---



---

Table B.19: The vertices of a rhombic enneacuboctahedron - continued.

---



---

$\left(\frac{1}{6}(3 + \sqrt{5}), -\sqrt{\frac{1}{6}(3 - \sqrt{5})}, -\frac{1}{3} + \sqrt{5}\right)$ $\left(\frac{1}{6}(3 + \sqrt{5}), \sqrt{\frac{1}{6}(7 + 3\sqrt{5})}, -\frac{7}{3}\right)$ $\left(\frac{1}{3}(1 + \sqrt{5}), \sqrt{\frac{2}{3}(3 + \sqrt{5})}, \frac{2}{3}(-1 + \sqrt{5})\right)$ $\left(\frac{1}{6}(5 + \sqrt{5}), -\sqrt{\frac{5}{6}(3 + \sqrt{5})}, \frac{2}{3}(-2 + \sqrt{5})\right)$ $\left(\frac{1}{6}(5 + \sqrt{5}), \sqrt{\frac{5}{6}(3 + \sqrt{5})}, \frac{2}{3}(-2 + \sqrt{5})\right)$ $\left(\frac{1}{6}(7 + \sqrt{5}), -\sqrt{\frac{7}{6} + \frac{\sqrt{5}}{2}}, \frac{1}{3}(-7 + \sqrt{5})\right)$ $\left(\frac{1}{2}(1 + \sqrt{5}), -\sqrt{\frac{1}{6}(3 + \sqrt{5})}, -2\right)$ $\left(\frac{1}{2}(1 + \sqrt{5}), \sqrt{\frac{1}{6}(3 + \sqrt{5})}, -2\right)$ $\left(\frac{1}{3}(3 + \sqrt{5}), 0, -\frac{2}{3} + \sqrt{5}\right)$ $\left(\frac{1}{6}(5 + 3\sqrt{5}), -\sqrt{\frac{7}{6} + \frac{\sqrt{5}}{2}}, -1 + \frac{2\sqrt{5}}{3}\right)$ $\left(\frac{1}{6}(5 + 3\sqrt{5}), \sqrt{\frac{1}{6}(7 + 3\sqrt{5})}, -1 + \frac{2\sqrt{5}}{3}\right)$ $\left(\frac{1}{3}(4 + \sqrt{5}), \frac{1}{\sqrt{3}}, \frac{2}{3}(-1 + \sqrt{5})\right)$ $\left(\frac{1}{6}(7 + 3\sqrt{5}), -\sqrt{\frac{1}{6}(3 + \sqrt{5})}, \frac{1}{3}(-6 + \sqrt{5})\right)$ $\left(\frac{1}{6}(7 + 3\sqrt{5}), \sqrt{\frac{1}{6}(3 + \sqrt{5})}, \frac{1}{3}(-6 + \sqrt{5})\right)$ $\left(\frac{1}{3}(5 + \sqrt{5}), 0, \frac{1}{3}(-5 + \sqrt{5})\right)$	$\left(\frac{1}{6}(3 + \sqrt{5}), \sqrt{\frac{1}{6}(3 - \sqrt{5})}, -\frac{1}{3} + \sqrt{5}\right)$ $\left(\frac{1}{3}(1 + \sqrt{5}), -\sqrt{\frac{2}{3}(3 + \sqrt{5})}, \frac{2}{3}(-1 + \sqrt{5})\right)$ $\left(\frac{1}{6}(5 + \sqrt{5}), -\sqrt{\frac{5}{6}(3 + \sqrt{5})}, \frac{1}{3}(-7 + 2\sqrt{5})\right)$ $\left(\frac{1}{6}(5 + \sqrt{5}), \sqrt{\frac{5}{6}(3 + \sqrt{5})}, \frac{1}{3}(-7 + 2\sqrt{5})\right)$ $\left(\frac{2\sqrt{5}}{3}, 0, -\frac{7}{3}\right)$ $\left(\frac{1}{6}(7 + \sqrt{5}), \sqrt{\frac{1}{6}(7 + 3\sqrt{5})}, \frac{1}{3}(-7 + \sqrt{5})\right)$ $\left(\frac{1}{2}(1 + \sqrt{5}), -\sqrt{\frac{1}{6}(3 + \sqrt{5})}, -1 + \sqrt{5}\right)$ $\left(\frac{1}{2}(1 + \sqrt{5}), \sqrt{\frac{1}{6}(3 + \sqrt{5})}, -1 + \sqrt{5}\right)$ $\left(\frac{1}{6}(5 + 3\sqrt{5}), -\sqrt{\frac{7}{6} + \frac{\sqrt{5}}{2}}, \frac{2}{3}(-3 + \sqrt{5})\right)$ $\left(\frac{1}{6}(5 + 3\sqrt{5}), \sqrt{\frac{1}{6}(7 + 3\sqrt{5})}, \frac{2}{3}(-3 + \sqrt{5})\right)$ $\left(\frac{1}{3}(4 + \sqrt{5}), -\frac{1}{\sqrt{3}}, \frac{2}{3}(-1 + \sqrt{5})\right)$ $\left(\frac{2}{3}(1 + \sqrt{5}), 0, \frac{1}{3}(-7 + \sqrt{5})\right)$ $\left(\frac{1}{6}(7 + 3\sqrt{5}), -\sqrt{\frac{1}{6}(3 + \sqrt{5})}, \frac{1}{3}(-3 + \sqrt{5})\right)$ $\left(\frac{1}{6}(7 + 3\sqrt{5}), \sqrt{\frac{1}{6}(3 + \sqrt{5})}, \frac{1}{3}(-3 + \sqrt{5})\right)$ $\left(\frac{1}{3}(5 + \sqrt{5}), 0, \frac{1}{3}(-2 + \sqrt{5})\right)$
--	---

---



---

## B.4 Additional Visual Representations

In this section we give visual representations of some of the data in Tables B.3, B.13 and B.14, as well as of the crystal structures we obtained for our cap [109] and hammerhead shark [281] models.

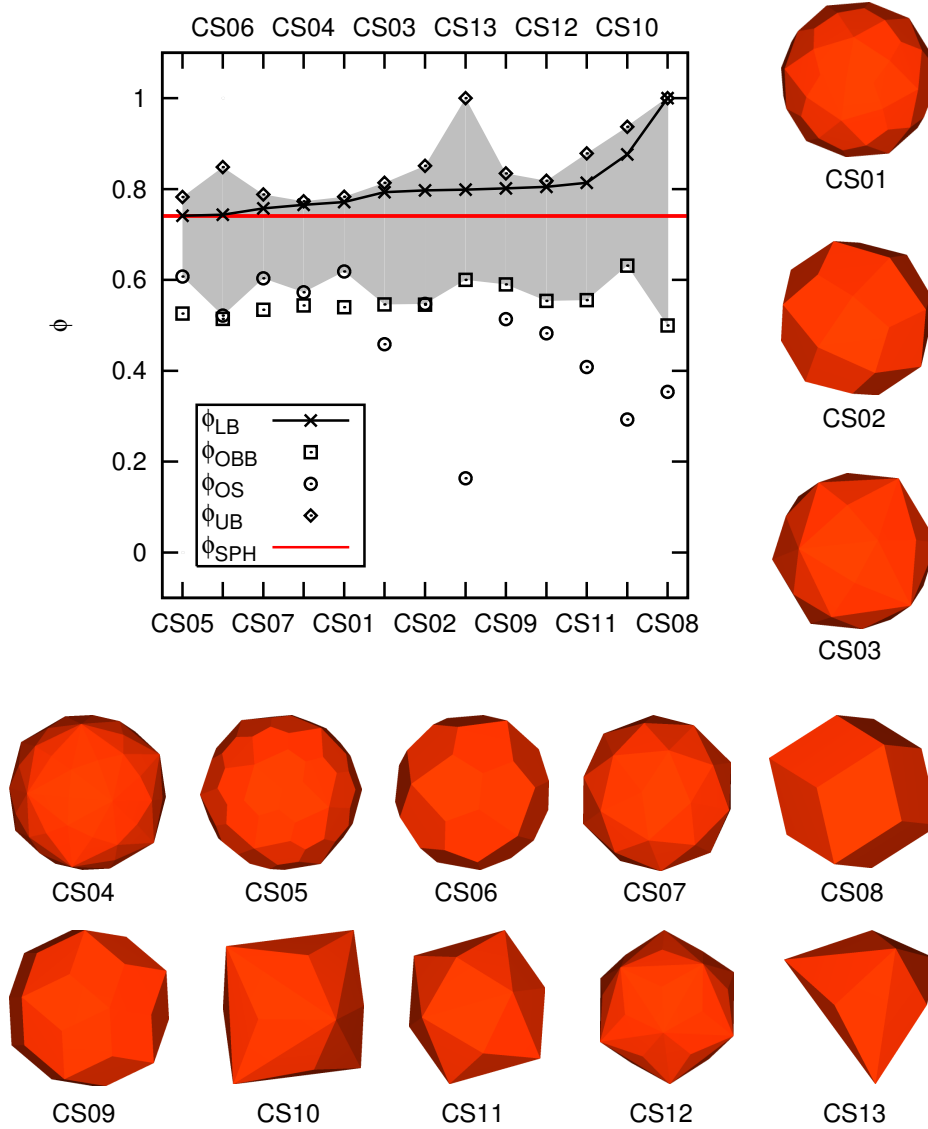


**Figure B.1:** Bounds to the packing fraction  $\phi_D$  of the densest structure for 13 Catalan solids. We show  $\phi_{LB}$  (connected crosses),  $\phi_{OS}$  (circles),  $\phi_{OBB}$  (squares),  $\phi_{UB}$  (diamonds),  $\phi_{SPH} = \pi/\sqrt{18}$  (red line), and visual representations of the models (shaded red). See Table B.3 for the naming convention and the numerical values. The grey area shows the old bounds to  $\phi_D$ ; the area above  $\phi_{LB}$  curve the improved bounds that were obtained using our FBMC technique.

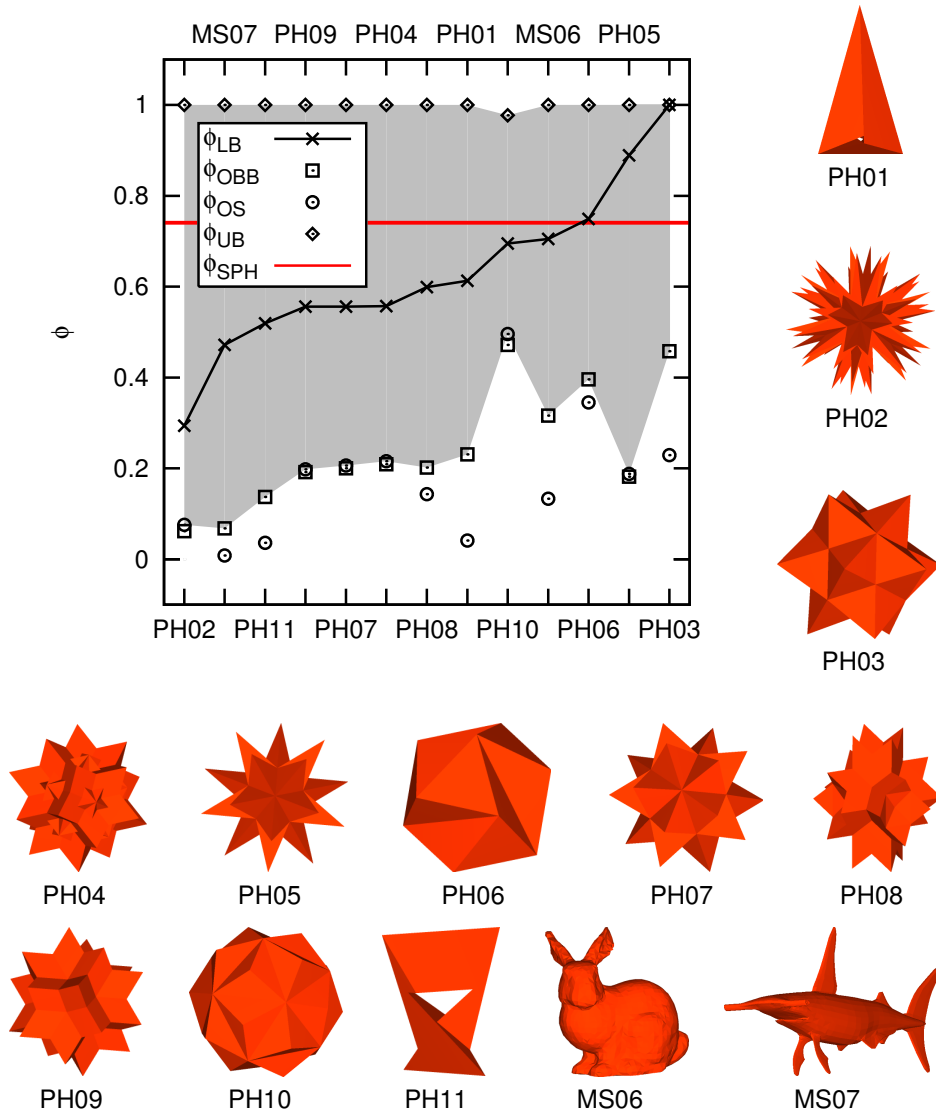


**Figure B.2:** Bounds to the packing fraction  $\phi_D$  of the densest structure for 13 nonconvex solids. We show  $\phi_{LB}$  (connected crosses),  $\phi_{OS}$  (circles),  $\phi_{OBB}$  (squares),  $\phi_{UB}$  (diamonds),  $\phi_{SPH} = \pi/\sqrt{18}$  (red line), and visual representations of the models (shaded red). See Tables B.13 and B.14 for the naming convention and the numerical values. The grey area shows the old bounds to  $\phi_D$ ; the area above  $\phi_{LB}$  curve the improved bounds that were obtained using our FBMC technique.

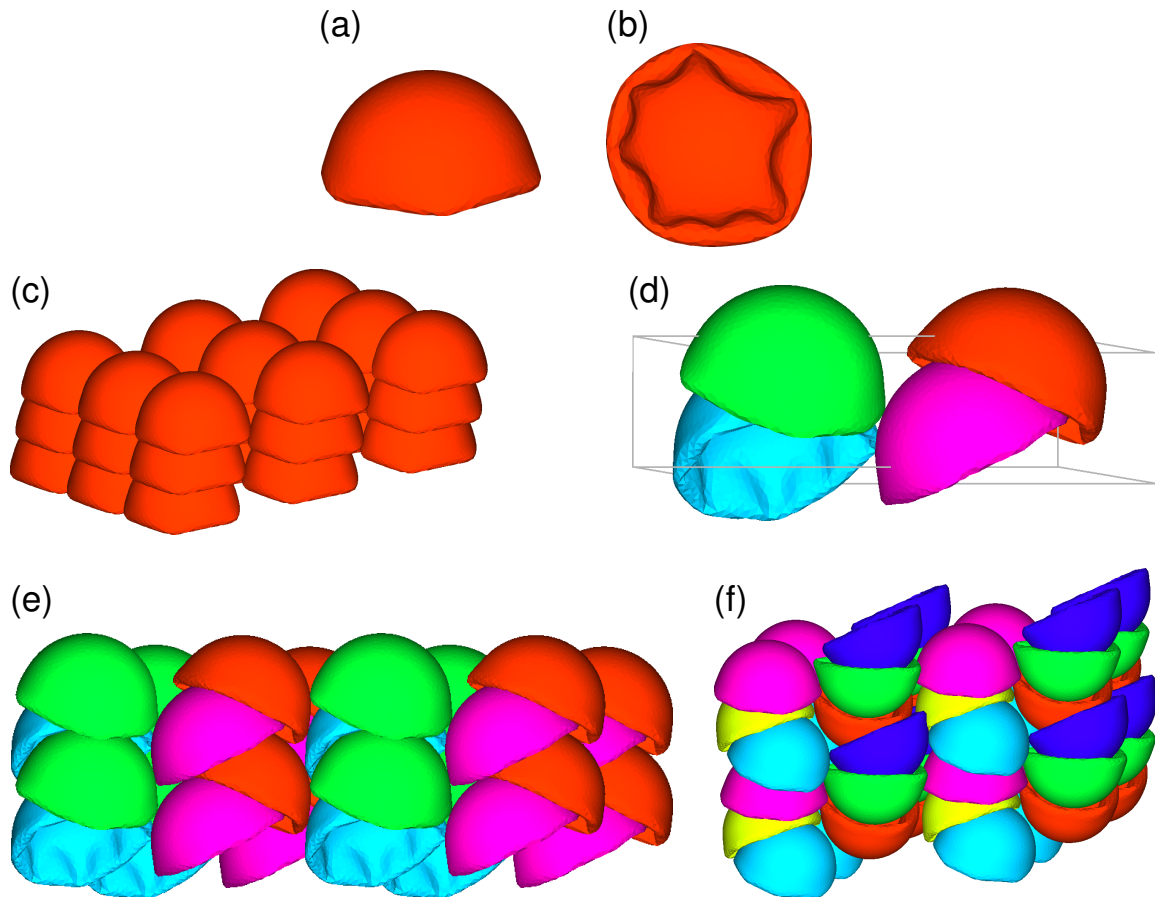


**Figure B.3:** Two views (a) and (b) of the cap model used in our simulations. Note the buckling that has occurred in the impression left by the shell collapse. (c) A columnar phase ( $N = 1$ ), 27 periodic images are shown. For  $N = 2, 3, 4$ , and 5, we obtain braided phases without inversion [176]. (d) The caps and unit cell for  $N = 4$ . The different caps are labelled with different colours. (e) The structure this unit cell generates is a binary braided configuration, only 8 periodic images are shown. (f) A rough braided phase with inversions ( $N = 6$ ), which looks similar to the ‘IB phase’ predicted in Ref. [176], again only 8 periodic images are shown.

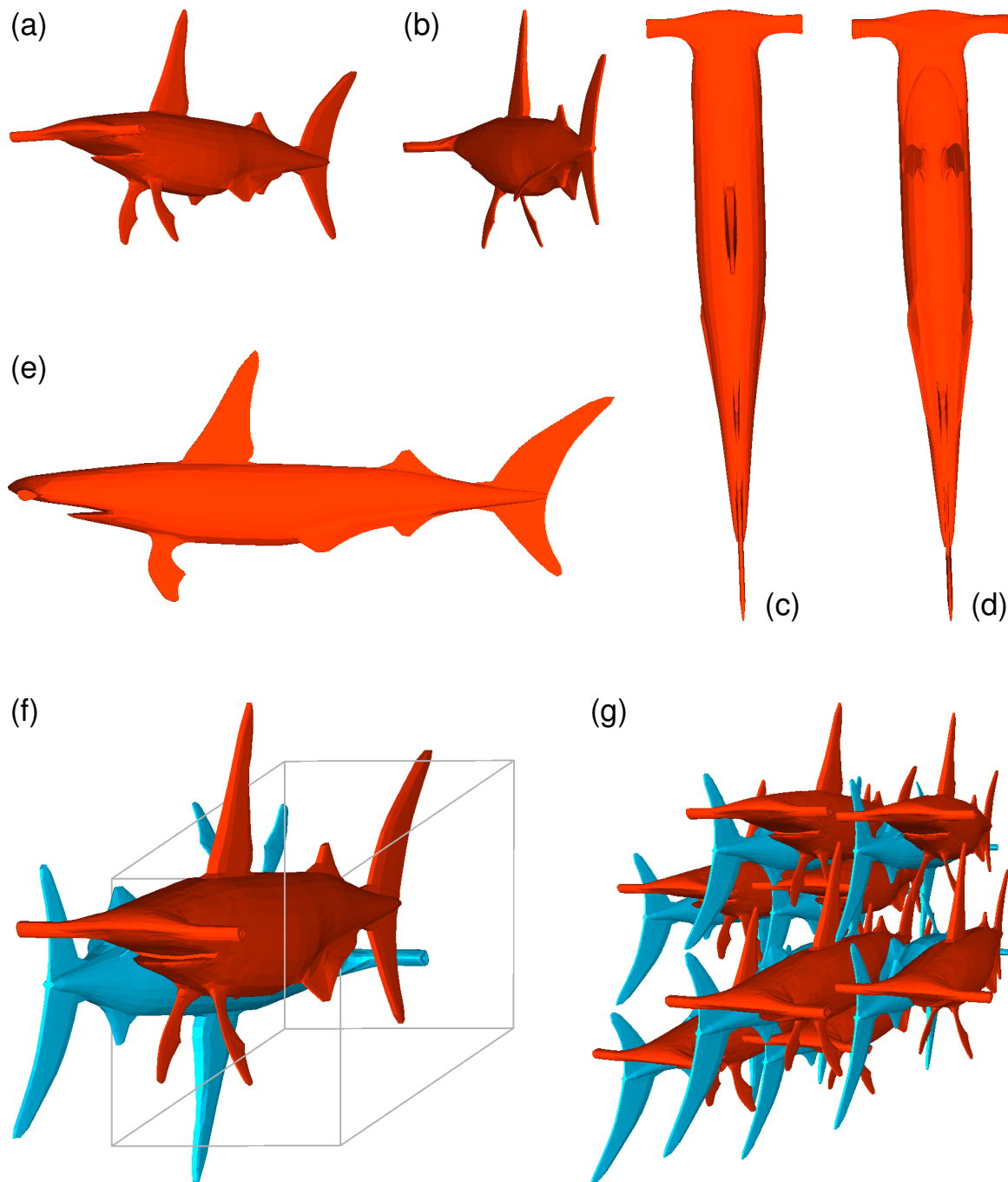


**Figure B.4:** Different views (a) - (e) of a hammerhead-shark model [281]. The unit cell of the densest regular packing ( $\phi_{LB} = 0.472\dots$ ) is shown in (f) and a piece of the crystal in (g). The crystal structure is a double lattice where two hammerhead sharks (red, blue) point in opposite directions and one is rotated by an angle of  $\pi$  radians around its long axis with respect to the other, thereby forming a centrosymmetric dimer.

# References

- [1] A. D. McNaught. *IUPAC compendium of chemical terminology*. Blackwell Science Inc. (Hoboken), 2nd edition, 1997.
- [2] T. Graham, *Liquid diffusion applied to analysis*. Phil. Trans. R. Soc. London, 151:183, 1861.
- [3] R. Brown, *A brief account of microscopical observations made in the months of June, July and August 1827 on the particles contained in the pollen of plants; and on the general existence of active molecules in organic and inorganic bodies*. Phil. Mag., 4:161, 1828.
- [4] D. Layton, *The original observations of Brownian motion*. J. Chem. Edu., 42:367, 1965.
- [5] J. Klafter, M. F. Shlesinger, and G. Zumofen, *Beyond Brownian motion*. Physics Today, 49:33, 1996.
- [6] P. Hänggi, F. Marchesoni, and F. Nori, *Brownian motors*. Ann. Phys. (Berlin), 14:51, 2005.
- [7] W. E. Leonard. *De Rerum Natura: The Latin Text of Lucretius*. University of Wisconsin Press (Madison), 1st edition, 2008.
- [8] A. Einstein, *Über die von der molekularkinetischen theorie der wärme geforderte bewegung von in ruhenden flüssigkeiten suspendierten teilchen*. Ann. Phys. (Leipz.), 17:549, 1905.
- [9] W. Sutherland, *A dynamical theory of diffusion for non-electrolytes and the molecular mass of albumin*. Phil. Mag., 9:781, 1905.
- [10] J. Perrin, *Mouvement Brownien et réalité moléculaire*. Ann. Chim. Phys., 18:5, 1909.
- [11] J. Perrin. *Les atomes*. Alacan (Paris), 1st edition, 1913.
- [12] Scientific Committee on Emerging and Newly Identified Health Risks (SCENHIR). *The appropriateness of existing methodologies to assess the potential risks associated with engineered and adventitious products of nanotechnologies*. [http://ec.europa.eu/health/ph\\_risk/committees/04\\_scenihir/docs/scenihir\\_o\\_003b.pdf](http://ec.europa.eu/health/ph_risk/committees/04_scenihir/docs/scenihir_o_003b.pdf), 2006.
- [13] J. Turkevich, G. Garton, and P. C. Stevenson, *The color of colloidal gold*. J. Colloid Sci., 9:26, 1954.
- [14] K. S. Novoselov, A. K. Geim, S. V. Morozov, D. Jiang, Y. Zhang, S. V. Dubonos, I. V. Grigorieva, and A. A. Firsov, *Electric field effect in atomically thin carbon films*. Science, 306:666, 2004.
- [15] McGraw-Hill. *McGraw-Hill Encyclopedia of Science & Technology*. McGraw-Hill Professional Publishing (New York), 9th edition, 2002.
- [16] I. W. Hamley. *Introduction to Soft Matter: Synthetic and Biological Self-Assembling Materials*. John Wiley & Sons (New York), 1st edition, 2007.
- [17] S. Fraden, G. Maret, D. L. D. Caspar, and R. B. Meyer, *Isotropic-nematic phase transition and angular correlations in isotropic suspensions of tobacco mosaic virus*. Phys. Rev. Lett., 63:2068, 1989.
- [18] P. A. Buining, A. P. Philipse, and H. N. W. Lekkerkerker, *Phase behavior of aqueous dispersions of colloidal boehmite rods*. Langmuir, 10:2106, 1994.

- [19] Z. Dogic and S. Fraden, *Smectic phase in a colloidal suspension of semiflexible virus particles*. Phys. Rev. Lett., 78:2417, 1997.
- [20] F. M. van der Kooij and H. N. W. Lekkerkerker, *Formation of nematic liquid crystals in suspensions of hard colloidal platelets*. J. Phys. Chem. B, 102:7829, 1998.
- [21] D. van der Beek and H. N. W. Lekkerkerker, *Liquid crystal phases of charged colloidal platelets*. Langmuir, 20:8582, 2004.
- [22] E. van den Pol, A. V. Petukhov, D. M. E. Thies-Weesie, D. V. Byelov, and G. J. Vroege, *Liquid crystal phase behavior of sterically-stabilized goethite*. J. Colloid Interface Sci., 352:354, 2010.
- [23] E. van den Pol, D. M. E. Thies-Weesie, A. V. Petukhov, D. V. Byelov, and G. J. Vroege, *Uniaxial and biaxial liquid crystal phases in colloidal dispersions of board-like particles*. Liquid Crystals, 37:641, 2010.
- [24] A. Kuijk, A. van Blaaderen, and A. Imhof, *Synthesis of monodisperse, rodlike silica colloids with tunable aspect ratio*. J. Am. Chem. Soc., 133:2346, 2011.
- [25] D. Zerrouki, J. Baudry, D. Pine, P. Chaikin, and J. Bibette, *Chiral colloidal clusters*. Nature, 455:380, 2008.
- [26] B. Madivala, J. Fransaer, and J. Vermant, *Self-assembly and rheology of ellipsoidal particles at interfaces*. Langmuir, 25:2718, 2009.
- [27] J. He, Z. Niu, R. Tangirala, J.-Y. Wang, X. Wei, G. Kaur, Q. Wang, G. Jutz, A. Böker, B. Lee, S. V. Pingali, P. Thiyagarajan, T. Emrick, and T. P. Russell, *Self-assembly of tobacco mosaic virus at oil/water interfaces*. Langmuir, 25:4979, 2009.
- [28] M. E. Leunissen, H. R. Vutukuri, and A. van Blaaderen, *Directing colloidal self-assembly with biaxial electric fields*. Adv. Mater., 21:3116, 2009.
- [29] D. J. Kraft, W. S. Vlug, C. M. van Kats, A. van Blaaderen, A. Imhof, and W. K. Kegel, *Self-assembly of colloids with liquid protrusions*. J. Am. Chem. Soc., 131:1182, 2009.
- [30] A. F. Demirörs, P. M. Johnson, C. M. van Kats, A. van Blaaderen, and A. Imhof, *Directed self-assembly of colloidal dumbbells with an electric field*. Langmuir, 26:14466, 2010.
- [31] L. Fillion, M. Hermes, R. Ni, E. C. M. Vermolen, A. Kuijk, C. G. Christova, J. C. P. Stiefelhagen, T. Vissers, A. van Blaaderen, and M. Dijkstra, *Self-assembly of a colloidal interstitial solid with tunable sublattice doping*. Phys. Rev. Lett., 107:168302, 2011.
- [32] Q. Chen, S. C. Bae, and S. Granick, *Directed self-assembly of a colloidal kagome lattice*. Nature, 469:381, 2011.
- [33] H. R. Vutukuri. *Complex Colloidal Structures by Self-Assembly in Electric Fields*. PhD thesis, Utrecht University, 2012. ISBN 978-90-393-5729-3.
- [34] D. V. Talapin, E. V. Shevchenko, A. Kornowski, N. Gaponik, M. Haase, A. L. Rogach, and H. Weller, *A new approach to crystallization of CdSe nanoparticles into ordered three-dimensional superlattices*. Adv. Mater., 13:1868, 2001.
- [35] D. V. Talapin, E. V. Shevchenko, C. B. Murray, A. Kornowski, S. Förster, and H. Weller, *CdSe and CdSe/CdS nanorod solids*. J. Am. Chem. Soc., 126:12984, 2004.
- [36] E. V. Shevchenko, J. B. Kortright, D. V. Talapin, S. Aloni, and A. P. Alivisatos, *Quasi-ternary nanoparticle superlattices through nanoparticle design*. Adv. Mater., 19:4183, 2007.
- [37] Z. Chen and S. O'Brien, *Structure direction of II-VI semiconductor quantum dot binary nanoparticle superlattices by tuning radius ratio*. ACS Nano, 2:1219, 2008.

- [38] D. Nykypanchuk, M. M. Maye, D. van der Lelie, and O. Gang, *DNA-guided crystallization of colloidal nanoparticles*. *Nature*, 451:549, 2008.
- [39] S. Y. Park, A. K. R. Lytton-Jean, B. Lee, S. Weigand, G. C. Schatz, and C. A. Mirkin, *DNA-programmable nanoparticle crystallization*. *Nature*, 451:553, 2008.
- [40] W. H. Evers, H. Friedrich, L. Filion, M. Dijkstra, and D. Vanmaekelbergh, *Observation of a ternary nanocrystal superlattice and its structural characterization by electron tomography*. *Angew. Chem. Int. Ed.*, 48:9655, 2009.
- [41] A. Guerrero-Martínez, J. Pérez-Juste, E. Carbó-Argibay, G. Tardajos, and L. M. Liz-Marzán, *Gemini surfactant-directed self-assembly of monodisperse gold nanorods into standing superlattices*. *Angew. Chem. Int. Ed.*, 48:9484, 2009.
- [42] F. Li, W. C. Yoo, M. B. Beernink, and A. Stein, *Site-specific functionalization of anisotropic nanoparticles: From colloidal atoms to colloidal molecules*. *J. Am. Chem. Soc.*, 131:18548, 2009.
- [43] P. Podsiadlo, E. M. Arruda, E. Kheng, A. M. Waas, J. Lee, K. Critchley, M. Qin, E. Chuang, A. K. Kaushik, H.-S. Kim, Y. Qi, S.-T. Noh, and N. A. Kotov, *LBL assembled laminates with hierarchical organization from nano- to microscale: High-toughness nanomaterials and deformation imaging*. *ACS Nano*, 3:1564, 2009.
- [44] A. Snezhko, M. Belkin, I. S. Aranson, and W.-K. Kwok, *Self-assembled magnetic surface swimmers*. *Phys. Rev. Lett.*, 102:118103, 2009.
- [45] J. W. Ciszek, *Assembly of nanorods into designer superstructures: The role of templating, capillary forces, adhesion, and polymer hydration*. *ACS Nano*, 4:259, 2010.
- [46] M. R. Jones, R. J. Macfarlane, B. Lee, J. Zhang, K. L. Young, A. J. Senesi, and C. A. Mirkin, *DNA-nanoparticle superlattices formed from anisotropic building blocks*. *Nature Mater.*, 9:913, 2010.
- [47] A. G. Dong, J. Chen, P. M. Vora, J. M. Kikkawa, and C. B. Murray, *Binary nanocrystal superlattice membranes self-assembled at the liquid-air interface*. *Nature*, 466:474, 2010.
- [48] K. Liu, Z. Nie, N. Zhao, W. Li, M. Rubinstein, and E. Kumacheva, *Step-growth polymerization of inorganic nanoparticles*. *Science*, 329:197, 2010.
- [49] W. H. Evers, B. de Nijs, L. Filion, S. Castillo, M. Dijkstra, and D. Vanmaekelbergh, *Entropy-driven formation of binary semiconductor-nanocrystal superlattices*. *Nano Lett.*, 10:4235, 2010.
- [50] D. Baranov, A. Fiore, M. van Huis, C. Giannini, A. Falqui, U. Lafont, H. Zandbergen, M. Zanella, R. Cingolani, and L. Manna, *Assembly of colloidal semiconductor nanorods in solution by depletion attraction*. *Nano Lett.*, 10:743, 2010.
- [51] M. I. Bodnarchuk, M. V. Kovalenko, W. Heiss, and D. V. Talapin, *Energetic and entropic contributions to self-assembly of binary nanocrystal superlattices: Temperature as the structure-directing factor*. *J. Am. Chem. Soc.*, 132:11967, 2010.
- [52] A. Snezhko and I. S. Aranson, *Magnetic manipulation of self-assembled colloidal asters*. *Nature Mater.*, 10:698, 2011.
- [53] F. Li, D. P. Josephson, and A. Stein, *Colloidal assembly: The road from particles to colloidal molecules and crystals*. *Angew. Chem. Int. Ed.*, 50:360, 2011.
- [54] K. Miszta, J. de Graaf, G. Bertoni, D. Dorfs, R. Brescia, S. Marras, L. Ceseracciu, R. Cingolani, R. van Roij, M. Dijkstra, and L. Manna, *Hierarchical self-assembly of suspended branched colloidal nanocrystals into superlattice structures*. *Nature Mater.*, 10:872, 2011.

- [55] G. C. L. Wong, J. X. Tang, A. Lin, Y. Li, P. A. Janmey, and C. R. Safinya, *Hierarchical self-assembly of F-actin and cationic lipid complexes: Stacked three-layer tubule networks*. Science, 288:2035, 2000.
- [56] V. Ottani, D. Martini, M. Franchi, A. Ruggeri, and M. Raspanti, *Hierarchical structures in fibrillar collagens*. Micron, 33:587, 2002.
- [57] G. M. Whitesides and B. Grzybowski, *Self-assembly at all scales*. Science, 295:2418, 2002.
- [58] S. Zhang, *Fabrication of novel biomaterials through molecular self-assembly*. Nature Biotech., 21:1171, 2003.
- [59] J. Orgel, T. C. Irving, A. Miller, and T. J. Wess, *Microfibrillar structure of type I collagen in situ*. Proc. Natl. Acad. Sci. USA, 103:9001, 2006.
- [60] Y. He, T. Ye, M. Su, C. Zhang, A. E. Ribbe, W. Jiang, and C. Mao, *Hierarchical self-assembly of DNA into symmetric supramolecular polyhedra*. Nature, 452:198, 2008.
- [61] S. M. Douglas, H. Dietz, T. Liedl, B. Hogberg, F. Graf, and W. M. Shih, *Self-assembly of DNA into nanoscale three-dimensional shapes*. Nature, 459:414, 2009.
- [62] H. K. Murnen, A. M. Rosales, J. N. Jaworski, R. A. Segalman, and R. N. Zuckermann, *Hierarchical self-assembly of a biomimetic diblock copolypeptoid into homochiral superhelices*. J. Am. Chem. Soc., 132:16112, 2010.
- [63] T. P. J. Knowles, T. W. Oppenheim, A. K. Buell, D. Y. Chirgadze, and M. E. Welland, *Nanostructured films from hierarchical self-assembly of amyloidogenic proteins*. Nature Nano., 5:204, 2010.
- [64] G. M. Whitesides and M. Boncheva, *Beyond molecules: Self-assembly of mesoscopic and macroscopic components*. Proc. Natl. Acad. Sci. USA, 99:4769, 2002.
- [65] V. J. Anderson and H. N. W. Lekkerkerker, *Insights into phase transition kinetics from colloid science*. Nature, 416:811, 2002.
- [66] A. Yethiraj and A. van Blaaderen, *A colloidal model system with an interaction tunable from hard sphere to soft and dipolar*. Nature, 421:513, 2003.
- [67] A. van Blaaderen and P. Wiltzius, *Real-space structure of colloidal hard-sphere glasses*. Science, 270:1177, 1995.
- [68] V. Prasad, D. Semwogerere, and E. R. Weeks, *Confocal microscopy of colloids*. J. Phys.: Condens. Matter, 19:113102, 2007.
- [69] J. N. Israelachvili. *Intermolecular and Surface Forces*. Academic Press (London), 2nd edition, 1992.
- [70] R. Piazza, T. Bellini, and V. Degiorgio, *Equilibrium sedimentation profiles of screened charged colloids: A test of the hard-sphere equation of state*. Phys. Rev. Lett., 71:4267, 1993.
- [71] Z. Cheng, J. Zhu, P. M. Chaikin, S.-E. Phan, and W. B. Russel, *Nature of the divergence in low shear viscosity of colloidal hard-sphere dispersions*. Phys. Rev. E, 65:041405, 2002.
- [72] G. Bryant, S. R. Williams, L. Qian, I. K. Snook, E. Perez, and F. Pincet, *How hard is a colloidal "hard-sphere" interaction?* Phys. Rev. E, 66:060501, 2002.
- [73] W. C. K. Poon, E. R. Weeks, and C. P. Royall, *On measuring colloidal volume fractions*. Soft Matter, 8:21, 2012.

- [74] L. Filion and M. Dijkstra, *Prediction of binary hard-sphere crystal structures*. Phys. Rev. E, 79:046714, 2009.
- [75] L. Filion, M. Marechal, B. van Oorschot, D. Pelt, F. Smalenburg, and M. Dijkstra, *Efficient method for predicting crystal structures at finite temperature: Variable box shape simulations*. Phys. Rev. Lett., 103:188302, 2009.
- [76] M. E. Leunissen, C. G. Christova, A. Hynninen, C. P. Royall, A. I. Campbell, A. Imhof, M. Dijkstra, R. van Roij, and A. van Blaaderen, *Ionic colloidal crystals of oppositely charged particles*. Nature, 437:235, 2005.
- [77] T. Vissers, A. Wysocki, M. Rex, H. Lowen, C. P. Royall, A. Imhof, and A. van Blaaderen, *Lane formation in driven mixtures of oppositely charged colloids*. Soft Matter, 7:2352, 2011.
- [78] S. Deka, D. Miszta, K. and Dorfs, A. Genovese, G. Bertoni, and L. Manna, *Octapod-shaped colloidal nanocrystals of cadmium chalcogenides via ‘one-pot’ cation exchange and seeded growth*. Nano Lett., 10:3770, 2010.
- [79] A. M. Wierenga, T. A. J. Lenstra, and A. P. Philipse, *Aqueous dispersions of colloidal gibbsite platelets: synthesis, characterisation and intrinsic viscosity measurements*. Colloids Surfaces A.: Physicochem. Eng. Aspects, 134:8582, 1998.
- [80] C. C. Ho, A. Keller, J. A. Odell, and R. H. Ottewill, *Preparation of monodisperse ellipsoidal polystyrene particles*. Colloid Polym. Sci., 271:469, 1993.
- [81] C. M. van Kats, P. M. Johnson, J. E. A. M. van den Meerakker, and A. van Blaaderen, *Synthesis of monodisperse high-aspect-ratio colloidal silicon and silica rods*. Langmuir, 20:11201, 2004.
- [82] S. C. Glotzer and M. J. Solomon, *Anisotropy of building blocks and their assembly into complex structures*. Nature Mater., 6:557, 2007.
- [83] S. Sacanna and D. J. Pine, *Shape-anisotropic colloids: Building blocks for complex assemblies*. Curr. Opin. Colloid Interface Sci., 16:96, 2011.
- [84] Y. Sun and Y. Xia, *Shape-controlled synthesis of gold and silver nanoparticles*. Science, 298:2176, 2002.
- [85] X. Zhang, C. Dong, J. Zapfen, S. Ismathullakhan, Z. Kang, J. Jie, X. Zhang, J. Chang, C.-S. Lee, and S.-T. Lee, *Polyhedral organic microcrystals: From cubes to rhombic dodecahedra*. Angew. Chem. Int. Ed., 48:9121, 2009.
- [86] H.-L. Wu, C.-H. Kuo, and M. H. Huang, *Seed-mediated synthesis of gold nanocrystals with systematic shape evolution from cubic to trisoctahedral and rhombic dodecahedral structures*. Langmuir, 26:12307, 2010.
- [87] L. Rossi, S. Sacanna, W. T. M. Irvine, P. M. Chaikin, D. J. Pine, and A. P. Philipse, *Cubic crystals from cubic colloids*. Soft Matter, 7:4139, 2011.
- [88] Y. Zhang, F. Lu, D. van der Lelie, and O. Gang, *Continuous phase transformation in nanocube assemblies*. Phys. Rev. Lett., 107:135701, 2011.
- [89] A. Tao, P. Sinsermsuksakul, and P. Yang, *Polyhedral silver nanocrystals with distinct scattering signatures*. Angew. Chem. Int. Ed., 45:4597, 2006.
- [90] A. R. Tao, S. Habas, and P. Yang, *Shape control of colloidal metal nanocrystals*. Small, 4:310, 2008.

- [91] F. Kim, S. Connor, H. Song, T. Kuykendall, and P. Yang, *Platonic gold nanocrystals*. *Angew. Chem.*, 116:3759, 2004.
- [92] E. C. Greyson, J. E. Barton, and T. W. Odom, *Tetrahedral zinc blende tin sulfide nano- and microcrystals*. *Small*, 2:368, 2006.
- [93] B. Wiley, T. Herricks, Y. Sun, and Y. Xia, *Polyol synthesis of silver nanoparticles: Use of chloride and oxygen to promote the formation of single-crystal, truncated cubes and tetrahedrons*. *Nano Lett.*, 4:1733, 2004.
- [94] A. S. Barnard, X. M. Lin, and L. A. Curtiss, *Equilibrium morphology of face-centered cubic gold nanoparticles >3 nm and the shape changes induced by temperature*. *J. Phys. Chem. B*, 109:24465, 2005.
- [95] J. Tang, X. Zhou, D. Zhao, G. Q. Lu, J. Zou, and C. Yu, *Hard-sphere packing and icosahedral assembly in the formation of mesoporous materials*. *J. Am. Chem. Soc.*, 129:9044, 2007.
- [96] K. Kwon, K. Y. Lee, Y. W. Lee, M. Kim, J. Heo, and S. W. Ahn, S. J. and Han, *Controlled synthesis of icosahedral gold nanoparticles and their surface-enhanced Raman scattering property*. *J. Phys. Chem. C*, 111:1161, 2007.
- [97] P. M. Johnson, C. M. van Kats, and A. van Blaaderen, *Synthesis of colloidal silica dumbbells*. *Langmuir*, 21:11510, 2005.
- [98] A. Perro, E. Duguet, O. Lambert, J.-C. Taveau, E. Bourgeat-Lami, and S. Ravaine, *A chemical synthetic route towards "colloidal molecules"*. *Angew. Chem.*, 424:361, 2009.
- [99] R. Brescia, K. Miszta, D. Dorfs, L. Manna, and G. Bertoni, *Birth and growth of octapod-shaped colloidal nanocrystals studied by electron tomography*. *J. Phys. Chem. C*, 115:20128, 2011.
- [100] C. J. DeSantis, A. A. Peverly, D. G. Peters, and S. E. Skrabalak, *Octopods versus concave nanocrystals: Control of morphology by manipulating the kinetics of seeded growth via co-reduction*. *Nano Lett.*, 11:2164, 2011.
- [101] C. J. DeSantis and S. E. Skrabalak, *Size-controlled synthesis of au/pd octopods with high refractive index sensitivity*. *Langmuir*, ASAP:1, 2012.
- [102] L. Manna, D. J. Milliron, A. Meisel, E. C. Scher, and A. P. Alivisatos, *Controlled growth of tetrapod-branched inorganic nanocrystals*. *Nature Mater.*, 2:382, 2003.
- [103] M. C. Newton and P. A. Warburton, *ZnO tetrapod nanocrystals*. *Mater. Today*, 10:1369, 2007.
- [104] G. Zhou, M. Lü, Z. Xiu, S. Wang, H. Zhang, Y. Zhou, and S. Wang, *Controlled synthesis of high-quality PbS star-shaped dendrites, multipods, truncated nanocubes, and nanocubes and their shape evolution process*. *J. Phys. Chem. B*, 110:6543, 2006.
- [105] N. Zhao and L. M. Qi, *Low-temperature synthesis of star-shaped PbS nanocrystals in aqueous solutions of mixed cationic/anionic surfactants*. *Adv. Mater.*, 18:359, 2006.
- [106] T. Huang, Q. A. Zhao, J. Y. Xiao, and L. M. Qi, *Controllable self-assembly of PbS nanostars into ordered structures: Close-packed arrays and patterned arrays*. *ACS Nano*, 4:4707, 2010.
- [107] C. I. Zoldesi and A. Imhof, *Synthesis of monodisperse colloidal spheres, capsules, and microballoons by emulsion templating*. *Adv. Mater.*, 17:924, 2005.

- [108] D. Jagadeesan, U. Mansoori, P. Mandal, A. Sundaresan, and M. Eswaramoorthy, *Hollow spheres to nanocups: Tuning the morphology and magnetic properties of single-crystalline-Fe<sub>2</sub>O<sub>3</sub> nanostructures*. *Angew. Chem.*, 47:7685, 2008.
- [109] C. Quilliet, C. Zoldesi, C. Riera, A. van Blaaderen, and A. Imhof, *Anisotropic colloids through non-trivial buckling*. *Eur. Phys. J. E*, 27:13, 2008.
- [110] K.-H. Roh, D. C. Martin, and J. Lahann, *Biphasic Janus particles with nanoscale anisotropy*. *Nature Mater.*, 4:759, 2005.
- [111] L. Hong, S. Jiang, and S. Granick, *Simple method to produce Janus colloidal particles in large quantity*. *Langmuir*, 22:9495, 2006.
- [112] S. Jiang and S. Granick, *Controlling the geometry (Janus balance) of amphiphilic colloidal particles*. *Langmuir*, 24:2438, 2008.
- [113] S. Jiang, M. J. Schultz, Q. Chen, J. S. Moore, and S. Granick, *Solvent-free synthesis of Janus colloidal particles*. *Langmuir*, 24:10073, 2008.
- [114] B. Liu, W. Wei, X. Qu, and Z. Yang, *Janus colloids formed by biphasic grafting at a Pickering emulsion interface*. *Angew. Chem.*, 120:4037, 2008.
- [115] S. Jiang, Q. Chen, M. Tripathy, E. Luijten, K. S. Schweizer, and S. Granick, *Janus particle synthesis and assembly*. *Adv. Mater.*, 22:1060, 2010.
- [116] C. Chengliang Zhang, B. Liu, C. Tang, J. Liu, X. Qu, J. Li, and Z. Yang, *Large scale synthesis of Janus submicron sized colloids by wet etching anisotropic ones*. *Chem. Commun.*, 46:4610, 2010.
- [117] C. Casagrande and M. Veyssié, *'Grains Janus': Réalisation et premières observations des propriétés interfaciales*. *C. R. Acad. Sci. (Paris)*, 306:1423, 1988.
- [118] P. G. de Gennes, *Soft matter*. *Rev. Mod. Phys.*, 64:645, 1992.
- [119] A. Walther and A. H. E. Muller, *Janus particles*. *Soft Matter*, 4:663, 2008.
- [120] K. Zahn, R. Lenke, and G. Maret, *Two-stage melting of paramagnetic colloidal crystals in two dimensions*. *Phys. Rev. Lett.*, 82:2721, 1999.
- [121] A. R. Bausch, M. J. Bowick, A. Cacciuto, A. D. Dinsmore, M. F. Hsu, D. R. Nelson, M. G. Nikolaides, A. Travesset, and D. A. Weitz, *Grain boundary scars and spherical crystallography*. *Science*, 299:1716, 2003.
- [122] S. Reynaert, P. Moldenaers, and J. Vermant, *Control over colloidal aggregation in monolayers of latex particles at the oil-water interface*. *Langmuir*, 22:4936, 2006.
- [123] A. D. Dinsmore, M. F. Hsu, M. G. Nikolaides, M. Marquez, A. R. Bausch, and D. A. Weitz, *Colloidosomes: Selectively permeable capsules composed of colloidal particles*. *Science*, 298:1006, 2002.
- [124] S. U. Pickering, *CXCVI.-Emulsions*. *J. Chem. Soc., Trans.*, 91:2001, 1907.
- [125] R. Aveyard, B. P. Binks, and J. H. Clint, *Emulsions stabilised solely by colloidal particles*. *Adv. Colloid Interface Sci.*, 100:503, 2003.
- [126] B. P. Binks, A. K. F. Dyab, and P. D. I. Fletcher, *Contact angles in relation to emulsions stabilised solely by silica nanoparticles including systems containing room temperature ionic liquids*. *Phys. Chem. Chem. Phys.*, 9:6391, 2007.
- [127] S. Sacanna, W. K. Kegel, and A. P. Philipse, *Thermodynamically stable Pickering emulsions*. *Phys. Rev. Lett.*, 98:158301, 2007.

- [128] D. S. Home, *Protein-stabilized emulsions*. *Curr. Opin. Colloid Interface Sci.*, 1:752, 1996.
- [129] P. Pieranski, *Two-dimensional interfacial colloidal crystals*. *Phys. Rev. Lett.*, 45:569, 1980.
- [130] T. Terao and T. Nakayama, *Crystallization in quasi-two-dimensional colloidal systems at an air-water interface*. *Phys. Rev. E*, 60:7157, 1999.
- [131] R. Aveyard, J. H. Clint, D. Nees, and V. N. Paunov, *Compression and structure of monolayers of charged latex particles at air/water and octane/water interfaces*. *Langmuir*, 16:1969, 2000.
- [132] F. Reincke, S. G. Hickey, W. K. Kegel, and D. Vanmaekelbergh, *Spontaneous assembly of a monolayer of charged gold nanocrystals at the water/oil interface*. *Angew. Chem. Int. Ed.*, 43:458, 2004.
- [133] J. C. Loudet, A. M. Alsayed, J. Zhang, and A. G. Yodh, *Capillary interactions between anisotropic colloidal particles*. *Phys. Rev. Lett.*, 94:018301, 2005.
- [134] M. G. Basavaraj, G. G. Fuller, J. Fransaer, and J. Vermant, *Packing, flipping, and buckling transitions in compressed monolayers of ellipsoidal latex particles*. *Langmuir*, 22:6605, 2006.
- [135] J. C. Loudet and B. Pouligny, *Self-assembled capillary arrows*. *Europhys. Lett.*, 85:28003, 2009.
- [136] T. Nakashima and N. Kimizuka, *Water/ionic liquid interfaces as fluid scaffolds for the two-dimensional self-assembly of charged nanospheres*. *Langmuir*, 27:1281, 2011.
- [137] D. M. Kaz, R. McGorty, M. Mani, M. P. Brenner, and V. N. Manoharan, *Physical ageing of the contact line on colloidal particles at liquid interfaces*. *Nature Mater.*, AOP:1, 2012.
- [138] P. Singh, D. D. Joseph, S. K. Gurupatham, B. Dalal, and S. Nudurupati, *Spontaneous dispersion of particles on liquid surfaces*. *Proc. Natl. Acad. Sci. USA*, 106:19761, 2009.
- [139] P. Singh, D. D. Joseph, I. S. Fischer, and B. Dalal, *Role of particle inertia in adsorption at fluid-liquid interfaces*. *Phys. Rev. E*, 83:041606, 2011.
- [140] T. Young, *An essay on the cohesion of fluids*. *Phil. Trans. R. Soc. Lond.*, 95:65, 1805.
- [141] T. Ondarçuhu, P. Fabre, E. Raphaël, and M. Veyssié, *Specific properties of amphiphilic particles at fluid interfaces*. *J. Phys. France*, 51:1527, 1990.
- [142] B. P. Binks and P. D. I. Fletcher, *Particles adsorbed at the oil-water interface: A theoretical comparison between spheres of uniform wettability and "Janus" particles*. *Langmuir*, 17:4708, 2001.
- [143] L. Dong and D. T. Johnson, *Adsorption of acicular particles at liquid-fluid interfaces and the influence of the line tension*. *Langmuir*, 21:3838, 2005.
- [144] F. Bresme and J. Faraudo, *Orientational transitions of anisotropic nanoparticles at liquid-liquid interfaces*. *J. Phys.: Condens. Matter*, 19:375110, 2007.
- [145] Y. Nonomura, S. Komura, and K. Tsujii, *Adsorption of microstructured particles at liquid-liquid interfaces*. *J. Phys. Chem. B*, 110:13124, 2006.
- [146] S. Jiang and S. Granick, *Janus balance of amphiphilic colloidal particles*. *J. Chem. Phys.*, 127:161102, 2007.
- [147] J. de Graaf, M. Dijkstra, and R. van Roij, *Triangular tessellation scheme for the adsorption free energy at the liquid-liquid interface: Towards nonconvex patterned colloids*. *Phys. Rev. E*, 80:051405, 2009.

- [148] J. de Graaf, M. Dijkstra, and R. van Roij, *Adsorption trajectories and free-energy separatrixes for colloidal particles in contact with a liquid-liquid interface*. J. Chem. Phys., 132:164902, 2010.
- [149] D. Y. C. Chan, J. D. Henry, and L. R. White, *The interaction of colloidal particles collected at fluid interfaces*. J. Colloid Interface Sci., 79:410, 1981.
- [150] J. Faraudo and F. Bresme, *Stability of particles adsorbed at liquid/fluid interfaces: Shape effects induced by line tension*. J. Chem. Phys., 118:6518, 2003.
- [151] K. D. Danov, P. A. Kralchevsky, and M. P. Boneva, *Electrodipping force acting on solid particles at a fluid interface*. Langmuir, 20:6139, 2004.
- [152] M. Oettel, A. Domínguez, and S. Dietrich, *Attractions between charged colloids at water interfaces*. J. Phys.: Condens. Matter, 17:337, 2005.
- [153] M. Oettel, A. Domínguez, and S. Dietrich, *Effective capillary interaction of spherical particles at fluid interfaces*. Phys. Rev. E, 71:051401, 2005.
- [154] N. D. Vassileva, D. van den Ende, F. Mugele, and J. Mellema, *Capillary forces between spherical particles floating at a liquid-liquid interface*. Langmuir, 21:11190, 2005.
- [155] E. P. Lewandowski, P. C. Searson, and K. J. Stebe, *Orientation of a nanocylinder at a fluid interface*. J. Phys. Chem. B, 110:4283, 2006.
- [156] H. Lehle, E. Noruzifar, and M. Oettel, *Ellipsoidal particles at fluid interfaces*. Eur. Phys. J. E, 26:151, 2008.
- [157] H. Lehe and M. Oettel, *Stability and interactions of nanocolloids at fluid interfaces: effects of capillary waves and line tensions*. J. Phys.: Condens. Matter, 20:404224, 2008.
- [158] C. Huh and L. E. Scriven, *Shapes of axisymmetric fluid interface of unbound extent*. J. Colloid Interface Sci., 30:323, 1969.
- [159] A. V. Rapacchietta, A. W. Neumann, and S. N. Omenyi, *Force and free-energy analyses of small particles at fluid interfaces*. J. Colloid Interface Sci., 59:541, 1977.
- [160] A. W. Neumann, O. Economopoulos, and A. V. Boruvka, L. Rapacchietta, *Free energy analysis of heterogeneous cylindrical particles at fluid interfaces*. J. Colloid Interface Sci., 71:293, 1979.
- [161] F. Bresme and M. Oettel, *Nanoparticles at fluid interfaces*. J. Phys.: Condens. Matter, 19:413101, 2007.
- [162] J. He, Q. Zhang, S. Gupta, T. Emrick, T. P. Russell, and P. Thiyagarajan, *Drying droplets: A window into the behavior of nanorods at interfaces*. Small, 3:1214, 2007.
- [163] E. P. Lewandowski, J. A. Bernate, P. C. Searson, and K. J. Stebe, *Rotation and alignment of anisotropic particles on non planar interfaces*. Langmuir, 24:9302, 2008.
- [164] W. H. Evers and D. Vanmaekelbergh. *Unpublished research results on the behaviour of truncated nanocubes at a liquid-liquid interface*. Private Communication., 2011.
- [165] S. M. Woodley and R. Catlow, *Crystal structure prediction from first principles*. Nature Mater., 7:937, 2008.
- [166] S. Torquato and Y. Jiao, *Dense packings of polyhedra: Platonic and Archimedean solids*. Phys. Rev. E, 80:041104, 2009.
- [167] S. Torquato and Y. Jiao, *Dense packings of the Platonic and Archimedean solids*. Nature Lett., 460:876, 2009.

- [168] Y. Jiao, F. H. Stillinger, and S. Torquato, *Optimal packings of superballs*. Phys. Rev. E, 79:041309, 2009.
- [169] E. R. Chen, M. Engel, and S. C. Glotzer, *Dense crystalline dimer packings of regular tetrahedra*. Discrete Comput. Geom., 44:253, 2010.
- [170] R. D. Batten, F. H. Stillinger, and S. Torquato, *Phase behavior of colloidal superballs: Shape interpolation from spheres to cubes*. Phys. Rev. E, 81:061105, 2010.
- [171] R. Ni, A. P. Gantapara, J. de Graaf, R. van Roij, and M. Dijkstra, *Phase diagram of colloidal hard superballs: from cubes via spheres to octahedra*. ArXiv, 1111.4357v2:1, 2012.
- [172] U. Agarwal and F. A. Escobedo, *Mesophase behaviour of polyhedral particles*. Nature Mater., 10:230, 2011.
- [173] A. Haji-Akbari, M. Engel, and S. C. Glotzer, *Phase diagram of hard tetrahedra*. J. Chem. Phys., 135:194101, 2011.
- [174] P. F. Damasceno, M. Engel, and S. C. Glotzer, *Structural diversity and the role of particle shape and dense fluid behaviour in assemblies of hard polyhedra*. ArXiv, 1202.2177v1:1, 2012.
- [175] Y. Jiao, F. H. Stillinger, and S. Torquato, *Optimal packings of superdisks and the role of symmetry*. Phys. Rev. Lett., 100:245504, 2008.
- [176] M. Marechal, R. J. Kortschot, A. F. Demirörs, A. Imhof, and M. Dijkstra, *Phase behavior and structure of a new colloidal model system of bowl-shaped particles*. Nano Lett., 10:1907, 2010.
- [177] J. Pannetier, J. Bassas-Alsina, J. Rodriguez-Carvajal, and V. Caignaert, *Prediction of crystal structures from crystal chemistry rules by simulated annealing*. Nature, 346:343, 1990.
- [178] H. R. Karfunkel and R. J. Gdanitz, *Ab initio prediction of possible crystal structures for general organic molecules*. J. Comput. Chem., 13:1171, 1992.
- [179] D. Gottwald, G. Kahl, and C. N. Likos, *Predicting equilibrium structures in freezing processes*. J. Chem. Phys., 122:204503, 2005.
- [180] A. R. Oganov and C. W. Glass, *Crystal structure prediction using ab initio evolutionary techniques: Principles and applications*. J. Chem. Phys., 124:244704, 2006.
- [181] D. J. Wales and H. A. Scheraga, *Global optimization of clusters, crystals, and biomolecules*. Science, 285:1368, 1999.
- [182] J. C. Schon, Z. P. CanCarevic, A. Hannemann, and M. Jansen, *Free enthalpy landscape of SrO*. J. Chem. Phys., 128:194712, 2008.
- [183] R. Martoňák, A. Laio, and M. Parrinello, *Predicting crystal structures: The Parrinello-Rahman method revisited*. Phys. Rev. Lett., 90:075503, 2003.
- [184] T. C. Hales and S. P. Ferguson, *The Kepler conjecture*. Discrete Comput. Geom., 36:1, 2006.
- [185] G. Szpiro, *Mathematics: Does the proof stack up?* Nature, 48:12, 2003.
- [186] T. C. Hales, *Formal proof*. North Am. Math. Soc., 55:1370, 2008.
- [187] M. Gardner. *The Colossal Book of Mathematics: Classic Puzzles, Paradoxes, and Problems*. W. W. Norton & Company (New York), New York, 1st edition, 2001.

- [188] A. Khan, K. Fontell, and B. Lindman, *Liquid crystallinity in systems of magnesium and calcium surfactants: Phase diagrams and phase structures in binary aqueous systems of magnesium and calcium di-2-ethylhexylsulfosuccinate*. J. Colloid Interface Sci., 101:193, 1984.
- [189] C. Kang and A. Khan, *Self-assembly in systems of didodecyldimethylammonium surfactants: Binary and ternary phase equilibria and phase structures with sulphate, hydroxide, acetate, and chloride counterions*. J. Colloid Interface Sci., 156:218, 1993.
- [190] L. Hong, A. Cacciuto, E. Luijten, and S. Granick, *Clusters of charged Janus spheres*. Nano Lett., 6:2510, 2006.
- [191] M. E. Leunissen, A. van Blaaderen, A. D. Hollingsworth, M. T. Sullivan, and P. M. Chaikin, *Electrostatics at the oil-water interface, stability, and order in emulsions and colloids*. Proc. Natl. Acad. Sci. USA, 104:2585, 2007.
- [192] B. V. Derjaguin and L. Landau, *Theory of the stability of strongly charged lyophobic sols and of the adhesion of strongly charged particles in solutions of electrolytes*. Acta Phys. Chim. URSS, 14:633, 1941.
- [193] E. J. Verwey and J. T. G. Overbeek. *Theory of the Stability of Lyophobic Colloids*. Elsevier (Amsterdam), 1st edition, 1948.
- [194] D. L. Chapman, *A contribution to the theory of electrocapillarity*. Phys. Rev., 25:475, 1913.
- [195] S. Alexander, P. M. Chaikin, P. Grant, G. J. Morales, P. Pincus, and D. Hone, *Charge renormalization, osmotic pressure, and bulk modulus of colloidal crystals: Theory*. J. Chem. Phys., 80:5776, 1984.
- [196] I. Rouzina and V. A. Bloomfield, *Macroion attraction due to electrostatic correlation between screening counterions. 1. Mobile surface-adsorbed ions and diffuse ion cloud*. J. Phys. Chem., 100:9977, 1996.
- [197] A. G. Moreira and R. R. Netz, *Binding of similarly charged plates with counterions only*. Phys. Rev. Lett., 87:078301, 2001.
- [198] A. Y. Grosberg, T. T. Nguyen, and B. I. Shklovskii, *Colloquium: The physics of charge inversion in chemical and biological systems*. Rev. Mod. Phys., 74:329, 2002.
- [199] P. Linse, G. Gunnarsson, and B. Jönsson, *Electrostatic interactions in micellar solutions. A comparison between Monte Carlo simulations and solutions of the Poisson-Boltzmann equation*. J. Phys. Chem., 86:413, 1982.
- [200] L. Guldbbrand, B. Jonsson, H. Wennerstrom, and P. Linse, *Electrical double layer forces. A Monte Carlo study*. J. Chem. Phys., 80:2221, 1984.
- [201] L. Degève, M. Lozada-Cassou, E. Sánchez, and E. González-Tovar, *Monte Carlo simulation for a symmetrical electrolyte next to a charged spherical colloid particle*. J. Chem. Phys., 98:8905, 1993.
- [202] G. Orkoulas and A. Z. Panagiotopoulos, *Free energy and phase equilibria for the restricted primitive model of ionic fluids from Monte Carlo simulations*. J. Chem. Phys., 101:1452, 1994.
- [203] C. Valeriani, P. J. Camp, J. W. Zwanikken, R. van Roij, and M. Dijkstra, *Computer simulations of the restricted primitive model at very low temperature and density*. J. Phys.: Condens. Matter, 22:104122, 2010.

- [204] C. Valeriani, P. J. Camp, J. W. Zwanikken, R. van Roij, and M. Dijkstra, *Ion association in low-polarity solvents: comparisons between theory, simulation, and experiment*. *Soft Matter*, 6:2793, 2010.
- [205] F. Cardinaux, A. Stradner, P. Schurtenberger, F. Sciortino, and E. Zaccarelli, *Modeling equilibrium clusters in lysozyme solutions*. *Europhys. Lett.*, 77:48004, 2007.
- [206] E. Sanz, E. Valeriani, T. Vissers, A. Fortini, M. E. Leunissen, A. van Blaaderen, D. Frenkel, and M. Dijkstra, *Out-of-equilibrium processes in suspensions of oppositely charged colloids: liquid-to-crystal nucleation and gel formation*. *J. Phys.: Condens. Matter*, 20:494247, 2008.
- [207] J. C. F. Toledano, F. Sciortino, and E. Zaccarelli, *Colloidal systems with competing interactions: from an arrested repulsive cluster phase to a gel*. *Soft Matter*, 5:2390, 2009.
- [208] J. Colombo and M. Dijkstra, *Effect of quenched size polydispersity on the fluid-solid transition in charged colloidal suspensions*. *J. Chem. Phys.*, 134:154504, 2011.
- [209] E. Eggen and R. van Roij, *Poisson-Boltzmann cell model for heterogeneously charged colloids*. *Phys. Rev. E*, 80:041402, 2009.
- [210] E. J. Eggen. *Orientalional Ordering of Charged Colloids*. PhD thesis, Utrecht University, 2010. ISBN 978-90-393-5301-1.
- [211] N. Boon, E. Carvajal Gallardo, S. Zheng, E. Eggen, M. Dijkstra, and R. van Roij, *Screening of heterogeneous surfaces: charge renormalization of Janus particles*. *J. Phys.: Condens. Matter*, 22:104104, 2010.
- [212] N. J. H. Boon. *Electrostatics in Ionic Solutions - Work and Energy, Charge Regulation, and Inhomogeneous Surfaces*. PhD thesis, Utrecht University, 2012. ISBN 978-90-393-5724-8.
- [213] H. Boroudjerdi, Y.-W. Kim, A. Naji, R. R. Netz, X. Schlagberger, and A. Serr, *Statics and dynamics of strongly charged soft matter*. *Phys. Rep.*, 416:129, 2005.
- [214] O. Punkkinen, A. Naji, R. Podgornik, I. Vattulainen, and P.-L. Hansen, *Ionic cloud distribution close to a charged surface in the presence of salt*. *Europhys. Lett.*, 82:48001, 2008.
- [215] C. Zeng, H. Bissig, and A. D. Dinsmore, *Particles on droplets: From fundamental physics to novel materials*. *Solid State Commun.*, 139:547, 2006.
- [216] J. Loudet and B. Pouligny, *How do mosquito eggs self-assemble on the water surface?* *Eur. Phys. J. E*, 34:76, 2011.
- [217] E. P. Lewandowski, J. A. Bernate, A. Tseng, P. C. Searson, and K. J. Stebe, *Oriented assembly of anisotropic particles by capillary interactions*. *Soft Matter*, 5:886, 2009.
- [218] GAMMA Research Group at the University of North Carolina. *RAPID - Robust and Accurate Polygon Interference Detection*. <http://gamma.cs.unc.edu/OBB/>, 1997.
- [219] G. van den Bergen. *FreeSolid*. <http://www.win.tue.nl/~gino/solid/>, 2004.
- [220] GAMMA Research Group at the University of North Carolina. *Collision detection algorithms*. <http://gamma.cs.unc.edu/software/#collision>, 2012.
- [221] K. Brakke, *The Surface Evolver*. *Exp. Math.*, 1:141, 1992.
- [222] R. Phelan, D. Weaire, and K. Brakke, *Computation of equilibrium foam structures using the Surface Evolver*. *Exp. Math.*, 4:181, 1995.
- [223] K. A. Brakke, *The Surface Evolver and the stability of liquid surfaces*. *Phyl. Trans. R. Soc. A*, 354:2143, 1996.

- [224] P. Bolhuis and D. Frenkel, *Tracing the phase boundaries of hard spherocylinders*. J. Chem. Phys., 106:666, 1997.
- [225] A. Cuetos and B. Martinez-Haya, *Columnar phases of discotic spherocylinders*. J. Chem. Phys., 129:214706, 2008.
- [226] R. Ni, S. Belli, R. van Roij, and M. Dijkstra, *Glassy dynamics, spinodal fluctuations, and the kinetic limit of nucleation in suspensions of colloidal hard rods*. Phys. Rev. Lett., 105:088302, 2010.
- [227] M. Marechal, A. Cuetos, B. Martinez-Haya, and M. Dijkstra, *Phase behavior of hard colloidal platelets using free energy calculations*. J. Chem. Phys., 134:094501, 2011.
- [228] J. S. Rowlinson and B. Widom. *Handbook of Surface and Colloid Chemistry*. Dover Publications (Mineola), 1st edition, 2003.
- [229] A. Amirfazli and A. W. Neumann, *Status of the three-phase line tension: a review*. Adv. Colloid Interface Sci., 110:121, 2004.
- [230] O. J. Cayre and V. N. Paunov, *Contact angles of colloid silica and gold particles at air-water and oil-water interfaces determined with the gel trapping technique*. Langmuir, 20:9594, 2004.
- [231] M. Minsky, *Memoir on inventing the confocal scanning microscope*. Scanning, 10:128, 1988.
- [232] A. Mohraz and M. J. Solomon, *Direct visualization of colloidal rod assembly by confocal microscopy*. Langmuir, 21:5298, 2005.
- [233] D. Mukhija and M. J. Solomon, *Nematic order in suspensions of colloidal rods by application of a centrifugal field*. Soft Matter, 7:540, 2011.
- [234] P. Langevin, *Sur la theorie du mouvement Brownian*. C. R. Acad. Sci. (Paris), 146:530, 1908.
- [235] J. K. G. Dhont. *An Introduction to Dynamics of Colloids*. Elsevier Science B.V. (Amsterdam), 2nd edition, 1996.
- [236] J.-B. Fournier and P. Galatola, *Anisotropic capillary interactions and jamming of colloidal particles trapped at a liquid-fluid interface*. Phys. Rev. E, 65:031601, 2002.
- [237] E. A. van Nierop, M. A. Stijnman, and S. Hilgenfeldt, *Shape-induced capillary interactions of colloidal particles*. Europhys. Lett., 72:671, 2005.
- [238] E. Noruzifar and M. Oettel, *Anisotropies in thermal Casimir interactions: Ellipsoidal colloids trapped at a fluid interface*. Phys. Rev. E, 79:051401, 2009.
- [239] K. D. Danov and P. A. Kralchevsky, *Capillary forces between particles at a liquid interface: General theoretical approach and interactions between capillary multipoles*. Adv. Colloid Interface Sci., 154:91, 2010.
- [240] F. Güther, F. Janoschek, S. Frijters, and J. Harting, *Lattice Boltzmann simulations of anisotropic particles at liquid interfaces*. ArXiv, 1109.3277v1:1, 2011.
- [241] R. Wang, N. Sakai, A. Fujishima, T. Watanabe, and K. Hashimoto, *Studies of surface wettability conversion on TiO<sub>2</sub> single-crystal surfaces*. J. Phys. Chem. B, 103:2188, 1999.
- [242] J. W. J. de Folter, A. P. Philipse, and W. K. Kegel. *Unpublished research results on the self-assembly of cubes at the oil-water interface*. Private Communication., 2012.

- [243] M. P. Aronson, A. C. Zettlemoyer, and M. C. Wilkinson, *On the properties of certain oil-water-solid-vapor configurations. i comments on the stability of a four-phase contact line*. J. Chem. Phys., 77:318, 1973.
- [244] B. Harke, C. K. Ullal, J. Keller, and S. W. Hell, *Three-dimensional nanoscopy of colloidal crystals*. Nano Lett., 8:1309, 2008.
- [245] S. W. Hell, R. Schmidt, and A. Egner, *Diffraction-unlimited three-dimensional optical nanoscopy with opposing lenses*. Nature Photon., 3:381, 2009.
- [246] M. Abramowitz and I. A. Stegun. *Handbook of Mathematical Functions with Formulas, Graphs, and Mathematical Tables*. Dover Publications (Mineola), 1st edition, 1972.
- [247] E. Matijevic, *Monodispersed metal (hydrous) oxides - a fascinating field of colloid science*. Acc. Chem. Res., 14:22, 1981.
- [248] A. Mews, A. V. Kadavanich, U. Banin, and A. P. Alivisatos, *Structural and spectroscopic investigations of cds/hgs/cds quantum-dot quantum wells*. Phys. Rev. B, 53:R13242, 1996.
- [249] J. de Graaf, R. van Roij, and M. Dijkstra, *Dense regular packings of irregular nonconvex particles*. Phys. Rev. Lett., 107:155501, 2011.
- [250] G. Kuperberg and W. Kuperberg, *Double-lattice packings of convex bodies in the plane*. Discete Comput. Geom., 5:389, 1990.
- [251] Y. Limon Duparcmeur, A. Gervois, and J. P. Troadec, *Dense periodic packings of regular polygons*. J. Phys. I France, 5:1539, 1995.
- [252] U. Betke and M. Henk, *Densest lattice packings of 3-polytopes*. Comput. Geom., 16:157, 2000.
- [253] D. Frenkel and B. Smit. *Understanding Molecular Simulation: From Algorithms to Applications*. Academic Press (London), 2nd edition, 2002.
- [254] N. Metropolis and S. Ulam, *The Monte Carlo method*. J. Amer. Stat. Assoc., 44:335, 1949.
- [255] F. J. Vesely, *Angular Monte Carlo integration using quaternion parameters: a spherical reference potential for CCl<sub>4</sub>*. J. Comput. Phys., 47:291, 1982.
- [256] W. Liu, B. Schmidt, G. Voss, and W. Müller-Wittig, *Accelerating molecular dynamics simulations using graphics processing units with CUDA*. Comput. Phys. Commun., 179:634, 2008.
- [257] T. Preis, P. Virnau, W. Paul, and J. J. Schneider, *GPU accelerated Monte Carlo simulation of the 2D and 3D Ising model*. J. Comput. Phys., 228:4468, 2009.
- [258] P. Lu, H. Oki, C. Frey, G. Chamitoff, L. Chiao, E. Fincke, C. Foale, S. Magnus, W. McArthur, D. Tani, P. Whitson, J. Williams, W. Meyer, R. Sicker, B. Au, M. Christiansen, A. Schofield, and D. Weitz, *Orders-of-magnitude performance increases in GPU-accelerated correlation of images from the International Space Station*. J. Real-Time Image Proc., 5:179, 2010.
- [259] A. Haji-Akbari, M. Engel, A. S. Keys, X. Zheng, R. G. Petschek, P. Palfy-Muhoray, and S. C. Glotzer, *Disordered, quasicrystalline and crystalline phases of densely packed tetrahedra*. Nature Lett., 462:773, 2009.
- [260] P. F. Damasceno, M. Engel, and S. C. Glotzer, *Crystalline assemblies and densest packings of a family of truncated tetrahedra and the role of directional entropic forces*. ACS Nano, 6:609, 2012.

- [261] A. Ostaszewski. *Advanced Mathematical Methods*. Cambridge University Press (Cambridge), 1st edition, 1991.
- [262] D. Eberly. *Intersection of convex objects: The method of separating axes*. <http://www.geometrictools.com/>, 2008.
- [263] B. S. John and F. A. Escobedo, *Phase behavior of colloidal hard tetragonal parallelepipeds (cuboids): A Monte Carlo simulation study*. J. Phys. Chem. B, 109:23008, 2005.
- [264] T. D. Nguyen, E. Jankowski, and S. C. Glotzer, *Self-assembly and reconfigurability of shape-shifting particles*. ACS Nano, 5:8892, 2011.
- [265] C. Avendano and F. A. Escobedo, *Phase behavior of rounded hard-squares*. Soft Matter, 8:4675, 2012.
- [266] W. Qi and M. Dijkstra. *Unpublished research results on the spherocylindrical octapod simulation model*. Private Communication., 2011.
- [267] C. De Michele, *Simulating hard rigid bodies*. ArXiv, 0903.1608v2:1, 2009.
- [268] S. Gottschalk, M. C. Lin, and D. Manocha. *OBBTree: a hierarchical structure for rapid interference detection*. In *Proceedings of the 23rd annual conference on Computer graphics and interactive techniques, SIGGRAPH '96*, page 171. Association for Computing Machinery (New York), 1996.
- [269] P. Ewald, *Die berechnung optischer und elektrostatischer gitterpotentiale*. Ann. Phys., 369:253, 1921.
- [270] H. T. Stokes, D. M. Hatch, and B. J. Campbell. *FindSym software package*. <http://stokes.byu.edu/isotropy.html>, 2007.
- [271] T. Hahn. *International Tables for Crystallography: Volume A, Space-Group Symmetry*. Springer (Berlin/Heidelberg), 5th edition, 2002.
- [272] C. for Computational Materials Science. *Database of molecular prototypes corresponding to the 230 existing space groups*. <http://cst-www.nrl.navy.mil/lattice/index.html>, 2008.
- [273] S. Gravel and V. Elser, *Divide and concur: A general approach to constraint satisfaction*. Phys. Rev. E, 78:036706, 2008.
- [274] Y. Kallus, V. Elser, and S. Gravel, *Dense periodic packings of tetrahedra with small repeating units*. Discrete Comput. Geom., 44:245, 2010.
- [275] J. D. Bernal and J. Mason, *Packing of spheres: Co-ordination of randomly packed spheres*. Nature, 188:910, 1960.
- [276] A. Donev, I. Cisse, D. Sachs, E. A. Variano, F. H. Stillinger, R. Connelly, S. Torquato, and P. M. Chaikin, *Improving the density of jammed disordered packings using ellipsoids*. Science, 303:990, 2004.
- [277] D. V. Talapin, E. V. Shevchenko, M. I. Bodnarchuk, X. Ye, J. Chen, and C. B. Murray, *Quasicrystalline order in self-assembled binary nanoparticle superlattices*. Nature, 461:964, 2009.
- [278] S. Torquato and Y. Jiao, *Exact constructions of a family of dense periodic packings of tetrahedra*. Phys. Rev. E, 81:041310, 2010.
- [279] J. de Graaf, R. van Roij, and M. Dijkstra. *Database containing the floppy-box Monte Carlo results for 159 particle models*. <http://web.science.uu.nl/SCM/>, 2012.

- [280] Stanford University Computer Graphics Laboratory. *Stanford bunny PLY-model*. <http://graphics.stanford.edu/data/3Dscanrep/>, 1993.
- [281] J. Burkardt. *Hammerhead shark PLY-model*. <http://people.sc.fsu.edu/~jburkardt/data/ply/ply.html>, 1993.
- [282] Wolfram Research, Inc. *Mathematica 7*. Software Package, 2009.
- [283] Y. Jiao and S. Torquato, *A packing of truncated tetrahedra that nearly fills all of space and its melting properties*. J. Chem. Phys., 135:151101, 2011.
- [284] N. Tsapis, E. R. Dufresne, S. S. Sinha, C. S. Riera, J. W. Hutchinson, L. Mahadevan, and D. A. Weitz, *Onset of buckling in drying droplets of colloidal suspensions*. Phys. Rev. Lett., 94:018302, 2005.
- [285] G. F. Tóth, *Densest packings of typical convex sets are not lattice-like*. Discrete Comput. Geom., 14:1, 1995.
- [286] S. Torquato and Y. Jiao, *Erratum: Dense packings of polyhedra: Platonic and Archimedean solids*. Phys. Rev. E, 81:049908(E), 2010.
- [287] J. Henzie, M. Grünwald, A. Widmer-Cooper, P. L. Geissler, and P. Yang, *Self-assembly of uniform polyhedral silver nanocrystals into densest packings and exotic superlattices*. Nature Mater., 11:131, 2012.
- [288] X. Xia, J. Zeng, L. K. Oetjen, Q. Li, and Y. Xia, *Quantitative analysis of the role played by poly(vinylpyrrolidone) in seed-mediated growth of Ag nanocrystals*. J. Am. Chem. Soc., 134:1793, 2012.
- [289] H. Minkowski, *Dichteste gitterförmige lagerung kongruenter körper*. Nachr. K. Ges. Wiss. Göttingen, 11:311, 1904.
- [290] A. P. Gantapara, J. de Graaf, R. van Roij, and M. Dijkstra. *Unpublished research results on the phase diagram of a family of truncated cubes*. Private Communication., 2012.
- [291] F. Smalenburg, L. Filion, M. Marechal, and M. Dijkstra, *Vacancy-stabilized crystalline order in hard cubes*. ArXiv, 1111.3466v2:1, 2012.
- [292] M. Marechal, U. Zimmermann, and H. Löwen, *Freezing of parallel hard cubes with rounded edges*. J. Chem. Phys., 136:144506, 2012.
- [293] E. G. Noya, C. Vega, J. P. K. Doye, and A. A. Louis, *Phase diagram of model anisotropic particles with octahedral symmetry*. J. Chem. Phys., 127:054501, 2007.
- [294] M. Moakher, *Means and averaging in the group of rotations*. SIAM J. Matrix Anal. A, 24:1, 2002.
- [295] I. Sharf, A. Wolf, and M. B. Rubin, *Arithmetic and geometric solutions for average rigid-body rotation*. Mech. Mach. Theory, 45:1239, 2010.
- [296] A. Striolo, J. Ward, J. M. Prausnitz, W. J. Parak, D. Zanchet, D. Gerion, D. Milliron, and A. P. Alivisatos, *Molecular weight, osmotic second virial coefficient, and extinction coefficient of colloidal CdSe nanocrystals*. J. Phys. Chem. B, 106:5500, 2002.
- [297] L. Bergström, *Hamaker constants of inorganic materials*. Adv. Colloid Interface Sci., 70:125, 1997.
- [298] G. Cao. *Nanostructures & Nanomaterials: Synthesis, Properties & Applications*. Imperial College Press (London), 1st edition, 2004.

- [299] H.-J. Butt, K. Graf, and M. Kappl. *Physics and Chemistry of Interfaces*. Wiley-VCH (Weinheim), 2nd edition, 2003.
- [300] M. Takenaga, S. Jo, M. Graupe, and T. R. Lee, *Effective van der Waals surface energy of self-assembled monolayer films having systematically varying degrees of molecular fluorination*. J. Colloid Interface Sci., 320:264, 2008.
- [301] M. Anand, S.-S. You, K. M. Hurst, S. R. Saunders, C. L. Kitchens, W. R. Ashurst, and C. B. Roberts, *Thermodynamic analysis of nanoparticle size selective fractionation using gas-expanded liquids*. Ind. Eng. Chem. Res., 47:553, 2008.
- [302] J. T. Woodward, A. Ulman, and D. K. Schwartz, *Self-assembled monolayer growth of octadecylphosphonic acid on mica*. Langmuir, 12:3626, 1996.
- [303] P. Linse, *Highly asymmetric electrolyte: Comparison between one- and two-component models at different levels of approximations*. J. Chem. Phys., 94:3817, 1991.
- [304] E. Trizac, L. Bocquet, and M. Aubouy, *Simple approach for charge renormalization in highly charged macroions*. Phys. Rev. Lett., 89:248301, 2002.
- [305] G. Téllez and E. Trizac, *Density functional theory study of electric potential saturation: Planar geometry*. Phys. Rev. E, 70:011404, 2003.
- [306] Y.-X. Yu, J. Wu, and G.-H. Gao, *Density-functional theory of spherical electric double layers and  $z$  potentials of colloidal particles in restricted-primitive-model electrolyte solutions*. J. Chem. Phys., 120:7223, 2004.
- [307] S. Pianegonda, M. C. Barbosa, and Y. Levin, *Charge reversal of colloidal particles*. Europhys. Lett., 71:831, 2005.
- [308] D. Ben-Yaakov, D. Andelman, D. Harries, and R. Podgornik, *Beyond standard Poisson-Boltzmann theory: ion-specific interactions in aqueous solutions*. J. Phys.: Condens. Matter, 21:424106, 2009.
- [309] M. M. Hatlo and L. Lue, *A field theory for ions near charged surfaces valid from weak to strong couplings*. Soft Matter, 5:125, 2009.
- [310] M. M. Hatlo and L. Lue, *Electrostatic interactions of charged bodies from the weak - to the strong-coupling regime*. Europhys. Lett., 89:25002, 2010.
- [311] A. P. dos Santos, A. Diehl, and Y. Levin, *Colloidal charge renormalization in suspensions containing multivalent electrolyte*. J. Chem. Phys., 132:104105, 2010.
- [312] R. H. Hardin, N. J. A. Sloane, and W. D. Smith. *Maximized minimum distance dataset for 100 points distributed over a 3D sphere*. <http://www2.research.att.com/~njas/packings/>, 2011.
- [313] E. Wigner and F. Seitz, *On the constitution of metallic sodium*. Phys. Rev., 43:804, 1933.
- [314] R. A. Marcus, *Calculation of thermodynamic properties of electrolytes*. J. Chem. Phys., 23:1057, 1955.
- [315] T. Ohtsuki, S. Mitaku, and K. Okano, *Studies of ordered monodisperse latexes. ii. Theory of mechanical properties*. Jpn. J. Appl. Phys., 17:627, 1978.
- [316] E. A. Hylleraas, *Linearization of products of jacobi polynomials*. Math. Scand., 10:189, 1962.
- [317] L. Belloni, *Ionic condensation and charge renormalization in colloidal suspensions*. Colloids Surfaces A: Physicochem. Eng. Aspects, 140:227, 1998.

- [318] L. Bocquet, E. Trizac, and M. Aubouy, *Effective charge saturation in colloidal suspensions*. J. Chem. Phys., 117:8138, 2002.
- [319] A. R. Denton, *Charge renormalization, effective interactions, and thermodynamics of deionized colloidal suspensions*. J. Phys.: Condens. Matter, 20:494230, 2008.
- [320] M. Kanduč, A. Naji, J. Forsman, and R. Podgornik, *Dressed counterions: Strong electrostatic coupling in the presence of salt*. J. Chem. Phys., 132:124701, 2010.
- [321] E. A. Alshina, N. N. Kalitkin, I. A. Panin, and I. P. Poshivailo, *Numerical integration of functions with singularities*. Dokl. Math., 74:2, 2006.
- [322] G. Vernizzi, R. Sknepnek, and M. Olvera de la Cruz, *Uniform partitions of 3-space, their relatives and embedding*. Europ. J. Combinatorics, 21:807, 2000.
- [323] I. R. Fisher, K. O. Cheon, A. F. Panchula, P. C. Canfield, M. Chernikov, H. R. Ott, and K. Dennis, *Magnetic and transport properties of single-grain R-Mg-Zn icosahedral quasicrystals [R=Y, (Y<sub>1-x</sub>Gd<sub>x</sub>), (Y<sub>1-x</sub>Tb<sub>x</sub>), Tb, Dy, Ho, and Er]*. Phys. Rev. B, 59:308, 1999.
- [324] J. Nozawa, K. Tsukamoto, W. van Enkevort, T. Nakamura, Y. Kimura, H. Miura, H. Satoh, K. Nagashima, and M. Konoto, *Magnetite 3D colloidal crystals formed in the early solar system 4.6 billion years ago*. J. Am. Chem. Soc., 133:8782, 2011.
- [325] Y. Saito, K. Mihama, and R. Uyeda, *Crystal structure and habit of fine metal particles formed by gas-evaporation technique; bcc metals (V, Fe, Cr, Mo and W)*. J. Cryst. Growth, 45:501, 1978.
- [326] Y. Saito, K. Mihama, and R. Uyeda, *Formation of ultrafine metal particles by gas-evaporation. VI. Bcc metals, Fe, V, Nb, Ta, Cr, Mo and W*. Jpn. J. Appl. Phys., 19:1603, 1980.
- [327] Wolfram Research, Inc. *Mathematica 1*. Software Package, 1988.

# Summary

In this thesis we considered so-called colloids, particles that are typically smaller than a thousandth of a millimetre in size. Colloids dispersed in a medium experience Brownian motion, i.e., random displacement and rotation, due to the constant bombardment by the much smaller solvent molecules. The random motion causes the particles to diffuse through the system and in principle fully sample phase space. This exploration of phase space gives rise to a strong relation between the way in which colloids organize into structures and the way in which molecular systems form phases, e.g., a gas, a liquid, and a solid. The formation of colloidal structures is referred to as self-assembly, when it is effected by Brownian motion and particle-particle interactions only.

An important advantage of colloidal matter over atomic and simple molecular systems is the far greater level of structural complexity that can be achieved. This, coupled with the fact that colloid properties are more easily modified in situ - making colloids ideally suited for industrial applications - is one of the main reasons to study these particles. Moreover, the time and length scales on which colloid dynamics occurs, are experimentally accessible by conventional optical techniques. This offers a tremendous opportunity to learn by analogy about processes, such as melting, nucleation, and defect formation, in molecular systems, where it is often not possible to perform a real-time, real-space analysis. The study of colloids is therefore also of fundamental importance.

Of particular interest is the way in which colloid behaviour is influenced by anisotropy. Even for seemingly simple systems consisting only of hard spheres there is a fascinating richness in the phases that can form. By considering spheres with isotropic soft (short- and long-range) interaction potentials, even more complex structures are made possible. This complexity is expected to increase further when anisotropic interactions are used. Recent advances in particle synthesis have yielded a huge variety of new colloid and nanoparticle building blocks: dumbbells, ellipsoids, cubes, tetrahedra, superballs, tetrapods, octapods, Janus particles, and many more. With these building blocks at our disposal many avenues for the creation of new phases with unprecedented properties can now be explored.

It proves beneficial to perform computer simulations and theoretical calculations to complement the experimental investigation into the phase behaviour of colloidal particles. Computer simulations are essentially ‘computer experiments’ that are carried out using a simplified model of the system of interest, for which there is absolute control over the parameters that govern the system. This control allows the complex phenomenology observed in experiments to be more easily unravelled. A theoretical calculation typically employs a higher level of abstraction and a more mathematical approach to the description of the system. The sampling of phase space in theory can be considered implicit and the sampling in a simulation explicit. In this thesis we took the simulation and theory route to study the influence of anisotropy on the behaviour of colloids. We discussed three topics for which shape and/or interaction anisotropy plays an important role and for which the recent development of the aforementioned particles has had a strong impact.

- *The adsorption of single particles at a liquid-liquid interface.* The behaviour of small particles adsorbed at a liquid-liquid interface is not only of importance to

our understanding of phase transitions and critical phenomena in two-dimensional (2D) systems, but also has great potential for use in industry. Possible applications include the encapsulation of drugs in emulsion droplets for medical purposes and the stabilization of foams and emulsions, which are relevant to the food industry.

- *Crystal-structure prediction for colloidal systems and the related phase behaviour.* Although there has been a tremendous increase in the ability to control the ways in which colloids and nanoparticles self-assemble, there are still many unanswered questions with regards to determining the specific particle properties that result in a desired structure. In particular, predicting crystal structures based only on knowledge of the interactions between particles has proven very challenging. However, an efficient ab initio way to predict crystal structures holds the key to designing new materials with predetermined properties and is therefore highly sought after.
- *The ion distribution around charged particles suspended in a dielectric medium.* In many colloidal suspensions electrostatic interactions play an important role and it is therefore important to characterise the nature of such interactions using theory and simulations. However, even for systems containing only homogeneously charged spherical colloids studying the physical properties by theory or by simulations is difficult due to the long range of the Coulomb interactions. These long-range interactions coupled with the presence of mobile ions that screen the colloid's bare charge present a complex many-body problem, which cannot be easily unravelled to yield effective colloid-colloid interactions. For anisotropic charge distributions the complexity of the problem increases significantly.

In Chapter 2 we described the numerical technique of triangular tessellation, by which the surface areas and line length that are associated with a plane-particle intersection can be approximated. Our method allowed us to determine the free-energy of adsorption for a single shape-anisotropic colloid with homogeneous surface properties adsorbed at a flat interface in the Pieranski approximation. We established that prolate ellipsoids and spherocylinders adsorb perpendicular to the interfacial normal. For prolate cylinders there can also be a metastable adsorption parallel to this normal. We continued our investigation in Chapter 3 where we considered the free energy in more detail and introduced simple dynamics to analyse the process of a particle attaching to the interface and relaxing to its equilibrium position and orientation. When there are metastable adsorption configurations, we showed that the orientation of a colloid at its initial contact with the interface has a strong influence on its final orientation. Within the confines of our model this resulted in an unexpectedly large domain of stability for the metastable configuration of relatively long cylindrical particles. We even encountered situations for which a particle (short cylinder) passed through the interface unhindered, despite there being deep minima in the free energy of adsorption that would ordinarily give rise to strong binding to the interface. Finally, in Chapter 4 we extended the triangular-tessellation technique to numerically determine the free energy of adsorption for a nonconvex colloidal particle with surface patterning. We showed that the equilibrium orientation of a truncated cube falls into one of three distinct categories we found; which of the three depends on the details of the contact-angle pattern. We also considered plane-particle

cross sections for octapod-shaped nanoparticles to illustrate the use of our technique on nonconvex shapes. Our results are a first step towards understanding the time-dependent behaviour of anisotropic colloids and nanoparticles in contact with a liquid-liquid or even liquid-gas interface.

In Chapter 5 we described the floppy-box Monte Carlo (FBMC) method by which it is possible to predict crystal-structure candidates. We also discussed two types of particle-overlap algorithm, the method of separating axes and a triangular-tessellation based technique. These overlap routines can be combined with the FBMC method to enable crystal-structure prediction for systems comprised of highly shape-anisotropic hard particles. In Chapter 6 we employed the FBMC technique to obtain regular packings of odd-shaped bodies. We examined the densest-known (regular) structures for 17 irregular nonconvex shapes and we confirmed several mathematical conjectures for the packings of a large set of 142 convex polyhedra. We also extended upon these conjectures and we *proved* that we have obtained the densest configurations of rhombicuboctahedra and rhombic enneacontrahedra, respectively. Moreover, we improved the value of the densest-known packing of enneagons and truncated tetrahedra. Finally, we considered a family of truncated cubes, which interpolates between a cube and an octahedron, for which we obtained a fascinating richness in crystal structures. For one family member, the octahedron, we determined the equation of state and examined the properties of the different phases. We found three phases: a liquid, a body-centred-cubic rotator phase, and a crystal phase. Our simulations demonstrated that there is a first-order phase transition between the liquid and crystal phase. The rotator phase was shown to be metastable with respect to this transition.

In Chapter 7 we analysed the recently observed hierarchical self-assembly of octapod-shaped nanocrystals (octapods) into three-dimensional (3D) superstructures. We devised a simulation model with simple empirical interaction potentials capable of reproducing the initial chain-formation step of the self-assembly. The van-der-Waals (vdW) interactions between octapods dispersed in an (a)polar liquid were obtained by means of a Hamaker-de-Boer-type integration and the nature of these interactions allowed us to justify elements of our empirical model. We used the theoretical vdW calculation, together with the experimental and simulation results, to formulate a mechanism that explains the observed self-assembly in terms of the solvent-dependence and directionality of the octapod-octapod interactions.

Finally, in Chapter 8 we studied the ionic screening of charged spherical Janus particles by primitive-model (explicit-ion) Monte Carlo (MC) simulations for a wide variety of parameters. We introduced a method to compare these results to the predictions of nonlinear Poisson-Boltzmann (PB) theory, which were derived using a Legendre-Fourier mode-expansion of the charge distribution. Our method of comparison and the large set of parameters studied allowed us to probe the range of validity of the PB approximation. For homogeneously charged spheres we found this range of validity to correspond well to the range that was predicted by field-theoretical studies of homogeneously charged flat surfaces. Moreover, similar ranges were obtained for colloids with a Janus-type charge distribution. It should be possible to implement effective interactions based on the mode-expanded PB theory in coarse-grained (implicit-ion) simulations for nonrotating charged Janus colloids in the domain of validity that we acquired.



# Samenvatting

In dit proefschrift hebben we zogenaamde colloïden bestudeerd, deeltjes die typisch kleiner zijn dan een duizendste van een millimeter. In moleculair medium, zoals water, ondergaan colloïden Brownse beweging, dat wil zeggen willekeurige verplaatsingen en draaiingen die worden veroorzaakt door het constante bombardement dat ze ondervinden van de veel kleinere moleculen van het medium. De willekeurige beweging zorgt ervoor dat de deeltjes door het systeem diffunderen en in principe de volledige faseruimte doorlopen. Deze verkenning van de faseruimte leidt tot een sterk verband tussen de wijze waarop colloïden zich schikken tot structuren en de manier waarop moleculaire systemen fasen vormen, bijvoorbeeld een gas, een vloeistof en een vaste stof. Het ontstaan van colloïdale structuren wordt zelforganisatie genoemd, indien zij teweeg wordt gebracht door enkel de Brownse beweging en deeltje-deeltje interacties (eventueel gestuurd door externe velden).

Een belangrijk voordeel van colloïdale materie boven atomaire en eenvoudige moleculaire systemen is de veel grotere mate van structurele complexiteit die kan worden bereikt. Dit, in combinatie met het feit dat colloïdale eigenschappen veel gemakkelijker in situ aangepast kunnen worden - waardoor colloïden bij uitstek geschikt zijn voor industriële toepassingen - is één van de hoofdredenen om deze deeltjes te bestuderen. Bovendien zijn de tijd- en lengteschalen waarop bijvoorbeeld de zelforganisatie optreedt, te observeren met behulp van conventionele optische technieken. De analogie met moleculaire systemen biedt een uitgelezen kans om via colloïden te leren over processen als smelten, nucleatie en defectvorming; in moleculaire systemen is het vaak niet mogelijk is om een dergelijke realtime, realspace analyse uit te voeren. Het bestuderen van colloïden is dan ook van fundamenteel belang.

Er gaat veel interesse uit naar de wijze waarop het gedrag van colloïden beïnvloed wordt door anisotropie in de vorm van en de interactie tussen de deeltjes. Zelfs voor ogenschijnlijk eenvoudige systemen bestaande uit enkel harde bollen is er een fascinerende rijkdom aan fasen die kunnen ontstaan. Door bollen met isotrope, zachte (korte- en langeafstands)interactie potentialen te gebruiken, worden nog complexere structuren mogelijk gemaakt. Deze complexiteit zal verder toenemen wanneer anisotrope interacties worden gebruikt. Recente ontwikkelingen in de synthese van deeltjes hebben geleid tot een grote verscheidenheid aan nieuwe colloïdale en nanobouwstenen: haltervormige deeltjes, ellipsoïden, kubussen, tetraëders, superballen, vierpoten, achtpoten, Janusdeeltjes, en nog veel meer. Met deze bouwstenen tot onze beschikking is de weg geopend voor de ontwikkeling van nieuwe fasen en structuren met ongekennde eigenschappen.

Het blijkt gunstig om computersimulaties en theoretische berekeningen uit te voeren als aanvulling op het experimentele onderzoek naar het fasegedrag van colloïdale deeltjes. Computersimulaties kunnen worden gezien als experimenten die worden uitgevoerd op een computer met een vereenvoudigd model van het betreffende systeem, waardoor er sprake is van absolute controle over de parameters die het systeem definiëren. Dit maakt het ontrafelen van de complexe fenomenologie in experimenten eenvoudiger. Een theoretische berekening gaat doorgaans uit van een hoger niveau van abstractie en een meer wiskundige benadering van de beschrijving van het systeem. De bemonstering van de faseruimte kan

in een theoretische benadering als impliciet worden beschouwd en die in een simulatie als expliciet. In dit proefschrift hebben we de simulatie- en theorieroute gevolgd voor het bestuderen van de invloed van anisotropie op het gedrag van colloïden. We hebben drie onderwerpen behandeld waarin de vorm- en/of interactieanisotropie een belangrijke rol speelt en waarop de recente ontwikkeling van de bovengenoemde deeltjes een sterke invloed heeft gehad.

- *De adsorptie van één deeltje aan een vloeistof-vloeistof grensvlak.* Het gedrag van kleine deeltjes geadsorbeerd aan een dergelijk grensvlak is niet alleen van belang voor ons begrip van de fase-overgangen en kritische verschijnselen in twee-dimensionale (2D) systemen, maar biedt ook grote mogelijkheden voor de industrie. Mogelijke toepassingen omvatten het stabiliseren van emulsiedruppeltjes die geneesmiddelen inkapselen en het voorkomen van fasescheiding voor schuimen en emulsies, die van belang zijn voor de voedingsmiddelenindustrie.
- *Kristalstructuurvoorspelling voor colloïdale systemen en het daaraan gerelateerde fasegedrag.* Ondanks de opzienbarende vorderingen in ons vermogen om de zelforganisatie van colloïden en nanodeeltjes te sturen, bestaan er nog veel open vragen met betrekking tot het bepalen van de specifieke deeltjeseigenschappen die resulteren in een gewenste structuur. Het voorspellen van kristalstructuren enkel gebaseerd op kennis van de interacties tussen de deeltjes blijkt bijzonder uitdagend. Echter, een efficiënte ab initio manier om kristalstructuren te voorspellen vormt de sleutel tot het ontwerpen van nieuwe materialen met vooraf bepaalde eigenschappen en er wordt daarom naarstig naar een dergelijk algoritme gezocht.
- *De ionverdeling rond geladen deeltjes gesuspendeerd in een diëlektrisch medium.* In veel colloïdale suspensies spelen elektrostatische interacties een belangrijke rol en het is daarom van belang de aard van deze interacties te karakteriseren met behulp van theorie en simulaties. Echter, zelfs voor systemen die enkel uit homogeen geladen bolvormige colloïden bestaan, is het bestuderen van de fysische eigenschappen met behulp van theorie of simulaties gecompliceerd vanwege de lange dracht van de Coulomb interacties. Deze langedrachtsinteracties leiden in combinatie met de aanwezigheid van bewegelijke ionen die de ‘naakte’ lading van het colloïd afschermen tot een complex veel-deeltjes probleem. Dit probleem laat zich niet eenvoudig ontrafelen waardoor het ingewikkeld is om tot effectieve colloïd-colloïd interacties te komen. Voor anisotrope ladingsverdelingen is de complexiteit van het probleem nog groter.

In hoofdstuk 2 hebben we de numerieke techniek die bekend staat als driehoeks-betegeling beschreven. Deze techniek stelt ons in staat de oppervlaktes en de lengte geassocieerd met een vlak-deeltjedoorsnede nauwkeurig te benaderen. Met behulp van onze methode kan de vrije energie van adsorptie worden bepaald voor een enkele vorm-anisotrope colloïd met homogene oppervlakte-eigenschappen aangehecht aan een vlak grensvlak in de Pieranski-benadering. We hebben vastgesteld dat langwerpige ellipsoïden en spherocylinders aan het grensvlak adsorberen loodrecht op de normaal van het grensvlak. Voor langwerpige cilindres kan er bovendien een metastabiele adsorptie zijn

parallel aan de normaal. We hebben dit onderzoek voortgezet in hoofdstuk 3, waarin we de vrije energie van adsorptie nader beschouwen en hieruit een eenvoudige theorie voor de beweging van een deeltje destilleren. Deze theorie gebruiken we om het proces te analyseren waarbij een deeltje aan het grensvlak aanhecht en uiteindelijk de evenwichtspositie en -oriëntatie bereikt. We hebben laten zien dat wanneer er metastabiele adsorptieconfiguraties zijn, de oriëntatie van een colloïd bij het eerste contact met het grensvlak een sterke invloed heeft op de uiteindelijke oriëntatie. Binnen de grenzen van ons model resulteert dit in een onverwacht grote stabiliteit van de metastabiele configuratie voor relatief lange cilindrische deeltjes. We hebben zelfs situaties gevonden waarbij het deeltje (een korte cilinder) ongehinderd het grensvlak doorkruiste, ondanks de diepe minima in de bijbehorende vrije energie, die normaliter zouden leiden tot een sterke binding aan het grensvlak. Tot slot hebben we in hoofdstuk 4 de driehoeksbetegelingstechniek uitgebreid om de vrije energie van adsorptie numeriek te kunnen bepalen voor een niet-convex colloïdaal deeltje met een oppervlaktepatroon. Zo hebben we laten zien dat de evenwichtsoriëntatie van een afgeknotte kubus in drie verschillende categorieën uiteen kan vallen; welke van de drie is afhankelijk van de details van het contacthoek patroon. We hebben ook vlak-deeltjedoorsneden voor achtpoot nanodeeltjes beschouwd om de toepassing van onze techniek op niet-convexe vormen te illustreren. Onze resultaten zijn een eerste stap op weg naar het begrijpen van het tijdsafhankelijke gedrag van anisotrope colloïden en nanodeeltjes in contact met een vloeistof-vloeistof- of zelfs vloeistof-gasgrensvlak.

In hoofdstuk 5 hebben we de floppy-box Monte Carlo (FBMC) methode beschreven, waarmee het mogelijk is om kandidaat-kristalstructuren te voorspellen. Ook hebben we twee soorten deeltjesoverlaproutines besproken: de methode van scheidende assen en een op driehoeksbetegeling gebaseerde techniek. Deze overlaproutines kunnen worden gecombineerd met de FBMC-methode om kristalstructuurvoorspelling mogelijk te maken voor systemen bestaande uit sterk vorm-anisotrope harde deeltjes. In hoofdstuk 6 hebben we de FBMC techniek gebruikt om regelmatige pakkingen van vreemd gevormde lichamen te verkrijgen. We hebben de dichtste, bekende (regelmatige) structuren onderzocht voor zeventien onregelmatige niet-convexe vormen en we hebben een aantal wiskundige vermoedens bevestigd voor de pakkingen van een grote set van 142 convexe veelvlakken. We hebben deze hypothesen ook uitgebreid en we hebben *bewezen* dat we de dichtste pakking voor romboëdrische kuboctaëders en romboëdrische enneacontrahedra hebben gevonden. Bovendien hebben we de waarde van de dichtste pakking (tot nu toe) van enneagonen en afgeknotte tetraëders verbeterd. Tot slot hebben we een familie van afgeknotte kubussen, die interpoleert tussen een kubus en een octaëder, bestudeerd en daarbij een fascinerende rijkdom aan kristalstructuren gevonden. Voor één familielid, de octaëder, hebben we de toestandsvergelijking bepaald en de eigenschappen van de verschillende fasen onderzocht. We hebben drie fasen gevonden: een vloeistof, een kubisch ruimtelijk-gecentreerde fase waarin de deeltjes vrij kunnen draaien, en de kristallijne fase. Uit de simulaties bleek dat er een eerste orde faseovergang tussen de vloeistof en kristallijne fase is. De fase waarin de deeltjes vrij kunnen draaien bleek metastabiël ten opzichte van deze overgang.

In hoofdstuk 7 hebben we de recentelijk waargenomen hiërarchische zelforganisatie van achtpoot-vormige nanokristallen (achtpoten) die leidt tot drie-dimensionale (3D) superstructuren geanalyseerd. We hebben een simulatiemodel geconstrueerd dat een eenvoudige empirische interactiepotentiaal gebruikt en in staat is om de eerste stap van de zelforgani-

satie, het vormen van ketens van achtpoten, te reproduceren. De vanderwaalsinteracties tussen achtpoten in een oplossing hebben we verkregen door middel van een Hamaker-de-Boer-achtige integratie. Met behulp van deze interacties kunnen we elementen van ons empirische model rechtvaardigen. We hebben de theoretische vanderwaalsberekeningen, gecombineerd met de experimentele en simulatieresultaten, gebruikt om een mechanisme te formuleren dat de waargenomen zelforganisatie verklaart in termen van de oplosmiddel- en richtingsafhankelijkheid van de achtpoot-achtpoot interacties.

Tenslotte hebben we in hoofdstuk 8 de ionische afscherming van geladen bolvormige Janusdeeltjes bestudeerd met behulp van Monte Carlo (MC) simulaties binnen het primitieve model dat uit gaat van expliciete ionen in een dielectrisch continuüm, voor een breed scala aan parameters. We hebben een methode geïntroduceerd om deze resultaten te vergelijken met de voorspellingen van niet-lineaire Poisson-Boltzmann (PB) theorie, die zijn afgeleid met behulp van een expansie van de ladingsverdeling in Legendre-Fourier modes. Onze methode van vergelijking en de grote set van de onderzochte parameters, stelt ons in staat het gebied waar de PB benadering geldig is te bepalen. Voor homogeen geladen bollen hebben we een goede overeenkomst gevonden met het gebied dat wordt voorspeld in veldtheoretische studies van homogeen geladen vlakke oppervlakken. Bovendien hebben we soortgelijke geldigheidsgebieden verkregen voor colloïden met een Janus-type ladingsverdeling. Effectieve interacties op basis van de mode-geëxpandeerde PB theorie kunnen nu worden toegepast in simulaties waarbij de ionen impliciet worden meegenomen voor niet-roterende Januscolloïden in het geldigheidsgebied dat we hebben vastgesteld.

# Acknowledgements

In almost a decade at Utrecht University, the last four years of which were spent working on my PhD thesis, I met a lot of people who have strongly influenced my life and in some way or another contributed to the work you are reading.

First and foremost, I would like to extend my sincerest gratitude towards René van Roij, my co-supervisor. We first met roughly eight years ago when I was a student following his second year Thermal Physics course. I was immediately captivated by his engaging style of teaching and the subject matter. It was therefore not surprising that I wrote my Bachelor's thesis on the behaviour of mixtures of rods in a dipolar external field under his supervision. This worked out so well, that no more than a year later I was back for more: this time a Master's thesis on the charging of an oil-water interface in the presence of salt. As a supervisor René's door was always open for me and I always left his office feeling more positive about the project I was undertaking, as well as more informed. I am glad that this also proved to be the case during the four years I worked on my PhD thesis. Without a doubt René is a great supervisor and has been a strong guiding force in my career choices.

I am also very grateful to Marjolein Dijkstra, the flip side of the supervisory coin, for giving me the opportunity to work on a PhD in her group. She in many ways complemented René's supervision perfectly and she taught me a lot about simulations and the scientific process in general. Discussions with Marjolein did not always go smoothly and I remember that we were often at odds about the way I did research. I did however take away a lot from Marjolein's advice, such as critical self-reflection and careful analysis of my scientific presentation, even though at times I must have come across as headstrong.

This thesis is not just the cumulation of four years of my own work, but also through collaboration the work of many others. I am truly grateful to my direct collaborators, whom I credited on a per chapter basis. Here, I would like to reiterate my appreciation for the hard work of those collaborators to whom I feel especially indebted. In particular I would like to thank Liberato Manna for giving me the opportunity to work on the octapod project and the many fruitful discussions we had concerning the experiments performed on these particles. Thinking of octapods, another name comes directly to mind. I am very grateful to Giovanni Bertoni for the lengthy discussions we had on the self-assembly of octapods - over 400 e-mails going back and forth - and the amount of work he put into making the figures for our publication, some of which I adapted for use in this thesis. I am truly thankful to Laura Fillion, Matthieu Marechal, and Tristan Hartskeerl for their contributions to the algorithm by which I could predict crystal structures comprised of anisotropic faceted particles. I would like to further thank Matthieu Marechal for providing me with his OpenGL code and for modifying it such that I could use it to render my 3D structures. Finally, I would like to mention Niels Boon, with whom I worked on charged Janus particles. Without his help this project would not have been possible.

It is also a great pleasure to thank Alfons van Blaaderen, Marjolein Dijkstra, Arnout Imhof, René van Roij and everyone who worked hard to create a group in which collab-

oration and the exchange of ideas through work discussions comes so naturally. Many thanks go out to my colleagues, for helping me out with problems, proofreading parts of the thesis, and the good times; you will have to forgive me for not mentioning all of you explicitly. I would, however, like to name my ‘partner in crime’ Johan Stiefelhagen, with whom I had a lot of fun doing unsanctioned experiments in the lab - too bad that we never got the bismuth to crystallise properly. Many thanks also to Anke Kuijk, who completed our lunch-time trio, for being good company and for putting up with all the nonsensical stories I had to tell. I am very grateful to my office mates Marjolein van der Linden and Kristina Milinkovic for sharing some of the best and worst of times with me and also for turning a blind eye to my ever increasing collection of plants, which constantly threatened to overrun the office.

I feel privileged to have friends who not only shared my enthusiasm for good food and cinema, but who were also there for me when I needed to unwind (having become frustrated with my research). Finally, I would like to thank my mother and sister for helping me with the Dutch summary, by suggesting improvements, checking my punctuation, and correcting my myriad spelling errors; and for being there for me.

# List of Peer-Reviewed Publications

This thesis is based on the following publications:

- J. de Graaf, R. van Roij, and M. Dijkstra, *Dense regular packings of irregular non-convex particles*, Phys. Rev. Lett. **107**, 155501 (2011)
- K. Miszta, J. de Graaf, G. Bertoni, D. Dorfs, R. Brescia, S. Marras, L. Ceseracciu, R. Cingolani, R. van Roij, M. Dijkstra, and L. Manna, *Hierarchical self-assembly of suspended branched colloidal nanocrystals into superlattice structures*, Nature Mater. **10**, 872 (2011)
- J. de Graaf, M. Dijkstra, and R. van Roij, *Adsorption trajectories and free-energy separatrixes for colloidal particles in contact with a liquid-liquid interface*, J. Chem. Phys. **132**, 164902 (2010)
- J. de Graaf, M. Dijkstra, and R. van Roij, *Triangular tessellation scheme for the adsorption free energy at the liquid-liquid interface: Towards nonconvex patterned colloids*, Phys. Rev. E **80**, 051405 (2009)

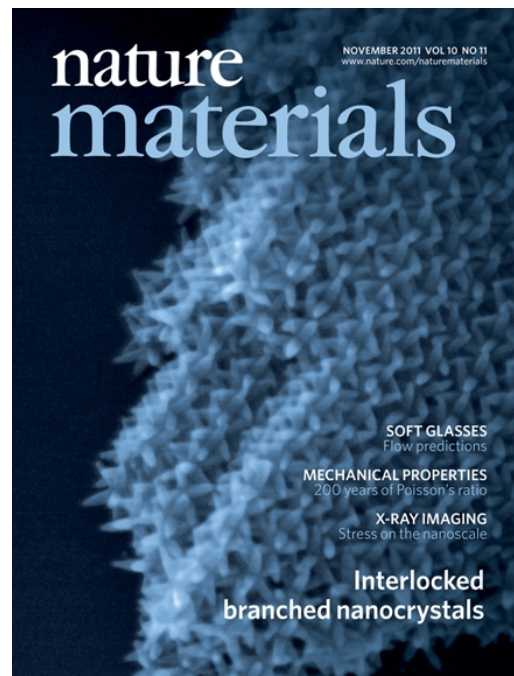


**Figure:** Covers featuring the research in Refs. [249] and [54], respectively. (left) Reprinted by permission from the American Physical Society: Physical Review Letters volume 107 issue 15, copyright (2011). (right) Reprinted by permission from Macmillan Publishers Ltd: Nature Materials volume 10 issue 11, copyright (2011).

Other publications by the author:

- M. Bier, J. de Graaf, J. Zwanikken, and R. van Roij, *Curvature dependence of the electrolytic liquid-liquid interfacial tension*, J. Chem. Phys. **130**, 024703 (2009)
- J. de Graaf, J. Zwanikken, M. Bier, A. Baarsma, Y. Oloumi, M. Spelt and R. van Roij, *Spontaneous charging and crystallization of water droplets in oil*, J. Chem. Phys. **129**, 194701 (2008)
- J. Zwanikken, J. de Graaf, M. Bier, and R. van Roij, *Stability of additive-free water-in-oil emulsions*, J. Phys.: Condens. Matter **20**, 494238 (2008)

# Oral and Poster Presentations

The contents of this thesis was presented at the following:

- 12th Dutch Soft Matter Meeting, Amsterdam, The Netherlands, Apr. 27, 2012  
Soundbite: *Poisson-Boltzmann Theory and Monte Carlo Simulations for Charged Janus Dipoles*
- SFB TR6 CODEF III, Bonn, Germany, Mar. 20-23, 2012  
Poster: *Crystal Structure Prediction and Self-Assembly of Nonconvex Branched Nanoparticles and Colloids*
- Physics@FOM, Veldhoven, The Netherlands, Jan. 17-18, 2012  
Talk: *Hierarchical Self-Assembly of Suspended Branched Colloidal Nanocrystals into Superlattice Structures*
- 11th Dutch Soft Matter Meeting, Eindhoven, The Netherlands, Nov. 07, 2011  
Invited Talk: *Hierarchical Self-Assembly of Suspended Branched Colloidal Nanocrystals into Super-Lattice Structures*
- 8th Liquid Matter Conference, Vienna, Austria, Sept. 06-10, 2011  
Poster: *Predicting Crystal Structures and Phase Behavior of Faceted Non-Convex Colloids and Nanoparticles*  
Poster: *Monte Carlo and Poisson Boltzmann Studies of Heterogeneously Charged Colloids in an Electrolyte*  
Poster: *The Dynamics of Adsorption for Anisotropic Colloids near Liquid-Liquid Interfaces*
- 10th Dutch Soft Matter Meeting, Utrecht, The Netherlands, May 23, 2011  
Soundbite: *The Assembly of Octapod Nanocrystals into Chains and 3D Superstructures*
- SFB TR6 Young Researcher Workshop, Utrecht, The Netherlands, Apr. 18-19, 2011  
Talk: *Triangular-Tessellation based Numerical Techniques and their Applications: Interfacial Adsorption and Crystal-Structure Prediction of Anisotropic Colloids*
- Physics@FOM, Veldhoven, The Netherlands, Jan. 18-19, 2011  
Talk: *Triangular-Tessellation based Numerical Techniques and their Applications: Interfacial Adsorption and Crystal-Structure Prediction of Anisotropic Colloids*
- 9th Dutch Soft Matter Meeting, Leiden, The Netherlands, Nov. 24, 2010  
Soundbite: *Triangular Tessellation: Crystal Structures of Anisotropic Particles*
- NanoSeminar, Utrecht, The Netherlands, Oct. 15, 2010  
Talk: *Triangular-Tessellation in Colloid Science: Interfacial Adsorption and Crystal Structure Prediction of Anisotropic Colloids*

- 2nd International Soft Matter Conference, Granada, Spain, Jul. 05-08, 2010  
Poster: *Towards the Dynamics of Colloid Adsorption to Liquid-Liquid Interfaces*
- 8th Dutch Soft Matter Meeting, Wagening, The Netherlands, Apr. 14, 2010  
Soundbite: *Towards Adsorption Dynamics of Colloids at the Liquid-Liquid Interface*
- IOP Complex Fluid-Fluid Interfaces, London, England, Feb. 25, 2010  
Talk: *Towards Adsorption Dynamics of Colloids at the Liquid-Liquid Interface: an Application of the Triangular Tessellation Scheme*
- Xth Dutch Polymer Days, Veldhoven, The Netherlands, Feb. 15-16, 2010  
Poster: *Interfacial Adsorption Dynamics of Colloids: Application of the Triangular Tessellation Technique*
- Physics@FOM, Veldhoven, The Netherlands, Jan. 20-21, 2010  
Poster: *Interfacial Adsorption Dynamics of Colloids: Application of the Triangular Tessellation Technique*
- SFB TR6 Young Researcher Workshop, Mainz, Germany, Nov. 26-27, 2009  
Talk: *The Adsorption Mechanism of Colloids near the Liquid-Liquid Interface: a Triangular Tessellation Scheme*

Other presentations by the author:

- Physics@FOM, Veldhoven, The Netherlands, Jan. 20-21, 2009  
Poster: *Ions Near Oil-Water Interfaces: Towards Understanding Emulsion Stability*

# Curriculum Vitae

Joost de Graaf was born in Middelburg on the second of June, 1985. He was brought up and attended primary school there: De Burg, Het Basiskwartier, and De Acasiahof. Joost graduated cum laude from secondary school, Stedelijke Scholen Gemeenschap Nehalennia, also in Middelburg. At the age of eighteen he moved to Utrecht, where he enrolled in the combined Physics and Mathematics Bachelor's at Utrecht University. In 2006 he obtained his Bachelor's degree in Physics and Mathematics (cum laude). Having a strong interest in both disciplines, Joost originally worked towards obtaining the Theoretical Physics and the Mathematics degree. Under the supervision of Dr. R. van Roij he wrote his Master's thesis on the distribution of ions near curved oil-water interfaces at the Institute for Theoretical Physics. Joost graduated cum laude in 2008 from Utrecht University obtaining his Master's degree in Theoretical Physics. In September 2008 he started his PhD under the joint supervision of Prof. dr. ir. M. Dijkstra and Dr. R. van Roij at the Soft Condensed Matter group of the Debye Institute for NanoMaterials Science, which resulted in this thesis. Joost has published four papers concerning parts of his PhD research in peer-reviewed scientific journals and has given oral and poster presentations at national and international conferences. He has also supervised a Master's student and has been a teaching assistant for undergraduate Physics courses.